Development of Perovskite and Spinel Based Molecular Level Nanocomposite Catalysts of Conventional and High Entropy Metal-Oxides for Dry Reforming of Methane

Thesis submitted for the Degree of

Doctor of Philosophy (Science)

By

Akbar Hossain
Index No. 20/21/Chem./27

DEPARTMENT OF CHEMISTRY
JADAVPUR UNIVERSITY
KOLKATA – 700032, INDIA
APRIL, 2025

JADAVPUR UNIVERSITY

KOLKATA – 700032, INDIA

Telephone: +91 33 2457 2767 (Office)
+91 8697671002 (Mobile)
E-mail : arup.gayen@jadavpuruniversity.in & agayenju@yahoo.com

Dr. Arup Gayen

PROFESSOR
PHYSICAL CHEMISTRY SECTION
DEPARTMENT OF CHEMISTRY

DATE: 28.04.2025

CERTIFICATE FROM THE SUPERVISOR

This is to certify that the thesis titled "***Development of Perovskite and Spinel Based Molecular Level Nanocomposite Catalysts of Conventional and High Entropy Metal-Oxides for Dry Reforming of Methane***" submitted by **Mr. Akbar Hossain,** who got his name registered on **16th March, 2021** for the award of Ph.D. (Science) degree of Jadavpur University, is absolutely based upon his own work under the supervision of **Dr. Arup Gayen** and neither this thesis nor any part of it has been submitted for either any degree/ diploma or any other academic award anywhere before.

Arup Gayen

Dr. Arup Gayen
Professor
Physical Chemistry Section
Department of Chemistry
Jadavpur University
Kolkata-700032

Dr. Arup Gayen
Professor
Department of Chemistry
Jadavpur University
Kolkata-700032

DECLARATION

I hereby declare that the work embodied in the present thesis titled **"*Development of Perovskite and Spinel Based Molecular Level Nanocomposite Catalysts of Conventional and High Entropy Metal-Oxides for Dry Reforming of Methane*"** is the result of investigations carried out by me in the Department of Chemistry of Jadavpur University under the supervision of **Dr. Arup Gayen** and neither this thesis nor any part of this thesis has been submitted for any degree earlier anywhere.

In keeping with the general practice of reporting scientific observations, due acknowledgement has been made whenever the work described has been based on the findings of the other investigators. Any omission which might have occurred by oversight or error in judgment is regretted.

Date:

_____

(Akbar Hossain)

Dedicated
To
All My Well-Wishers

Acknowledgement

My journey in completing the doctoral research work was a very challenging one for me, after introducing myself to the fascinating area of developing materials for heterogeneously catalyzed reactions. I faced a lot of ups and downs in this research work. However, there were a lot of people whose steadfast encouragement and support empowered me to make the right decision throughout this research journey. I would like to give every one of them my sincere respect.

I want to start by expressing my heartiest gratitude to my advisor, Prof. Arup Gayen, for welcoming me as his Ph.D. student and having a good attitude towards me. I consider myself extremely fortunate to have this chance to convey my genuine gratitude and respect to him, not only for his mentoring throughout my Ph. D. work but also for his inspiration and motivation for my future professional and personal lives. His precious advices helped me to take the right decision at the right moment during my Ph.D. journey. I was inspired to work hard by his insightful scientific contributions, freedom to work, and nice approach. His firmness and tireless effort allowed me to successfully complete my research work. His support allowed me to work on my own projects. He also gave me numerous forms of encouragement, which helped me become an energetic and self-assured person.

I would also like to express my gratitude to Dr. Md. Motin Seikh of Visva-Bharati University for his priceless motivation and guidance that benefitted me to complete my Ph.D. Throughout the course of my Ph.D. journey, he was always by my side as a friend, philosopher, and guide. His constant suggestions and evaluations of my research work greatly assisted me in moving in the forward direction.

My sincere gratitude is extended to Dr. Parthasarathi Bera of National Aerospace Laboratories (NAL), Bengaluru for his continuous assistance and positive teamwork in several cases, specially, of his expertise in analyzing and evaluating the XPS data.

Prof. Jordi Llorca of the Universitat Politècnica de Catalunya in Barcelona, Spain, has repeatedly done the XPS, HRTEM, and FESEM analyses of some of the samples for which I am extremely grateful to him. My research work was constantly made flexible by his assistance and recommendations.

I am deeply grateful to Prof. Mutta Vasundhara for her gracious assistance and analysis of XPS, HRTEM, and FESEM of some other samples at the Polymers and Functional Materials Department, CSIR-Indian Institute of Chemical Technology, Hyderabad.

I want to thank the Deans of the Science Faculty, the HoDs of the Department of Chemistry, and especially the Section-In-Charges of the Physical Chemistry Section for providing me all the laboratory facilities I needed to carry out my research.

I wish to express my special thanks to Dr. Bibhutibhushan Show (Department of Chemistry), Dr. Partha Pratim Ray (Department of Physics) and Prof. Swapan Kumar Bhattacharya (Department of Chemistry) of Jadavpur University for their help and inspiration in several occasions. I am grateful to Dr. Show for being the subject expert in the Research Advisory Committee (RAC).

I would like to express my earnest respect to Prof. Ambikesh Mahapatra, Prof. S. C. Bhattacharya, Prof. K. K. Das, Prof. C. R. Sinha, Prof. N. Chattopadhyay, Prof. R. Ghosh, Dr. Debajyoti Ghoshal, Prof. S. K. Baitalik, Dr. B. Bhattacharya, Dr. P. K. Mahapatra, Prof. S. Ghosh, Prof. C. K. Mondal, Prof. Suman Das, Prof. P. P. Parui, Dr. Sujit Kumar Ghosh, Dr. Soumik Bardhan, Dr. Shrabani Mondal, Prof. S. Chattopadhya, Prof. Saurav Das, Prof. P. Roy, Dr. M. Panda, Dr. A. Bhunia, Prof. A. Saha, Dr. S. Guha, Dr. A. Thakur, and Prof. T. Bhowmik for their inspiration, cooperation, guidance and motivation.

I especially thank Mosaraf Da, Satyajit Da and rest of the staff members of the Physical Chemistry Section for their cooperation and assistance.

No words can adequately explain how much I love my lab mates. I would like to express my gratitude to Dipak Da, Rajib Da, Sayantani Di, Mrinal Da, Kamalesh Da, Kalyan Da, Monotosh Da, Karan Di, Trilochan and Chandan for their collaboration, assistance, and for keeping the lab's atmosphere joyful. The conversations we had were very enjoyable, and I picked up a lot from their wealth of knowledge and experience.

Santu, Chiranjit, Sagnik, Pritam, Koyel, Subayu, Aishee, Anirban, Bimal and Ruchira deserve special thanks for their companionship during the M. Sc. project.

I want to extend my sincere gratitude to Manas Da, Malay Da, Ankita Di, Senjuti Di, Bappa Da, Rini Di, Snigdha Di, Yeasmin Di, Nayim Da, Sahanaj Di, Rabi Da, Ayan Da, Manisha Di, Tapas, Adwitiya, Mousumi, Anupam Da, Ariful Da, Uma Di, Debmalya Da, Prashanta da, Radhamadhab for their cooperation and cheerful company.

Additionally, I want to thank Mrs. Smita Gayen for her warm welcome. Thanks to Sanjukta and Agniva's adorable fun and amazing company.

Not a single phrases of dictionary is enough to express my gratefulness to my parents and extended family members for their constant love, affection, firm trust, and endless encouragement during every stage of my life. I couldn't have finished my doctoral programme without their well wishes, endless patience, and tremendous sacrifice. I am incredibly happy and delighted to thank my brother and sisters for their help and love.

My sincere thank goes to my wife Dr. Easira Banu for her trust and firm believe on me and stand by my side in every situation.

Finally, I want to express my gratitude to the Council of Scientific & Industrial Research (CSIR), Government of India, for providing me fellowship, DST (steered by SERB) for financial assistance, Jadavpur University for providing various instrumental facilities and last but not the least the ideal environment to achieve the highest academic degree.

Contents

Page No.

Chapter 1 ***A brief outline on nanostructured metal oxide-based catalysts for dry reforming of methane***

1.1. Introduction 1
1.2. Reasons of choosing DRM for environmental remediation 5
1.3. Types of methane reforming process 5
1.4. Factors affecting the dry reforming process 5
1.4.1. CH_4 and CO_2 ratio 5
1.4.2. Reaction temperature 6
1.4.3. Gas hourly space velocity 6

1.5. Basic requirements in choosing a photocatalyst 6
1.6. Limitations of dry reforming of methane 6
1.7. A historical review of transition metal oxides 7
1.7.1. Perovskite 7
1.7.2. Double perovskite 8
1.7.3. Spinel 9
1.7.4. Pyrochlore 10
1.7.5. Fluorite 11
1.7.6. High entropy oxides 11
1.7.6.1. High entropy perovskite oxides 11
1.7.6.2. High entropy spinel oxides 12
1.7.7. Other oxides 13
1.7.7.1. Scheelites 13
1.7.7.2. Palmeirites 13
1.7.7.3. Ruddlesden-Popper phases 13
1.7.8. Synthetic methods of oxide-based nanomaterials and nanocomposites 14
1.7.8.1. Sol-gel citrate synthesis 14
1.7.8.2. Solution combustion synthesis 15
1.7.8.3. Solid state route 15
1.7.8.4. Coprecipitation method 16
1.7.8.5. Hydrothermal method 16
1.7.8.6. Sonochemical method 17
1.8. Applications of nano oxide materials 18
1.9. Objective and scope of the present investigation 19
Reference 21

Chapter 2 ***Synthetic processes, characterization techniques, and DRM activity behavior of the materials***

2.1. Introduction 31
2.2. Chemicals used for synthesis of catalyst materials 32
2.3. Synthetic methods of the catalysts 32
2.3.1. Sol-gel citrate combustion 32
2.3.1.1. Single perovskite 32
2.3.1.2. Double perovskite 33
2.3.1.3. High entropy perovskite oxide 34
2.3.1.4. High entropy spinel oxide 35
2.3.2. Solution combustion synthesis 35
2.3.2.1. Perovskite 35
2.3.2.2. HEPO perovskite 36
2.3.2.3. HESO spinel 36
2.3.3. Ceramic method 36
2.3.3.1. Perovskite 36
2.3.3.2. Double perovskite 37
2.4 Material characterizations 37
2.4.1. Powder X-ray diffraction 37
2.4.2. Specific BET surface area (SBET) analysis 38
2.4.3. Field emission scanning electron microscopy 38
2.4.4. High-resolution transmission electron microscopy 38
2.4.5. X-ray photoelectron spectroscopy 38
2.4.6. Thermogravimetric analysis 39
2.5. DRM activity test 39
Reference 41

Chapter 3 ***Studies on Cu-doped $LaNiO_3$ perovskite catalyst***

3.1. Introduction 43
3.2. Experimental 45
3.3. Results and discussion 45
3.3.1. Powder X-ray diffraction analysis of the as-prepared perovskite samples 45
3.3.2 Screening of materials for DRM 46
3.3.3. Powder XRD studies of various forms of Cu20LNO catalyst 49
3.3.4. BET surface area measurement 53
3.3.5. Morphology study 55
3.3.6. HRTEM analysis 57
3.3.7. XPS analyses 58
3.3.8. Superiority of SGCA method over ceramic and SCS methods 61
3.3.9 Insights of catalyst regeneration at different calcination temperatures 63
3.3.10. TGA studies 67

3.4. Conclusions 68
References 68

Chapter 4 ***Studies on $La_2Ni(TM)O_6$ (TM= Cr, Mn, Fe, and Co) double perovskite materials***
4.1. Introduction 75
4.2. Experimental 78
4.3. Results and discussion 78
4.3.1. PXRD analysis of the as-prepared double perovskite materials 78
4.3.2. Materials screening 79
4.3.3. PXRD analyses of different forms of catalyst 81
4.3.4. BET surface area analyses 87
4.3.5. FESEM analyses of different forms of the catalyst 89
4.3.6. HRTEM analyses of different forms of the catalyst 90
4.3.7. XPS analyses 92
4.3.8. Advantage of SGCA process over conventional CM process 97
4.3.9. Insights of catalyst regeneration at different calcination temperature 98
4.3.10. TGA studies 99
4.4. Conclusions 102
References 102

Chapter **5** ***Studies on $Ln(Mn_{0.2}Fe_{0.2}Co_{0.2}Ni_{0.2}Cu_{0.2})O_3$ (Ln= lanthanide elements) high entropy perovskite oxides***
5.1. Introduction 109
5.2. Experimental 112
5.3. Results and discussion 112
5.3.1. PXRD studies of as-prepared HEPOs 112
5.3.2. DRM Activity Screening of Materials 113
5.3.3. PXRD analyses of different forms of La(TM)O catalyst: Correlation with the DRM data 116
5.3.4. Specific BET surface area measurement 120
5.3.5. FESEM analyses 123
5.3.6. HRTEM studies 124
5.3.7. XPS analyses 125
5.2.8. Advantage of SGCA process compared to the SCS process 127
5.3.9. Insights into catalyst regeneration: Influence of changes in calcination temperature 129
5.3.10. TGA analyses 131
5.4. Conclusions 134
References 135

Chapter 6 ***Studies on $(Mn_{0.2}Fe_{0.2}Co_{0.2}Ni_{0.2}Cu_{0.2})(TM)_2O_4$ (TM= transition metal) high entropy spinel oxides***

6.1. Introduction 141
6.2. Experimental details 144
6.3. Results and discussion 144
6.3.1. PXRD analyses of the as-synthesized HESOs 144
6.3.2. Screening of materials for DRM activity 145
6.3.3. PXRD analyses of different forms of MAlO catalyst: Relationship with DRM activity 148
6.3.4. BET specific surface area measurement 153
6.3.5. Morphology studies 155
6.3.6. HRTEM studies 156
6.3.7. XPS analyses 157
6.3.8. Advantage of sol-gel method compared to solution combustion method 160
6.3.9. Understandings of catalyst regeneration: Impact of variation of the calcination temperature 162
6.3.10. TGA studies 164
6.4. Conclusions 167
References 167

Chapter 7 ***Concluding remarks*** 174

Thesis abstract

Index No. 20/21/Chem./27

Title of the Thesis: ***Development of Perovskite and Spinel Based Molecular Level Nanocomposite Catalysts Designed from Conventional and High Entropy Metal-Oxides for Dry Reforming of Methane***

Name of the scholar: **Akbar Hossain**

The goal of this thesis is to synthesize some promising catalysts (perovskite and spinel oxides) for dry reforming of methane (DRM) reaction. DRM is a catalytic process that uses two powerful greenhouse gases, carbon dioxide (CO_2) and methane (CH_4) to synthesize syngas (H_2+CO), which is a useful feedstock for the preparation of chemicals and fuels. This reaction not only resolves the need for sustainable energy but also reduces greenhouse gas emissions. A number of industries that significantly rely on the use of hydrogen and syngas are given financial and environmental advantages through utilization of DRM reaction. The chemical equation for the DRM process is as follows:

$CH_4 + CO_2 \rightleftharpoons 2H_2 + 2CO$ ……. (1)

Despite its potential outcome, quick catalyst deactivation from sintering and carbon deposition are serious issues to commercialization of DRM reaction. Effective catalysts, mostly based on noble metals (Ru, Rh, Pd, and Pt) and transition metals (Ni, and Co), supported on a variety of materials to improve stability and activity, are the subject of recent studies. The design of modern catalysts, including the use of promoters and bimetallic systems, have been demonstrated to import improved catalytic efficiency and reduced carbon deposition. Even though DRM provides a sustainable method of producing syngas and lowering greenhouse gas emissions, its actual implementation will depend on resolving technical issues with catalyst stability and performance. To fully realize the impact of this promising technology, more research and innovation on catalyst development and process optimization are indispensable. For this research work, some catalysts based on perovskite and spinel oxides have been synthesized following various approach and deployed these catalysts for DRM reaction.

Chapter 1 provides a concise overview published in the literature on nanostructured metal oxide-based catalysts for DRM reaction, emphasizing the several relevant concerns.

Chapter 2 enunciated the many preparative methods utilized to synthesize the different catalyst components, along with the justification for selecting sol-gel citrate combustion as the optimal synthesis pathway. We have then summarized the working principle of the wide range of modern sophisticated characterization techniques that have been used to observe the physicochemical nature of the materials. These techniques include powder X-ray diffraction (PXRD), scanning electron microscopy (SEM), high resolution transmission electron microscopy (HRTEM) temperature programmed reduction (TPR), thermogravimetric analysis (TGA) and X-ray photoelectron spectroscopy (XPS). The gas-solid heterogeneous catalyst testing process have been discussed at the end of this chapter.

Chapter 3 deals with the synthesis, characterization, and catalytic activity of $LaNi_{1-x}Cu_xO_3$ (x= 0.1–0.8) perovskite nanomaterials. The current study provides a thorough analysis and comprehension of the DRM reaction employing Cu-doped $LaNiO_3$, offering a new perspective on its catalytic activity. The phase of pure $LaNi_{1-x}Cu_xO_3$ catalysts, in particular, $LaNi_{0.8}Cu_{0.2}O_3$, shows high catalytic activity towards the DRM reaction (97% CH_4 and 98% CO_2 conversion) with H_2/CO ratio ~1.2. Remarkably, the catalytic activity remains unchanged even after 100 h, despite the fact that the first perovskite phase mostly breaks down into component phases following the DRM. Based on extensive characterization of as-prepared and aged catalyst materials, we have explained the prolonged activity of the disintegrated perovskite catalysts in the context of nanocomposite formation at the molecular level in the reforming atmosphere along with the availability of Ni^0 and NiO.

Chapter 4 discusses the study of dry reforming of methane of the double perovskite series, with general formula $La_2Ni(TM)O_6$ (where, TM = Cr, Mn, Fe, and Co). All these

catalysts show significant catalytic activities towards DRM reaction. It has also been seen that La_2NiMnO_6 exhibits the highest DRM activity and its CH_4 and CO_2 conversion are 97% and 99%, respectively, along with a considerable H_2/CO ratio (0.9) after 10 h of reaction. The catalyst shows nearly similar DRM activity up to 100 h run time of DRM. After the reaction, the aged phase of the catalyst can be recovered to its original phase by heat treatment at ~ 800 °C for 3 h.

Chapter 5 gives an analysis of DRM activity of high entropy oxide perovskite series $Ln(Mn_{0.2}Fe_{0.2}Co_{0.2}Ni_{0.2}Cu_{0.2})O_3$ (where Ln = La, Ce, Pr, Nd, Sm and Gd). All these catalysts demonstrated a significant catalytic activity towards the DRM process. Out of all the synthesized catalysts, $La(Mn_{0.2}Fe_{0.2}Co_{0.2}Ni_{0.2}Cu_{0.2})O_3$ was found to exhibit the highest DRM activity. After 10 h of DRM reaction, its CH_4 and CO_2 conversions are 86% and 90%, respectively with a H_2/CO ratio close to unity. For 100 h of DRM reaction, this catalyst exhibits almost identical DRM activity and the catalyst phase form on ageing in the DRM atmosphere can be heat-treated for 3 h at 800 °C to regenerate to its initial phase.

Chapter 6 discusses the investigation of DRM activity of the high entropy oxide spinel systems MM'_2O_4 (where M = Mn, Fe, Co, Ni and Cu in equimolar proportion, M′ = Al, Cr, Mn, Fe, and Co). All the as-prepared samples of this series have shown promising DRM activities. $(Mn_{0.2}Fe_{0.2}Co_{0.2}Ni_{0.2}Cu_{0.2})Al_2O_4$ spinel oxide was found to be the most active catalyst in the series, having 97% CH_4 and 99% CO_2 conversions, respectively for 100 h of DRM. After ageing, the catalyst was degraded, but the degraded phases of the catalyst were successfully regenerated by heat treatment for 3 h even at lower temperature than the synthesis temperature. The regenerated phase also demonstrated a similar DRM activity with the as-prepared and aged samples.

Finally, we have summarized the key research findings and highlighted certain significant insights in **Chapter 7**. We have also pointed out the plausible future directions in this crucial and developing field of multifunctional nanostructured oxide materials.

Chapter 1

A brief outline on nanostructured metal oxide-based catalysts for dry reforming of methane

1.1. Introduction

The current and future challenges of modern society revolve around achieving environmental sustainability while addressing the global energy crisis. In other words, it is crucial to meet the increasing demand for energy without compromising environmental health, a longstanding issue. As a result, much of contemporary research is centered on energy-related concerns. The rapid industrial expansion, along with the reliance on coal, oil, natural gas, and other fossil fuels, as well as various human activities, release harmful gases and untreated wastewater, contributing to environmental pollution [1]. The condition of the environment is rapidly worsening due to increasing pollution and the contamination from human waste. The report published by the **European Centre for Medium-Range Weather Forecasts** (**ECMWF**) shows that in 2003, the global mean column-averaged concentration of CO_2 was around 375 ppm in the atmosphere for the annual average. On the other hand, in 2023, the CO_2 concentration was around 419.3 ppm, which is the maximum in the satellite record than any time in at least two million years, as shown in **Fig.1.1**. The annual average concentration of CO_2 was 2.5 ± 0.4 ppm in 2023 (0.6%) higher than 2022. The annual increase of CO_2 was also approximately 0.6%. Similarly, the global mean column-averaged atmospheric concentration of CH_4 was around 1750 ppb for the annual average in 2003, and 1903 ppb in 2023. The atmospheric CH_4 concentration was higher in 2023 (1903 ppb) than at any time in 800,000 years, as shown **Fig.1.2**. The global annual average concentration in 2023 was 11 ± 3 ppb, which is (0.6%) higher than in 2022. The rise in atmospheric concentrations of CO_2 and CH_4 is generally dominated by the impact of natural sources, sinks, and fossil-fuel-related human activities. Furthermore, the growing levels of greenhouse gases are contributing to global warming. As a result, we meet our growing energy demands at a high environmental cost. It is crucial to address these global challenges by focusing on clean energy solutions and a healthier environment. This requires the development of effective strategies to minimize pollutants from the environment and produce sustainable energy. Solar energy is a viable alternative, offering a clean, abundant, and accessible source of power.

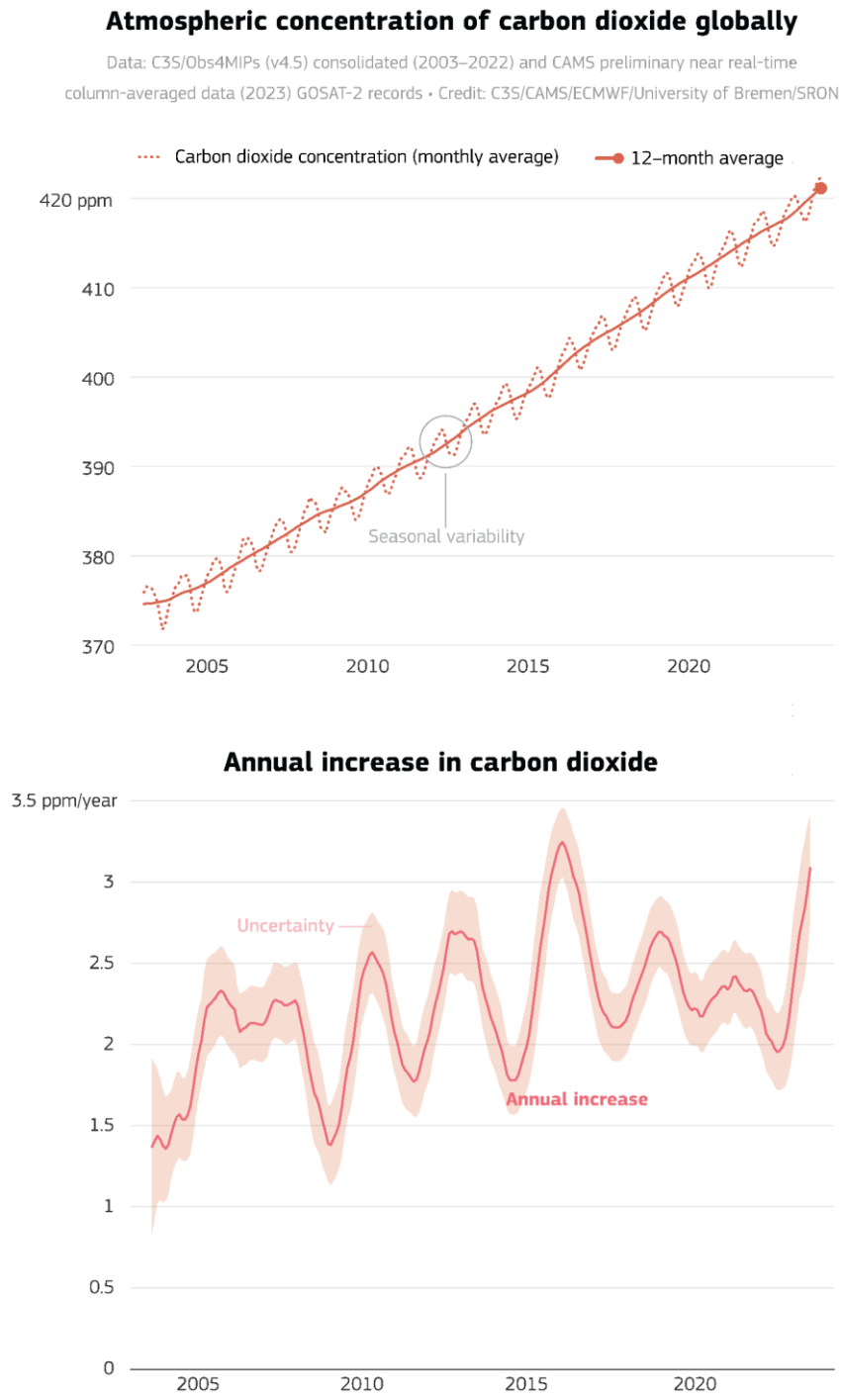

Fig.1.1. (Top) Global concentration of atmospheric column-averaged CO_2 (ppm) as measured by satellites for 2003–2023, showing monthly values (dotted line) and the trend obtained by 12-month averaging (solid line). (Bottom) Corresponding annual increase in CO_2 (ppm/year), showing monthly increase (red line) and uncertainty range (red shading). Data source: C3S/Obs4MIPs (v4.5) consolidated (2003–2022) and CAMS preliminary near real-time data (2023) GOSAT-2 records. Spatial range: 60°S–60°N over land. Credit: C3S/CAMS/ECMWF/University of Bremen/SRON.

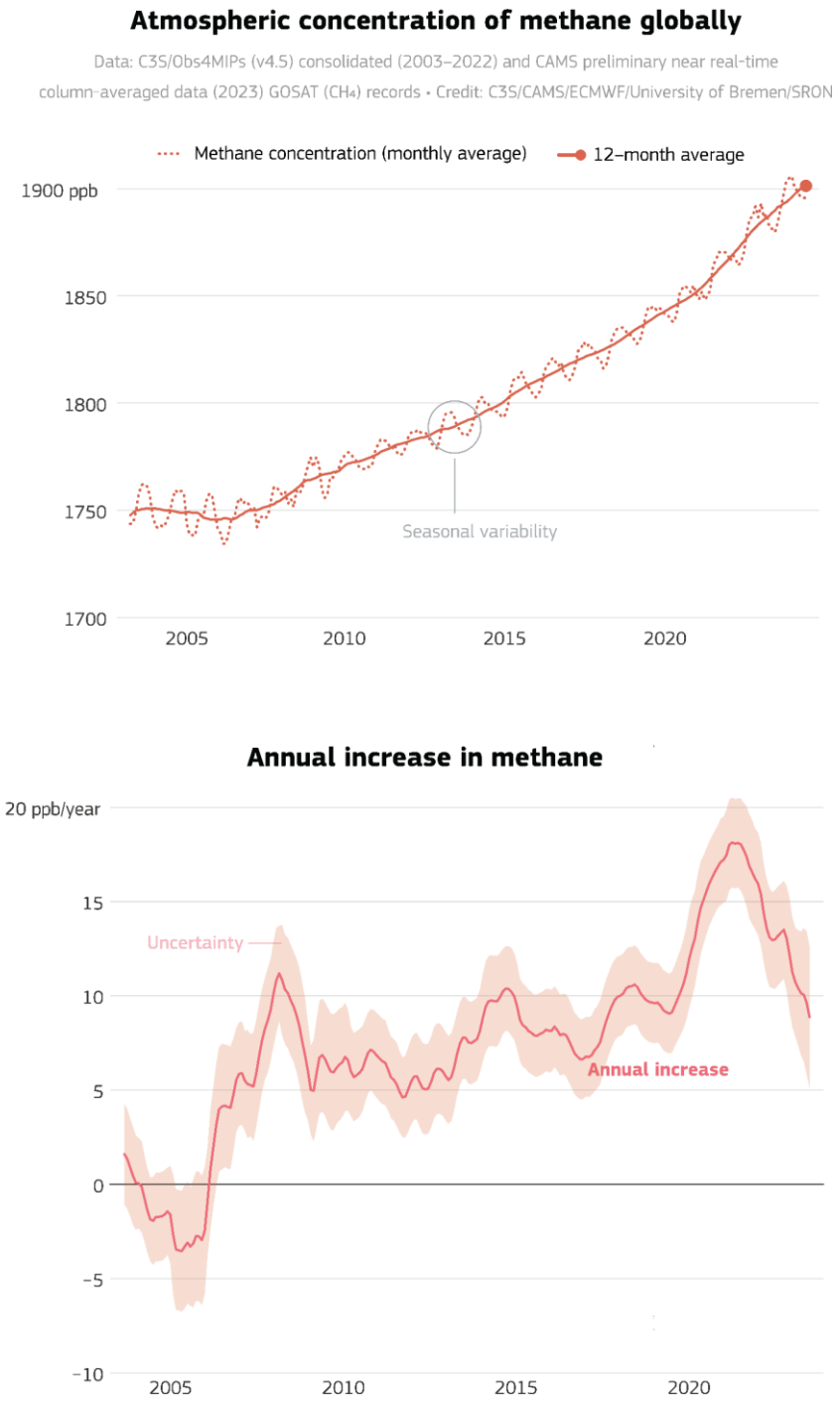

Fig.1.2. (Top) Global concentration of atmospheric column-averaged CH_4 (ppb) as measured by satellites for 2003–2023, showing monthly values (dotted line) and the trend obtained by 12-month averaging (solid line). (Bottom) Corresponding annual increase in CH_4 (ppb/year), showing monthly increase (red line) and uncertainty range (red shading). Data source: C3S/Obs4MIPs (v4.5) consolidated (2003–2022) and CAMS preliminary near real-time data (2023) GOSAT records. Spatial range: 60°S–60°N over land. Credit: C3S/CAMS/ECMWF/University of Bremen/SRON.

Hydrogen energy is considered a promising future energy source because of its environmentally friendly properties and high energy yield. Several catalytic processes are used for hydrogen production, such as dry reforming of methane (DRM), steam reforming of methane (SRM), as well as photochemical, photoelectrochemical, and electrochemical methods. DRM is an environmentally friendly and promising approach to tackling global issues and the energy crisis [2–5]. It is widely used due to its ease of catalyst preparation, low cost, and long-lasting catalyst performance. Additionally, DRM helps to reduce two major greenhouse gases (CH_4 and CO_2) while producing valuable syngas (H_2 + CO) and generating hydrogen at a relatively high degree. About 80%–85% of total hydrogen is produced through natural gas reforming as reported by Bian et al. [6]. Syngas is utilized for numerous applications, including hydrogen production [7, 8], production of diesel through the Fischer-Tropsch process [9], synthesis of methanol [10], and reduction of iron ore to produce sponge iron [11]. In the DRM process, coke deposition is the main subject of concern. The following reactions comprise the DRM process:

Dry reforming of methane [12–14]: $CH_4 + CO_2 \rightleftharpoons 2CO + 2H_2$ $\Delta H = 247$ kJ mol^{-1} …. (1.1)

Reverse water gas shift reaction [15]: $CO_2 + H_2 \rightleftharpoons H_2O + CO$ $\Delta H = 41$ kJ mol^{-1} …. (1.2)

Methane cracking [16]: $CH_4 \rightleftharpoons C + 2H_2$ $\Delta H = 75$ kJ mol^{-1} .... (1.3)

Boudouard reaction [17, 18]: $2CO \rightleftharpoons C + CO_2$ $\Delta H = -172$ kJ mol^{-1} …. (1.4)

The reactions mentioned above indicate that methane cracking (**eq. 1.3**) and carbon monoxide decomposition (**eq. 1.4**) are the primary contributors to coke formation. Amongst the catalysts based on transition metal oxides, nickel–based catalysts are typically highly active and stable for the DRM. Noble metal catalysts such as Ru, Pt, and Rh are also known for their high activity, stability, and lower coke production during DRM. However, despite their excellent performance, noble metal catalysts are not considered as a good choice due to their high cost and limited availability. In contrast, transition metal oxide catalysts serve as cost-effective and widely accessible alternatives. A major challenge with nickel-based catalysts is their tendency to undergo coking, which deactivates the active phase and decreases both reactivity and durability during the DRM process. Therefore, modifications of transition metal oxide-based catalysts are necessary to enhance their catalytic activity, stability, and resistance to coke formation. Significant global research efforts have thus been focused on identifying promising catalyst systems for DRM.

1.2. Reasons of choosing DRM for environmental remediation

The choice of heterogeneously catalyzed DRM reaction for environmental concerns is primarily due to the following advantages:

- The catalysts used in heterogeneous catalysis are comparatively easy to synthesize
- It requires a simple reaction setup to carry out the reaction
- DRM helps to minimize two main greenhouse gases (CH_4 and CO_2) while giving valuable syngas (H_2 + CO)
- Being heterogeneous catalysis, the catalyst can be easily recovered
- DRM is one of the most effective alternatives to fossil fuels in terms of product yield
- There are no harmful side products
- This process is useful for today's high energy demand

1.3. Types of methane reforming process

Reforming reactions are of two types, (a) dry reforming of methane and (b) steam reforming of methane. When we use carbon dioxide as a reformer of methane, then it is called DRM as shown in **eq. 1.1**. In this reaction, we obtain syngas as a product, which is a mixture of H_2 and CO. For this reaction, the theoretical value of H_2/CO is unity. When water is used as a reformer of methane, then it is known as SRM [19]. In this reaction, we get a mixture of H_2 and CO with the H_2/CO ratio of 3.

$CH_4 + H_2O \rightleftharpoons CO + 3H_2 \quad \Delta H = 206 \text{ kJ mol}^{-1}$ …… (1.5)

1.4. Factors affecting the dry reforming process

The reforming process involves several steps and the intermediate chemical species are sensitive to different factors. Apart from the nature and the synthetic procedure of catalyst, the dry reforming process primarily depends on the following parameters.

1.4.1. CH_4 and CO_2 ratio

In DRM reaction, the CH_4/CO_2 molar ratio is a vital parameter, which is 1:1 by stoichiometry. The variation in the ratio of CH_4/CO_2 may give a different result than the expected molar ratio of H_2/CO= one. For this reaction, CO_2 acts as the source of oxygen, so variations of oxygen could provide different results for H_2 and CO.

1.4.2. Reaction temperature

In general, the DRM is an energy-intensive reaction that requires high temperatures. Generally, 600 °C to 1000 °C and atmospheric pressure (1 bar) are suitable depending on the activity of the catalyst.

1.4.3. Gas hourly space velocity

Gas hourly space velocity (GHSV) represents the ratio of the gas flow rate to the volume of catalyst. This is typically expressed as the actual volumetric gas flow rate per hour divided by the volume of the catalyst present. The increases in GHSV lead to a decline in CH_4 conversion. This behavior is associated with the effect of residence time, as a higher GHSV reduces the contact time between the reactants and the catalyst, thereby decreasing the catalytic activity.

1.5. Fundamental requirements for selecting a DRM catalyst

The proper choice of a heterogeneous catalyst is focused by the following factors:

- Catalysts should be suitable for heterogeneous catalysis
- The synthetic method of the catalyst should be cost-effective and very simple
- The catalyst should be stable before and after the catalytic reaction
- Catalyst should have regeneration and reusable capability
- The catalysts should have recycling activity behavior

1.6. Limitations of dry reforming of methane

DRM has the following limitations that need the attention of the researchers for improving the efficiency of the catalysts.

- Instability of the catalysts
- Coke deposition
- Lack of long-time durability
- Sintering of the metal component(s)
- Breakdown of the active catalysts
- Regeneration and reusability of the catalysts

1.7. A historical review of transition metal oxides

Transition metal oxides are widely known for their applications in both homogeneous and heterogeneous catalysis, as well as in photocatalysis and photo electrocatalysis. They exhibit excellent chemical and physical stability, along with notable optical, electrical, magnetic, and semiconductor properties. The varieties of surface structures found in transition metal oxides can influence the surface energy, chemical behavior, and catalytic efficiency. The acidity and basicity of the surface atoms are affected by the coordination between the metal cation and oxygen anion, which in turn impacts their catalytic activity. Additionally, metal oxides demonstrate notable conductivity and sensitivity to electromagnetic radiation, making them ideal candidates for various redox reactions, isotope exchange processes, and surface interactions.

Oxide materials can be classified into several types, including fluorite (AO_2), perovskite (ABO_3), double perovskite ($A_2B_2O_6$), spinel (AB_2O_4), scheelites (ABO_4), pyrochlore ($A_2B_2O_7$), palmeirites ($A_3B_2O_8$), and Ruddlesden-Popper phases (A_2BO_4) etc. These oxides and their nanocomposites play a crucial role in the catalytic process. Our primary focus is to synthesize transition metal-based perovskite, spinel, and recently studied high entropy oxide (HEO) systems for DRM.

1.7.1. Perovskite

Perovskite oxide materials, represented by the formula ABO_3 are a significant category of functional oxides that display a variety of stoichiometries and crystal structures. In the perovskite structure, the A-site cations, typically in +2 or +3 oxidation states, are coordinated with 12 oxygen atoms, while the B-site cations, typically in +4 or +3 oxidation states, are coordinated with 6 oxygen atoms. The A-site cations are larger and positioned at the edges of the structure, while the B-site cations, being smaller are found at the center of the octahedron. The ionic radii of A and B cations are typically larger than 0.09 nm and 0.051 nm, respectively. Additionally, various elements can be substituted at the A and B sites, leading to the formation of a wide range of substituted perovskite materials. The difference in the ionic sizes of the A and B cations often causes lattice distortions, which can alter the symmetry of the structure, resulting in cubic, orthorhombic, tetragonal, monoclinic, rhombohedral, or triclinic forms. These structural changes can influence catalytic properties, photoexcitation behavior, and charge transfer dynamics. Furthermore, modifications such as doping with metals or nonmetals, forming composites, making cation or oxygen vacancies, and altering the

composition and symmetry can enhance the band structure, optical properties, adsorption characteristics, and catalytic efficiency of perovskite materials. As a result, the catalytic performance of perovskites can be easily adjusted due to the flexibility of lattice site modifications. Perovskite oxide materials are highly active for DRM [20–24].

In a very recent report, we have shown that copper doped lanthanum nickel oxide single perovskite ($LaCu_{0.2}Ni_{0.8}O_3$) is a highly active catalyst for DRM [25] that forms the basis of chapter 3 of this thesis.

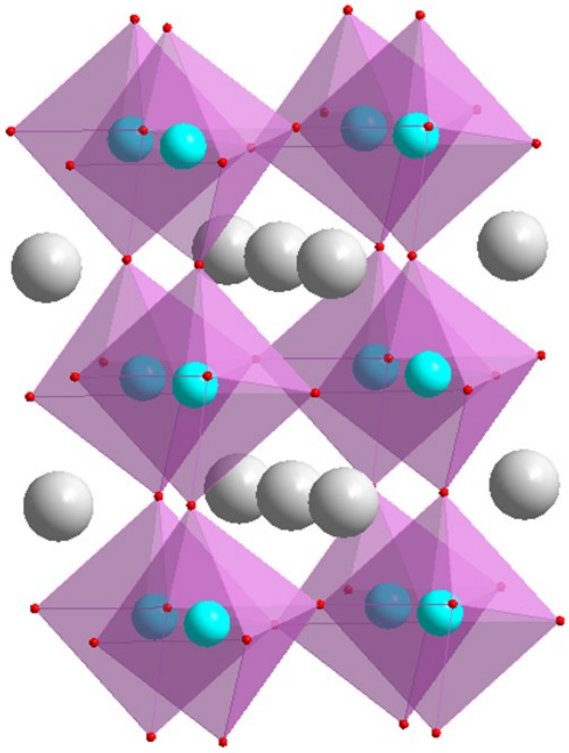

Fig.1.3: Crystal structure of single perovskite ABO_3.

1.7.2. Double perovskite

Several coexisting features, including ferromagnetic ordering, magnetoresistance, and magnetodielectric coupling, make double perovskite (of general formula $A_2B_2O_6$) materials a natural choice of researchers interested in multifunctional properties. In this structure, A site metal may be the same or different and similarly, B site atom may also be the same or different. As a result, it offers excellent potential for spintronics applications [26]. The $A_2B\ B'O_6$ double perovskite structure has an alternate arrangement of corners, sharing BO_6 and $B'O_6$ octahedra. The spaces between the two octahedra are occupied by A site metal ions. $A_2B\ B'O_6$ typically exhibits antisite disorder or partial interexchange of B and B′ ions. The ferromagnetic ordering

in $A_2B\,B'O_6$ is caused by the super exchange interaction between alternately organized B^{2+} and B'^{4+} ions at Curie temperature (T_c) of 280 K [27]. Several reports suggest that double perovskite materials serve as a good catalyst for DRM [20, 28–31]. In chapter 4, we have included the findings on DRM behavior of several double perovskite materials, among which La_2NiMnO_6 is shown to be the most active catalyst [32].

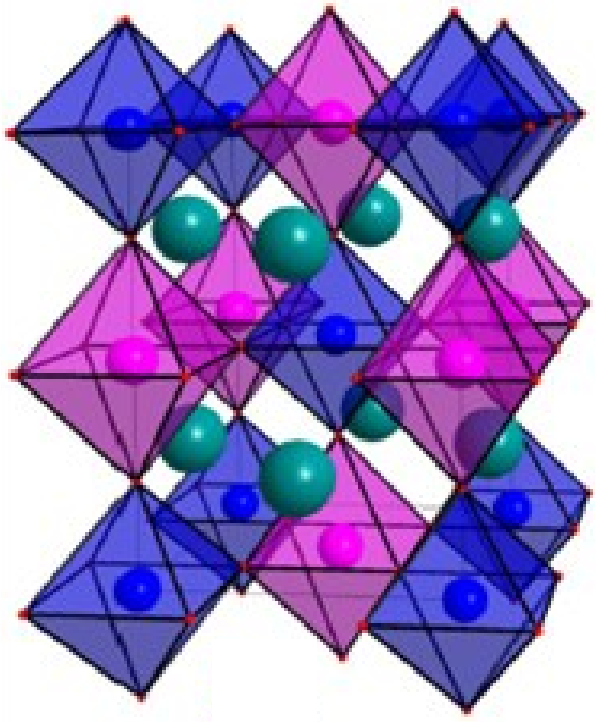

Fig.1.4: Crystal structure of double perovskite $A_2B_2O_6$.

1.7.3. Spinel

Spinel oxides are typically ternary compounds with the general formula AB_2O_4, where A and B are cations with oxidation states of +2 and +3, respectively. In the crystal structure of spinel oxides, the cations occupy either octahedral (Oh) or tetrahedral (Td) lattice sites, while the oxygen atoms are arranged in a cubic close packed configuration. The distribution of A^{2+} and B^{3+} cations between Oh and Td sites is influenced by the crystal field stabilization energy (CFSE), and based on how these sites are occupied, spinel oxides can be classified into three types: normal spinel, inverse spinel, and mixed spinel. In a normal spinel structure, the A^{2+} cations occupy the Td sites, and the B^{3+} cations are located in the Oh sites, which is usually represented by $[A^{2+}]_{Td}[B_2{}^{3+}]_{Oh}O_4$. An example of this type is $ZnFe_2O_4$. In an inverse spinel, all the A^{2+} cations and half of the B^{3+} cations occupy the Oh sites, while the remaining B^{3+} cations

occupy the Td sites. This structure is represented as $[B^{3+}]_{Td}[A^{2+}B^{3+}]_{Oh}O_4$, with examples including Fe_3O_4, $CoFe_2O_4$, $CuFe_2O_4$, and $NiFe_2O_4$. In a mixed spinel structure, both A^{2+} and B^{3+} cations are distributed across both the Td and Oh sites. The structural formula for mixed spinel is represented as $[A^{2+}_{1-d}B^{3+}_{d}]_{Td}[\ A^{2+}_{d}B^{3+}_{1-d}]_{Oh}O_4$, where "d" indicates the degree of inversion. An example of a mixed spinel is $MnFe_2O_4$, where d= 0.2, and its structural formula is $[Mn^{2+}_{0.8}Fe^{3+}_{0.2}]_{Td}[\ Mn^{2+}_{0.2}Fe^{3+}_{0.8}]_{Oh}O_4$. Several research works have been done on DRM using spinel oxides as catalyst [33–37].

Spinel oxides materials are categorized into the following groups

- Aluminium based spinel (Aluminate):

  MAl_2O_4 (M = Be, Mg, Mn, Fe, Co, Ni, Cu, Zn, Ba, etc.)
- Iron based spinel (Ferrite):

  MFe_2O_4 (M = Mn, Fe, Co, Ni, Cu, Zn etc.)
- Chromium based spinel (Chromite):

  MCr_2O_4 (M = Mn, Fe, Co, Ni, Cu, Zn etc.)
- Others metal oxides-based spinel structure:

  Coulsonite: FeV_2O_4

  Magnesiocoulsonite: MgV_2O_4

  Ringwoodite: Mg_2SiO_4 and Fe_2SiO_4

1.7.4. Pyrochlore

The pyrochlore crystal structure is commonly found in compounds with the general chemical formula $A_2B_2O_7$, where A and B represent different-sized cations. This structure is often observed in various oxides and is characterized by a well-ordered, cubic framework. The pyrochlore structure crystallizes in the F-dodecahedral (Fd-3m) space group and is composed of a three-dimensional network of corner-sharing tetrahedra and octahedra. In this arrangement, the A cations are situated at 8-fold coordinated corner of the structure, while the B cations occupy 6-fold coordination sites at the center of the octahedral units. The oxygen atoms are positioned in a way that supports the formation of both tetrahedral and octahedral configurations with the metal ions. Typically, the A cations are larger ions, often from the rare earth or alkaline earth elements, whereas the B cations are smaller, frequently transition metals or other smaller ions. The pyrochlore structure is of significant interest due to its stability and its unique electronic, magnetic, and ionic properties, making it a valuable subject of study in solid-state physics, materials science and in DRM [38–41].

1.7.5. Fluorite

Fluorite oxides contain oxide ions (O^{2-}) instead of fluoride ions (F^{-}). A well-known example of a fluorite oxide is cerium dioxide (CeO_2). The general formula for these compounds is MO_2, where M represents a metal cation and O represents an oxide ion (O^{2-}). The metal cations occupy the tetrahedral sites, typically being 8-fold coordinated with oxide ions in a cubic arrangement. Some common fluorite oxides are (ceria, CeO_2 i.e., cerium (IV) oxide), (zirconia, ZrO_2 i.e., zirconium (IV) oxide), and (uranium dioxide, UO_2 i.e., uranium (IV) oxide) occupy the tetrahedral sites, and the overall structure offers high symmetry, contributing to the stability and efficient ionic conductivity of the material. Fluorite oxides like CeO_2 and ZrO_2 are particularly valued for their oxide-ion conductivity, making them useful in applications such as solid oxide fuel cells (SOFCs) catalysis and in DRM [42–47]. Fluorite oxides share the same structural framework as fluorite (CaF_2).

1.7.6. High entropy oxides

High entropy oxides are oxides that consist of five or more distinct metal cations and maintain a single-phase crystal structure. The first HEO, $(MgNiCuCoZn)_{0.2}O$, with a rock salt structure, was introduced by Rost et al. in 2015 [48]. Since then, HEOs have been successfully synthesized in various crystal structures, such as fluorite [49], perovskite [50, 51], and spinel [52, 53]. These materials are currently under investigation for their potential as multifunctional materials. The concept of high entropy materials was first explored through high entropy alloys (HEAs), which were initially reported by Yeh et al. in 2004 [54]. HEAs consist of five or more major metallic elements and have demonstrated promising mechanical properties, such as maintaining strength and hardness at elevated temperatures. The field of high entropy materials got expanded to encompass high entropy metal diborides, carbides [55, 56], sulfides [57, 58], and alumino-silicates [59].

1.7.6.1. High entropy perovskite oxides

In the case of high entropy perovskite oxides (HEPOs), A or B site is substituted by five or more metals in equimolar proportion. The presence of these metals with different radii gives different bond lengths, which facilitates various catalytic reactions. The improper charge balance helps to form oxygen vacancies in the catalyst material, which is very much needed for catalytic reactions. Jiang et al. have synthesized a high entropy oxides perovskite

$Sr(ZrSnTiHfMn)_{0.2}O_3$ [60], substituted the B site by five equimolar atoms. There are some recent reports available in open literature on DRM using HEPO catalysts [61–63].

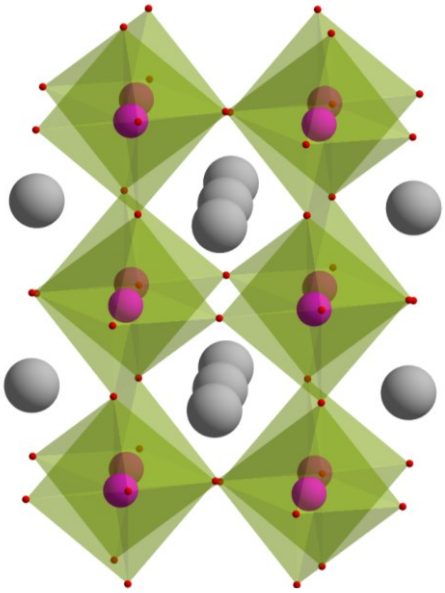

Fig.1.5: Crystal structure of HEPO $La(M_1M_2M_3M_4M_5)O_3$.

1.7.6.2. High entropy spinel oxides

In similarity with high entropy perovskites, in high entropy spinel oxides (HESOs), the A or B site can be substituted by compatible metal ions to synthesize the desired high entropy spinel. Dabrowa et al. have prepared high entropy spinel oxide $(CoCrFeMnNi)_{0.6}O_4$ [64], by substituting both the A and the B sites simultaneously. Thus, there is a large variety of spinel oxide materials that are suitable for DRM [37, 61, 65, 66].

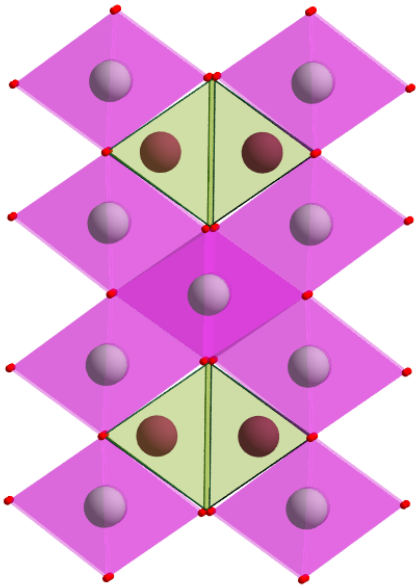

Fig.1.6: Crystal structure of HESO $(M_1M_2M_3M_4M_5)Al_2O_4$.

1.7.7. Other oxides

1.7.7.1. Scheelites

The scheelite group minerals have the general formula ABO_4, where "A" typically represents a metal cation, and "B" is a heavier metal, often tungsten or molybdenum. The oxygen atoms are arranged around the B cation to form a $[BO_4]^{2-}$ tetrahedron. Specifically, in scheelite ($CaWO_4$), the tungsten (W) is surrounded by four oxygen atoms, forming this tetrahedral structure. The A-site cation, such as calcium (Ca), is coordinated with more oxygen atoms, generally six, leading to a 6-fold coordination. Scheelite crystallizes in the tetragonal system, with crystals often showing elongation or a tabular shape along the c-axis. In this structure, the tungsten ions are situated within the tetrahedra formed by oxygen atoms, while calcium ions are interspersed between these tetrahedra to stabilize the overall structure. The scheelite group also includes related minerals, like wulfenite ($PbMoO_4$), which share similar structural features but have different cations at the A and B positions [67]. For example, DRM activity of $SrWO_4$ and $Sr_{0.5}Ce_{0.35}WO_4$ has been reported by Passos et al. [68], where $SrWO_4$ catalyst has shown 40% methane conversion but the doped system has shown comparatively higher methane conversion of 65%.

1.7.7.2. Palmeirites

Palmeirites ($A_3B_2O_8$) seems to be a type of complex oxide, but detailed information about this specific compound is quite scarce. Based on its formula, $A_3B_2O_8$ suggests a compound containing three atoms of element A, two atoms of element B, and eight oxygen atoms. This structure likely forms a complex oxide, potentially with a network or layered arrangement where oxygen atoms bridge the metal cations (A and B). To fully understand its crystal structure, knowing the specific elements that correspond to A and B would be crucial. In many oxide compounds, A and B typically represent different metal cations, which could be transition metals or rare earth elements, and the oxygen atoms are arranged in a way that ensures the charge balance to stabilize the structure.

1.7.7.3. Ruddlesden-Popper phases

Ruddlesden-Popper (RP) phases with the formula A_2BO_4 are a group of materials with a layered perovskite structure. These oxides are characterized by alternating layers of perovskite (ABO_3) and rock salt-like (AO) units. In the perovskite layer, the A cations are positioned in larger octahedral sites, while the smaller B cations occupy octahedral sites surrounded by oxygen atoms. The rock salt layer consists of A cations arranged in a simple

cubic lattice, with oxygen anions filling the interstitial spaces between them. The RP structure is formed by the stacking of these alternating layers, with each A_2BO_4 unit containing two A cations for every B cation, and oxygen atoms linking both types of cations. A well-known example of a Ruddlesden-Popper oxide is La_2NiO_4, where La is the A cation and Ni is the B cation, forming a structure made up of alternating $LaNiO_3$ and LaO layers. In summary, Ruddlesden-Popper oxides such as A_2BO_4 exhibit a distinctive layered configuration that combines perovskite and rock salt-like structures, contributing to their unique properties [1, 20 22]. DRM activity of $Sm_{1.5}Sr_{0.5}NiO_4$ Ruddlesden-Popper phase have been reported by Nezhad et al. [69]. Methane and carbon dioxide conversion of $Sm_{1.5}Sr_{0.5}NiO_4$ catalyst were 89 and 92%, respectively. In a report, Marin et al. have shown the formation of Ruddlesden-Popper phase in DRM medium from $La_{0.8}Sr_{0.2}Co_{0.9}M_{0.1}O_3$ perovskite oxide [70]. For 10 h of DRM, the catalyst CH_4 conversion was 80% and CO_2 conversion was 90%. The catalytic role of La_2NiO_4 in DRM has been investigated by Aathira et al. [71], where the catalyst is in the most active form at 900 °C, converting 89.9 and 95% of CH_4 and CO_2, respectively, with H_2/CO ratio 0.49.

1.7.8. Synthetic methods of oxide-based nanomaterials and nanocomposites

Metal oxides, mixed metal oxides, and particularly their nanocomposites are widely recognized as benchmark catalysts in the field of heterogeneous catalysis. These promising features of oxides and nanocomposites are constant inspiration of researchers in developing various types of new and novel materials with diverse compositions, resulting in unique properties for environmental and other applications. The preparation techniques for these classes of materials are similar and include the methods such as sol-gel citrate synthesis, solution combustion synthesis, hydrothermal, solid-state synthesis, template-assisted precipitation, sonochemical processes, microwave irradiation, chemical vapor deposition, plasma techniques, soft chemical treatments, coprecipitation, microemulsion-based methods, electrochemical processes and others. A summary of the synthetic methods used to prepare the samples for this research work and some other methods are discussed below.

1.7.8.1. Sol-gel citrate synthesis

The sol-gel citric acid (SGCA) combustion method usually produces materials with a specific shape and consistent size. Hence, it is one of the most promising chemical methods for the synthesis of catalyst materials. Because of its simplicity, this synthetic approach is well-known in the field of nanotechnology. By altering the pH, annealing temperature, and reaction

conditions, it is feasible to change the morphology and particle size in this method. Alkoxide-based metal precursors undergo hydrolysis and polycondensation to form an inorganic bridging network in SGCA process. The solvated metal precursors that form through a colloidal type solution are referred to as "sol". The resulting sol is subsequently transformed into a dense liquid phase called "gel", which is a polymeric network. In this synthetic method, a “sol” is developed by dissolving metal precursors and chelating agent(s) in a suitable amount of solvent. Hydrolysis of metal precursors that are chemically unstable in aqueous medium can be avoided by appropriate addition of a strong acid. The resulting solution is then heated at ~180–200 °C to evaporate water, forming the metal-citrate gel, which starts to burn (~200–250 °C) into a fluffy pile immediately upon completion of evaporation. Following a thorough grinding to fine powder, the fluffy mass is then calcined at a higher temperature to eliminate the nitrate residue and other impurities, resulting the final production of the necessary SGCA materials [5, 16, 20, 22–25, 26, 72–76].

1.7.8.2. Solution combustion synthesis

The solution combustion synthesis (SCS) is one of the easiest and minimum time-consuming processes. It is very often used to prepare the catalyst samples because the phase of the catalyst forms at a comparatively lower temperature. This method is widely accepted as it is very easy to handle and the desired sample may be obtained within a few minutes. The preparation of the catalyst in the SCS method involves combustion of the stoichiometric composition of the metal salts with organic fuel, dissolved in minimum volume of water in a borosilicate dish. The homogenized solution then needs to be transferred into a preheated muffle furnace controlled at ~300–500 °C. The solution gets ignited when it reaches the point of spontaneous combustion, giving an immediate flame and a solid, fluffy end product. The sample is then thoroughly ground into powder to get the desired catalyst material [77–90]**.**

1.7.8.3. Solid state route

A straightforward chemical process for preparing metal oxide-based catalysts is the solid-state approach. Because of its simplicity, it is the traditional and widely used method for the preparation of different kinds of pure oxides, and doped oxides as well as their nanocomposite materials. This method involves physically mixing the pre-synthesized parent materials or components of the nanocomposites by grinding them in a pestle and mortar for about 1 to 3 h, and then drying them at a low temperature (about 80 to 100 °C) to generate the desired nano oxide materials [91–97]. It is then used directly for catalytic application purposes.

Sometime the desired phase of the catalysts does not obtain due to the lesser degree of mixing between the parent components. In order to address these issues, many researchers have employed heat treatment or ultrasonication of the parent components mixture in an appropriate solvent, such as ether, water, or alcohol, followed by solvent evaporation at about 80 °C and, lastly, calcining the solid mass at higher temperatures, which improves the mixing between the parent phases. It should be noted that when heat treatment is done to produce nanocomposite materials, the temperature does not rise above the initial synthesis temperature of the parent materials.

1.7.8.4. Coprecipitation method

One of the best and most popular methods is coprecipitation for the synthesis of metal oxides and doped oxides as well as nanocomposite materials. This approach is a very straightforward, efficient, inexpensive, and time saving synthetic approach and is based on the bottom-up methodology. The surfactant assisted coprecipitation approach requires less chemicals because the surfactant serves as template, structure directing agent, and element source. Because the parent phases easily make good heterojunction contact, it is also a very popular and practical method for the synthesis of nanocomposite materials. Initially, the metal salts are taken in a beaker with minimum volume of water. Then an appropriate precipitating agent is added to carry out the precipitation reactions. The coprecipitation method involves the following reaction steps: (i) mixing the parent precursors with water to form a saturating condition; (ii) nucleation of precursors; (iii) growing the precursor nuclei; (iv) aggregating the nuclei; (v) separating the precipitate from the aqueous solution and drying the obtained product; and (vi) calcining the dry precipitate to form the desired materials [98−101].

1.7.8.5. Hydrothermal method

The hydrothermal process is a chemical reaction used to get metal oxides, mixed metal oxides, and their nanocomposite systems under certain conditions of high temperature and high water-pressure. This method uses a particular reactor apparatus called an "autoclave" or "bomb," which is constructed of high-quality stainless steel. To prevent contamination, a teflon beaker is placed inside the autoclave’s inner core. This process produces different kinds of catalyst materials with unique morphologies and particle sizes. This kind of synthetic method needs water or any other non-explosive solvent. Typically, the hydrothermal process is carried out at extremely high pressure and low temperatures. This process involves completely

dissolving the metal precursors with precise stoichiometry in water or other solvents, then vigorously stirring the mixture to get a homogenised solution. It should be mentioned that the solvothermal method is the term used when other solvents are employed in place of water. After that, the homogenized solution is moved to the stainless-steel autoclave lined with teflon. After being tightly locked, the autoclave is placed in an oven that is kept at a precise temperature for certain time. To obtain the desired material, the end product is repeatedly cleaned with water and alcohol before being dried in an oven. When preparing catalyst materials for a variety of catalytic applications, the hydrothermal method offers greater advantages than the other methods [102–106]. The approach has many benefits: (i) it is well known and relatively cost-effective method for getting metal-oxide and nanocomposites; (ii) it has quick reaction kinetics; (iii) it produces a variety of morphologies, surface areas, and particle sizes; (iv) it can be used to prepare new kinds of composite materials at the nano scale; (v) it is a pollutant free synthetic route because the reaction is carried out in a closed environment; (vi) it is associated to high material purity and large scale production rate; and (vii) it doesn't require addition of any external reagent or surfactant.

1.7.8.6. Sonochemical method

Considering an innovative and efficient technology in nanoscience for the development of metal oxide catalysts, the sonochemical mixing method is relatively new and has been applied by numerous research groups since 2006. The sonochemical method is the most basic and simple. The key benefits of this process are as follows: (1) an increase in effective surface areas and active sites; (2) the formation of uniformly distributed particles; (3) a very easy, low-cost, and time-efficient procedure; and (4) an efficient method for developing nano-sized catalysts. Typically, this process involves mixing the metal precursors in an appropriate solvent, then stirring with a magnetic stirrer. The precipitating agent is then gradually added to the mixture solution after it has been ultrasonicated for the required time period. The final product is then obtained by drying and heating to the necessary temperature. Well dispersed parent materials can combine sonochemically to form an effective nano-catalyst materials since the development of the nano-sized catalyst is dependent on the degree of mixing associated with the dispersion.

1.8. Applications of nano oxide materials

Nanomaterials have numerous applications in diverse areas of interest. A few of these include paints [107], filters [108], insulation [109], biosensor [110], medicines [111, 112], semiconductor [113], agriculture [114], electronics [115], cosmetics [116], automobiles [117] etc. Nanomaterials are used in paints to enhance UV protection and cleaning purpose. Nanostructured species are capable of producing high quality filters. Nanotechnology was utilized in the air filtration industry to stop the MERS virus from spreading in Saudi Arabian hospitals in 2012. Additionally, it has been discovered that oxide nanoparticles work well as catalysts for a variety of heterogeneous chemical reactions [118−121], such as those involving gas-solid, liquid-solid, or gas-liquid interactions. Nanomaterials can be used to remove trace quantities of hazardous products from the environment.

Nanosized materials with interesting physical and microstructural features can be made to have strong catalytic properties, stability, and sensitivity by modifying their size, shape, and morphology. These materials could be useful in many different applications. The inherent possibilities of nanoparticles inspire materials chemistry and physics researchers to develop better nanomaterials and explore their as-yet-undiscovered features. Nanomaterials can have intriguing properties for a number of reasons;

- Because of its smaller size, the nanomaterial has a high surface area to volume ratio
- A nanomaterial's primary component must have a large surface area since this greatly increases the probability of contact between the catalyst and the molecules of the reactant. In the heterogeneous catalytic process, greater contact over a nano catalyst enables a better reaction rate that is close to its homogeneous equivalent
- Because of the materials' easy control over size, shape, and morphology, it is possible to synthesise consciously the materials that are specifically needed for a given catalytic application. It is possible to adjust the properties of materials by developing synthetic procedures
- Even with the systematic and cautious application of numerous procedures such as distillation, chromatographic separation, and extraction, the removal of microscopic quantities of homogeneous catalyst continues to be a difficult problem. The ease with which nanomaterials can be separated in heterogeneous catalysis, in addition to their performance, is highly helpful in this regard. Metal contamination is strictly regulated, particularly in the drug and pharmaceutical industries, so it is essential that it be kept separated from the final product

- Using magnetic nanoparticles as a catalyst makes it easy and efficient to separate the catalysts from the reaction mixture using an external magnet

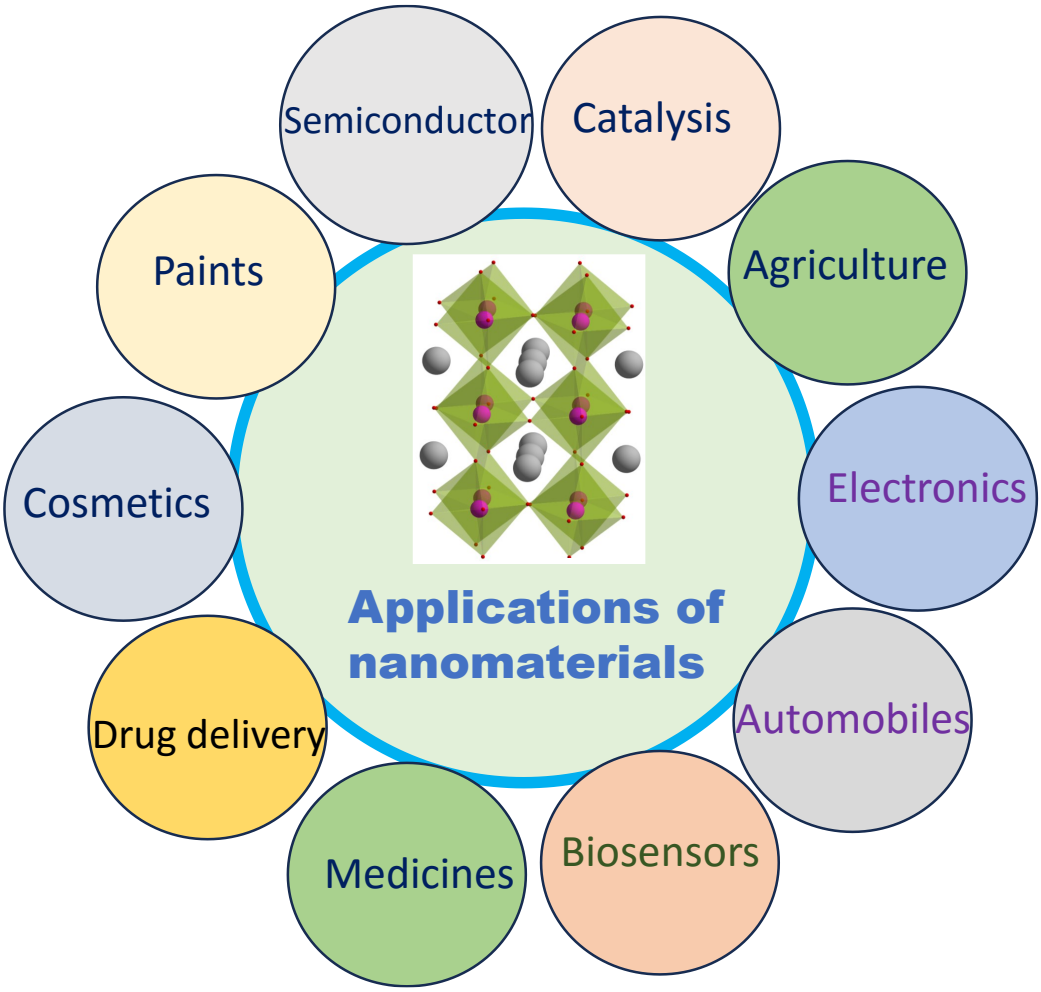

Fig.1.7: Applications of nanosized oxide materials in various field.

1.9. Objective and scope of the present investigation

It is apparent from the above discussion that the synthesis and development of nanomaterials based on metal oxide materials offer a significant opportunity in the field of catalysis. These synthesized materials show great promise for a range of catalytic uses. The activities of humans have a significant impact on our environment. It is especially important to reduce greenhouse gases (GHGs) emissions. DRM is a promising alternative as it uses two greenhouse gases to give effective syngas as product.

A highly active catalyst that satisfies the requirements must be less expensive, environmentally benign, have sufficient physical and chemical stability, be simple to synthesize etc. According to this perspective, catalyst materials based on metal oxides and their nanocomposite forms are by far the most suitable option for heterogeneously catalysed

reactions. There are several advantages of metal oxide-based nano catalyst materials in DRM: (i) nanosized metal oxide catalysts are very effective, (ii) physico-chemical properties of nano oxide materials are very prominent, (iii) there is no problem of catalyst separation, (iv) catalysts show very high recycling activity, (v) its catalytic efficiency as well as durability is very promising.

In DRM, metal oxides mostly act as catalysts. The oxide catalysts help with the activation of methane and carbon dioxide by providing active sites for adsorption that facilitates the desired DRM reactions. The catalytic performance can often be optimized by influencing the size and dispersion of the active metal particles, enhancing oxygen mobility, and adjusting the surface acidity/basicity of the catalysts. Typically, common metal oxides are used, including basic oxides, rare earth metal oxides, and transition metal oxides, which can be used in mixed oxide combinations to achieve better stability and activity against carbon deposition. Some metal oxides such as lanthanum oxide La_2O_3, alumina (Al_2O_3), ceria (CeO_2), or zirconia (ZrO_2), MnO_2 often serve as supports for active metal catalysts. The support materials help to disperse the active metal catalyst, increasing its surface area and enhancing its catalytic efficiency. They stabilize the active catalysts against sintering and deactivation. Support materials also improve the stability and durability of the metal oxide catalysts. Certain metal oxide materials, predominantly ceria and zirconia, have strong redox properties. These materials can easily undergo cycling between different oxidation states (Ce^{3+} and Ce^{4+} in the case of ceria), which is crucial for the activation of CH_4 and CO_2. The ability of metal oxide catalysts (such as CeO_2 and ZrO_2) can participate in storing and releasing oxygen, which is beneficial for DRM. These help for the activation of reactant species and facilitate the DRM reaction. Oxygen from the metal oxide-based phases helps to activate methane and carbon dioxide, promoting the formation of intermediate species essential for the reaction. This also helps in mitigating coke deposition (coking), a common issue for DRM. Metal oxide support materials help to the stability of the catalyst by stopping the metal from sintering or deactivating due to coking. Materials like ceria or alumina can provide structural integrity to the catalyst, prolonging its durability under the selected reaction conditions of DRM. The DRM reaction is prone to coking on the catalyst surface, especially in the absence of appropriate oxygen atoms. Metal oxides, particularly those with redox activity, can help prevent the build-up of carbon by facilitating the removal of carbon species through the oxygen release mechanism.

Several metal oxides act as a promoter in DRM, like CuO, MnO. So, the *in situ* formation of these metal oxides promotes the DRM. Basically, metal oxide-based catalysts act as structural supports, redox participants, and stabilizers, enhancing the catalytic process in

DRM while preventing issues such as sintering and coking. For the improvement of the metal oxide catalysts, pure metal oxides have been doped as well as their nanocomposite materials also synthesized. Our current research focusses on the synthesis of metal oxide-based pure and doped nanocatalyst systems using various synthetic approaches, including SGCA synthesis, SCS, and solid-state methods, in light of the present state of heterogeneous catalysis, and ways to further contribute to the development of the field. Numerous techniques, including BET surface area, transmission electron microscopy (TEM), high resolution transmission electron microscopy (HRTEM), field emission scanning electron microscopy (FESEM), powder X-ray diffraction (PXRD), and X-ray photoelectron spectroscopy (XPS), have been used to characterize the synthesized materials. The catalytic activity of the materials has been tested for the DRM.

Reference

[1] N. Zibouche, M.S. Islam, Structure-electronic property relationships of 2D ruddlesden−popper tin and lead-based iodide perovskites, ACS Appl Mater Interfaces., 2020, 13, 15328–15337.

[2] N. Das, S. Kandimalla, Application of perovskites towards remediation of environmental pollutants: an overview, Int. J. Environ. Sci. Technol., 2017, 14, 1559–1572.

[3] O.A.L. Santos, M. Sneha, T. Devarani, M. Bououdina, B.P. Backx, J.J. Vijaya, S. Bellucci, Review—perovskite/spinel-based graphene derivatives electrochemical and biosensors, J. Electrochem. Soc., 2021, 168, 067506.

[4] J. Han, M. Sharipov, S. Hwang, Y. Lee, B.T. Hu, Y. Lee, Water stable perovskite loaded nanogels containing antioxidant property for highly sensitive and selective detection of roxithromycin in animal derived food products, Sci. Rep., 2022, 12, 3147

[5] M.C. Chen, P.W. Koh, V.K. Ponnusamy, S.L. Lee, Titanium dioxide and other nanomaterials based antimicrobial additives in functional paints and coatings, Review, Prog., Org. Coat., 2022, 163, 106660.

[6] Y. Bian, S. Wang, L. Zhang, C. Chen, Influence of fiber diameter, filter thickness, and packing density on $PM_{2.5}$ removal efficiency of electrospun nanofiber air filters for indoor applications, Build. Environ., 2020, 170, 106628.

[7] C. Kang, Z. Zhou, J.E. Halpert, A.K. Srivastava, Inkjet printed patterned bank structure with encapsulated perovskite colour filters for modern display, Nanoscale., 2022, 14, 8060.

[8] C. Yilmaz, A. Sirman, A. Halder, A, Busnaina, High-rate assembly of nanomaterials on insulating surfaces using electro-fluidic directed assembly, ACS Nano., 2017, 11, 7679−7689.
[9] I. Ali, A. Basheer, A. Kucherova, N. Memetov, T. Pasko, K. Ovchinnikov, V. Pershin, D. Kuznetsov, E. Galunin, V. Grachev, Atkachev, Advances in carbon nanomaterials as lubricants modifiers, J. Mol. Liq., 2019, 279, 251–266.
[10] Y. Hu, Y. Huang, C. Tan, X. Zhang, Q. Lu, M. Sindoro, X. Huang, W. Huang, L. Wang, H. Zhang, Two-dimensional transition metal dichalcogenide nanomaterials for biosensing applications, Mater. Chem. Front., 2017, 1, 24.
[11] C. Zhang, W.J. Qin, X.F. Bai, X.Z. Zhang, Nanomaterials to relieve tumour hypoxia for enhanced photodynamic therapy, Nano Today., 2020, 35, 100960.
[12] M.I.L. Cazares, F.P. Rodriguez, J. Mendez, M.C. Sanchez, L.F.C. Ruiz, Improved conductivity and antibiofouling of cation exchange membranes by AgNPs-GO nanocomposites, J. Membr. Sci., 2018, 565, 463–479.
[13] H. Xiao, S. Liu, 2D nanomaterials as lubricant additive: A review, Mater. Des., 2017, 135, 319–332.
[14] Q. Zhang, X. Yang, J. Guan, Applications of magnetic nanomaterials in heterogeneous catalysis, ACS Appl. Nano Mater., 2019, 2, 4681−4697.
[15] M. Qu, X. Ding, Z. Shen, M. Cui, F.E. Oropeza, G. Gorni, V.A. O'Shea, W. Li, D. C. Qi, K.H.L. Zhang, Tailoring the electronic structures of the La_2NiMnO_6 double perovskite as efficient bifunctional oxygen electrocatalysis, Chem. Mater., 2021, 33, 2062−2071.
[16] A. Hossain, A.K.M.A. Ullah, P.S. Guin, S. Roy, An overview of La_2NiMnO_6 double perovskites: synthesis, structure, properties, and applications, J. Solgel Sci Technol., 2020, 93, 479–494.
[17] M. Hashisaka, D. Kan, A. Masuno, T. Terashima, M. Takano, K. Mibu, Spin-filtering effect of ferromagnetic semiconductor La_2NiMnO_6, J. Magn. Magn., 2007, 310, 1975–1977.
[18] D.A.B. Barbosa, C.W.A. Paschoal, Raman evidence for presence of high-temperature ferromagnetic clusters in magnetodielectric compound Ba-doped La_2NiMnO_6, Spectrochim. Acta A Mol. Biomol. Spectrosc., 2017, 185, 125–129.
[19] H. Zhang, Z. Sun, Y.H. Hu, Steam reforming of methane: Current states of catalyst design and process upgrading, Renew. Sustain. Energy Rev., 2021, 149, 111330.
[20] S. Bhattar, M.A. Abedin, S. Kanitkar, J.J. Spivey, A review on dry reforming of methane over perovskite derived catalysts, Catal. Today., 2021, 365, 2–23.

[21] A. Shahnazi and S. Firoozi, Improving the catalytic performance of $LaNiO_3$ perovskite by manganese substitution via ultrasonic spray pyrolysis for dry reforming of methane, J. CO2 Util., 2021, 45, 101455.
[22] A. Jahangiri, H. Aghabozorg and H. Pahlavanzadeh, Effects of Fe substitutions by Ni in La-Ni-O perovskite-type oxides in reforming of methane with CO_2 and O_2, Int. J. Hydrogen Energy, 2013, 38, 10407–10416.
[23] H. Wang, X. Dong, T. Zhao, H. Yu and M. Li, Dry reforming of methane over bimetallic Ni-Co catalyst prepared from $La(Co_xNi_{1-x})_{0.5}Fe_{0.5}O_3$ perovskite precursor: Catalytic activity and coking resistance, Appl. Catal. B, 2019, 245, 302–313.
[24] G. R. Moradi, F. Khosravian and M. Rahmanzadeh, effects of partial substitution of Ni by Cu in $LaNiO_3$ perovskite catalyst for dry methane reforming, Chin. J. Catal., 2012, 33, 797–801.
[25] A. Hossain, K. Ghorai, T. Bhunia, J. Llorca, M. Vasundhara, P. Bera, A. Bhaskaran, S. Roy, M.M. Seikh, A. Gayen, Cu-doped $LaNiO_3$ perovskite catalyst for DRM: Revisiting it in the light of molecular level nanocomposite, Phys. Chem. Chem. Phys., 26 (2024) 26603–26621.
[26] M. Nasir, A. Ahmed, H.J. Park, S. Sen, Evidence of spin-phonon coupling in La_2NiMnO_6 double perovskite, Korean Cryst. Growth Cryst., 2021, 31, 1–4.
[27] M. Qu, X. Ding, Z. Shen, M. Cui, F.E. Oropeza, G. Gorni, V.A. O'Shea, W. Li, D. Qi, K.H.L. zhang, Tailoring the electronic structures of the La_2NiMnO_6 double perovskite as efficient bifunctional oxygen electrocatalysis, Chem. Mater., 2021, 33, 2062−2071.
[28] M. Huzaifah, A.R. Siddique, M.N. Alam, Z.U. Haq, Dry reforming of methane over Ni_5 nanocluster supported on double perovskite surface−A DFT study, Comput. Theor. Chem., 12024, 238, 114747.
[29] P.B. Managutti, S. Tymen, X. Liu, O. Hernandez, C. Prestipino, A. Salle, S. Paul, L.J. Duhamel, V. Dorcet, A. Billard, P. Briois, M. Bahout, Exsolution of Ni Nanoparticles from A-Site-Deficient Layered Double Perovskites for Dry Reforming of Methane and as an Anode Material for a Solid Oxide Fuel Cell, ACS Appl. Mater. Interfaces., 2021, 13, 35719–35728.
[30] Z. Kun, S. Yang, H. Fang, H, Zhen, W. Guoqiang, Z. Anqing, L. Haibin Z. Zengli, Preparation of double perovskite-type oxide $LaSrFeCoO_6$ for chemical looping steam methane reforming to produce syngas and hydrogen, J. Rare Earths., 2016, 34, 1032.
[31] H. Ruisheng, B. Yaqin, D. Hangyu, Z. Huimin, D. Yanfei, Z. Junge, Z. Qihua

Surface structure and catalytic performance of Sr-doped La_2NiAlO_6 double perovskite catalysts for methane combustion, J. Rare Earths., 2015, 33, 1284.

[32] A. Hossain, M. Bhattacharjee, K. Ghorai, J. Llorca, M. Vasundhara, S. Roy, P. Bera, M.M. Seikh, A. Gayen, High activity in dry reforming of methane by thermally switchable double perovskite and in-situ generated molecular level nanocomposite, Phys. Chem. Chem. Phys., 2024, 26, 5447–5465.

[33] W. Jang, J. Shim, H. Kim, S. Yoo, H. Roh, A review on dry reforming of methane in aspect of catalytic properties, Catal. Today., 324 (2019) 15.

[34] F. Wen, C. Xu, N. Huang, T. Wang, X. Sun, H. Li, R. Zhang, G. Xia, Exceptional stability of spinel Ni–$MgAl_2O_4$ catalyst with ordered mesoporous structure for dry reforming of methane, Int. J. Hydrogen Energy., 2024, 69 1481–1491.

[35] A. Choya, B. Rivas, M.L. No, Jose I.G. Ortiz, R.L. Fonseca, Dry reforming of methane over sub-stoichiometric $NiAl_2O_4$ mediated Ni/ Al_2O_3 catalysts, Fuel., 2024, 358, 130166.

[36] Y. Escalante, M.N. Barroso, A.M. Tarditi, J Munera, Exploring the potential of cobalt-based catalysts in the methane dry reforming for sustainable energy applications, Mol. Catal., 2024, 569,114575.

[37] A.K. Datye, C.R. Riley, B. Burnside, R. Alcala, N. Valdez, S. Porter, W.L. Huang, A.D. Riva, P. Salinas, R. Grant, M. Rodriguez, J. Miller, Structurally regenerable high entropy aluminate spinel catalysts for dry reforming of methane, ChemCatChem., 2025, 17, e202401949.

[38] S. Gaur, D.J. Haynes, J.J. Spivey, Rh, Ni, and Ca substituted pyrochlore catalysts for dry reforming of methane, Appl. Catal. A: Gen., 2011, 403, 142–151.

[39] Z. Zhou, C. Li, J. Zhang, Q. Gao, J. Wang, Q. Zhang, Y. Han, Dry reforming of methane over pyrochlore-type $La_2Ce_2O_7$ supported Ni catalyst: Effect of particle size of support, Mol., 2024, 29, 1871.

[40] T. Deng, C. Gao, Z. Lv, J. Li, C. Qin, Dry reforming of toluene over Ni/pyrochlore catalysts with A-site Sr doping, Int. J. Hydrogen Energy., 2024, 87, 138–147.

[41] L. Mao, Z. Le, J. Ma, T. Liu, W. Huang, J. Xu, X. Xu, X. Wang, Y. Liu, X. Fang, Mg bulk and surface modification on Ni/$Y_2Ti_2O_7$ catalyst for dry reforming of methane, Int. J. Hydrogen Energy., 2024, 92, 1121–1132.

[42] L.N. Bobrova, A.S. Bobin, N.V. Mezentsev, V.A. Sadykov, J.W. Thybaut, G.B. Marin, Kinetic assessment of dry reforming of methane on Pt + Ni containing composite of fluorite-like structure, Appl. Catal. B: Environ., 2016, 182 513–524.

[43] Y. Xu, J. Qiao, W. Sun, Z. Wang, K. Sun, Enhancement of CO_2 activation and coke-resistant ability on Ni/CeO_2 catalyst with La doping for dry reforming of methane, Int. J. Hydrogen Energy., 2024, 88, 1451–1462.
[44] M.M. Hossain, M.R. Ahasan, R. Wang, Influence of catalyst shape on plasma-assisted dry reforming of methane: A comparative study of Ni-CeO_2 nano-cubes and nano-octahedra, Chem. Eng. J., 2024, 496, 154193.
[45] P.K. Yadav, P. Verma, S. Sharma, Bimetal (CuNi and CuCo) substituted CeO_2: An approach for low temperature dry reforming of methane, Mol. Catal., 2024, 565, 114398.
[46] R. Khatun, R.S. Pal, M.A. Shoeb, D. Khurana, S. Singhl, N. Siddiqui, M.K. Poddar, T.S. Khan, R. Bal, Generation of active oxygen species by CO_2 dissociation over defect-rich Ni-Pt/CeO_2 catalyst for boosting methane activation in low-temperature dry reforming: Experimental and theoretical study, Appl. Catal. B: Environ., 2024, 340, 123243.
[47] K. Kang, N. Kayama, T. Higo, C. Sampson, Y. Sekine, Low-temperature catalytic chemical looping dry reforming of methane over Ru/$La_2Ce_2O_7$, Catal. Sci. Technol., 2024, 14, 3609.
[48] C.M. Rost, E. Sachet, T. Borman, A. Moballegh, E.C. Dickey, D. Hou, J.L. Jones, S. Curtarolo, J.-P. Maria, Entropy-stabilized oxides, Nat. Commun., 2015, 6, 8485.
[49] L. Spiridigliozzi, C. Ferone, R. Cioffi, G.D. Agli, A simple and effective predictor to design novel fluorite-structured High Entropy Oxides (HEOs), Acta Mater., 2021, 202, 181–189.
[50] Z. Liu, S. Xu, T. Li, B. Xie, K. Guo, J. Lu, Microstructure and ferroelectric properties of high-entropy perovskite oxides with A-site disorder, Ceram. Int., 2021, 47, 33039–33046.
[51] J. Ma, K. Chen, C. Li, X. Zhang, L. An, High-entropy stoichiometric perovskite oxides based on valence combinations, Ceram. Int. 2021, 47, 24348–24352.
[52] H. Zhu, H. Xie, Y. Zhao, S. Dai, M. Li, X. Wang, Structure and magnetic properties of a class of spinel high-entropy oxides, J. Magn. Magn. Mater., 2021, 535, 168063.
[53] A. Mao, H.X Xie, H.Z. Xiang, Z.G. Zhang, H. Zhang, S. Ran, A novel six-component spinel-structure high-entropy oxide with ferrimagnetic property, J. Magn. Magn. Mater., 2020, 503, 166594.
[54] J.W. Yeh, S.K. Chen, J.Y. Gan, S.J. Lin, T.S. Chin, T.T. Shun, C.H. Tsau, S.Y. Chang, Formation of simple crystal structures in Cu–Co–Ni–Cr–Al–Fe–Ti–V alloys with multiprincipal metallic elements, Metall. Mater. Trans. A: Phys., 2004, 35A, 2533-2536.
[55] H. Long, S, Guan, Z. Zhang, Y. Wang, W. Liang, J. Chen, R. Zhang, P. He, L. Ran,

P. Yang, F. Peng, Mechanical, thermal properties, and extreme phase stability of high-entropy diborides $(V_{0.2}Nb_{0.2}Ta_{0.2}Cr_{0.2}W_{0.2})B_2$., Inorg. Chem. 2024, 63, 12721−12729.

[56] T. Qureshi, M.M. Khan, H.S. Pali, Review: High- entropy borides-challenges and opportunities, J Mater Sci., 2024, 59, 15921–15991.

[57] Y. He, Z. Liu, B. Zhang, H. Wu, H. Liu, K. Nishimura, Y. Xu, Z. Huang, Dual sinter-aids to fabricate high-entropy transition metal carbide ceramic and their properties, Ceram. Int., 2024, 50, 28899–28906.

[58] C. Fan, J. Sun, J. Zhao, X. Yun, High entropy alloy bonded cemented carbides: Composition, processing, microstructure, properties and applications, Ceram. Int., 2024, 50, 37460–37503.

[59] J. Tan, C. Shi, Y. Liu, T. Deng, Q. Wu, Y. Du, Thermodynamic descriptions of the CaO–Al_2O_3 and CaO–Al_2O_3–SiO_2 systems over the whole compositionand temperature ranges, J Am Ceram Soc., 2024, 107, 6388–6409.

[60] S. Jiang, T. Hu, J. Gild, N. Zhou, J. Nie, M. Qin, T. Harrington, K. Vecchio, J. Luo, A new class of high-entropy perovskite oxides, Scr. Mater., 2018, 142, 116–120.

[61] A. Bhaskaran, S. Roy, Exploring dry reforming of CH_4 to syngas using high-entropy materials: A novel emerging approach, ChemCatChem., 2025, 17, e202401297

[62] T. Zhao, Q. Shen, M. Andersson, S. Li, J. Yuan, Surface of high-entropy perovskite catalyst $La(CoCuFeAlCe)_{0.2}O_3$ (100): Experimental study of methanol steam reforming for hydrogen production and DFT mechanism research, Appl. Surf. Sci., 2025, 684, 161917.

[63] Y. Shao, C. Wu, S. Xi, P. Tan, X. Wu, S. Saqline, W.Liu, Halite-structured (MgCoNiMnFe)Ox high entropy oxide (HEO) for chemical looping dry reforming of methane, Appl Catal B-Environ Energy., 2024, 355, 124191.

[64] J. Dabrowa, M. Stygar, A. Mikula, A. Knapik, K. Mroczka, W. Tejchman, M. Danielewski, M. Martin, Synthesis and microstructure of the $(Co,Cr,Fe,Mn,Ni)_3O_4$ high entropy oxide characterized by spinel structure, Mater. Lett., 2018, 216, 32–36.

[65] S. Zhang, Q. Niu, P. Zhang, An entropy engineering strategy to design sulfur-resistant catalysts for dry reforming of methane, Chem. Eng. J., 2024, 482, 149026.

[66] W. Li, G. Zhao, J. Zhong, J. Xie, Upgrading renewable biogas into syngas via bi-reforming over high-entropy spinel-type catalysts derived from layered double hydroxides, Fuel., 2024, 358, 130155.

[67] J.C. Vedrine, Heterogeneous catalysis on metal oxides, Catalysts 2017, 7, 341.

[68] R.H.D Passos, C.P. Souza, C. Leroux, M. Arab, Catalytic properties of $Sr_{1-x}Ce_xWO_4$: The role of mixed conduction in methane oxidation, Int. J. Hydrogen Energy., 2018, 43, 15918-15930.

[69] P.D.K. Nezhad, M.F. Bekheet, N Bonmassar, A. Gili, F. Kamutzki, A. Gurlo, A. Doran, S. Schwarz, J. Bernardi, S. Praetz, A. Niaei, A. Farzi, S. Penner, Elucidating the role of earth alkaline doping in perovskite-based methane dry reforming catalysts, Catal. Sci. Technol., 2022, 12, 1229.

[70] C.M. Marin, E.J. Popczun, T.D.N. Phan, D.N. Tafen, D. Alfonso, I. Waluyo, A. Hunt, D.R. Kauffm, Designing perovskite catalysts for controlled active-site exsolution in the microwave dry reforming of methane, Appl. Catal. B: Environ., 2021, 284, 119711.

[71] A. Bhaskaran, S.A. Singh, P.D. Costa, S. Roy, Unveiling the catalytic behaviour of $LaNiO_3$ and La_2NiO_4 for dry reforming of methane, Int. J. Hydrogen Energy., 2024, 68, 623–634.

[72] S. Zhang, J. Wang, H. Liu, X. Wang, One-pot synthesis of Ni-nanoparticle-embedded mesoporous titania/silica catalyst and its application for CO_2-reforming of methane, Catal. Commun., 2008, 9, 995–1000.

[73] J.C.S. Araujo, D. Zanchet, R. Rinaldi, U. Schuchardt, C.E. Hori, J.L.G. Fierro, J.M.C. Bueno, The effects of La_2O_3 on the structural properties of La_2O_3–Al_2O_3 prepared by the sol–gel method and on the catalytic performance of Pt/ La_2O_3–Al_2O_3 towards steam reforming and partial oxidation of methane, Appl. Catal. B: Environ., 2008, 84, 552–562.

[74] B.Q. Xu, J.M. Wei, H.Y. Wang, K.Q. Sun, Q.M. Zhu, Nano-MgO: Novel preparation and application as support of Ni catalyst for CO_2 reforming of methane, Catal. Today., 2001, 68, 217–225.

[75] Z. Hao, Q. Zhu, Z. Jiang, B. Hou, H. Li, Characterization of aerogel Ni/Al_2O_3 catalysts and investigation on their stability for CH_4–CO_2 reforming in a fluidized bed, Fuel Process. Technol., 2009, 90, 113 – 121.

[76] D.H. Chen, X.R. He, Synthesis of nickel ferrite nanoparticles by sol-gel method, Mater. Res. Bull., 2001, 36, 1369–1377.

[77] T.Mimani, K.C.Patil, Solution combustion synthesis of nanoscale oxides and their composites, Mater.Phys.Mech., 2001, 4, 134–137.

[78] K.C Patil, S.T. Aruna, S. Ekambaram, Combustion synthesis, Current opinion in solid state & materials science 1997, 2, 156-l 65.

[79] K.R. Venkatachari, D. Huang, S.P. Ostrander, A combustion synthesis process for synthesizing nanocrystalline zirconia powders. J. Mater. Res., 1995, 10, 748–755.

[80] S. Shikao, W. Jiye, Combustion synthesis of Eu^{+} activated $Y_3Al_5O_{12}$ phosphor nanoparticles, J. Alloys Compd., 2001, 327, 82–86.

[81] T.V. Anuradha, S. Ranganathan, T, Mimani, K.C. Patil, Combustion synthesis of nanostructured barium titanate, Scr. Mater., 2001, 44, 2237–2241.

[82] P. Bera, K.C. Patil, V. Jayaram, M.S. Hegde, G.N. Subbanna, Combustion synthesis of nanometal particles supported on α–Al_2O_3: CO oxidation and NO reduction catalysts, J. Mater. Chem., 1999, 9, 1801–1805.

[83] A.C.F.M. Costa, M.R. Morelli, R.H.G.A. Kiminami, Combustion synthesis: Effect of urea on the reaction and characteristics of Ni-Zn ferrite powders. J. Mater. Synth. Process. 2001, 9, 347–352.

[84] E. Flahaut, A. Govindaraj, A. Peigney, C. Laurent, A. Rousset, C.N.R. Rao, Synthesis of single-walled carbon nanotubes using binary (Fe, Co, Ni) alloy nanoparticles prepared in situ by the reduction of oxide solid solutions, Chem. Phys. Lett., 1999, 300, 236–242.

[85] H. Jin, T. Okamoto, M. Ishida, Development of a novel chemical-looping combustion: Synthesis of a looping material with a double metal oxide of CoO–NiO, Energy Fuels. 1998, 12, 1272–1277.

[90] Q, Dong, Q, Tang, W.C. Li, D.Y. Wu, Thermodynamic analysis of combustion synthesis of Al_2O_3–TiC–ZrO_2 nanoceramics, J. Mater. Res., 2001, 16, 2494–2498.

[91] F. Li, X. Yu, H. Pan, M. Wang, X. Xin, Syntheses of MO_2 (M=Si, Ce, Sn) nanoparticles by solid-state reactions at ambient temperature, Solid State Sci., 2000, 2, 767–772.

[92] L.P. Wang, G.Y. Hong, A new preparation of zinc sulfide nanoparticles by solid state method at low temperature, Mater. Res. Bull., 2000, 35, 695–701.

[93] X.R. Ye, D.Z. Jia, J.Q. Yu, X.Q. Xin, Z. Xue, One-step solid-state reactions at ambient temperatures—A novel approach to nanocrystal synthesis, Adv. Mater. 1999, 11, 941–942.

[94] J. Schoonman, Nanostructured materials in solid state ionics, Solid State Ion., 2000, 135, 5–19.

[95] L. Rapoport, Y. Bilik, Y. Feldman, Hollow nanoparticles of WS_2 as potential solid-state lubricants. Nat., 1997, 387, 791–793.

[96] M.A. Pen, J.L.G. Fierro, Chemical structures and performance of perovskite oxides, *Chem. Rev.* 2001, 101, 1981–2018.

[97] M. Wang, L. Sun, X. Fu, C. Liao, C. Yan, Synthesis and optical properties of ZnS: Cu(II) nanoparticles, Solid State Communications 2000, 115, 493–496.
[98] Q. Chen, A.J. Rondinone, B.C. Chakoumakos, Z.J. Zhang, Synthesis of superparamagnetic $MgFe_2O_4$ nanoparticles by coprecipitation, J. Magn. Magn. Mater., 1999, 194, 1–7.
[99] D.K. Kim, Y. Zhang, W. Voit, K.V. Rao, M. Muhammed, Synthesis and characterization of surfactant-coated superparamagnetic monodispersed iron oxide nanoparticles, J. Magn. Magn. Mater., 2001, 225, 30–36.
[100] T.M. Chen, S.C. Chen, C.J. Yu, Preparation and characterization of garnet phosphor nanoparticles derived from oxalate coprecipitation, J. Solid State Chem., 1999, 144, 437–441
[101] P. Vaqueiro, M. Arturo L. Quintela J. Rivas, Synthesis of yttrium iron garnet nanoparticles via coprecipitation in microemulsion, J. Mater. Chem., 1997, 7, 501–504.

[102] T. Adschiri, Y. Hakuta, K. Sue, Hydrothermal synthesis of metal oxide nanoparticles at supercritical conditions, J. Nanoparticle Res., 2001, 3, 227–235.
[103] M. Hirano, M. Imai, M Inagaki, Preparation of $ZnGa_2O_4$ spinel fine particles by the hydrothermal method, J. Am. Chem. Soc., 2000, 83, 977–979.
[104] Y. He, Y. Li, J. Yu, Y. Qian, Chemical control synthesis of nanocrystalline SnO_2 by hydrothermal reactions, Mater. Lett., 40 1999 23–26.
[105] K. Riwotzki, M. Haase, Wet-chemical synthesis of doped colloidal nanoparticles: YVO_4: Ln (Ln= Eu, Sm, Dy), J. Phys. Chem. B, 1998, 102, 10129–10135.
[106] S.W. Lu, B.I. Lee, Z.L. Wang, W.D. Samuels, Hydrothermal synthesis and structural characterization of $BaTiO_3$ nanocrystals, J. Cryst. Growth., 2000, 219, 269–276.
[107] I. Hincapie, A.C. Guzman, D. Hiltbrunner, B. Nowack, Use of engineered nanomaterials in the construction industry with specific emphasis on paints and their flows in construction and demolition waste in Switzerland, J. Waste Manag., 2015, 43, 398–406.
[108] H. Saleem, S.J. Zaidi, Developments in the application of nanomaterials for water treatment and their impact on the environment, Nanomater., 2020, 10, 1764.
[109] A. Abdelrady, M.H. Abdelhafez, A. Ragab, Use of insulation based on nanomaterials to improve energy efficiency of residential buildings in a hot desert climate, Sustainability., 2021, 13 (9), 5266.
[110] H. Xiao, S. Liu, 2D nanomaterials as lubricant additive: A review, Mater. Des., 2017, 135, 319–332.

[111] L. Li, T. Wang, Y. Zhong, R. Li, W. Deng, X. Xiao, Y. Xu, J. Zhang, X. Hu, Y. Wang, A review of nanomaterials for biosensing applications, J. Mater. Chem. B, 2024, 12, 1168–1193.
[112] Y. He, C. Hu, Z. Li, C. Wu, Y. Zeng, C. Peng, Multifunctional carbon nanomaterials for diagnostic applications in infectious diseases and tumors, Mater. Today Bio., 2022, 14, 100231.
[113] J. Li, J.Z. Zhang, Optical properties and applications of hybrid semiconductor nanomaterials, Coord. Chem. Rev., 2009, 253, 3015–3041.
[114] L.R. Khot, S. Sankaran, J.M. Maja, R. Ehsani, E.W. Schuster, Applications of nanomaterials in agricultural production and crop protection: A review, Crop Prot., 2012, 35, 64–70.
[115] K. Kang, Y. Cho, K.J. Yu, Novel Nano-materials and nano-fabrication techniques for flexible electronic systems, Micromachines., 2018, 9, 263.
[116] M. Bilal, H.M.N. Iqbal, New insights on unique features and role of nanostructured materials in cosmetics, Cosmetics., 2020, 7, 24.
[117] K. Virmani, C. Deepak, S. Sharma, U. Chadha, S.K. Selvaraj, Nanomaterials for automotive outer panel components: a review, Eur. Phys. J. Plus., 2021, 136, 921.
[118] N. Sharma, H. Ojha, A. Bharadwaj, D.P. Pathak, R.K. Sharma, Preparation and catalytic applications of nanomaterials: a review, RSC Adv., 2015, 5, 53381–53403.
[119] Q. Zhang, X. Yang, J. Guan, Applications of magnetic nanomaterials in heterogeneous catalysis, ACS Appl. Nano Mater. 2019, 2, 4681−4697.
[120] F. Zaera, Nanostructured materials for applications in heterogeneous catalysis, Chem. Soc. Rev., 2013, 42, 2746.
[121] D. Astruc, Introduction: Nanoparticles in catalysis, Chem. Rev., 2020, 120, 461−463.

Chapter 2

Synthetic processes, characterization techniques, and DRM activity test of the materials

Chapter abstract: *This chapter describes the synthetic techniques used to prepare the materials of this research work. This is followed by the details of wide variety of advanced instrumental procedures that are used to analyze the physical nature of the materials. The chapter ends with the description of the reaction system utilized for DRM test.*

2.1. Introduction

Microstructure, characteristics, and applicability of a material depend on a number of variables. The development of a material with high activity demands precise knowledge about the synthetic process and the parameters involved in the process. The microstructure of the synthesized materials is significantly influenced by the preparation technique. Researchers typically appreciate materials with novel features because of the variety of uses they may be put to. When utilized as heterogeneous catalysts, the materials are often synthesized using straightforward techniques with little control over the solid component's physical characteristics. In order to raise the surface to volume ratio and lower the cost of the catalyst, expensive noble metals are often disseminated onto inexpensive transition metal oxide substrates with high surface areas [1, 2]. Synthesis of a specific material with high activity in a variety of applications is thus the main problem faced by the material community. In recent years, solid materials with clearly defined structural properties have been developed using revolutionary nanotechnology principles. Typically, the materials are prepared using wet chemical processes such as sol-gel citrate method [3–5], solution combustion synthesis [6, 7], solid state synthesis [8], coprecipitation [9], surfactant assisted coprecipitation method [10, 11], hydrothermal [12, 13], and Pechini [14, 15] methods.

In addition to the difficulties with material synthesis, thorough ex-situ and in-situ characterizations are the main things for understanding the properties of the material. The relationship between structure and activity may be identified, and the hidden features can be described which improve the design and development of a multifunctional nanomaterial. One can establish the mechanism with the aid of a number of characterization techniques, such as in-situ analysis methods like spectroscopic analysis carried out under simulated reaction conditions. In heterogeneous catalysis, the active catalytic site(s) can also be determined by

correlating structural (bulk as well as surface) data with reaction data like conversion or selectivity.

2.2. Chemicals used for synthesis of catalyst materials

To prepare the oxide-based catalyst materials of this research work, corresponding nitrate salts of metal, $La(NO_3)_3.6H_2O$ (Spectrochem, >99.99%), $Cu(NO_3)_2.3H_2O$, $Ni(NO_3)_2.6H_2O$ (Merck, >98%), $Mn(NO_3)_3.4H_2O$ (Sigma Aldrich, ≥97%), $Cr(NO_3)_3.9H_2O$ (SRL, >96%), $Fe(NO_3)_3.6H_2O$ (Merck, ≥97%), $Co(NO_3)_2.6H_2O$ (Merck, ≥97%), $Al(NO_3)_3.9H_2O$ (Merck, ≥ 99.99%), $(NH_4)_2[Ce(NO_3)_6]$ (Merck, > 98.5%), $Pr(NO_3)_3.6H_2O$ (Merck, ≥ 99.9%), $Nd(NO_3)_3.6H_2O$ (Merck, ≥ 99%), $Sm(NO_3)_3.6H_2O$ (Merck, ≥ 99.9%) $Gd(NO_3)_3.6H_2O$ (Merck, ≥ 99.9%), oxalyldihydrazide ($C_2H_6N_4O_2$, ODH) as the fuel in solution combustion synthesis and citric acid monohydrate, $C_6H_8O_7.H_2O$ (Merck, >99%), as the fuel as well as complexing agent in sol-gel synthesis were taken without further purification. ODH was prepared by the reaction of hydrazine hydrate with diethyl oxalate in an aqueous solution under ice-cooled condition. Millipore water (ultra-pure water) was used as the solvent in the synthetic procedure.

2.3. Synthetic methods of the catalysts

The development of materials is significantly influenced by the synthetic process as discussed in Chapter 1. By altering the synthesis process, materials can gain structural and functional improvements. Thus, a variety of synthetic techniques, including sol-gel citrate combustion (SGCA), solution combustion synthesis (SCS), ceramic method (CM) were used in order to synthesize the desired materials of this investigation.

2.3.1. Sol-gel citrate combustion

2.3.1.1. Single perovskite

Sol-gel synthesis was used to get a series of $LaNi_{1-x}Cu_xO_3$ (x = 0.1, 0.2, 0.3, 0.4, 0.6, and 0.8 that are named as CuXLNO, where X = 10–80, the atom percentage of Cu-doping, i.e., X= 100x) perovskite materials, a typical process of which is shown schematically in **Scheme 2.1**. Stoichiometrically, the relevant metal nitrates were taken in a beaker containing 50–60 mL of millipore water and kept under stirring for around 2 h in order to dissolve the metal nitrates thoroughly and make a homogeneous solution. Specifically, for the preparation of $LaNi_{0.8}Cu_{0.2}O_3$, i.e., Cu20LNO, 1.763 g of $La(NO_3)_3.6H_2O$, 0.196 g of $Cu(NO_3)_2.3H_2O$, 0.947

g of $Ni(NO_3)_2.6H_2O$, and 7.6905 g of $C_6H_8O_7.H_2O$ were taken in a beaker. Then the resulting solution was heated at ~180–200 °C to evaporate the water to form the gel. After the evaporation was complete, the xerogel instantly began to burn ~200–220 °C into a fluffy end product. The end product was then calcined at 800 °C for 3 h in static air in a muffle furnace to obtain the desired sample [16].

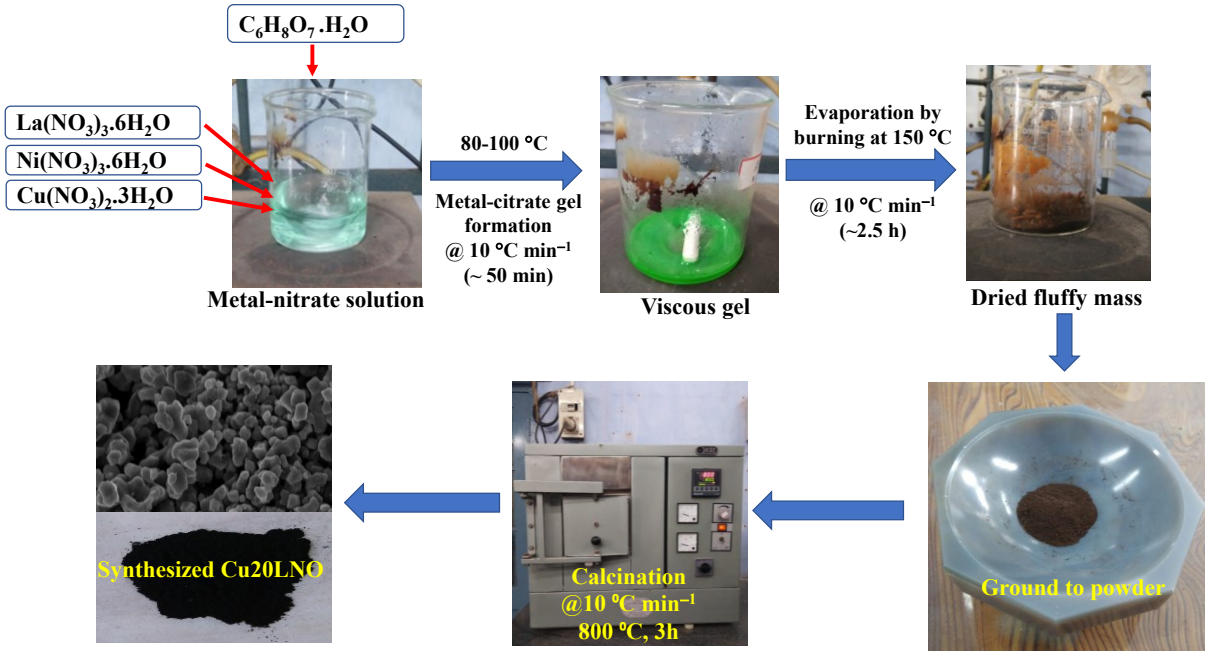

Scheme 2.1: Diagram illustrating the sol-gel process for preparing the $LaNi_{0.8}Cu_{0.2}O_3$, i.e., Cu20LNO catalyst.

2.3.1.2. Double perovskite

The double perovskite materials, La_2NiMO_6 (M= Cr, Mn, Fe and Co; that are named as LNMO) were prepared via the conventional SGCA method, a typical one of which is shown in **Scheme 2.2**. Typically, for the preparation of La_2NiMnO_6, 1.732 g of $La(NO_3)_3.6H_2O$, 0.502 g of $Mn(NO_3)_3.4H_2O$, 0.58 g of $Ni(NO_3)_2.6H_2O$ and 6.720 g of $C_6H_8O_7.H_2O$ were taken in a beaker. The solution that was formed was subsequently heated between 180 and 200 °C in order to evaporate the water resulting the metal-citrate gel formation, which on further heating at ~200–220 °C give a fluffy mass. The resulting mass was calcined similarly calcined (at 800 °C for 3 h) to get the anticipated LNMnO sample [17].

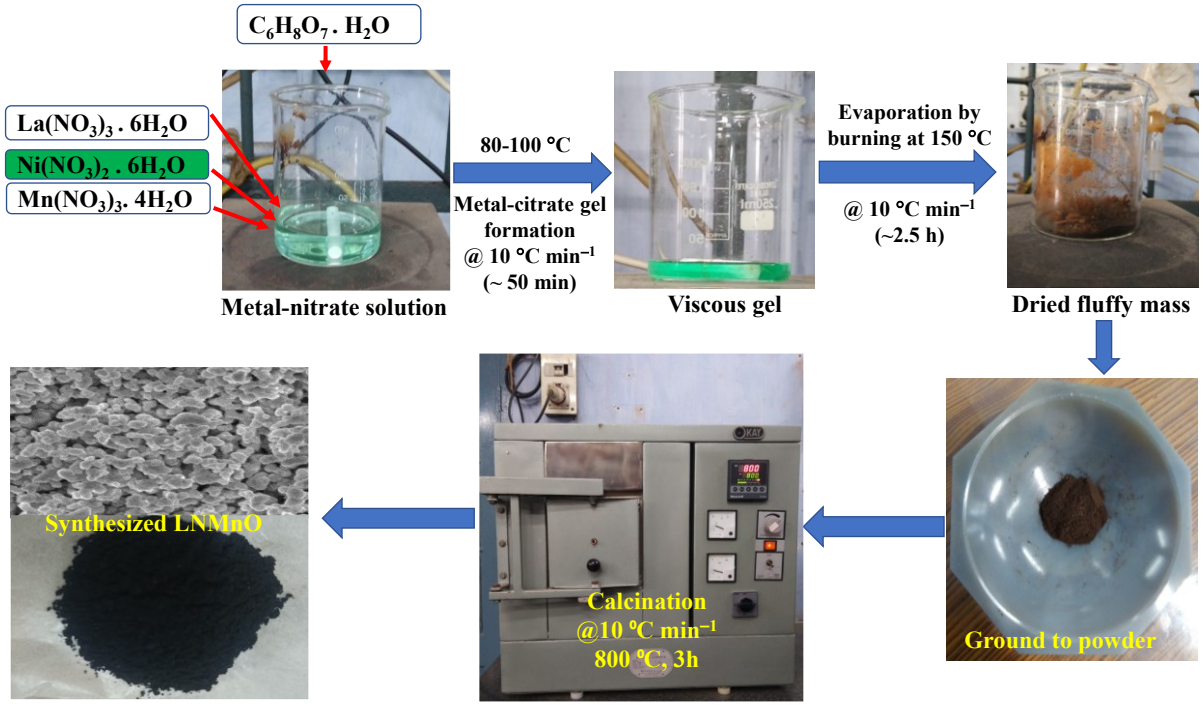

Scheme 2.2: Schematic representation of the sol-gel method adopted for the synthesis of La_2NiMnO_6, i.e., LNMnO double perovskite.

2.3.1.3. High entropy perovskite oxide

The high entropy perovskite oxide (HEPO) material $Ln(Mn_{0.2}Fe_{0.2}Co_{0.2}Ni_{0.2}Cu_{0.2})O_3$ [henceforth denoted as Ln(TM)O, where TM stands for an equimolar proportion of Mn, Fe, Co, Ni, and Cu and Ln= La, Ce, Pr, Nd, Sm and Gd] was synthesized using the traditional SGCA process as shown in **Scheme 2.3**. Specifically, 1.730 g of $La(NO_3)_3.6H_2O$, 0.2 g of $Mn(NO_3)_3.4H_2O$, 0.323 g of $Fe(NO_3)_3.6H_2O$, 0.233 g of $Co(NO_3)_2.6H_2O$, 0.233 g of $Ni(NO_3)_2.6H_2O$, 0.192 g of $Cu(NO_3)_2.3H_2O$, and 6.720 g of $C_6H_8O_7.H_2O$ were taken in a beaker with 50 mL of millipore water to prepare the $La(Mn_{0.2}Fe_{0.2}Co_{0.2}Ni_{0.2}Cu_{0.2})O_3$ HEPO catalyst. The resulting solution was then heated ~180–200 °C for getting the viscous gel, continuous heating of this gel at ~200–220 °C give a dried fluffy pile. The required calcination temperature for this case was higher by 100 °C, while the duration was same. Then the sample was quenched in air resulting in the anticipated HEPO material. Similarly, the other lanthanide-based HEPOs were prepared.

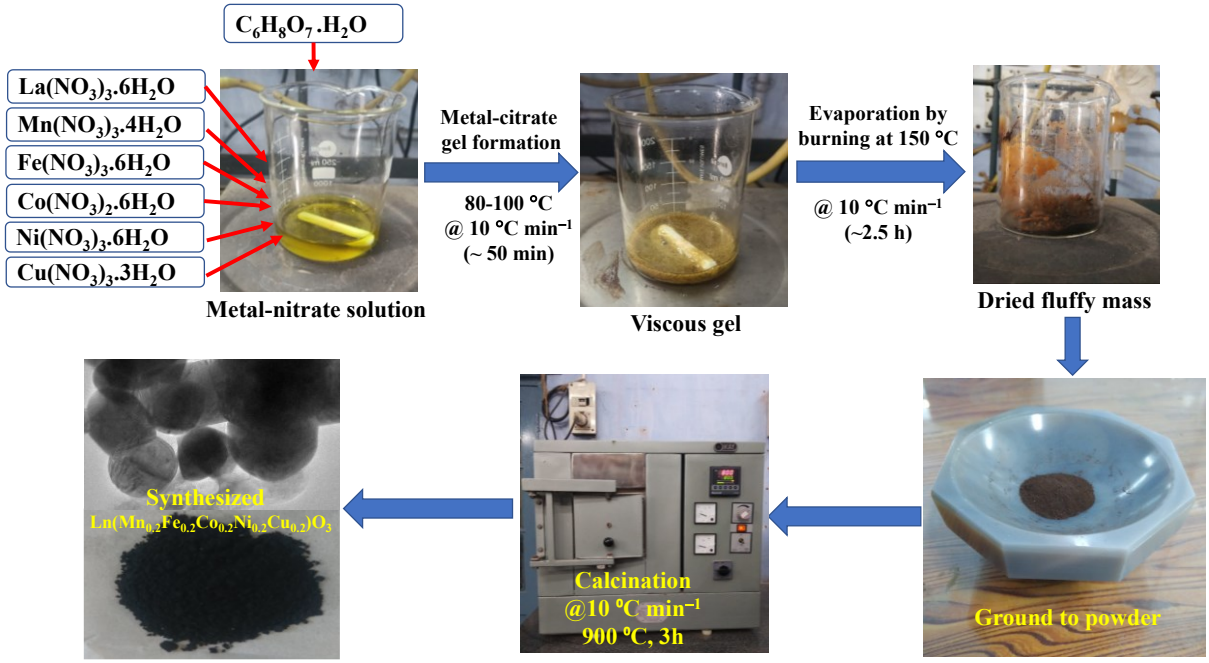

Scheme 2.3: Schematic illustration of the sol-gel method used for the synthesis of $La(Mn_{0.2}Fe_{0.2}Co_{0.2}Ni_{0.2}Cu_{0.2})O_3$ HEPO perovskite.

2.3.1.4. High entropy spinel oxide

Adopting the traditional SGCA method, the high entropy spinel oxide (HESO) materials $(Mn_{0.2}Fe_{0.2}Co_{0.2}Ni_{0.2}Cu_{0.2})Al_2O_4$ (denoted as MAlO, where M= Mn, Fe, Co, Ni, and Cu in equimolar proportion) was prepared. To prepare the expected MAlO spinel oxide, in a beaker containing ~50 mL of millipore water, typically, 0.2 g of $Mn(NO_3)_3.4H_2O$, 0.323 g of $Fe(NO_3)_3.6H_2O$, 0.233 g of $Co(NO_3)_2.6H_2O$, 0.233 g of $Ni(NO_3)_2.6H_2O$, 0.193 g of $Cu(NO_3)_2.3H_2O$, 3 g of $Al(NO_3)_3.9H_2O$ and 10.08 g of $C_6H_8O_7.H_2O$ were used.

The mixture solution was at that moment heated at ~180–200 °C that form the metal-citrate viscous gel. After the end of gel combustion, it was further heated at ~200–220 °C for getting the dried fluffy end product. The end product formed was crushed well and subsequently calcined at 900 °C with same time period to remove the additional contaminants and leftover nitrate residue. After that, the sample was air quenched to get the expected HESO material. Other HESO's, MCrO, MMnO, MFeO and MCoO were prepared similarly.

2.3.2. Solution combustion synthesis

2.3.2.1. Perovskite

To compare the catalytic activity of the Cu20LNO catalyst, the SCS method was also used to prepare the catalyst that is named as Cu20LNO SCS. The preparation of Cu20LNO SCS

involved combustion of stoichiometric composition of the metals nitrate salts with organic fuel. Typically 1.732 g of $La(NO_3)_3.6H_2O$, 0.1928 g of $Cu(NO_3)_2.3H_2O$, 0.93 g of $Ni(NO_3)_2.6H_2O$, and 2.5 g of ODH were dissolved in minimum volume of millipore water in a borosilicate dish. The homogenized solution was then transferred into a preheated muffle furnace controlled at ~450 °C for combustion. When the solution reached the point of spontaneous combustion, it ignited, producing an instant flame as well as a solid feathery final product. The end product was a feathery mass that was thoroughly ground into powder to get the Cu20LNO SCS catalyst [16].

2.3.2.2. HEPO perovskite

The La(TM)O HEPO catalyst was prepared in a similar manner by the combustion of 1.730 g of $La(NO_3)_3.6H_2O$, 0.2 g of $Mn(NO_3)_3.4H_2O$, 0.323 g of $Fe(NO_3)_3.6H_2O$, 0.233 g of $Co(NO_3)_2.6H_2O$, 0.233 g of $Ni(NO_3)_2.6H_2O$, 0.192 g of $Cu(NO_3)_2.3H_2O$ and 2.6 g of ODH that was named as La(TM)O SCS.

2.3.2.3. HESO spinel

A typical SCS route for the synthesis of HESO catalyst, MAlO SCS, involved the combustion of 0.2 g of $Mn(NO_3)_3.4H_2O$, 0.323 g of $Fe(NO_3)_3.6H_2O$, 0.233 g of $Co(NO_3)_2.6H_2O$, 0.233 g of $Ni(NO_3)_2.6H_2O$, 0.193 g of $Cu(NO_3)_2.3H_2O$, 3 g of $Al(NO_3)_3.9H_2O$ and 1.935 g of ODH at ~450 °C.

2.3.3. Ceramic method

2.3.3.1. Perovskite

For further comparison of catalytic behavior, the individual oxide components, namely La_2O_3, CuO, and NiO, corresponding to the stoichiometry of sol-gel made Cu20LNO catalyst, were synthesized similarly using the SGCA route. The stoichiometric proportion of these oxides were then mixed thoroughly in a mortar with pestle for 3 h with gradual additions of acetone. The mixture obtained so was divided into two parts. One part of the intimately mixed components was calcined at 1200 °C for 3 h to get the desired catalyst following the conventional ceramic method that is designated as Cu20LNO CM. The other part that is designated as physical mixture (PM, catalyst being named as Cu20LNO PM) is directly used for DRM [16].

2.3.3.2. Double perovskite

The preparation of double perovskite via ceramic method involves the thorough mixing of NiO, MnO and La_2O_3 individual oxide materials for ~ 3 h in the required stoichiometric ratio with the interim addition of acetone. The resulting mixture of individual oxides was then separated into two parts. One part of the physical mixture that is named as LNMnO PM was directly deployed for DRM. Another part of the physical mixture was at first calcined at 800 °C for 3 h, and then at 900 °C for 3 h to get the catalyst via ceramic method and hence named as LNMnO CM [17].

2.4. Material characterizations

This section provides a detailed discussion of all the characterisation methods used to examine the chemical and physical characteristics of the synthesized materials. Initially, the phase purity of the synthesized samples was confirmed from powder X-ray diffraction (PXRD) analysis. BET surface area measurement gave the specific surface areas (S_{BET}) of different samples. A preliminary DRM test was performed to finalize the most active catalyst amongst all the synthesized materials. After that, the different forms of the final catalyst material have been characterized by the field emission scanning electron microscopy (FESEM), high resolution transmission electron microscopy (HRTEM), X-ray photoelectron spectroscopy (XPS) and thermogravimetric analysis (TGA).

2.4.1. Powder X-ray diffraction

The powder X-ray diffraction technique was used to confirm that the pure phase of the synthesized materials was formed. Bruker D8 Advance diffractometer of Cu Kα radiation (λ =1.5418 Å) operated at 40 kV and 40 mA with the 1D position-sensitive LYNXEYE detector at a scan rate of 1 s per step in the 2θ range of 10º to 80º was used to record the PXRD patterns. Using Scherrer's equation (**eq. 2.1**), average particle sizes (τ) were determined from the line-width broadening of the peaks.

$$\tau = \frac{0.9\lambda}{\beta \cos\theta} \qquad \text{..... (2.1)}$$

where (ß) is the full width at half maximum (FWHM) of the diffraction peak.

2.4.2. Specific BET surface area (S_{BET}) analysis

N_2 sorption isotherms were obtained in an Autosorb iQ2 gas sorption instrument (Quantachrome Instruments, USA). This technique was used to get the catalysts specific BET surface areas (S_{BET}), pore volumes, and pore size distributions. Prior to measurement, the FLOVAC degasser unit was used to degas the catalyst for 4 h at 120 ºC and 0.3 torr of vacuum. Pore size distributions and pore volumes of the catalysts were determined using the non-local density function theory (NLDFT) method, and S_{BET} were determined using the multi-point BET method.

2.4.3. Field emission scanning electron microscopy

Field emission scanning electron microscopy (FESEM) and energy dispersive X-ray spectroscopy (EDXS) were done to get the surface morphology and elemental composition of the samples, respectively using (JEOL, Model no. JSM-5600LV) instrument.

2.4.4. High-resolution transmission electron microscopy

Transmission electron microscopy (TEM) and high-resolution transmission electron microscopy (HRTEM) (JEOL, Model No. JEM-2100) were used to analyse the microstructure of the sample at a 200 kV accelerating voltage.

2.4.5. X-ray photoelectron spectroscopy

The surface characterization of the samples using X-ray photoelectron spectroscopy (XPS) was carried out on two spectrometers. The Thermo Scientific K-Alpha surface analysis spectrometer was fitted with a monochromatic Al Kα radiation (1486.6 eV) as an X-ray source and was operated at 12 kV and 6 mA. Pass energy of 200 eV and step increment of 1 eV were used to obtain individual core level spectra of the elements. The binding energies were calibrated against the standard C 1s peak at 284.6 eV. The XPS analysis was performed with the powder samples stuck on carbon tape under the base pressure at the analysing chamber maintained at 5×10^{-9} mbar.

For some of the catalysts, analysis was done using a SPECS spectrometer with an AlKα source worked at 150 W and a Phoibos 150 MCD-9 detector in analyses compartment with the pressure lower than 10^{-7} Pa. Catalysts were pressed to form pellets with 10 mm diameter and their 2 mm × 2 mm sample region was studied. The hemispherical analyzer's pass energy and energy step were set at 25 eV and 0.1 eV, respectively. The SPECS Flood Gun FG 15/40 was

employed to stabilise the charge in accordance with C 1s binding energy value of 284.8 eV. The data were analysed using PeakFit v4.12 software.

2.4.6. Thermogravimetric analysis

In order to determine the extent of coke that was deposited on the sample's surface during the DRM, thermogravimetric analysis (TGA) was done. The Perkin Elmer Pyris Diamond TG/DTA instrument was used where temperature range was 30 to 900 °C at a heating rate of 10 °C min^{-1}.

2.5. DRM activity test

A reaction set up was fabricated in the laboratory by which the DRM activities of the synthesized materials were evaluated (see **Fig. 2.1**). All the gases (reactant as well as carrier) pass through 1/8-inch stainless steel tube to prevent any chemical reaction. The gas flow rates were monitored by thermal mass flow controllers (MFC, Bronkhorst High-Tech BV). After leaving the MFC, the gas can go in any of the three available directions: (i) to the microreactor for DRM, or (ii) to the bypass line for the analysis of gas mixture or (iii) directly to a bubble flow meter (BFM) for checking the set value of the flow rates with the manually determined value.

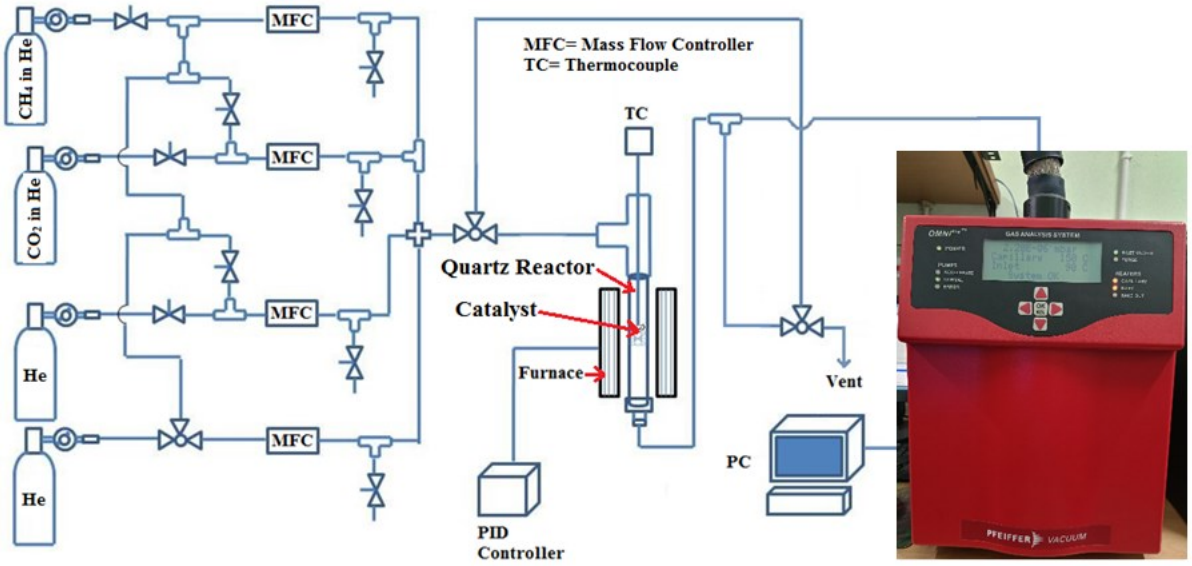

Figure 2.1. The reaction setup for conducting gas solid heterogeneous catalytic experiments is shown schematically.

Initially, a pellet was made from the as-prepared catalyst powder and crushed to get 85–100 mesh before being put through a catalytic test. A down flow quartz micro-reactor with an inner diameter of 6 mm was used to carry out the DRM reaction at atmospheric pressure. In a typical catalytic test, 100 mg of solid catalyst was packed on a layer of quartz wool in the micro-reactor and placed in a vertical tube furnace. A K-type thermocouple (Omega, UK) positioned closely in contact with the catalyst bed was utilized to monitor the actual reaction temperature, while the temperature of the furnace was controlled by a thyristor-powered Eurotherm PID controller (model 2416). The flow rates of the calibration gas mixtures, 10.3% CH_4 in helium & 9.7% CO_2 in helium along with the carrier gas helium were set at the required values with a total flow of 56 mL min^{-1} to keep the CH_4/CO_2 molar ratio as per DRM stoichiometry. A fixed gas hourly space velocity (GHSV) of 34000 mL g_{cat}^{-1} h^{-1} was used throughout the catalytic tests. The preliminary tests were carried out at different temperatures ranging from 500 to 900 °C to optimize the reaction temperature. The as-prepared catalysts were found to be most active at 800 °C. Further tests, like the durability tests were thus carried out at this temperature. The outgoing gases were detected and analyzed using an OMNI^{Star} gas analysis system equipped with quadrupole mass spectrometer, where the characteristic m/z (m = mass of the gas, z = charge on the ion) value of the constituent gases (*X*) is acquired. The catalytic activities were computed using the conversions of CH_4, CO_2, and H_2/CO molar ratio. The CH_4 and CO_2 conversions were calculated using the following conversion formula by taking the initial (i.e., before reaction, $A_{X,\,in}$) and steady-state (after 1 h of reaching the target temperature of 800 °C, $A_{X,\,out}$) ion current values for each component, which correspond to a fixed value of m/z. This is because the ion current is directly proportional to the concentration of the gas analysed.

$$\%\ of\ CH_4\ conversion = \frac{A_{CH_4,in} - A_{CH_4,out}}{A_{CH_4,in}} \times 100 \quad \text{..... (2.2)}$$

$$\%\ of\ CO_2\ conversion = \frac{A_{CO_2,in} - A_{CO_2,out}}{A_{CO_2,in}} \times 100 \quad \text{..... (2.3)}$$

$$H_2\ yield\ (\%) = \frac{A_{H_2,out}}{2A_{CH_4,in}} \times 100 \quad \text{..... (2.4)}$$

$$CO\ yield\ (\%) = \frac{A_{CO,out}}{(A_{CH_4,in} + A_{CO_2,in})} \times 100 \quad \text{..... (2.5)}$$

$$H_2\ selectivity\ (\%) = \frac{A_{H_2,out}}{2(A_{CH_4,in} - A_{CH_4,out})} \times 100 \ldots\ldots\ldots\ldots (2.6)$$

$$CO\ selectivity\ (\%) = \frac{A_{CO,out}}{(A_{CH_4,in} - A_{CH_4,out}) + (A_{CO_2,in} - A_{CO_2,out})} \times 100 \ldots. (2.7)$$

The relevant mass signals (m/z), which were set in the instrument to be 2 amu for H_2, 4 amu for He, 16 amu for CH_4, 18 amu for H_2O, 28 amu for CO, and 44 amu for CO_2, were used to analyse the outlet gas composition. The H_2/CO ratio is calculated by calculating the simple ratio of each of their individual ion current values, $\frac{A_{H_2,out}}{A_{CO,out}}$, which has a theoretical value of one for the DRM reaction.

References

[1] A.S. Khader, S.A. Ahmed, H.M. Altass, M. Morad, A.A. Ibrahim, CO oxidation over noble metals supported on copper oxide: effect of Cu^{+}/Cu^{2+} ratio, J. Mater. Res. Technol., 2020, 9, 14200–14211.

[2] Q. Zhou, Z.Q. Wang, Z. Li, J. Wang, M. Xu, S. Zou, J. Yang, Y. Pan, X. Q. Gong, L. Xiao, J. Fan, $CH_3^{\bullet}$-generating capability as a reactivity descriptor for metal oxides in oxidative coupling of methane, ACS Catal., 2021, 11, 14651−14659.

[3] T. Luo, C. Luo, Z. Shi, X. Li, F. Wu, L. Zhang, Optimization of sol-gel combustion synthesis for calcium looping CO_2 sorbents, part I: Effects of sol-gel preparation and combustion conditions, Sep. Purif. Technol., 2022, 292, 121081.

[4] Y.Y. Meng, M.H. He, Q. Zeng, D.L. Jiao, S. Shukla, R.V. Ramanujan, Z.W. Liu, Synthesis of barium ferrite ultrafine powders by a sol–gel combustion method using glycine gels, J. Alloys Compd., 2014, 583, 220–225.

[5] M.M. Arman, The effect of the rare earth A-site cation on the structure, morphology, physical properties, and application of perovskite $AFeO_3$, Mater. Chem. Phys., 2023, 304, 127852.

[6] D.P. Tarrago, C.F. Malfatti, V.C. Sousa, Influence of fuel on morphology of LSM powders obtained by solution combustion synthesis, Powder Technol., 2015, 269, 481–487.

[7] G. Takalkar, R.R. Bhosale, F. Almomani, S. Rashid, H. Qiblawey, M.A.S. Saad, M. Khraisheh, G Kumar, R.B. Gupta, R.V. Shende, Fuel., 2021, 285, 119154.

[8] A. Zuzi, A. Ressler, J. Macan, Evaluation of carbonate precursors in manganite coprecipitation synthesis by Fourier transform infrared (FTIR) spectroscopy, Solid State Commun., 2022, 341, 114594.
[9] H. Li, J. Yu, Y. Gong, N. Lin, Q. Yang, X. Zhang, Y. Wang, Perovskite catalysts with different dimensionalities for environmental and energy applications: A review, Sep. Purif. Technol., 2023, 307, 122716.
[10] J. Yang, N. Gong, L. Wang, Y Wu, T. Zhang, C. Zeng, Y. Tan, Insights into the one-step ethanol synthesis through CO hydrogenation over surfactant-assisted preparation of $CuCo/SiO_2$ catalyst, Fuel., 2022, 327, 125078.
[11] G. Kesavan, M. Pichumani, S.M. Chen, C.S. Ko, Surfactant-assisted (CTAB, PVA, PVP) thermal decomposition synthesis of strontium spinel ferrite nanocrystals for electrochemical sensing of cytostatic drug flutamide, Mater. Today Chem., 2022, 26, 101045.
[12] R. Monsef, M.S. Niasari, M.M. Arani, hydrothermal synthesis of spinel-perovskite Li−Mn−Fe−Si nanocomposites for electrochemical hydrogen storage, Inorg. Chem., 2022, 61, 6750−6763.
[13] P. Deng, H. Fang, R. Liu, X. Guo, P. Chen, One-pot hydrothermal synthesis of flower-like MnO_2 nanostructure with rich oxygen vacancy for catalysis thermal-induced pyrolysis of energetic molecular perovskite, Vacuum., 2022, 203, 111234.
[14] Z. Heydariyan, R. Monsef, M.S. Niasari, Insights into impacts of Co_3O_4-CeO_2 nanocomposites on the electrochemical hydrogen storage performance of g-C_3N_4: Pechini preparation, structural design and comparative study, J. Alloys Compd., 2022, 924, 16656.
[15] H.J. Munoz, S.A. Korili, A. Gil, progress and recent strategies in the synthesis and catalytic applications of perovskites based on lanthanum and aluminum, Mater., 2022, 15, 3288.
[16] A. Hossain, K. Ghorai, T. Bhunia, J. Llorca, M. Vasundhara, P. Bera, A. Bhaskaran, S. Roy, M.M. Seikh, A. Gayen, Cu-doped $LaNiO_3$ perovskite catalyst for DRM: revisiting it as a molecular-level nanocomposite, Phys. Chem. Chem. Phys., 2024, 26, 26603–26621.
[17] A. Hossain, M. Bhattacharjee, K. Ghorai, J. Llorca, M. Vasundhara, S. Roy, P. Bera, M.M. Seikh, A. Gayen, High activity in dry reforming of methane by thermally switchable double perovskite and in-situ generated molecular level nanocomposite, Phys. Chem. Chem. Phys., 2024, 26, 5447–5465.

Chapter 3

Studies on Cu-doped $LaNiO_3$ perovskite catalyst

Chapter abstract: *This chapter deals with the synthesis, characterization, and DRM activity of Cu-substituted $LaNiO_3$ perovskite materials. The phase pure $LaNi_{0.8}Cu_{0.2}O_3$ nanomaterial catalyst shows high catalytic activity (97% CH_4 conversion and 98% CO_2 conversion) with H_2/CO ratio ~1.2. Remarkably, the catalytic activity is not impacted and is sustained even after 100 h, despite the fact that the pristine perovskite phase mostly breaks down into component phases following the DRM. Based on the findings from characterization of the different forms of the catalyst, we have explained the prolonged activity of the disintegrated perovskite catalyst in the context of nanocomposite formation at the molecular level along with the availability of Ni^0 and NiO.*

3.1. Introduction

As the energy produced from fossil fuels is insufficient to meet the demands of current day-to-day activities, it is necessary to look into other energy sources. Apart from others, the environmental imbalance is also contributed from the uncontrolled use of fossil fuels. The main greenhouse gases that come from the combustion of fossil fuels are CH_4 and CO_2, which cause life unsustainable for humans to live in. Numerous studies have suggested that green H_2 energy may be a viable replacement for fossil fuels. Hydrogen energy is currently considered a promising source of energy for the future for its outstanding energy output and excellent eco-friendliness. Several catalytic approaches, such as DRM, photochemical, and electrochemical processes are available for the production of H_2. DRM is one of the most effective processes because of its low cost, long-term catalyst activity, and ease of catalyst preparation. In addition, it produces H_2 at a comparatively higher rate and returns effective feedstock, syngas (H_2 + CO), by consuming two important greenhouse gases (CH_4 and CO_2). Recently, DRM has drawn the interest of industrial and academic researchers for its various applications in the industry [1, 2] and environment [3-7] along with academic aspects [8, 9]. Syngas finds application in multiple fields, including H_2 production [10–13], diesel production using the Fischer–Tropsch method [14–15], methanol preparation [16–18], iron ore reduction to obtain sponge iron [19–21] etc. But DRM reaction has a few major disadvantages, such as coke deposition [22–25] and deactivation of the catalyst in the reaction atmosphere.

The reactions involved in DRM (discussed in chapter 1, **Sec.1.1**) suggest that CH_4 cracking (**eq. 1.3**) and CO disintegration (**eq. 1.4**) are the primary causes of carbon deposition. Nickel-containing transition metal oxide catalysts are typically very active and long-lasting for the DRM process. During DRM, noble metal catalysts such as Ru [33–35], Pt [36–38], and Rh

[39–42] are also very stable, highly active, and produce lower amounts of coke. Despite these positive factors, noble metal catalysts are not considered for DRM because of their high cost and limited availability. However, due to the more widespread availability and lower cost, transition metal oxide catalysts make viable replacements for noble metal oxide catalysts. The main problem with catalysts based on nickel is that they are very eager to coking, which leads to a rapid deactivation of the active phase and decreases the catalyst's durability and reactivity during the DRM reaction. In order to minimize coke deposition or boost catalytic activity, durability, and coke resistance, transition metal oxide catalysts must also be improved. Extensive research activities have been done all around the world to find numerous potential catalyst systems that have high coking resistance, high durability, and high catalytic activity. The scientific community has been working to develop improved transition metal-based oxide catalysts that are effective for the DRM process, such as perovskite, spinel, hercynite, and pyrochlore. Shahnazi et al. have demonstrated the impact of partially substituted Ni by Mn in the $LaNi_{1-x}Mn_xO_3$ perovskite catalyst [43], which was synthesized by ultrasonic spray pyrolysis, for 10 h DRM reaction in the temperature range 600 °C and 800 °C. They found ~50% CH_4 and 85% CO_2 conversions respectively, having H_2/CO ratio 1.1. Jahangiri et al. have reported and investigated the catalytic impact of Fe-substituted $LaNiO_3$ catalyst [44] by SGCA method. They have explored the activities of the catalysts at various temperatures ranging 600-800 °C. Their results have shown that all the doped materials have a relatively less amount of activity in DRM for 20 h. In order to explore the role of tri-metal substitution at the B site while maintaining the A site constant, Kim et al. have prepared the $LaNi_{0.34}Co_{0.33}Mn_{0.33}O_3$ catalyst [30] modified with Co and Mn at the B site using the microwave-assisted Pechini method. Although nearly 92% conversion of CH_4 has been achieved, the catalyst's activity is only stable for 14 h. Valderrama et al. have reported the perovskite $LaNi_{1-x}Mn_xO_3$ catalyst [45], doping Mn at the Ni site and checked its DRM activity. The freshly prepared $LaNi_{0.2}Mn_{0.8}O_3$ sample was the most active at 750 °C, converting 77% of CH_4 and 84% of CO_2, with H_2/CO ratio close to the expected value of unity. The GHSV for the reforming reaction was 15000 mL g_{cat}^{-1} h^{-1}. Hu et al. have investigated the catalytic role of the Ni/MgO catalyst [46] in DRM reaction. In their report, they found the conversions of CH_4 and CO_2 are 91% and 98%, respectively and the H_2/CO ratio was 0.92 for a duration of 120 h with GHSV of 60000 mL g_{cat}^{-1} h^{-1}. Parallel research work has been further extended by Song et al. by using Mo as a dopant with the Ni/MgO catalyst [47]. Durability of their Ni/Mo/Cat catalyst was for 850 h with 75% CH_4 and 80% CO_2 conversion and H_2/CO ratio was observed to be 0.86. The GHSV used for this gas mixture was 60000 mL g_{cat}^{-1} h^{-1}. Wang et al. have

investigated the DRM activity using $La(Co_xNi_{1-x})_{0.5}Fe_{0.5}O_3$ as a catalyst [48] where the H_2/CO ratio was found to be 0.92 with CH_4 and CO_2 conversions of respectively 70% and 80% for the composition x= 0.1 with GHSV of 36000 mLg_{cat}^{-1} h^{-1}. The catalytic activity in the DRM reaction of Cu-doped $LaNiO_3$ produced by SGCA method utilising propanoic acid as fuel was previously reported by Moradi et al. [49]. The 20% Cu-doped sample $LaNi_{0.8}Cu_{0.2}O_3$ was found to be the most active catalyst, converting 73% of CH_4 and 90% of CO_2 with a H_2/CO ratio of 0.8. However, they only tested their catalyst for 20 h, during which time they observed that the parent Cu-substituted perovskite breaks down into individual oxides and metallic Ni. However, additional studies on this catalyst system relating to phase regeneration and long-term durability of the catalyst have not been done. In the context of this, it would be interesting to thoroughly investigate the Cu-doped $LaNiO_3$ catalysts for the DRM activity by utilising a variety of material synthesis techniques. A thorough characterization of both the aged and pure catalyst was done in order to determine structure-activity correlations and to comprehend the origins of activity behaviour. The results show that the SGCA method of preparing catalysts is superior compared to both SCS and traditional CM methods. Additionally, it has been noted that the DRM activity persists even after the pristine catalysts break down into simple binary oxides of the component elements and metallic nickel, generating a molecular-level nanocomposite a few hours after the catalysis reaction started. Most notably, an in-situ oxidation at a temperature lower than needed for the production of the parent perovskite can readily restore the starting catalyst phase from the disintegrated phases. One noteworthy result of this work is the reversibility of the pure and degraded phases of the aged catalyst by in-situ heat treatment.

3.2. Experimental

The synthesis of the catalyst materials, the characterization techniques and catalytic tests are discussed in detail in Chapter 2 **(Sec. 2.3.1.1.)**.

3.3. Results and Discussion

3.3.1. Powder X-ray diffraction analysis of the as-prepared perovskite samples

The PXRD analysis of CuXLNO (X= 10–80) is shown in **Fig. 3.1**. It is apparent from **Fig. 3.1** that, up to $x = 0.6$, phase pure perovskite is achieved. The projected perovskite phase then appears along with some impurity peaks, including La_2O_3, NiO, and CuO, as the

percentage of Cu-doping is gradually increased. The diffraction peaks of the $LaNi_{1-x}Cu_xO_3$ perovskite phase are observed at 2θ values of 23.2°, 32.8°, 33.4°, 41.5°, 42.3°, 47.3°, 52.6°, 53.2°, 58.5°, 59.5°, 68.7°, 69.74°, 78.02°, and 79.4°, which, consequently, fit with the lattice planes (012), (110), (104), (202), (006), (024), (122), (116), (214), (018), (220), (208), (134), and (128) of the perovskite (JCPDS PDF # 880633). The Scherrer sizes of the as-synthesized samples LNO, Cu10LNO, Cu20LNO, Cu30LNO, Cu40LNO, Cu60LNO, and Cu80LNO are 16.3 nm, 23.9 nm, 24.2 nm, 23.4 nm, 17.4 nm, 56.0 nm and 63.2 nm, respectively.

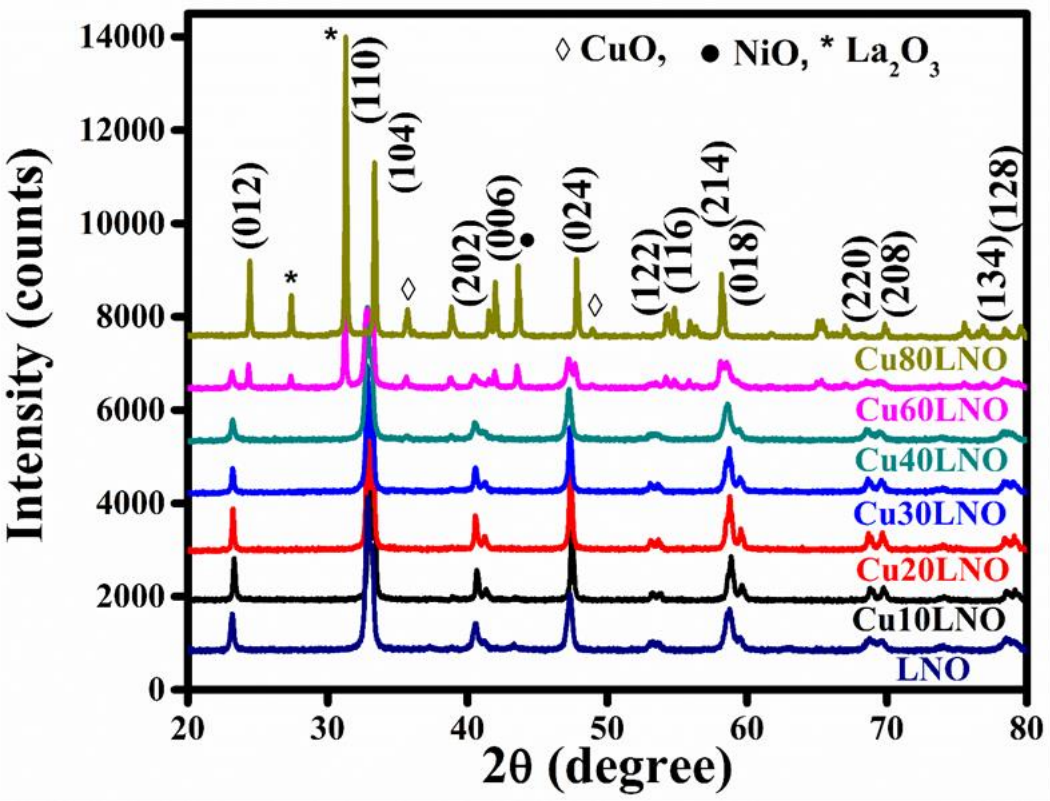

Fig. 3.1: PXRD patterns of as-prepared CuXLNO (X= 10–80, the atom percentage of Cu-doping) perovskite materials.

3.3.2. Screening of materials for DRM

To determine the optimal catalyst, a 10 h preliminary catalytic activity test was performed on all the as-prepared samples. **Fig. 3.2(a–c)** depict the behaviours of the catalytic activity. As-prepared samples, LNO, Cu10LNO, Cu20LNO, Cu30LNO, Cu40LNO, Cu60LNO, and Cu80LNO have the CH_4 conversions of respectively 72%, 92%, 97%, 93%, 92%, 80%, and 77%. The samples have CO_2 conversions of 85%, 95%, 99%, 97%, 93%, 91%, and 90%, respectively. The H_2/CO ratio for this catalytic process is observed to vary between 0.6 and 1.9 for all the samples. It is thus clear that all the doped catalysts have demonstrated

superior DRM activities than the original LNO system and follow the order Cu20LNO> Cu30LNO> Cu40LNO> Cu10LNO> Cu60LNO> Cu80LNO> LNO. Thus, with partial replacement of Ni by Cu in $LaNiO_3$, all the as-prepared perovskite catalysts series have shown higher catalytic activities than the parent LNO, of which Cu20LNO shows the highest activity toward DRM. In this regard, the Cu doping percentage is significant. To throw further light on the Cu20LNO perovskite catalyst and its durability in the reforming reaction, a continuous 100 h DRM reaction has been carried out subsequently.

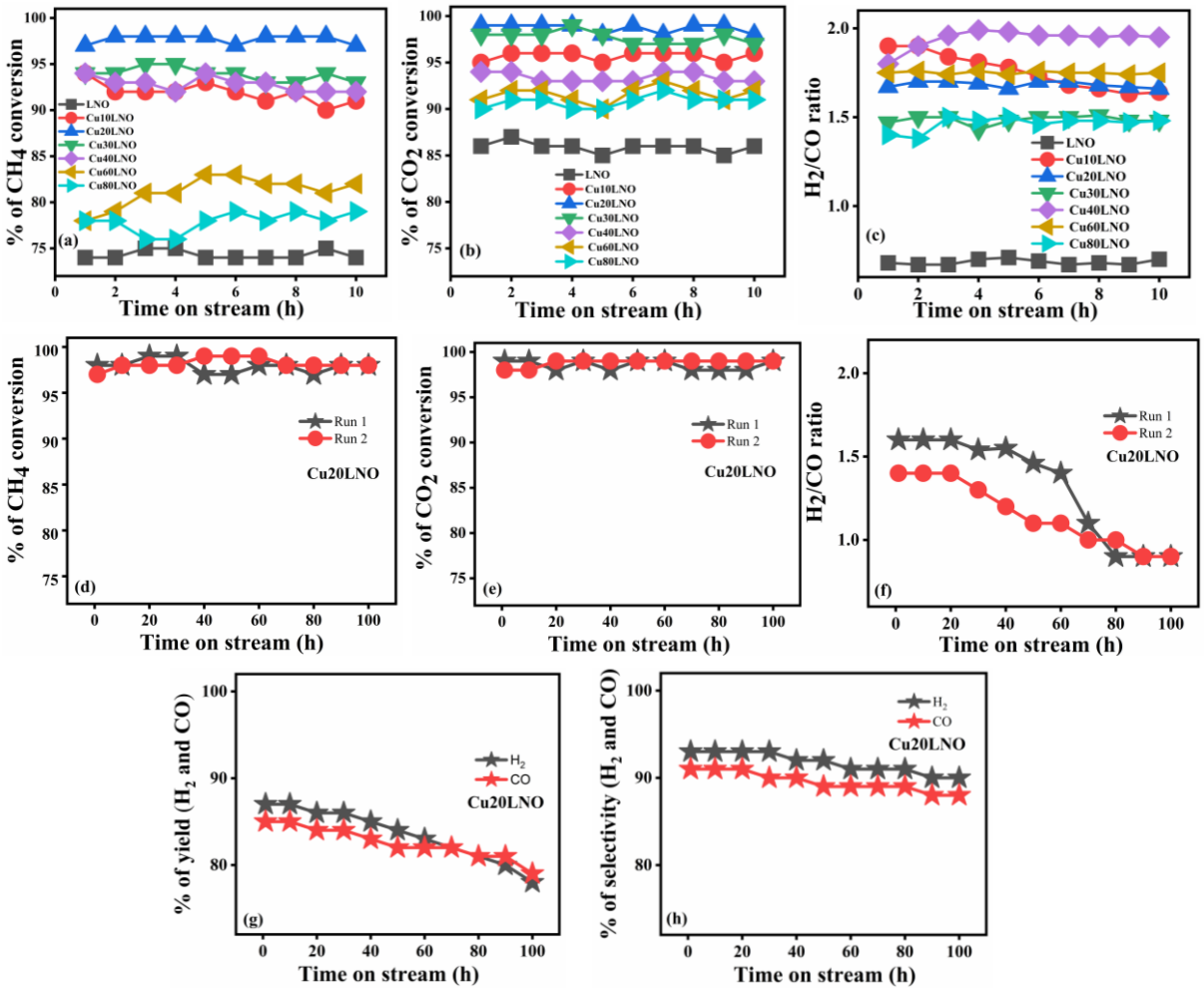

Fig. 3.2: Catalytic activity of as-prepared CuXLNO (X= 0–80) perovskite samples for 10 h and 100 h DRM at GHSV of 34000 mL g_{cat}^{-1} h^{-1} and temperature of 800 °C: (a, d) CH_4 conversion, (b, e) CO_2 conversion (c, f) H_2/CO ratio and (g, h) H_2/CO yield and selectivity.

The CH_4 conversion, CO_2 conversion, and H_2/CO ratio of Cu20LNO catalyst are displayed in **Fig. 3.2(d–f)**. Conversion data reveals that the Cu20LNO has shown remarkable conversions of 97% for CH_4 and 99% for CO_2 during the course of the 100 h DRM reaction, where the H_2/CO ratio varies from 1.4 to ~1. The H_2/CO ratio at first surpasses unity, indicating

the existence of the Boudouard reaction **(eq. 1.4)**, where the produced CO gets converted to carbon and carbon dioxide. As a consequence, the overall amount of CO decreases and the H_2/CO ratio becomes 1.4 for the first 10 h of DRM reaction. Deposition of coke in the reaction atmosphere frequently slows down the reaction, but the Boudouard and reverse Boudouard reactions occur at the same time to facilitate DRM reaction. As expected, the H_2/CO ratio progressively approached unity. **Fig**. **3**.**2(g)** shows that the production of H_2 falls in the range 87% (at the initial stage) and 78% at the termination of 100 h DRM reaction, whereas CO yield varies from 85% to 79% during this period. **Fig**. **3**.**2(h)** shows H_2 selectivity is ~92% with typical CO selectivity ~90%. The reaction was stopped after 100 h, and the aged catalyst was cooled in a helium atmosphere to room temperature. The aged catalyst was also regenerated by annealing at 800 °C. The aged and regenerated forms of the catalyst were then carefully characterized and compared with the as-prepared catalyst in order to figure out the changes in the catalyst in the course of DRM and in the regeneration process.

The apparent activation energies of the reforming reaction related to the different forms of Cu20LNO and as-prepared LNO have been calculated to correlate them with the DRM activity data. For the kinetic investigations, the fixed-bed down flow reactor was loaded with 30 mg of catalyst that had been mixed with 70 mg of purified silica of equal mesh size (85–100), keeping all the other experimental conditions unaltered. The temperature range is varied from 400 to 460 °C in order to keep all the conversions below 20%. Arrhenius plots of LNO and different forms of Cu20LNO catalysts are shown in **Fig. 3**.**3.** The apparent activation energies (considering formation rates of H_2 in the above-mentioned temperature range) calculated from the slopes of the Arrhenius plots are 105.5 kJ mol^{-1} for LNO, 81.5 kJ mol^{-1} for as-prepared Cu20LNO, 66.7 kJ mol^{-1} for aged Cu20LNO, and 74.8 kJ mol^{-1} for regenerated Cu20LNO (see **Fig. 3.3(a)**). Noticeably, the calculated apparent activation energies for the formation of CO are comparatively lower from those for the production of H_2, which are 72.7 kJ mol^{-1} (LNO), 54.0 kJ mol^{-1} (as-prepared Cu20LNO), 37.3 kJ mol^{-1} (aged Cu20LNO) and 54.0 kJ mol^{-1} (regenerated Cu20LNO) (see **Fig. 3.3(b)**). It is evident that pristine LNO has the highest activation energy (105.5 kJ mol^{-1} and 72.7 kJ mol^{-1} for H_2 and CO formation, respectively) and aged form of the catalyst Cu20LNO has the lowest activation energy barrier (66.7 kJ mol^{-1} and 37.3 kJ mol^{-1} for H_2 and CO formation, respectively) among the different forms of the catalyst. It may thus be concluded that once aged, the Cu20LNO catalyst transforms into its most active form. The regenerated form of the catalyst has an activation energy barrier higher than the aged catalyst but still lower than that of the as-prepared catalyst.

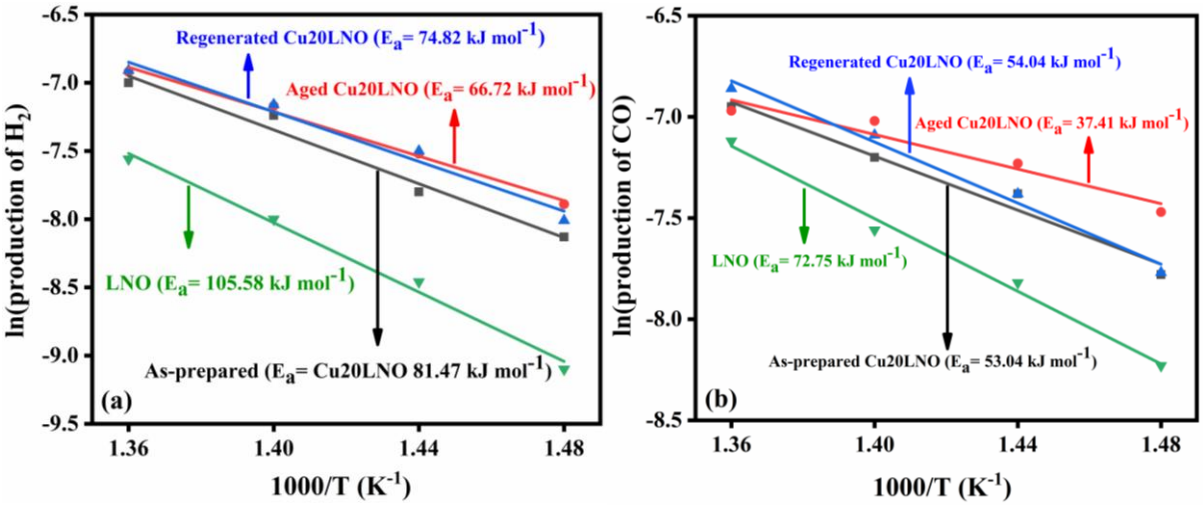

Fig. 3.3: Arrhenius plots for the formation of (a) H_2 and (b) CO for LNO, as-prepared Cu20LNO, aged Cu20LNO and regenerated Cu20LNO catalysts at GHSV = 113300 mL g_{cat}^{-1} h^{-1}).

Table 3.1: DRM activity data of as-prepared catalysts.

Catalyst	CH_4 conversion (%)		CO_2 conversion (%)		H_2/CO ratio	
	10 h	100 h	10 h	100 h	10 h	100 h
Cu10LNO	92	–	95	–	1.7	–
Cu20LNO	97	97	99	99	1.5	1.2
Cu30LNO	93	–	97	–	1.5	–
Cu40LNO	92	–	93	–	1.9	–
Cu60LNO	77	–	91	–	1.7	–
Cu80LNO	75	–	90	–	1.4	–
LNO	72	–	85	–	0.7	–

3.3.3. Powder XRD studies of various forms of Cu20LNO catalyst

Fig. 3.4 shows PXRD patterns of the different forms of Cu20LNO catalyst. It clearly indicates that the typical diffraction pattern of the perovskite phase of the catalyst is completely suppressed with the appearance of several diffraction peaks in the aged sample. These new peaks resemble the simple binary oxide phases as designated in the graph, which apparently come out after the degradation of the initial perovskite phase. It may also be noted that a similar structural change occurs after 10 h of DRM reaction. These phases are closely resembled with

ICDD PDF # 831349 for La_2O_3 (*), 897128 for Ni (○), 140481 for NiO (•), 782076 for CuO (◊), and 832034 for $La(OH)_3$ (▪). Numerous research has confirmed that the catalyst breaks down into its individual metal oxides in the reaction atmosphere [26, 35, 37–43], losing its parent perovskite oxide phase. The catalyst with same composition, $LaNi_{0.8}Cu_{0.2}O_3$ have reported by Moradi et al. [49], similarly broke down into binary oxide phases together with nickel metal in the reaction environment. They recognized the decomposed phases to be La_2O_3 (*) as presented by the peaks at 2θ values of 26.3°, 28, and 48.6°, CuO (◊) at 2θ values of 36.2° and 42.5°, NiO (•) at 2θ values of 31.7°, 44.3°, 51.5° and 55.3° and metallic nickel at 2θ value of 44.3°. However, their investigation was not focussed on regenerating the aged catalyst along with its activity behaviour and the subject of reproducibility. The beauty of the Cu20LNO catalyst in the present findings is that the aged (in the DRM reaction environment) catalyst phase could be regenerated fully by heat treatment for 3 h in static air (see **Fig.3.4**). It may therefore be expected that the initial perovskite phase and the decomposed phase along with metallic nickel will exhibit comparable activity behaviour as shown later. The aged and regenerated Cu20LNO samples have Scherer sizes of 13 nm and 23.5 nm, respectively. Increase in specific surface area of the aged catalyst (from 35 to 54 $m^2\ g^{-1}$ on ageing) from BET measurement is thus well-supported by the reduction of the Scherer size of the sample in the DRM environment.

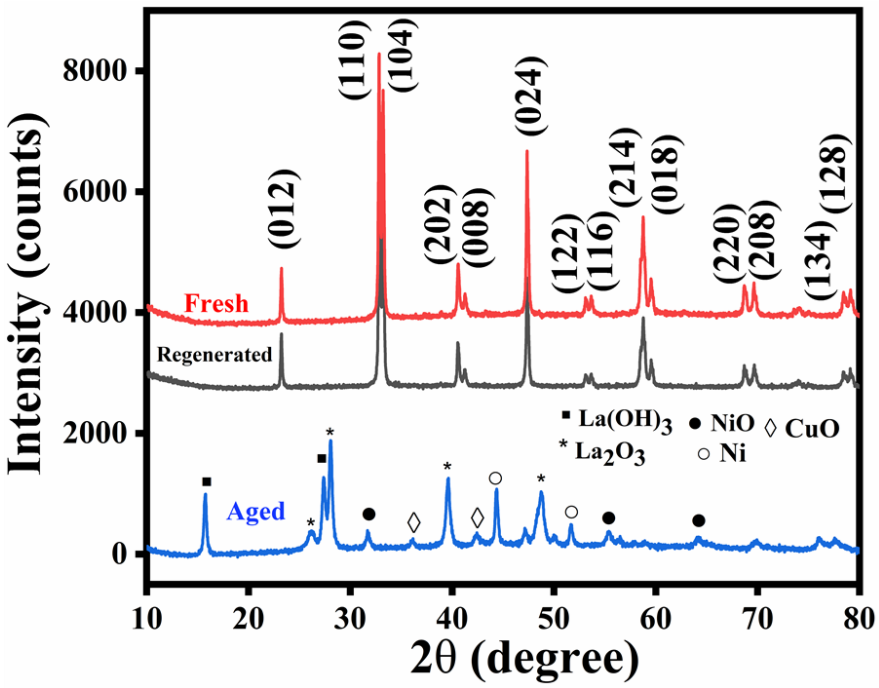

Fig. 3.4: Powder XRD patterns of as-prepared, aged and regenerated forms of Cu20LNO perovskite catalyst.

We then performed structural refinement of the powder XRD data of the two forms in order to find the structural characteristic features of the pristine and regenerated samples. Refinement of the XRD patterns of both the samples has been done with the help of the FullProf Suite software. The rhombohedral ($R\bar{3}c$) space group is properly fitted with both the pristine and regenerated phase patterns during analysis of the PXRD data. The absence of any signature of extra peaks in the refined patterns of the PXRD indicates their phase purity. **Fig. 3.5** shows the refined PXRD patterns of the regenerated and pristine samples. The characteristic phase of the pristine and regenerated components is suggested by the refinement results, which are reliable with accounts from the literature. **Table 3.2** displays the structural and refinement parameters for both phases. It is clear that the diffraction peaks in the regenerated component of the catalyst are not as intense as in the pristine phase. This is simply for the amount of sample used for diffraction, as the regenerated sample is relatively less in quantity. This supports the structural congruity between the pristine and regenerated phases [50].

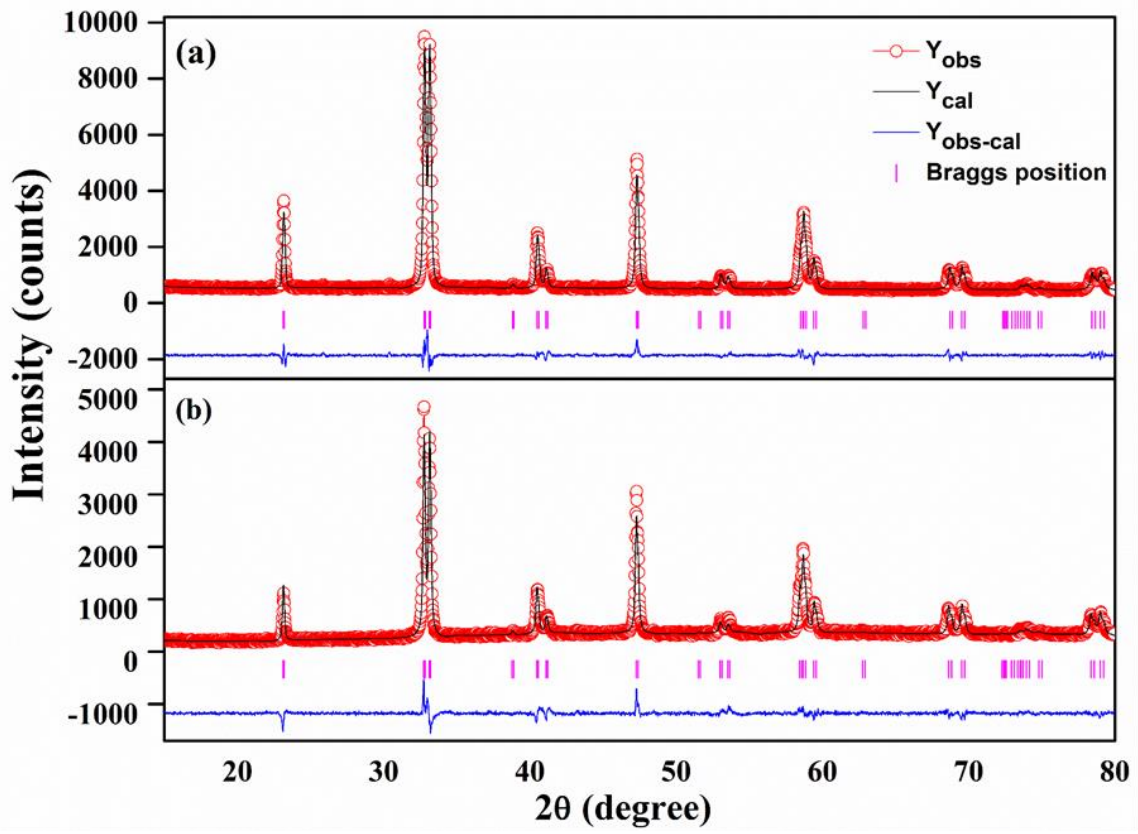

Fig. 3.5: Rietveld powder X-ray diffraction patterns of the (a) as-prepared and (b) regenerated Cu20LNO catalysts. The experimental data, computed pattern, difference curve, and Bragg position are represented, respectively, by the open red circles, black lines, bottom blue lines, and vertical magenta bars.

Table 3.2: Structural and refinement parameters of the Cu20LNO perovskite material in as-synthesized and regenerated forms.

Catalyst	Cell parameters	Bond length (Å)	Bond angle (°)	Atomic Coordinates
Cu20LNO As-prepared Rhombohedral $R\bar{3}c$	a = 5.460 Å b = 5.460 Å c = 13.167 Å V = 339.98 Å^3 γ = 120° R_{Braggs} = 3.32 % R_f = 2.36 % χ^2 = 2.75	Ni/Cu—O: 1.943(9)	Ni/Cu—O—Ni/Cu: 162.22	Atom x y z La 0.00000 0.00000 0.25000 Ni 0.00000 0.00000 0.00000 Cu 0.00000 0.00000 0.00000 O 0.55500 0.00000 0.25000
Cu20LNO Regenerated Rhombohedral $R\bar{3}c$	a = 5.465 Å b = 5.465 Å c = 13.161 Å V = 340.42 Å^3 γ = 120° R_{Braggs} = 6.11 % R_f = 3.39 % χ^2 = 3.20	Ni/Cu—O: 1.944(0)	Ni/Cu—O—Ni/Cu: 162.50	La 0.00000 0.00000 0.25000 Ni 0.00000 0.00000 0.00000 Cu 0.00000 0.00000 0.00000 O 0.55410 0.00000 0.25000

Regeneration of the aged catalyst has subsequently been done *in situ* to further guarantee that the catalytic activity persisted similarly after regeneration. Initially, we subjected the Cu20LNO sample to a 10 h DRM test at 800 °C. Helium gas was used to clean the gas pipelines for 30 minutes after the reaction was stopped. After that, the catalyst was regenerated at 800 °C for 3 h with zero air flow instead of the helium gas flow. The catalytic activity data of the as-synthesised and regenerated Cu20LNO catalysts are shown in **Fig. 3.6**, which indicates almost total retention of activity upon regeneration. The activity test of the regenerated Cu20LNO was conducted under identical reaction conditions. The presence of the Boudouard reaction, which turns CO into carbon and carbon dioxide, is suggested by the as-synthesized catalyst's H_2/CO ratio being greater than unity. As a result, the H_2/CO ratio reaches 1.5 and the total amount of CO decreases within the first 10 h of the reaction. However, during the 100 h reaction, the H_2/CO ratio gradually gets closer to unity [50]. The H_2/CO ratio for the regenerated catalyst ranges from 1.3 to 1. In this instance, the Boudouard reaction is

predominant over the reverse water gas shift reaction (RWGS). However, the H_2/CO ratio approaches unity within about 5 h of the reaction starting, showing a minimum occurrence of both side reactions **(**see **Fig. 3.6).**

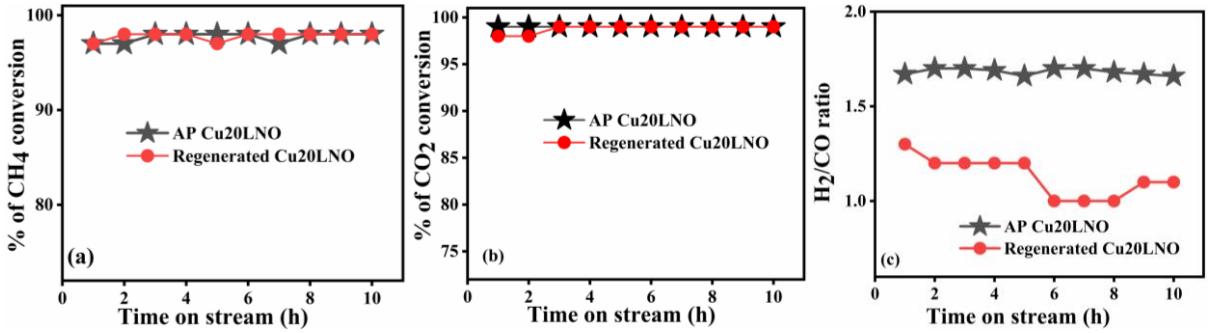

Fig. 3.6: (a) CH_4 conversion, (b) CO_2 conversion, and (c) H_2/CO ratio of the as-prepared and in-situ regenerated Cu20LNO catalyst materials for 10 h of DRM reaction at GHSV= 34000 mL g_{cat}^{-1} h^{-1}, 800 °C).

3.3.4. BET surface area measurement

Fig. 3.7 displays the specific surface area (S_{BET}), N_2 adsorption-desorption isotherms (in the P/P_0 range 0 to 1) of the as-synthesized CuXLNO (where X=10, 20, and 30), aged and regenerated Cu20LNO catalysts and the corresponding inset displays their pore size distribution curves. **Table 3.3** includes the surface area, pore volume, and pore size distribution of the different forms of the catalyst. **Fig. 3.7** reveals that the volume of N_2 gas adsorbed is less at low relative pressure and gradually rises at high relative pressure, signifying the formation of a Type IV isotherm with the type H3 hysteresis loop. The surface areas of the samples, Cu10LNO, Cu20LNO, Cu30LNO, aged Cu20LNO and regenerated Cu20LNO, are about 26, 35, 31, 54, and 51 m^2 g^{-1}, respectively. Compared to all the other samples in the series, Cu20LNO has the highest surface area, which supports its maximum DRM activity. After ageing in the reaction atmosphere, the Cu20LNO catalyst's surface area increased to 54 m^2 g^{-1} from 35 m^2 g^{-1}. This may be because the catalyst has broken down into its individual metal oxides and the particle size was reduced to 13 nm. Larger surface area of the regenerated catalyst in contrast to the as-synthesized catalyst contributes to the high catalytic activity of this catalyst.

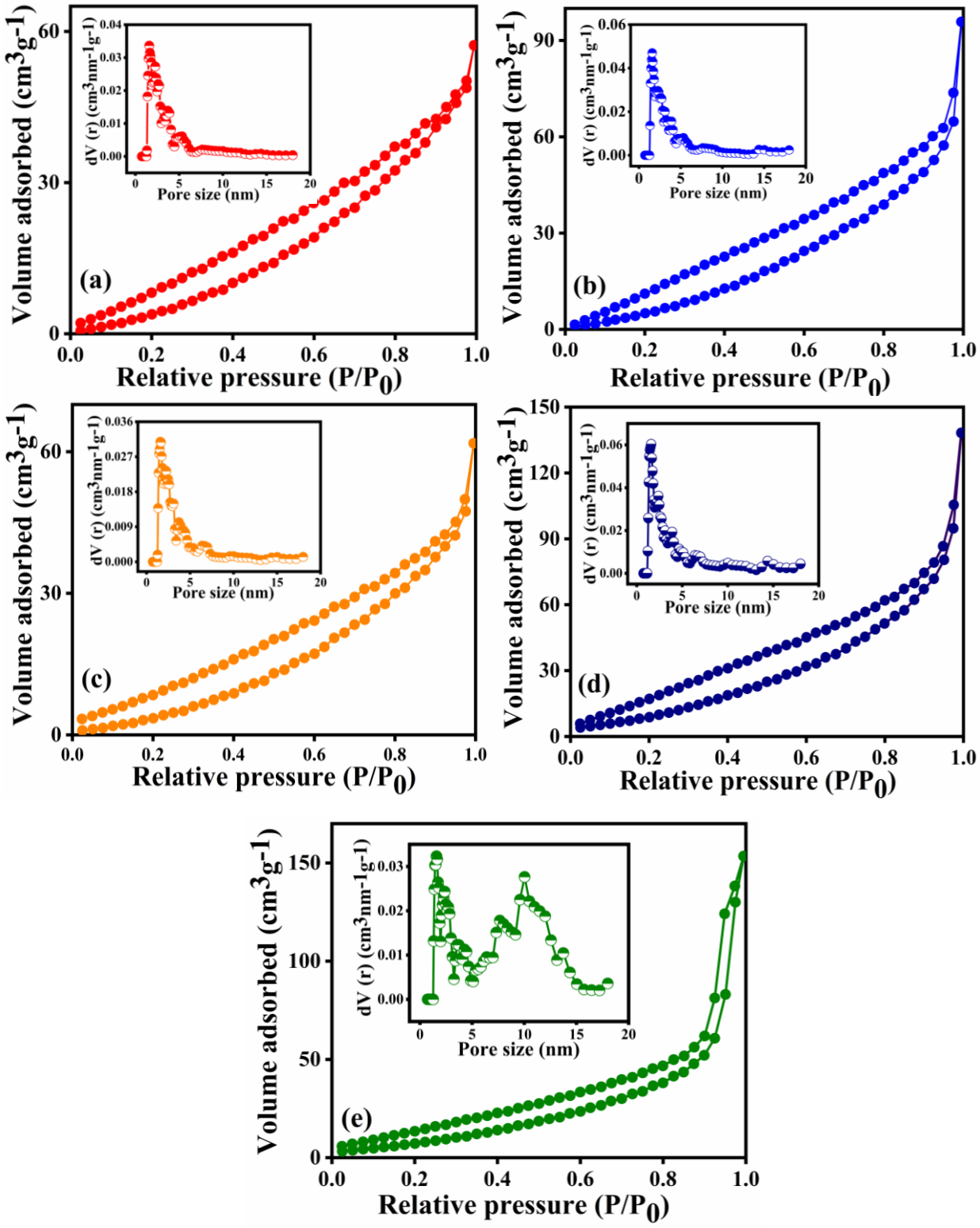

Fig. 3.7: Nitrogen adsorption-desorption isotherms and pore size distribution curves (in the inset) of (a) Cu10LNO, (b) Cu20LNO, (c) Cu30LNO, (d) aged Cu20LNO, and (e) regenerated Cu20LNO.

Table 3: Textural characteristics of different CuXLNO (where X = 10, 20, and 30) aged and regenerated Cu20LNO catalysts with the formation rates of H_2 and CO per unit area (BET specific surface area) and per unit mass of the catalyst.

Catalyst	S_{BET} ($m^2\ g^{-1}$)	Pore volume ($cm^3\ g^{-1}$)	Pore size (nm)	Production rate of $H_2 \times 10^3$		Production rate of $CO \times 10^3$	
				R_1[a]	R_2[b]	R_1[a]	R_2[b]
Cu10LNO	26	0.073	1.58	0.195	50.7	0.189	49.3
Cu20LNO	35	0.101	1.58	0.152	53.5	0.146	51.5
Cu30LNO	31	0.071	1.58	0.165	51.3	0.163	50.4
Aged Cu20LNO	54	0.144	1.38	0.100	53.5	0.096	51.5
Regenerated Cu20LNO	51	0.139	1.36	0.104	53.5	0.100	51.5

[a] in mol $h^{-1}\ m^{-2}$ g; [b] in mol $h^{-1}\ g^{-1}$

3.3.5. Morphology study

The surface morphology and elemental composition of the as-prepared, aged and regenerated samples are studied using FESEM microscopic analysis. From FESEM analyses, it is observed that Cu20LNO exists as aggregated combination of spherical, cubic, and hexagonal-shaped nanoparticles shown in **Fig. 3.8(a–d)**. The morphology of the aged catalyst has transformed from its original shape to a semi-spherical or rod shape, which may be the consequence of the catalyst disintegrating in the reaction environment (see **Fig. 3.7(g–j)**). The regenerated Cu20LNO catalyst has a resembling surface morphology to that of the as-prepared catalyst presented in **Fig. 3.8(k–n)**. Surface morphology and smoothness of the catalyst is almost regained upon regeneration. It is found that the regenerated Cu20LNO catalyst is a highly aggregated combination of nanoparticles with hexagonal, spherical, and cubic shapes, based on FESEM experiments. The EDX of the as-prepared, aged and regenerated forms of Cu20LNO indicates presence of La, Cu, Ni, and O (see **Fig. 3.8(e, f, o)**). As prepared Cu20LNO catalyst has a smooth and clear surface that can be found, but the smoothness of the aged sample is diminished, which is possibly due to the catalyst fragmented in aged form.

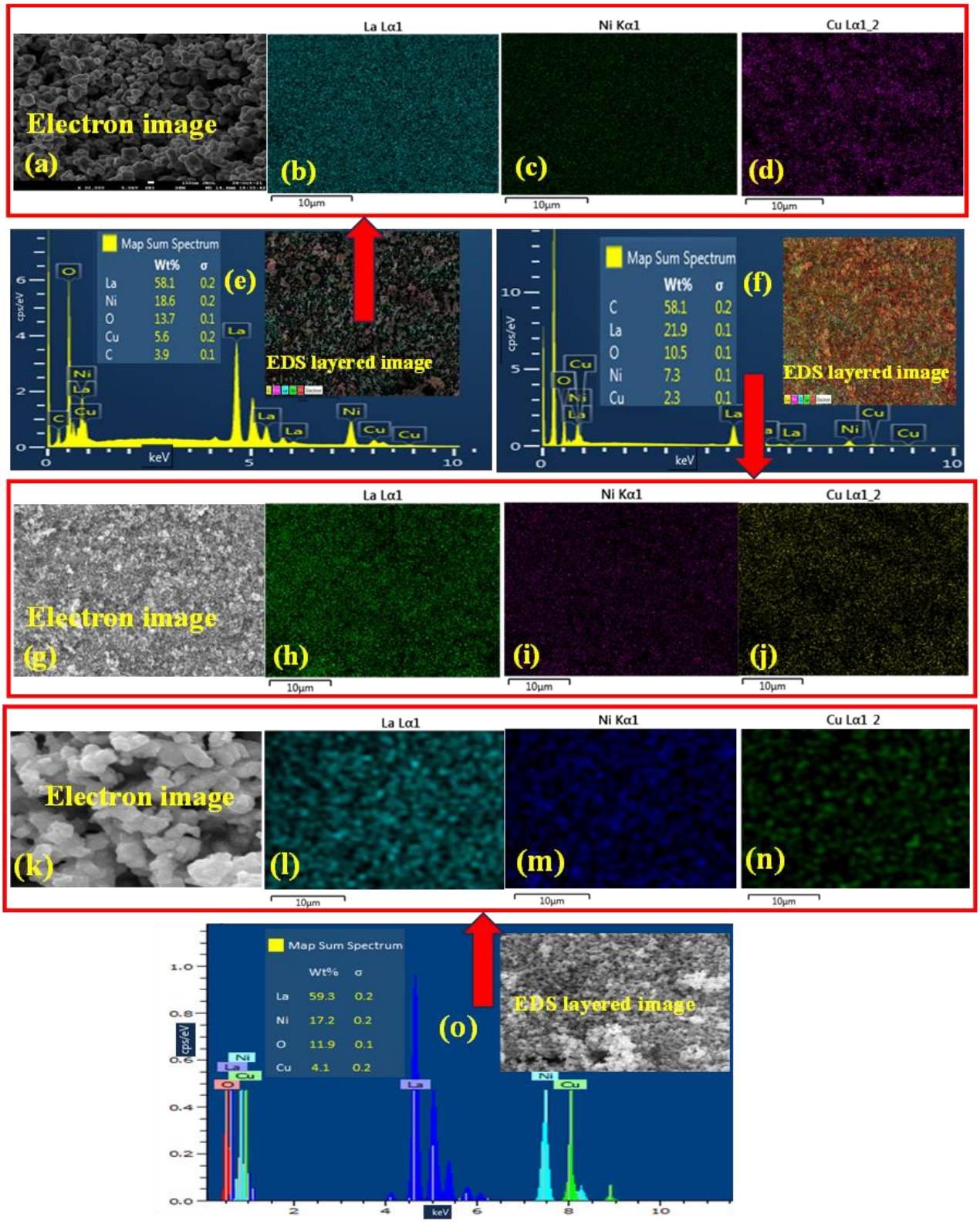

Fig. 3.8: FESEM images (a, g, k); elemental mapping for La (b, h, l), Ni (c, i, m), Cu (d, j, n), and (e, f, o) EDX spectra of fresh, aged and regenerated Cu20LNO, respectively.

3.3.6. HRTEM analysis

TEM and HRTEM analyses are employed to determine the microstructure of as-prepared and aged Cu20LNO. The findings are shown in **Fig. 3.9**. The as-prepared Cu20LNO catalyst has a combination of an irregular spherical, hexagonal, as well as some cube-like morphology (see **Fig. 3.9(a)**). In contrast, in aged form, granular-like morphology (see **Fig. 3.9(e)**) was found. A lattice fringe (*d* spacing) of 0.272 nm, that corresponds to the as-synthesized Cu20LNO sample's (110) lattice plane, can be found in the HRTEM image (**Fig. 3.9(c)**) of the as-synthesized Cu20LNO sample. The data obtained from HRTEM analyses matches well with the findings of the XRD of fresh Cu20LNO. The 0.23 nm lattice fringe corresponds to the (102) lattice plane of NiO (see **Fig. 3.8(g)**) in the aged form of the Cu20LNO catalyst. The XRD analysis of a Cu20LNO sample has been done after the DRM reaction to further support this result, which shows that fresh Cu20LNO transforms into its individual metal oxide phases in the DRM atmosphere. **Fig. 3.9(d)** displays the selected area electron diffraction (SAED) of the fresh Cu20LNO catalyst and the corresponding lattice planes of aged Cu20LNO samples are indicated with the SAED pattern demonstrated in **Fig. 3.9(h).** The ring-shaped diffraction patterns indicate that the catalysts are polycrystalline in nature.

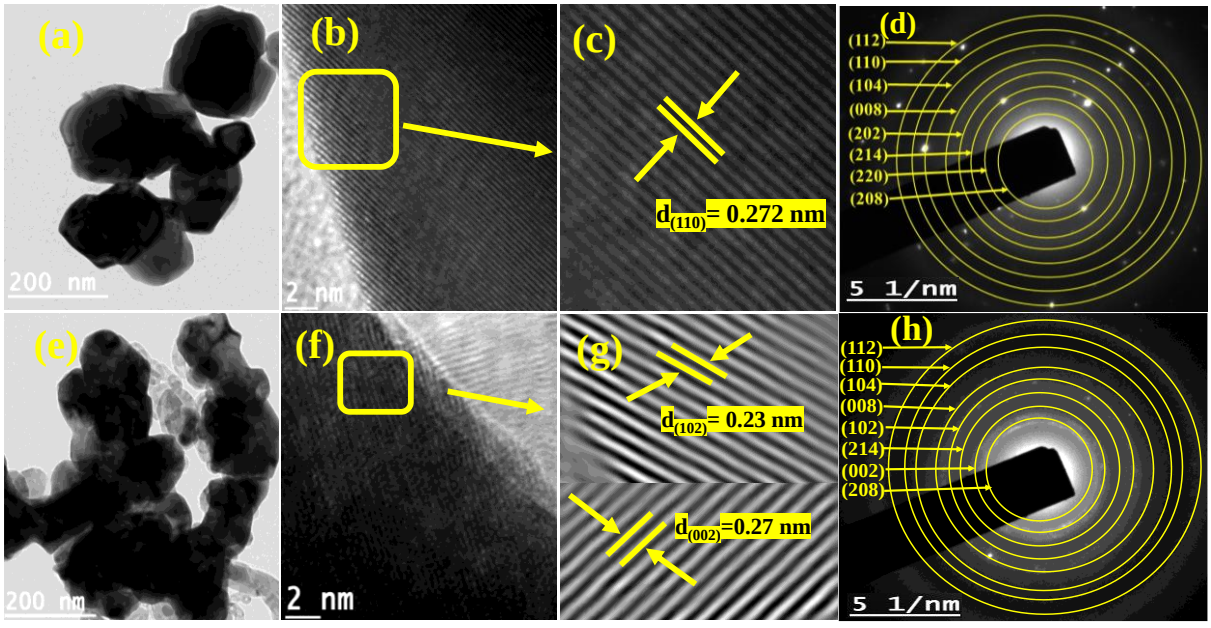

Fig. 3.9: (a, e) TEM images, (b, f) HRTEM image, (c, g) enlarged portion of HRTEM and (d, h) SAED pattern of as-prepared and aged Cu20LNO catalysts, respectively.

3.3.7. XPS analyses

To comprehend the existence of components and their oxidation states in the freshly prepared and aged Cu20LNO samples, XPS investigations are conducted and are presented in **Fig. 3.10**. The different forms of Cu20LNO catalysts contain La, C, O, and Cu according to the XPS survey spectra shown in **Fig. 3.10(a)**. Ni $2p_{3/2}$ core level peak cannot be observed accurately as it is overlapped with La $3d_{3/2}$ core level peak. However, Ni $2p_{1/2}$ core level peak along with its satellite peak is observed in the survey spectra of all the catalysts.

La 3d and Ni 2p core level spectra of as-prepared, aged, and regenerated Cu20LNO are shown in **Fig. 3.10(b)**. A relatively strong peak at around 855 eV compared to surrounding peaks is observed in the spectra of catalysts, which suggests the presence of Ni species in the La 3d core level area. La 3d core level region of as-prepared catalysts shows La $3d_{5/2, 3/2}$ doublet peaks at 835.2, 851.9 eV that correspond to $La(OH)_3$ species present in the catalyst. Observed significant tail peaks with considerable intensities around 833.6 and 850.2 eV are attributed to La_2O_3. The values are in good agreement with literature [51, 52]. These doublet peaks are associated with several initial and final states related to $3d^94f^1$ (lower binding energy) and $3d^94f^0$ (higher binding energy). The board intense peak around 855.0 eV is composed of both La $3d_{3/2}$ $3d^94f^0$ final state of La^{3+} species and Ni $2p_{3/2}$ of Ni^{3+} species [51, 53]. The broad intense peak at 863.5 eV contains satellite peaks of Ni^{3+} and La^{3+}. Peaks at 872.2 and 880.4 eV are attributed to Ni $2p_{1/2}$ of Ni^{3+} species and related satellites. For the aged catalyst, the nature of La 3d + Ni 2p spectral region is slightly different from that of the pristine catalyst. The intense $3d_{5/2}$ peak at 835.4 eV signifies the existence of $La(OH)_3$ species on its surface. There is a small tail peak at 833.9 eV related to La_2O_3. In the XRD pattern of aged catalyst, a peak due to $La(OH)_3$ is observed, which agrees well with XPS observations in the aged catalyst [51, 52]. Decreased relative intensity around 855 eV and low-deep valley around 853.4 eV compared to as-prepared catalyst indicates the presence of reduced Ni species such as Ni metal and Ni^{2+} on the surface of aged catalyst during DRM reaction that is consistent with powder XRD findings (see **Fig. 3.4**). La 3d core level spectrum of the regenerated catalyst looks more or less similar to that of as-prepared catalyst. However, peaks related to $La(OH)_3$ at 835.3 and 852.0 eV become prominent, which is due to the regeneration process of the catalyst**. Fig. 3.10(c)** displays the Cu 2p core level spectra of as-prepared, aged, and regenerated catalyst, respectively. It contains peak at 933.5 eV along with satellite peaks at 941.5 and 943.5 eV, indicating the presence of Cu^{2+} species [54–56]. Satellite peaks are characteristics of transition metal oxides. There is no significant change in the Cu 2p spectral feature in the aged catalyst.

However, catalyst is regenerated as evident from the corresponding Cu 2p core level spectrum of regenerated catalyst. Further, Cu^{2+} peaks are found to be intense and sharp compared to as-prepared catalyst which is attributed to the regeneration process of the catalyst as also observed in La 3d + Ni 2p spectra. C 1s core level spectra of as-prepared, aged, and regenerated Cu20LNO catalysts indicate the presence of different carbon species on the catalyst surface as displayed in **Fig. 3.10(d)**. Correspondingly, the core level peaks at 284.9, 286.2, and 289.1 eV are associated with C–C/C–H, C–O, and carbonate species (CO_3^{2-}). The intensity of C–O species gets increased at the cost of carbonate species in the aged catalyst. There is no significant change in C 1s core level spectrum of regenerated catalyst with respect to as-prepared catalyst, confirming the regeneration of the catalyst [50]. O 1s core level spectra of as-prepared and aged Cu20LNO catalysts are broad, whereas regenerated catalyst shows a distinct peak in the low binding energy region as presented in **Fig. 3.10(e)**. Peaks observed at 528.6, 530.5, 531.7, 532.5, and 533.4 eV are associated with La–O, Cu–O, adsorbed hydroxyl (OH^-), adsorbed carbonate, and adsorbed water species, respectively [57, 58] In the regenerated catalyst, presence of intense and separated La–O peak is because of the regeneration process of the aged catalyst.

Relative surface concentrations of La, Ni, and Cu of as-prepared, aged and regenerated catalysts are estimated by the relations given below [59]:

$$C_{La} = \frac{\frac{A_{La}}{\sigma_{La}\lambda_{La}}}{\frac{A_{La}}{\sigma_{La}\lambda_{La}} + \frac{A_{Ni}}{\sigma_{Ni}\lambda_{Ni}} + \frac{A_{Cu}}{\sigma_{Cu}\lambda_{Cu}}} \quad \text{.....(3.1)}$$

$$C_{Ni} = \frac{\frac{A_{Ni}}{\sigma_{Ni}\lambda_{Ni}}}{\frac{A_{La}}{\sigma_{La}\lambda_{La}} + \frac{A_{Ni}}{\sigma_{Ni}\lambda_{Ni}} + \frac{A_{Cu}}{\sigma_{Cu}\lambda_{Cu}}} \quad \text{.....(3.2)}$$

$$C_{Cu} = \frac{\frac{A_{Cu}}{\sigma_{Cu}\lambda_{Cu}}}{\frac{A_{La}}{\sigma_{La}\lambda_{La}} + \frac{A_{Ni}}{\sigma_{Ni}\lambda_{Ni}} + \frac{A_{Cu}}{\sigma_{Cu}\lambda_{Cu}}} \quad \text{.....(3.3)}$$

where C, A, σ, and λ are the surface concentration, peak area, photoionization cross-section, and mean escape depth, respectively. Integrated areas of La $3d_{5/2}$, Ni $2p_{1/2}$, and Cu 2p peaks have been taken into account to estimate the concentration, whereas photoionization cross-sections and mean escape depths have been obtained from the literature [60, 61]. Relative surface concentrations (at. %) of La, Ni and Cu in Cu20LNO are shown in **Table 3.4**.

It is clear from the table that increase of Cu surface concentration and simultaneous decrease of La and Ni surface concentrations are observed in the aged catalyst indicating the segregation of Cu on the surface of the aged catalyst. However, surface concentrations of La and Ni are found to increase in the regenerated catalyst.

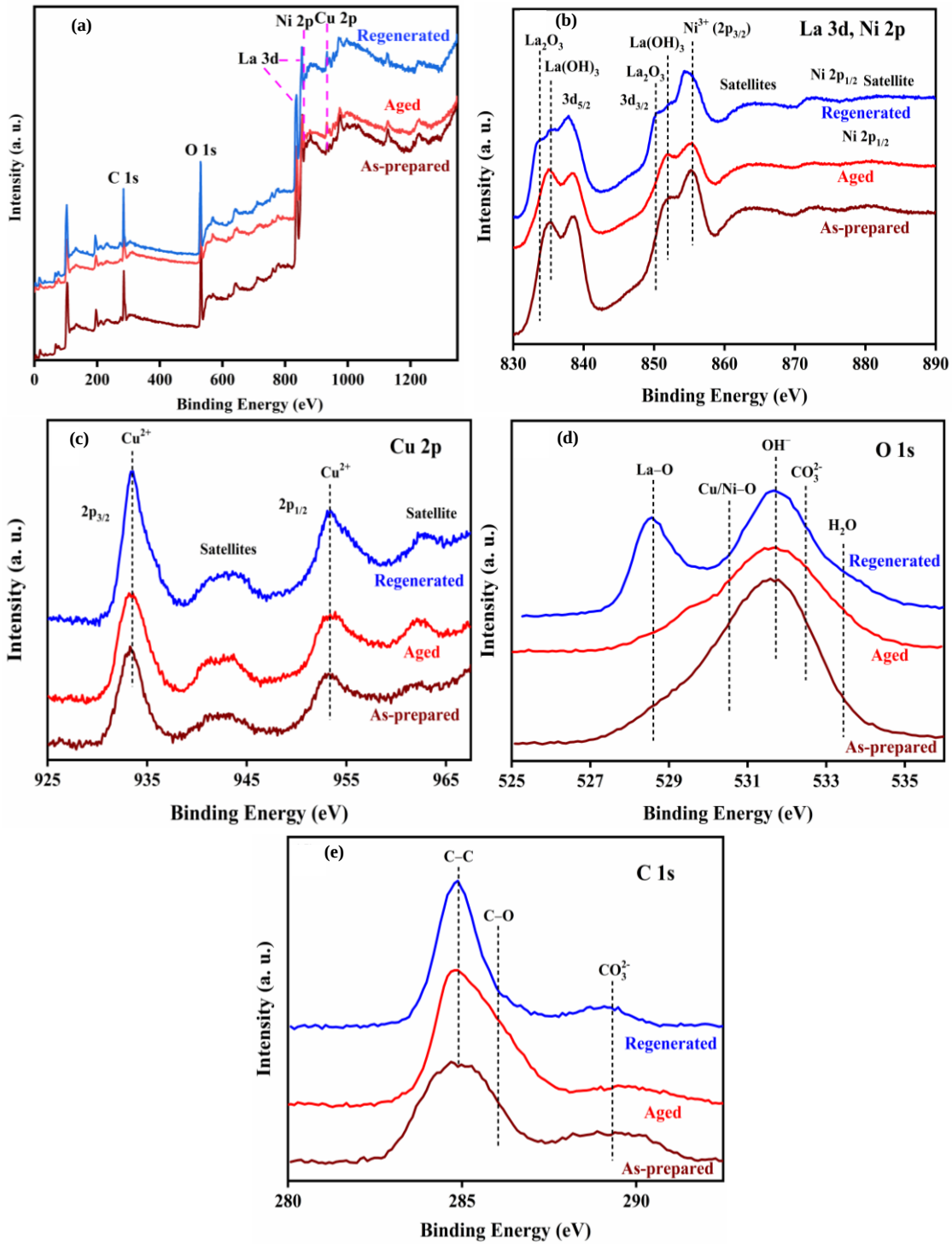

Fig. 3.10: XPS (a) survey spectra, as well as (b) La 3d + Ni 2p, (c) Cu 2p, (d) O 1s, and (e) C1s core level regions of the different forms of Cu20LNO catalyst

Table 3.4: Surface concentrations (at. %) of La, Ni and Cu in as-prepared, aged and regenerated Cu20LNO catalysts.

Form of Cu20LNO catalyst	Surface atomic concentration (at. %)		
	La	Ni	Cu
As-prepared	0.59	0.28	0.13
Aged	0.51	0.26	0.23
Regenerated	0.53	0.27	0.20

3.3.8. Superiority of SGCA method over ceramic and SCS methods

From the earlier findings, it may be projected that any synthetic route leading to a nanocomposite of the necessary component phases of the nanodimensional perovskite catalyst will demonstrate comparable DRM behaviour. The prospect of preparing a catalyst system corresponding to perovskite oxide by mixing the component oxides and then comparing the DRM activity of this Cu20LNO PM with the SGCA made catalyst was the additional factor we took into consideration. The individual metal oxides La_2O_3, CuO, and NiO were prepared via the similar SGCA method [50]. In order to compare the PM's catalytic activity behevior with that in-situ formed catalyst during the first 10 h of the DRM reaction, was subjected directly to the DRM process under identical reaction conditions. The XRD analysis of Cu20LNO CM is shown in **Fig. 3.11(a)**). For the comparison of the DRM activity of the Cu20LNO sample, the SCS method was also involved in preparing the sample and named as Cu20LNO SCS, which is discussed in detail in Chapter 2 **(Sec. 2.3.2.1.)**.

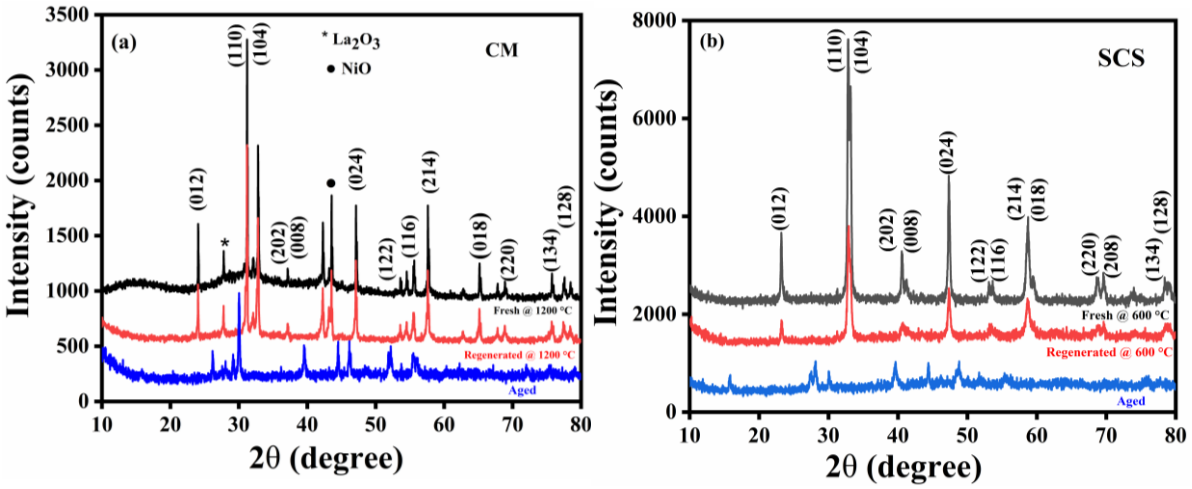

Fig. 3.11: Powder XRD patterns of different forms of Cu20LNO material synthesized via (a) CM and (b) SCS methods.

DRM activity test of Cu20LNO, Cu20LNO PM, Cu20LNO CM, and Cu20LNO SCS catalyst was done under the same reaction conditions. It is noteworthy that the catalyst prepared by the SGCA method surpasses the CM and SCS methods for 10 h of the DRM reaction. The catalyst Cu20LNO CM shows ~70% CH_4 conversion, 89% CO_2 conversion, and an H_2/CO ratio of 1.3 (see **Fig. 3.12**), which is significantly less than the catalyst synthesized using the SGCA method. The Cu20LNO SCS catalyst exhibited H_2/CO ratio 1.3 and around 65% CH_4 conversion with 85% CO_2 conversion. Remarkably, almost no DRM activity was observed for the Cu20LNO PM. Analysis of the powder XRD pattern of the PM after 10 h of the DRM reaction did not show any signs of metallic nickel. Consequently, Ni^0 is only produced during the perovskite phase's breakdown, and this phase is necessary for the catalyst to show DRM activity whether it is prepared using a SGCA process, a conventional CM approach, or SCS. It should be mentioned that the DRM activity was not positively impacted by the physical combination of the component phases. So, in DRM medium, Ni^0 is only produced upon the breakdown of the pristine perovskite phase, whether the catalyst is synthesized via SGCA, CM, or SCS process. Based on this data, we concluded that the component phases' spatial distribution impact more than their presence in the catalyst matrix.

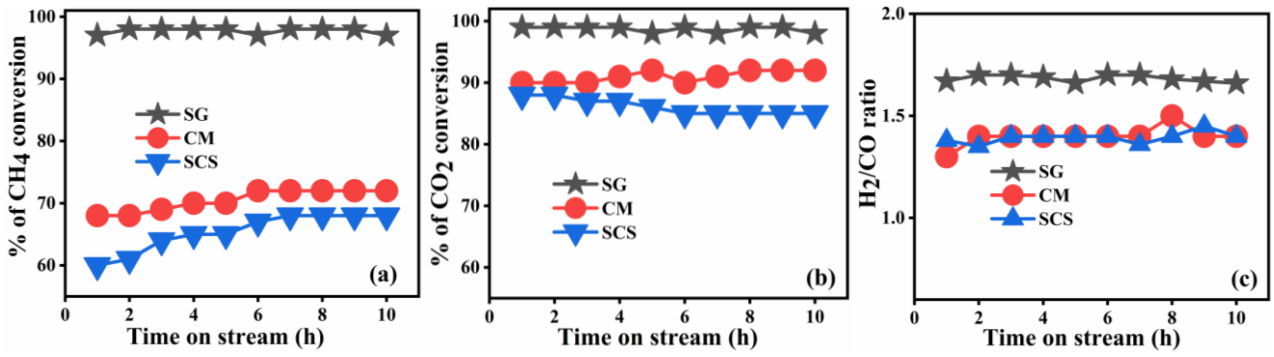

Fig. 3.12: Activity behaviour of the Cu20LNO (made via SG, CM and SCS methods) catalyst materials for 10 h of DRM reaction: (a) CH_4 conversion, (b) CO_2 conversion and (c) H_2/CO ratio at GHSV= 34000 mL g_{cat}^{-1} h^{-1} and 800 °C.

Table 3.5 Compares the Cu20LNO catalyst to other catalysts of the same type that are available in the literature in terms of time-on-stream, GHSV, ratio of H_2/CO, methane and carbon dioxide conversion, and temperature.

Table 3.5: Comparison of the Cu20LNO catalyst with the literature data.

Catalyst	CH_4 conversion (%)	CO_2 conversion (%)	H_2/CO ratio	GHSV (mL g_{cat}^{-1} h^{-1})	Duration of Stability test (h)	Reference
$LaNi_{0.34}Co_{0.33}Mn_{0.33}O_3$	92	96	1.20	12000	14	30
$LaNi_{0.6}Mn_{0.4}O_3$	50	85	1.10	15000	10	43
$LaNi0._8Fe_{0.2}O_3$	50	40	0.80	15000	20	44
$LaNi_{0.2}Mn_{0.8}O_3$	77	84	1.10	15000	14	45
Ni/MgO	91	98	0.92	60000	120	46
Ni/Mo/MgO	75	80	0.86	60000	850	47
$La(Co_{0.1}Ni_{0.9})_{0.5}Fe_{0.5}O_3$	70	80	0.92	36000	5	48
$LaNi_{0.8}Cu_{0.2}O_3$	73	90	0.84	-	20	49
$LaNi_{0.8}Cu_{0.2}O_3$ (Cu20LNO)	97	99	1.3–0.9	34000	100	Our work

3.3.9. Insights of catalyst regeneration at different calcination temperatures

We have previously observed that the aged perovskite sample can be regenerated fully by calcination at the same synthesis reaction temperature of 800 °C, for 3h. It is observed that all the characteristic diffraction peaks of the regenerated catalyst are at the same 2θ position as the pure catalyst, undoubtedly indicating that it has undergone complete phase regeneration on heating (see **Fig. 3.13**). It also suggests that the catalyst can be useful in a cyclic way and hence has promising potential application in DRM reaction. The fact that we were able to effectively regenerate the catalyst through calcination even at lower temperatures of 700 °C and 600 °C (with trace amounts of NiO, peak at 43.2°) for 3 h is even more intriguing (see **Fig. 3.13**). As a result, phase regeneration was accomplished by calcination at the same temperature of 1200 °C, which was necessary for the synthesis of the Cu20LNO CM catalyst, which required comparatively higher temperature for phase formation (see **Fig. 3.11(a)**). However, in order to maintain a similarity with the SGCA produced sample, the phase formation temperature was used for the regeneration of the SCS catalyst (see **Fig. 3.11(b)**).

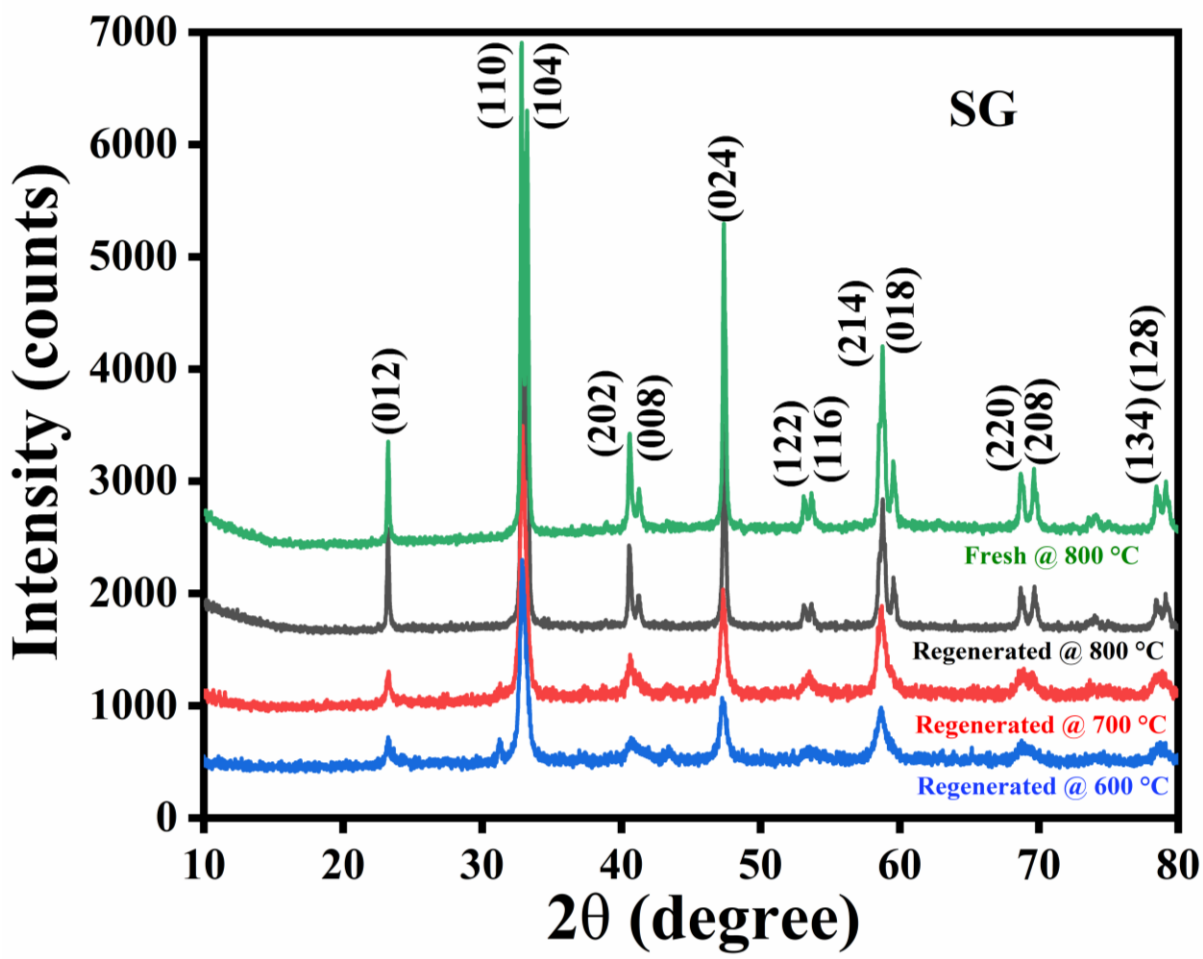

Fig. 3.13: Powder XRD patterns of as-prepared as well as regenerated (at various temepartures) of SGCA synthesized Cu20LNO catalyst.

The DRM activity behaviour of the SGCA synthesized Cu20LNO catalyst, regenerated catalysts at the same reaction conditions but at different calcination temperatures, is displayed in **Fig. 3.14**. Evidently, the catalyst forms that were regenerated at lower temperatures (than synthesis) of 700 and 600 °C show comparable conversion for CH_4 and CO_2, as well as H_2/CO ratios, to the sample that was regenerated at 800 °C. Because of this, the DRM activity remains essentially comparable irrespective of the regeneration temperature. A slight variation was observed for the H_2/CO ratio only. The regeneration temperatures do not affect the DRM activity (see **Fig. 3.14(a–c)**). The H_2/CO ratio should ideally be unity. The variation in the H_2/CO ratio is caused by certain side reactions that take place within the reaction medium and are viable thermodynamically at that temperature. The catalyst that was regenerated at 800 °C had H_2/CO ratio that ranges from 1.4 to 1.1, which preferably indicates the existence of the Boudouard reaction. The Boudouard reaction in the DRM reaction medium is assumed to steadily decrease as the H_2/CO ratio approaches unity. The H_2/CO ratio for the catalyst that

underwent regeneration at 700 °C falls between 0.9 and 1.1. This implies that a small extent of reverse water gas shift reaction (RWGS) takes place during the initial stage. Furthermore, until the H_2/CO ratio gets close to unity, the RWGS gradually decreases. For the catalyst that was regenerated at 600 °C, the H_2/CO ratio ranges from 1.1 to 0.9 (**Fig. 3.14(c)**), which is quite near to unity and indicates the minimum existence of both the reverse water gas shift process and the Boudouard reaction.

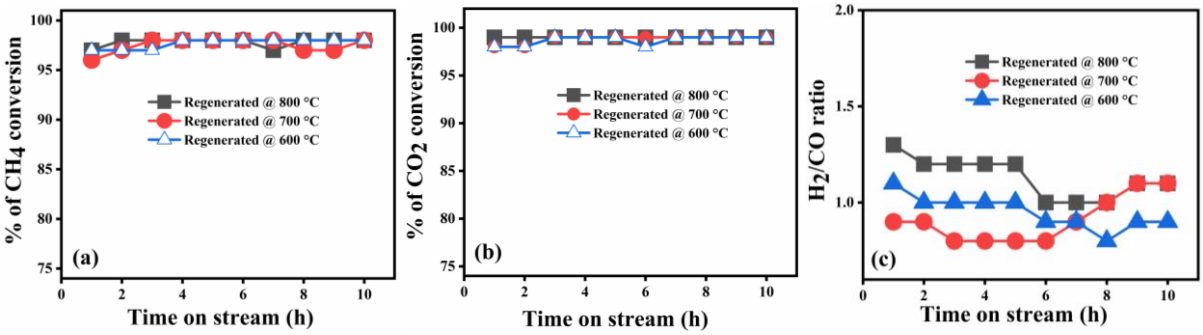

Fig. 3.14: Catalytic activity of Cu20LNO catalyst regenerated at various temperatures: (a) CH_4 conversion (b) CO_2 conversion, and (c) H_2/CO ratio.

3.3.10. TGA studies

Using thermogravimetric analysis of the aged form of the Cu20LNO catalyst, the carbon deposition on the catalyst surface during the long run (100 h of DRM reaction) has been evaluated and compared with that of the pristine sample (see **Fig. 3.15**). The as-prepared does not lose mass when the temperature steadily rises to 900 °C. However, for the aged sample, there are two instances of mass loss were observed: the smaller one appears at 348 °C, while the larger one appears at 490 °C. About 34% of the mass loss is caused by the removal of carbon from the catalyst surface, most likely in the form of CO_2. The influence of carbon formed on DRM activity and durability of Ni-carbon composite catalysts on the surface of the mesocellular silica (MS) synthesized using chemical vapor deposition (CVD) process has been explored by Donphai et al. [62]. According to their study, the synthesis temperature of CVD has a significant impact on both the catalytic activity and durability of the catalysts by affecting the amorphous carbon to CNTs transition. Mass losses were recognized as amorphous carbon happening at 300–400 °C, less stable CNTs at 400–540 °C, and highly stable CNTs at 540–750 °C. In Ni-CNTs composite catalysts, however, the less stable CNTs and amorphous carbon partially encased the nickel catalyst that could be gasified or hydrogenated by methanation. The peak at around ~500 °C is due to the oxidation of amorphous carbon, while the peak at about ~640 °C is caused by carbon nanotubes. Consequently, at lower temperatures, amorphous

carbon develops more readily, and at higher temperatures, it finally turns into graphite carbon. It appears that the coke's structure has a bigger impact than its content [63]. It is believed that the encasement of active catalyst particles in carbon, both graphitic and amorphous carbon layers, slows down the process of methane conversion [64]. The absence of evidence of crystalline forms of carbon in the Cu20LNO aged catalyst examined in this study by XRD and HRTEM is likely to reveal the amorphous character of the coke generated. According to the TGA analysis, mass losses were at about 500 °C. This further corroborates the amorphous character of the deposited coke [44, 50]. It's also possible that the carbon forms separately from the catalyst particles or crystallites and then joins with them to form the nanocomposite. A schematic illustration of a possible reversible in-situ structural transition is presented in **Fig. 3.16**. The starting perovskite Cu20LNO (left) broke down to the component metal/metal oxides in-situ in the reforming reaction (right), but did not significantly alter their initial position within the perovskite structure. These components are then positioned at the corresponding sites of the metal ions in the pristine perovskite structure. Due to their close proximity (~atomic dimension), the components can be readily transformed back to their original perovskite structure when heated in air at around 600 °C. This kind of structure also appears to allow for the easy removal of the formed amorphous carbon species after calcination, resulting in an intact catalyst surface. DRM activity is therefore the same in both phases. The simultaneous occurrence of the Boudouard and reverse Boudouard processes are also suggested by the consistent conversion behaviour over 100 h course of reaction [30–32]. Coke is deposited as a result of the first procedure, but the second step also occurs concurrently to ensure the DRM process runs well. Sustained DRM activity also suggests the reverse water gas-shift reaction and the methanation process, which should not be completely ignored [16]. In a nutshell, the Cu20LNO catalyst can be thought of as a molecular nanocomposite made up of specific metallic Ni and individual oxide components that are observed to Cu20LNO. Based on the results, we have concluded that the individual oxides and metallic nickel forming a molecular level nanocomposite are the real performers in the perovskite catalyst system, enhancing the DRM activity under the selected reaction conditions while other oxides like La_2O_3 and CuO act as support and promoters inside the reaction medium, are responsible for the observed high DRM activity behaviour. The resulting Ni^0/NiO nanocomposite, which is the active phase of the dry methane reformation, is highly dispersed over the La_2O_3 surface [45]. These are separate structures that can be reduced to form uniformly dispersed small sized metal particles on the surface of a basic support. The catalyst's stability and activity are improved while carbon

deposition is inhibited by the small-size particle. The surface carbonaceous species are oxidized when the oxides $La_2O_2CO_3$-CuO (produced in situ during the DRM reaction) [45] form with carbon deposited on Ni particles. This is subsequently disintegrated to release CO_2, thereby restoring fresh La_2O_3 and re-establishing Ni activity for CH_4 reforming. This nanocomposite showed reversible thermal switching involving the pristine perovskite and the nanocomposite, which is responsible for the high DRM activity of the Cu20LNO catalyst.

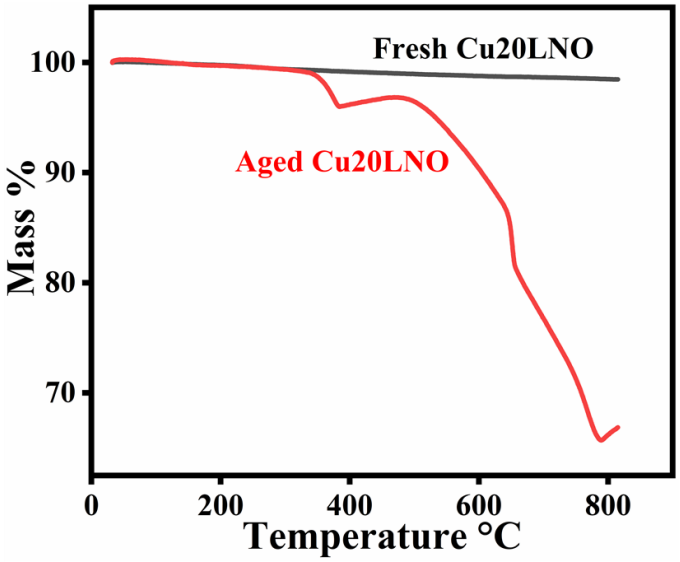

Fig. 3.15: TGA curves of as-prepared and aged forms of Cu20LNO catalyst.

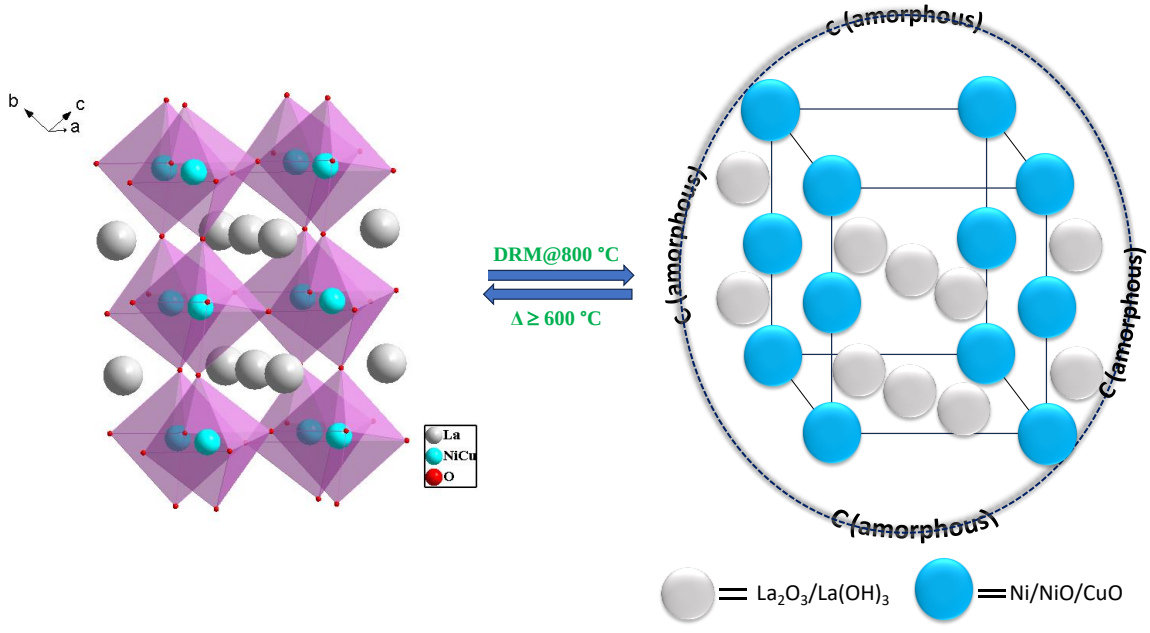

Fig. 3.16: Diagram illustrating the reversible thermal switching (≥ 600 °C) between the pristine perovskite and the molecular level nanocomposite of perovskite that is formed in-situ during the DRM. A schematic representation of amorphous carbon deposition on the nanocomposite is also provided.

3.4. Conclusions

The present study used the traditional one-pot SGCA approach to prepare nano-sized Cu-doped $LaNiO_3$ (LNO) catalysts. PXRD analyses confirm that as-prepared catalyst adopts the rhombohedral phase. Preliminary, the DRM test was run 10 h at 800 °C for all the as-prepared samples. DRM reaction was conducted using the most active Cu20LNO catalyst for 100 h under similar reaction conditions. The individual components, La_2O_3, Ni, NiO, CuO, and $La(OH)_3$, were formed by the disintegration of the pristine catalyst in the DRM reaction atmosphere, as shown by thorough characterization using several techniques of both as-prepared and aged forms of the Cu20LNO catalyst. Smaller-sized discrete metal oxide phases and metallic nickel on the catalyst surface are very crucial for the enhancement of the catalyst's activity in the DRM reaction environment. Other oxides like La_2O_3 act as support and CuO acts as promoters inside the reaction medium, and the nickel oxides along with metallic nickel form a molecular-level nanocomposite that are the actual performers in the perovskite catalyst system for enhancing the DRM activity under chosen reaction conditions. The lost perovskite phase of the aged catalyst has been brought back by simple calcination of the aged catalyst at 800 °C for 3 h. The XRD studies clearly show that the characteristic peaks of the perovskite phase in the regenerated catalyst reappear at the same 2θ positions as the as-prepared form of the catalyst. Interestingly, phase regeneration is also found even at 600 °C, the lowest calcination temperature. The results of the XPS surface characterisation match the other information as well. The XPS result of the regenerated sample is fairly close to the as-prepared catalyst, supporting the regeneration and their comparable active behaviour.

Reference

[1] A. Abdulrasheed, A.A. Jalil, Y. Gambo, M. Ibrahim, H.U. Hambali, M.Y.S. Hamid, A review on catalyst development for dry reforming of methane to syngas: Recent advances, Renew. Sust. Energ. Rev., 2019, 108**,** 175–193.

[2] M. Li, A.C. Veen, Coupled reforming of methane to syngas ($2H_2$-CO) over Mg-Al oxide supported Ni catalyst, Appl. Catal. A, 2018, 550, 176–183.

[3] S. A. Arni, B. Bosio, E. Arato, Syngas from sugarcane pyrolysis: An experimental study for fuel cell applications, Renew. Energy., 2010, 35, 29–35.

[4] C.C. Liu, S.S. Shy, C.W. Chiu, M.W. Peng, H.J. Chung, Hydrogen/carbon monoxide syngas burning rates measurements in high-pressure quiescent and turbulent environment, Int. J. Hydrog. Energy., 2011, 36, 8595-8603.

[5] S. You, Y.S. Ok, S.S. Chen, D.C.W. Tsang, E. E. Kwon, J. Lee, C.H. Wang, A critical review on sustainable biochar system through gasification: Energy and environmental applications, Bioresour. Technol., 2017, 246, 242–253.

[6] X.H. Pham, U.P.M. Ashik, J.I. Hayashi, A.P. Alonso, D. Pla, M. Gomez, D.P. Min, Review on the catalytic tri-reforming of methane - Part II: Catalyst development, Appl. Catal. A., 2021, 623, 118286.

[7] R.C. Canatoy, S.T. Jeong, S.J.C. Galgo, P.J. Kim, S.R. Cho, Biochar as soil amendment: Syngas recycling system is essential to create positive carbon credit, Sci. Total Environ., 2022, 809, 151140.

[8] S. Singh, R. Kumar, H.D. Setiabudi, S. Nanda, D.V.N. Vo, Advanced synthesis strategies of mesoporous SBA-15 supported catalysts for catalytic reforming applications: A state-of-the-art review, Appl. Catal. A., 2018, 559, 57–74.

[9] G. Chen, I.A. Jamro, S.R. Samo, T. Wenga, H.A. Baloch, B. Yan, W. Ma, Hydrogen-rich syngas production from municipal solid waste gasification through the application of central composite design: An optimization study, Int. J. Hydrog. Energy., 2020, 45, 33260–33273.

[10] A.C.V. Olivares, M.N. Barroso, C.A. Lopez, J. Llorca, M.C. Abello, Chelating agent effects in the synthesis of supported Ni nanoparticles as catalysts for hydrogen production, Appl. Catal. A., 2021, 622, 118219.

[11] V.L. Parola, L.F. Liotta, G. Pantaleo, M.L. Testa, A.M. Venezia, CO_2 reforming of CH_4 over Ni supported on SiO_2 modified by TiO_2 and ZrO_2: Effect of the support synthesis procedure, Appl. Catal. A., 2022, 642, 118704.

[12] P. Nikolaidis, A. Poullikkas, A comparative overview of hydrogen production processes, Renew. Sust. Energ. Rev., 2017, 67, 597–611.

[13] Z. Ou, Z. Zhang, C. Qin, H. Xia, T. Deng, J. Niu, J. Ran, C. Wu, Highly active and stable Ni/perovskite catalysts in steam methane reforming for hydrogen production, Sustain. Energ. Fuel., 2021, 5, 1845–1856.

[14] D. Luo, X. Liu, T. Chang, J. Bai, W. Guo, W. Zheng, X. Wen, Towards understanding the lower CH_4 selectivity of HCP-Co than FCC-Co in Fischer–Tropsch synthesis, Phys. Chem. Chem. Phys., 2024, 26, 5704-5712.

[15] R.G. Santos, A.C. Alencar, Biomass-derived syngas production via gasification process and its catalytic conversion into fuels by Fischer Tropsch synthesis: A review, Int. J. Hydrog. Energy., 2020, 45, 18114–18132.

[16] L. Ma, B. Wang, M. Fan, L. Ling, R. Zhang, A specific defect type of Cu active site to suppress Water-Gas-Shift reaction in syngas conversion to methanol over Cu catalysts, Chem. Eng. Sci., 2023, 269, 118496.
[17] S. Asthana, K. Tripathi, K.K. Pant, Impact of La engineered stable phase mixed precursors on physico-chemical features of Cu- based catalysts for conversion of CO_2 rich syngas to methanol, Catal. Today., 2022, 404, 154–168.
[18] P. Luo, Y. Liu, K. Wang, Z. Li, C. Zhang, Y. Wu, X. Zan, W. Huang, Investigation of Al precursor for ethanol synthesis from syngas on Cu-based multifunctional catalyst, Fuel Process. Technol., 2023, 245, 107728.
[19] M. Shahabuddin, G. Brooks, M.A. Rhamdhani, Decarbonisation and hydrogen integration of steel industries: Recent development, challenges and technoeconomic analysis, J. Clean. Prod., 2023, 395, 136391.
[20] H. Elsheikh, V. Eveloy, Assessment of variable solar- and grid electricity-driven power-to-hydrogen integration with direct iron ore reduction for low-carbon steel making, Fuels., 2022, 324, 124758.
[21] I.N. Zaini, A. Nurdiawati, J. Gustavsson, W. Wei, H. Thunman, R. Gyllenram, P. Samuelsson, W. Yang, Decarbonising the iron and steel industries: Production of carbon-negative direct reduced iron by using biosyngas, Energy Convers. Manag., 2023, 281, 116806.
[22] L.A. Schulz, L.C.S. Kahle, K.H. Delgado, S.A. Schunk, A. Jentys, O. Deutschmann, J.A. Lercher, On the coke deposition in dry reforming of methane at elevated pressures, Appl. Catal. A., 2015, 504, 599–607.
[23] F.G. Denardin, A.R. Muniz, O.W. Perez-Lopez, Nature of the interactions between Fe and Zr for the methane dehydroaromatization reaction in ZSM-5, J. Mol. Struct., 2020, 1220, 128720.
[24] X. Li, Q. Hu, Y. Yang, Y. Wang, F. He, Studies on stability and coking resistance of Ni/$BaTiO_3$-Al_2O_3 catalysts for lower temperature dry reforming of methane (LTDRM), Appl. Catal. A., 2012, 413-414, 163-169.
[25] N. Vosooghi, S. Askari, M. Rashidzadeh, S. Sadighi, Promotion of the acidity and textural properties of NiMo/γ-Al_2O_3 catalyst by applying fluorine, boron and phosphorus in hydrodesulfurization of diesel fuel, J. Mol. Struct., 2022, 1270, 133911.
[26] W. Liu, L. Li, S. Lin, Y. Luo, Z. Bao, Y. Mao, K. Li, D. Wu, H. Peng, Confined Ni–In intermetallic alloy nanocatalyst with excellent coking resistance for methane dry reforming, J. Energy Chem., 2022, 65, 34–47.

[27] W. Wattanathan, N. Nootsuwan, C. Veranitisagul, N. Koonsaeng, N. Laosiripojana, A. Laobuthe, Simple cerium-triethanolamine complex: Synthesis, characterization, thermal decomposition and its application to prepare ceria support for platinum catalysts used in methane steam reforming, J. Mol. Struct., 2015, 1089, 9–15.

[28] A. Abanades, E. Ruiz, E.M. Ferruelo, F. Hernandez, A. Cabanillas, J.M.M. Val, J.A. Rubio, C. Lopez, R. Gavela, G. Barrera, C. Rubbia, D. Salmieri, E. Rodilla, D. Gutierrez, Experimental analysis of direct thermal methane cracking, Int. J. Hydrog. Energy., 2011, 36, 12877–12886.

[29] M. Yousefi, S. Donne, Technical challenges for developing thermal methane cracking in small or medium scales to produce pure hydrogen - A review, Int. J. Hydrog. Energy., 2022, 47, 699–727.

[30] W.Y. Kim, J.S. Jang, E. C. Ra, K.Y. Kim, E.H. Kim, J.S. Lee, Reduced perovskite $LaNiO_3$ catalysts modified with Co and Mn for low coke formation in dry reforming of methane, Appl. Catal. A., 2019, 575, 198–203.

[31] D. Wang, P. Littlewood, T.J. Marks, P.C. Stair, E. Weitz, Coking can enhance product yields in the dry reforming of methane, ACS Catal., 2022, 12, 8352−8362.

[32] S. Sun, Y. Zhang, C. Li, Y. Wang, C. Zhang, X. Zhao, H. Sun, C. Wu, Upgrading CO_2 from simulated power plant flue gas via integrated CO_2 capture and dry reforming of methane using Ni-CaO, Sep. Purif. Technol., 2023, 308, 122956.

[33] Y.O. Sokefun, J. Trottier, M.M. Yung, B. Joseph, J.N. Kuhn, Low temperature dry reforming of methane using Ru-Ni-Mg/ceria-zirconia catalysts: Effect of Ru loading and reduction temperature Appl. Catal. A., 2022, 645, 118842.

[34] I. Luisetto, C. Sarno, D.D. Felicis, F. Basoli, C. Battocchio, S. Tuti, S. Licoccia, E.D. Bartolomeo, Ni supported on γ-Al_2O_3 promoted by Ru for the dry reforming of methane in packed and monolithic reactors, Fuel Process. Technol., 2017, 158, 130–140.

[35] P.F. Qu, G.C. Wang, Theoretical insight into the strong size-dependence of dry reforming of methane over Ru/CeO_2, J. CO2 Util., 2022, 65, 102221.

[36] D.G. Araiza, D.G. Arcos, A.G. Cortes, G. Díaz, Dry reforming of methane over Pt-Ni/CeO_2 catalysts: Effect of the metal composition on the stability, Catal. Today., 2021, 360, 46–54.

[37] M. Usman, W.M.A.W. Daud, H.F. Abbas, Dry reforming of methane: Influence of process parameters—A review, Renew. Sust. Energ. Rev., 2015, 45, 710–744.

[38] J.J.T. Herrera, S.A. Korili, A. Gil, Bimetallic (Pt–Ni) La-hexaaluminate catalysts obtained from aluminum saline slags for the dry reforming of methane, J. Chem. Eng., 2022, 433, 133191.

[39] D.J. Xu, J. Wu, Z. Liu, L.Y. Qiao, S.S. Zong, Z.F. Zhou, Y.G Yao, Doping low amount of Zirconium in Rh-LTO to prepare durable catalysts for dry reforming of methane, Mol. Catal., 2023, 535, 112822.

[40] V.A. Kondratenko, U. Karimov, A.A. Kasimov, E.V. Kondratenko, Methane conversion into synthesis gas over supported well-defined Pt, Rh or Ru nanoparticles: Effects of metal and support, Appl. Catal. A., 2021, 619, 118143.

[41] S. Katheria, G. Deo, D. Kunzru, Rh-Ni/$MgAl_2O_4$ catalyst for steam reforming of methane: Effect of Rh doping, calcination temperature and its application on metal monoliths, Appl. Catal. A., 2019, 570, 308–318.

[42] N.E. McGuire, N.P. Sullivan, O. Deutschmann, H. Zhu, R.J. Kee, Dry reforming of methane in a stagnation-flow reactor using Rh supported on strontium-substituted hexaaluminate, Appl. Catal. A., 2011, 394, 257–265.

[43] A. Shahnazi, S. Firoozi, Improving the catalytic performance of $LaNiO_3$ perovskite by manganese substitution via ultrasonic spray pyrolysis for dry reforming of methane, J. CO2 Util., 2021, 45, 101455.

[44] A. Jahangiri, H. Aghabozorg, H. Pahlavanzadeh, Effects of Fe substitutions by Ni in La-Ni-O perovskite-type oxides in reforming of methane with CO_2 and O_2, Int. J. Hydrog. Energy., 2013, 38, 10407–10416.

[45] G. Valderrama, A. Kiennemann, C.U. Navarro, M.R. Goldwasser, $LaNi_{1-x}Mn_xO_3$ perovskite-type oxides as catalysts precursors for dry reforming of methane, Appl. Catal. A., 2018, 565**,** 26–33.

[46] Y.H. Hu, E. Ruckenstein, Comment on “Dry reforming of methane by stable Ni–Mo nanocatalysts on single-crystalline MgO”, Science, 2020, 368**,** 6492.

[47] Y. Song, E. Ozdemir, S. Ramesh, A. Adishev, S. Subramanian, A. Harale, M. Albuali, B. A. Fadhel, A. Jamal, D. Moon, S.H. Choi, C.T. Yavuz, Dry reforming of methane by stable Ni–Mo nanocatalysts on single-crystalline MgO, Science, 2020, 367, 777–781.

[48] H. Wang, X. Dong, T. Zhao, H. Yu, M. Li, Dry reforming of methane over bimetallic Ni-Co catalyst prepared from $La(Co_xNi_{1-x})_{0.5}Fe_{0.5}O_3$ perovskite precursor: Catalytic activity and coking resistance, Appl. Catal. B, 2019, 245, 302–313.

[49] G.R. Moradi, F. Khosravian, M. Rahmanzadeh, Effects of partial substitution of Ni by Cu in $LaNiO_3$ perovskite catalyst for dry methane reforming, Chin. J. Catal., 2012, 33, 797–801.
[50] A. Hossain, M. Bhattacharjee, K. Ghorai1, J. Llorca, M. Vasundhara, S. Roy, P. Bera, M.M. Seikh, A. Gayen, High activity in dry reforming of methane by thermally switchable double perovskite and in-situ generated molecular level nanocomposite, Phys. Chem. Chem. Phys., 2024, 26, 5447–5465.
[51] S. Mickevicius, S. Grebinskij, V. Bondarenka, B. Vengalis, K. Sliuzien, B.A. Orlowski, V. Osinniy, W. Drube, Investigation of epitaxial $LaNiO_{3-x}$ thin films by high-energy XPS, J. Alloys Compd., 2006, 423, 107–111.
[52] V. Celorrio, E. Dann, L. Calvillo, D.J. Morgan, S.R. Hall, D.J. Fermin, Oxygen reduction at carbon-supported lanthanides: The role of the B-site, ChemElectroChem., 2016, 3, 283–291.
[53] S. Viswanathan, L. Mohan, S. John, P. Bera, C. Anandan, Effect of surface finishing on the formation of nanostructure and corrosion behavior of Ni–Ti alloy, Surf. Interface Anal., 2017, 49, 450–456.
[54] T. Baidya, T. Mazumder, K.Y. Koltunov, P.R. Likhar, A.H. Clark, K. Tiwari, V.I. Sobolev, S. Payra, T. Murayama, M. Lin, P. Bera, S. Roy, K. Biswas, O. Safonova, B.S. Rao, M. Haruta, Low-temperature propylene epoxidation activity of $CuO{-}CeO_2$ catalyst with $CO + O_2$: Role of metal−support interaction on the reducibility and catalytic property of CuO_x Species, J. Phys. Chem. C., 2020, 124, 14131−14146.
[55] S. Maiti, A.K. Kundu, O.I. Lebedev, P. Bera, C. Anandan, A. Gayen, M.M. Seikh, Synthesis and magnetic properties of nano-dimensional $Fe_{1-x}Cu_xAl_2O_4$ ($0.3 \leq x \leq 0.8$), RSC Adv., 2015, 5, 83809–83817.
[56] S. Malwadkar, P. Bera, C.V.V. Satyanarayana, Influence of cobalt on performance of $Cu–CeO_2$ catalysts for preferential oxidation of CO, J. Rare Earths, 2020, 38, 941−950.
[57] K. Ghorai, A. Panda, A. Hossain, M. Bhattacharjee, M. Chakraborty, S. K. Bhattacharya, B. Show, A. Sarkar, P. Bera, H. Kim, M.M. Seikh, A. Gayen, $LaNiO_3$/g-C_3N_4 nanocomposite: An efficient Z-scheme photocatalyst for wastewater treatment using direct sunlight, J. Rare Earths, 2022, 40, 725−736.
[58] S.D. Senanayake, D. Stacchiola, P. Liu, C.B. Mullins, J. Hrbek, J.A. Rodriguez, Interaction of CO with OH on Au(111): HCOO, CO_3, and HOCO as key intermediates in the water-gas shift reaction, J. Phys. Chem. 2009, 113, 19536–19544.
[59] C.J. Powell, P.E. Larson, Quantitative surface analysis by X-ray photoelectron spectroscopy, Appl. Surf. Sci. 1978, 1, 186−201.

[60] J.H. Scofield, Hartree-Slater subshell photoionization cross-sections at 1254 and 1487 eV, J. Electron Spectrosc. Relat. Phenom. 1976, 8, 129–137.
[61] D.R. Penn, Quantitative chemical analysis by ESCA, J. Electron Spectrosc. Relat. Phenom. 1976, 9, 29–40.
[62] W. Donphai, T. Witoon, K. Faungnawakij, M. Chareonpanich, Carbon-structure affecting catalytic carbon dioxide reforming of methane reaction over Ni-carbon composites, J. CO2 Util., 2016, 16, 245–256.
[63] D. Xu, Y. Xiong, S. Zhang, Y. Su, The synergistic mechanism between coke depositions and gas for H_2 production from co-pyrolysis of biomass and plastic wastes via char supported catalyst, J. Waste Manag., 2021, 121, 23–32.
[64] A.J. Carrillo, J.M. Serra, Exploring the Stability of Fe–Ni alloy nanoparticles exsolved from double–layered perovskites for dry reforming of methane, Catalysts., 2021, 11, 741.

Chapter 4

Studies on $La_2Ni(TM)O_6$ (TM= Cr, Mn, Fe, and Co) double perovskite materials

Chapter Abstract: *In this present work, we have explored the DRM activity of the double perovskite oxide systems $A_2BB'O_6$ (A= lanthanide metals, B and B′= transition metals). A series of double perovskite oxide system, $La_2Ni(TM)O_6$ (where TM = Cr, Mn, Fe, and Co) were synthesized by the SGCA method and used it for DRM reaction for the first time. All these catalysts showed a promising activity. La_2NiMnO_6 exhibits the highest activity with CH_4 and CO_2 conversions of 97% and 99%, respectively with a considerable H_2/CO ratio varying from* 1.5 to 0.9 *for 100 h. The pure phase of the catalyst disintegrated in the DRM atmosphere, but the original phase of the catalyst can be recovered by heat treatment at ~ 800 ℃ for 3 h. PXRD, BET surface area, XPS, FESEM, TEM, HRTEM, and TGA analyses were used to characterize the samples.*

4.1. Introduction

Fossil fuel is the major source of energy which fulfils our energy demands. But the combustion of fossil fuel in various man-made activities to meet the energy demands that produce different types of pollution, which is one of the biggest threats in our modern life. The produced gases from the fossil fuels are greenhouse gases (mainly CO_2 and CH_4) which continuously increase the temperature of environment. Extensive research indicates that green hydrogen energy (H_2 energy) is one of the best alternative sources of fossil fuels. H_2 energy is considered as a sustainable fuel source because it acts as a high energy fuel source as well as very eco-friendly. Most of H_2 energy production occurs through different catalytic or photocatalytic reaction routes such as DRM, SRM, electrochemical, photoelectrochemical and photochemical reactions. Among all these processes, DRM reaction for H_2 production is one of the best processes because in DRM reaction amounts of H_2 production is very high, long-term catalyst durability (more than 100 h), with a low-cost catalyst, and a simplistic synthetic method for the preparation of DRM catalyst. Furthermore, the efficient process for producing syngas (H_2 + CO) by utilizing two harmful greenhouse gases (CH_4 and CO_2) is one of the major advantages of DRM reaction [1–3]. On the other hand, H_2 energy production via other processes like electrochemical/photoelectrochemical water splitting or photocatalytic H_2 production is not suitable as the amount of H_2 produced is very less, which does not meet today's energy demands, less durability of catalyst (hardly 24 h), it needs high-cost catalyst materials, and finally, multistep with long term process for the synthesis of catalysts.

Therefore, DRM has attracted the attention of the scientific community in the last few decades for its numerous potential applications in various field such as chemical industry [4–8], academic interests as well as environmental aspects [9–12]. Syngas can be used in various fields, like hydrogen production [13–18], preparation of methanol preparation [19–21], diesel production via the Fischer-Tropsch process [22], iron ore reduction to sponge iron [23, 24], preparation of illuminating gas for gas lighting etc. However, the DRM method has a few disadvantages, such as catalyst instability and coke deposition, which blocks the catalysts' active sites and quickly deactivates them in the reaction environment [25]. The reactions related to DRM are discussed in details in chapter 1 (**Sec.1.1**). So, coke deposition is mainly occurring due to reactions (**eq. 1.3**) and (**eq. 1.4**). Thus, the optimization of suitable catalysts is an important issue which can overcome these drawbacks of DRM. Based on the review of the literature, catalysts of nickel with some noble metals like Ru, Pt, and Rh have shown high activity and low coke deposition in DRM. Instead of being a good catalytic performer in DRM reaction, noble metal catalysts are not effective from the viewpoint of high cost and limited availability. On the other hand, extensive research study indicates that the transition metal or metal oxide-based catalysts are very effective, low-cost and easily available due to their extended resources, which can offer an alternative to noble metals for the applications in various research fields, especially for DRM. Among the transition metal oxide-based catalysts, especially nickel containing catalysts are effective in terms of catalytic activity. Unfortunately, in some cases, nickel-based catalysts are also susceptible to coking in DRM which decreases the activity as well as durability of the catalysts. Khalighi et al. have prepared a highly active $X/CoAl_2O_4$ (X=Ni, Co, Rh, and Ru) catalyst [35], which was active for almost 50 h with 90% catalytic activity in DRM reaction. Kennema et al. [36] showed the quantification of carbonization of Ni catalysts during DRM reaction. From the viewpoint of catalysis in DRM, Ni-based catalysts are also needed to be improved in terms of their activity, long durability and coke resistance. Research work has been focused to develop some suitable catalyst with high activity, durability, and resistance to coking. Many efforts by various researchers worldwide have been focused on synthesizing some promising Ni-based metal oxides belonging to different classes of metal oxides, such as perovskite, double perovskite, spinel, pyrochlore etc. Carrillo et al. have investigated the role of double perovskite $Sr_2Fe_xNi_{1-x}MoO_{6-y}$ for DRM reaction for 10 h at 850 °C with 50% of CH_4 conversion [37]. Bhattar et al. have done a review on the extensive features of DRM over doped and pure perovskite derived catalysts [38]. They showed that $LaNiO_3$ prepared by SGCA method, calcined at 750 °C for 4 h is the highly active

catalyst which showed 97% activity in DRM reaction, but it quickly deactivated due to the coke deposition. $LaNiO_3$ prepared via hydrothermal method showed 90% conversion of methane in DRM, but it's very difficult to regenerate the catalyst and each time it produces different kind of internal morphology. $LaNiO_3$ synthesized via SCS method showed the lowest catalytic activity in DRM reaction owing to the presence of amorphous NiO. The small particle sized perovskite $La_{0.46}Sr_{0.34}Ti_{0.9}Ni_{0.1}O_3$ material synthesized by SCS method reduced the coke deposition in DRM, but the DRM activity was very low (only 40% and stable only 20 h). The perovskite catalyst $SmCoO_3$ prepared using the SGCA method by Osarieme et al. [39], calcined at 850 °C was stable up to 55 h but showed comparatively lower DRM activity. It showed only 73% methane conversion in DRM reaction. Therefore, the extensive research work is carried out by the researches to find the suitable catalyst for DRM. Interestingly, it is found that double perovskite materials meet all the criteria for a suitable catalyst for DRM. General research trends indicate that pure double perovskite and a partial substitution of A site or B site of double perovskite materials are reported as an efficient catalyst for DRM reaction [37, 38, 40]. Qiu et al. have synthesized the double perovskite oxide material $Sr_2Co_{0.4}Fe_{1.2}Mo_{0.4}O_{6-y}$ [41] keeping the A site constant, while doping transition metals at B site by SGCA method, which is highly active for DRM reaction (90% methane conversion in DRM reaction). They prepared the catalyst using the SGCA method then heat treatment have been done at 1100 °C in air for 24 h, then again heated at 700 °C for 24 h to get their desired product. The catalyst $Sr_2Co_{0.4}Fe_{1.2}Mo_{0.4}O_{6-y}$ was highly active with 90% catalytic activity in DRM reaction but got deactivated after 24 h. Zhang et al. have shown the superior activity of $NiAl_2O_4$ spinel [42]. They synthesized the catalyst via SGCA method and calcined at 800 °C for 6 h then checked the catalytic activity. The catalyst was durable for 100 h but showed lower activity, 65−69% of methane conversion in DRM reaction. A highly active spinel nano-catalyst $Ni/MeAl_2O_4–MgAl_2O_4$ (Me= Co, Cu, Fe, Mg, Ni, Zn) has been reported by Jalali et al. [43]. They synthesized the catalyst via the deposition-precipitation method and investigated the role of $Ni/MeAl_2O_4–MgAl_2O_4$ (Me= Co, Cu, Fe, Mg, Ni, Zn) varying the A site of the spinel. $Ni/NiAl_2O_4–MgAl_2O_4$ catalyst was the most active with 90% of methane conversion, but the catalyst deactivated nearly after 16 h. A series of pyrochlore oxides $La_2Zr_{1.44}Ni_{0.56}O_{7-d}$, $La_{1.95}Ca_{0.05}Zr_{1.44}Ni_{0.56}O_{7-d}$ and $La_2Sr_{0.05}Zr_{1.44}Ni_{0.56}O_{7-d}$ have been synthesized via Pechini method and investigated the role of the catalyst for in DRM by Bhattar et al. [38]. According to their study, $La_2Sr_{0.05}Zr_{1.44}Ni_{0.56}O_{7-d}$ catalyst was the most effective and stable up to 100 h with 45% of methane conversion at 800 °C.

Keeping all these aforementioned facts in mind, we have decided to synthesize a double perovskite $La_2Ni(M)O_6$ (M= V, Cr, Mn, Fe, and Co) to investigate the role of these catalysts in DRM. Keeping the A site of the double perovskite $La_2Ni(M)O_6$ constant, we have substituted the B site with different transition metal ions and checked their preliminary DRM activity behavior for 10 h. Among the as-prepared catalysts, La_2NiMnO_6 shows the highest catalytic activity of 97% of CH_4 conversion, and 99% of CO_2 conversion in DRM reaction. On the basis of preliminary catalytic performances, the catalyst durability test was performed with a long DRM run time with the most active catalyst. The La_2NiMnO_6 catalyst shows a similar DRM activity for 100 h (under similar reaction conditions). The interesting fact about the catalyst is that in DRM atmosphere it lost its characteristics double perovskite phase, but the lost phase of the catalyst has been regenerated by the heat treatment of the aged catalyst at 800 °C for 3 h. It indicates the recycling behavior of the catalyst. The aged and regenerated phases of the catalyst thoroughly characterized to compare with the as-prepared form of the catalyst.

4.2. Experimental

Chapter 2 **(Sec. 2.3.1.1.)** provides details regarding the catalyst synthesis and other experimental details.

4.3. Results and Discussion

4.3.1. PXRD analysis of the as-prepared double perovskite materials

Figure **4.1** shows the PXRD patterns of the double perovskite LNMO materials. The diffraction patterns indicate that the samples are well-crystallized. The peaks position at 2θ values are 23.0°, 32.5°, 32.8°, 38.8°, 40.0°, 40.9°, 47.0°, 52.6°, 53.2°, 58.1°, 59.1°, 68.1°, 69.1°, 73.3°, 77.6°, and 78.5° that correspond to the lattice planes are (012), (110), (104), (113), (202), (008), (024), (122), (116), (214), (018), (220), (208), (036), (134), and (128), respectively. The PXRD patterns indicate that the LNMnO double perovskite system forms rhombohedral phase. The PXRD data of LNMnO well matches with the reports given by Dutta et al. [44]. But after Rietveld refining, it comes to light that the patterns fit fine when a mixed phase made up of monoclinic and rhombohedral phases is taken into account. No characteristic peaks related to any other impurities are observed in the as-prepared catalyst materials which confirm the phase purity of the compounds. Scherrer sizes of the LNCrO, LNMnO, LNFeO, and LNCoO materials are ~ 40, 22, 17, and 23 nm, respectively.

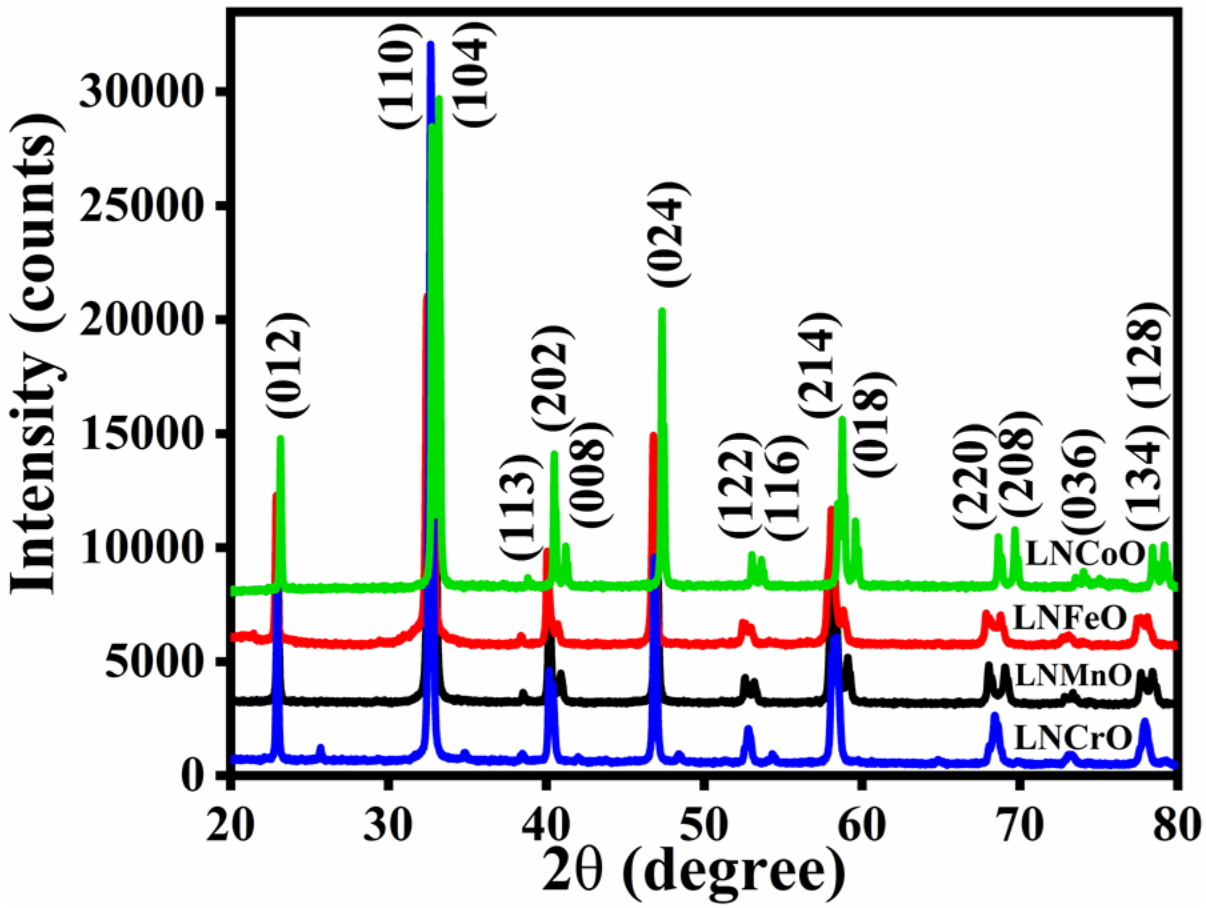

Fig. 4.1: PXRD patterns of as-prepared LNMO (M= Cr, Mn, Fe and Co) double perovskites.

4.3.2. Materials screening

A preliminary catalytic activity test was run on the as-prepared samples for 10 h to optimize the most active catalyst. **Fig. 4.2(a-c)** displays the CH_4 conversion, CO_2 conversion, and H_2/CO ratio of the as-prepared samples. **Fig. 4.2** clearly shows the reactivity of metals towards DRM. The following is the metal ion activity order Mn > Fe≈ Co > Cr. LNMnO exhibits the highest catalytic activity, converting CH_4 and CO_2 97% and 99%, respectively, with the H_2/CO ratio of 1.3. About 92% of CH_4 is converted by both LNCoO and LNFeO. However, the former has an H_2/CO ratio of 1.9 and the latter of 2.4. LNCrO has the lowest DRM activity with 85% of CH_4 conversion and 87% of CO_2 conversion with H_2/CO ratio of 1.9. As a result, there is not much activity difference between Mn and Fe/Co perovskite. These initial screening results reveal that the catalyst La_2NiMnO_6 in the double perovskite oxide series exhibits the maximum methane conversion in DRM. For better understanding about this double perovskite catalyst, a continuous 100 h DRM reaction was then conducted with La_2NiMnO_6 as the catalyst. This helped us in determining the double perovskite catalyst's

durability and catalytic activity. **Fig. 4.2(d–f)** show the CH_4 conversion, CO_2 conversion, and H_2/CO ratio of the La_2NiMnO_6 sample respectively, for 100 h DRM. In order to ascertain the repeatability, results from a second catalytic run are also included in the graph. It was found that La_2NiMnO_6 shows 98% of CH_4 conversion, 99% of CO_2 conversion and the ratio of H_2/CO variation is from 1.5 to 0.9 for 100 h of DRM. Initially, the H_2/CO ratio was higher than unity, indicating the occurrence of the Boudouard reaction **(eq. 1.4),** where CO is decomposed into carbon and carbon dioxide, because of which the amount of CO is decreased, and the H_2/CO ratio started from 1.5. Generally, coke deposition in the reaction medium is observed to compete with the reaction, but the Boudouard and reverse Boudouard reactions effectively support the catalytic activity in the reaction medium. Gradually, the H_2/CO ratio reaches 0.9, which is practically close to the theoretical value of unity. After 100 h of continuous reaction, the reaction was stopped, and the catalyst was subsequently cooled down to room temperature in the helium atmosphere. The aged catalyst was regenerated via calcination at synthesis temperature. Then the aged and regenerated forms of the catalyst have been characterized and compared with the as-prepared catalyst to observe the changes in the catalyst after ageing and after regeneration.

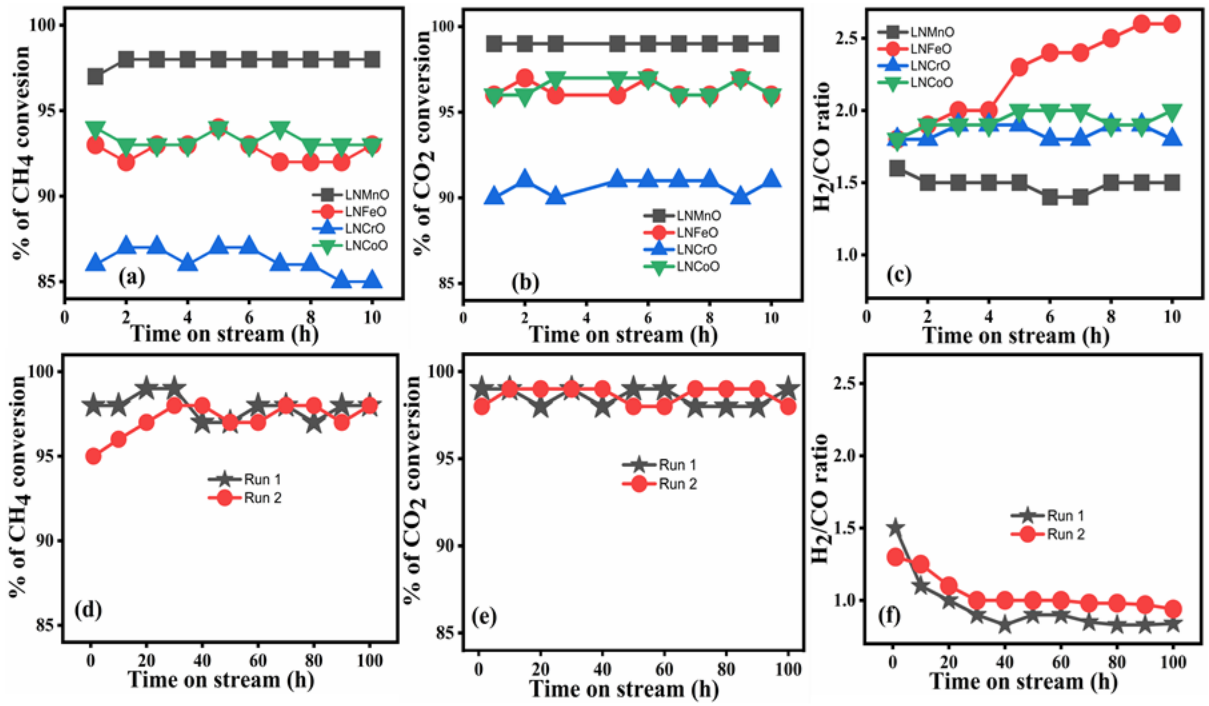

Fig. 4.2: DRM activity of LNMO (M= Cr, Mn, Fe and Co) catalysts for 10 h and those of the most active LNMnO catalyst for 100 h (a, d) CH_4 conversion, (b, e) CO_2 conversion and (c, f) H_2/CO ratio at GHSV of 34000 mL $gcat^{-1}$ h^{-1} and temperature of 800 °C.

4.3.3. PXRD analyses of different forms of catalyst

The PXRD patterns of as-prepared, aged, and regenerated forms of LNMnO are shown in **Fig. 4.3**. The normalized intensity obtained by dividing the observed intensity with that of the most intense peak in the respective diffractogram is plotted to compare the patterns. The XRD patterns of the aged LNMnO catalyst indicate that the newly formed metal oxides can be identified as La_2O_3, NiO, MnO and $La(OH)_3$, which closely matches with JCPDS PDF # 894016 for La_2O_3 (*), 751090 for MnO (◊), 897390 for NiO (•), 897128 for Ni (○), and 832034 for $La(OH)_3$ (▪), respectively. Except the main peak located at $2\theta = 15.8°$, of $La(OH)_3$ all other peaks associated with the $La(OH)_3$ component merge with the diffraction peaks of La_2O_3 component in the powder XRD pattern. The Scherrer size of the regenerated LNMnO catalyst is 18 nm, which is close to the size of the as-synthesized material (22 nm). The Scherrer sizes of the other phases in the aged sample are calculated from the FWHM values of the corresponding planes of (110) for La_2O_3, (100) for $La(OH)_3$, (222) for MnO, (012) for NiO and (111) for Ni. Crystalline sizes of the various phases are observed 13 nm for La_2O_3, 29 nm for $La(OH)_3$, 20 nm for both the oxide phases of Mn and Ni, and for metallic nickel 30 nm. It should be noted that the pristine double perovskite phase's activity behaviour is identical to that of the decomposed phases. Therefore, under the chosen reaction conditions, the individual oxides and metallic nickel are the actual performers in the double perovskite catalyst system, for high DRM activity. Several studies have revealed that the catalyst typically breaks down into its component oxides in the reaction environment, losing its parent oxide phases [11, 25, 28, 33, 35, 42, 44]. The regeneration of the pristine phase out of the disintegrated compositions by heating at a temperature lower than the initial synthesis temperature is the most amazing aspect of this double perovskite oxide catalyst. Double perovskite phase regeneration can be done even by heating at 600 °C or 700 °C for 3 h, although the synthesis temperature was 800 °C. The regeneration of the catalyst is confirmed by the PXRD data that indicate the diffraction peaks appear in the same 2θ position with the as-prepared catalyst (see **Fig. 4.3**). It is important to note that the DRM behaviours of the pristine and degraded phases are almost similar. It is also important to note that even when the double perovskite decomposes after approximately an hour (the signature of metallic Ni production appears after about 30 minutes of reaction (see **Fig. 4.5**) from the start of the DRM reaction, the activity is well-maintained for 100 h. In order to assess the structural correlation of the as-prepared and regenerated phases, we have done structural refinement on the PXRD patterns of both phases. Refinement of PXRD patterns was done using the FullProf Suite program [44]. Both the patterns of as-synthesized and regenerated

catalyst phases require biphasic rhombohedral ($R\bar{3}c$) and monoclinic ($P2_1/n$) space groups for suitable indexing. The refined patterns do not show any signature of impurity, confirming their phase purity. The refined patterns of as-synthesized and regenerated materials are shown in **Fig. 4.4**. In fact, the structure of LNMnO is extremely sensitive to the synthesis condition and annealing temperature [45, 46]. There are several reports which claim the biphasic nature of LNMnO [47−50]. The structural and refinement parameters for both the catalysts are given in **Table 4.1**.

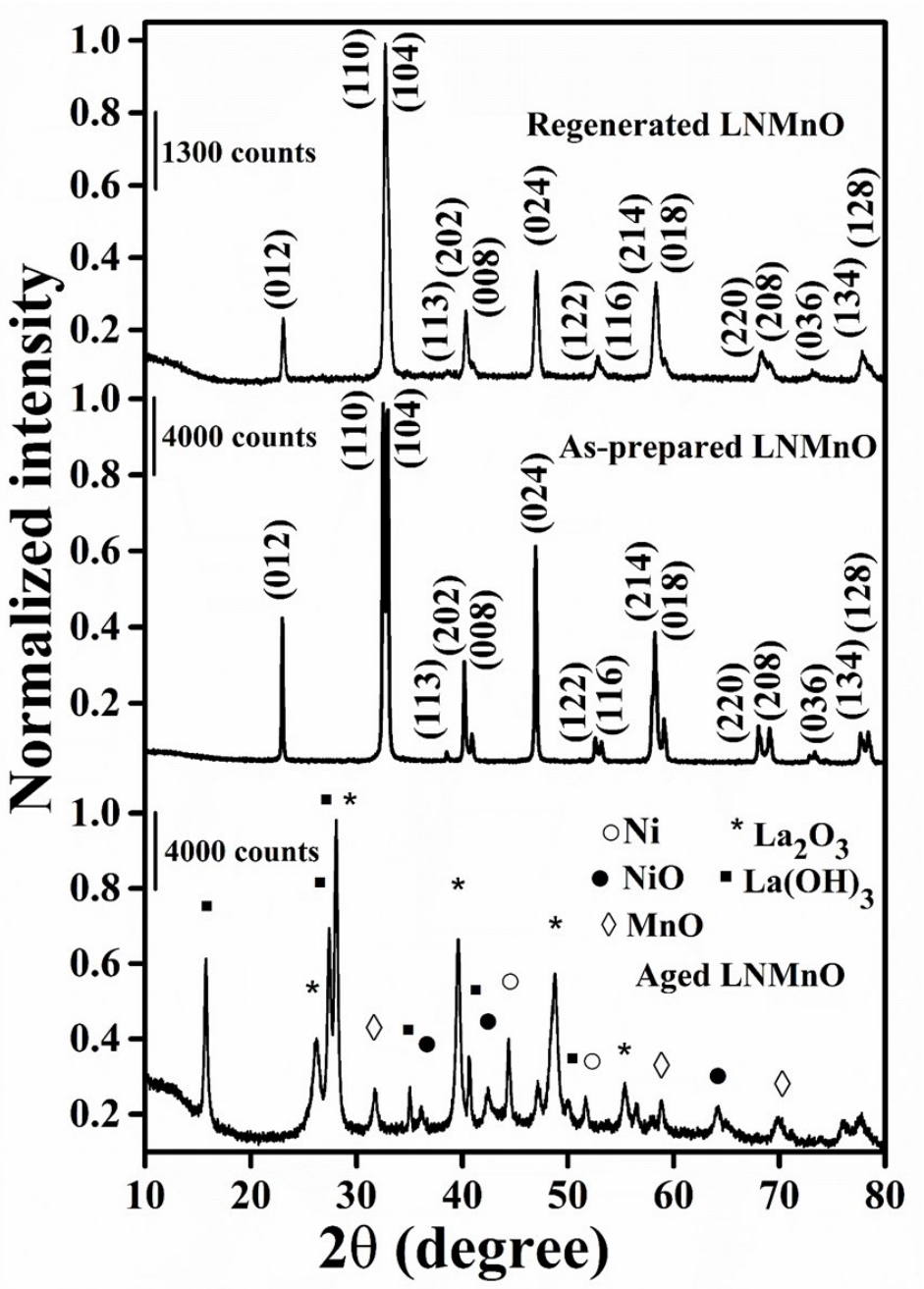

Fig. 4.3: Normalized PXRD patterns of as-prepared, aged (100 h), and regenerated LNMnO double perovskite catalysts.

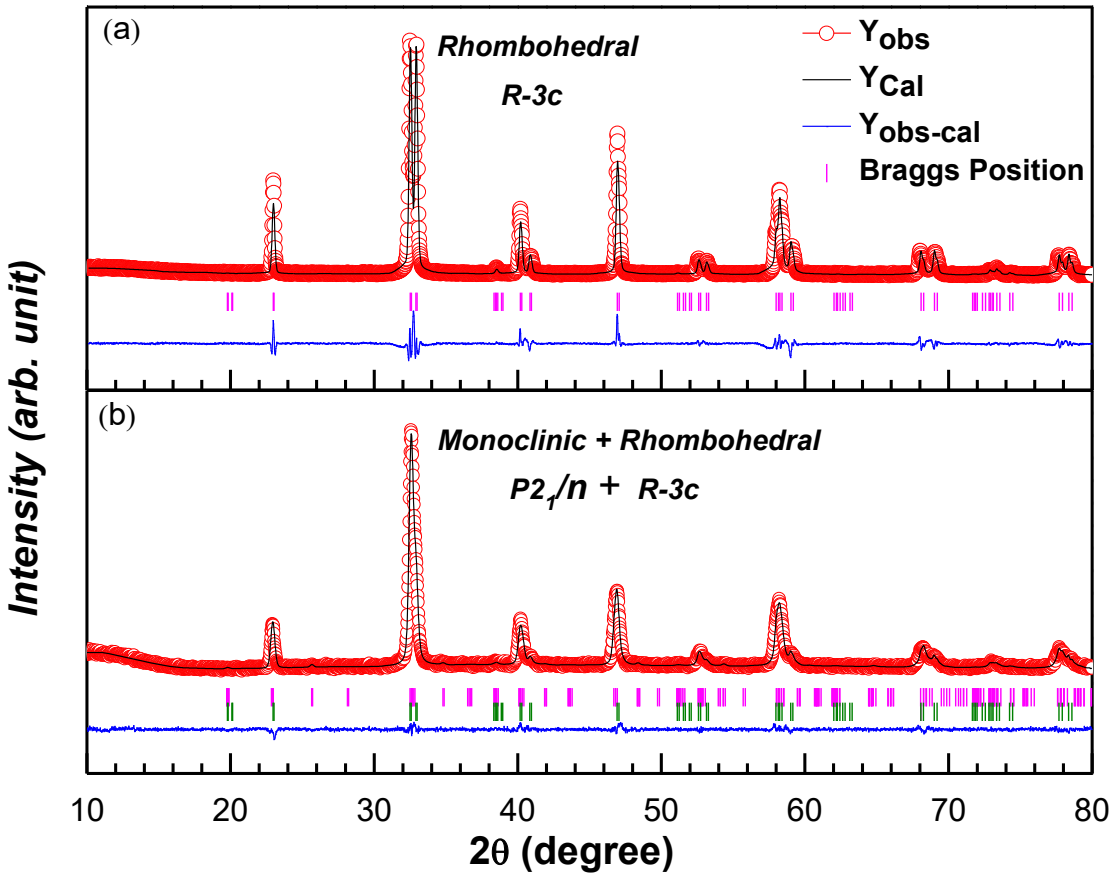

Fig. 4.4: Rietveld powder X-ray diffraction patterns of (a) as-prepared and (b) regenerated LNMnO catalysts. The open red circles, black lines, the bottom blue lines and vertical magenta (rhombohedral phase) and green (monoclinic phase) bars represent the experimental data, calculated pattern, difference curve and Bragg position, respectively.

For further confirmation that the activity remains comparable upon regeneration, the catalyst regenerated in-situ. Initially, the DRM activity of the LNMnO sample was tested for 10 h under similar reaction conditions. The reaction was then stopped, and the gas lines were cleaned in helium for 30 min. The helium gas flow was then changed with zero air for the regeneration of the catalyst at 800 °C for 3 h. The DRM activity of the regenerated catalyst was then tested. The activity data of the as-prepared and regenerated LNMnO catalysts are shown in **Fig. 4.6,** which is nearly identical with the as-prepared catalyst.

Table 4.1: Structural and Rietveld refinement parameters of the LNMnO double perovskite catalyst materials in as-prepared and regenerated forms.

Composition	Cell and refinement parameters		Bond length (Å)	Bond angle (°)
La_2NiMnO_6 (As-prepared) Rhombohedral (80%) & Monoclinic (20%) $R\bar{3}c$ & $P2_1/n$	a = 5.507 Å b= 5.507 Å c= 13.232 Å V= 347.64 Å^3 γ= 120 ° ($R\bar{3}c$)	a = 5.498 Å b= 5.450 Å c= 7.736 Å V= 231.86 Å^3 β= 89.97 ° ($P2_1/n$)	Mn/Ni—O: 1.957 ($R\bar{3}c$) Mn_1/Ni_1—O_1: 1.934 Mn_1/Ni_1—O_2: 1.890 Mn_1/Ni_1—O_3: 1.906 Mn_2/Ni_2—O_1: 2.025 Mn_2/Ni_2—O_2: 2.037 Mn_2/Ni_2—O_3: 2.035 ($P2_1/n$)	Mn/Ni—O—Mn/Ni: 162.27 ($R\bar{3}c$) Mn_1/Ni_1—O_1—Mn_2/Ni_2: 159.13 Mn_1/Ni_1—O_2—Mn_2/Ni_2: 162.41 Mn_1/Ni_1—O_3—Mn_2/Ni_2: 162.01 ($P2_1/n$)
	R_{Braggs}= 2.02% R_f= 1.70% χ^2 = 2.17			
La_2NiMnO_6 (Regenerated) Rhombohedral (40%) & Monoclinic (60%) $R\bar{3}c$ & $P2_1/n$	a = 5.504 Å b= 5.504 Å c= 13.247 Å V= 347.65 Å^3 γ= 120 ° ($R\bar{3}c$)	a = 5.506 Å b= 5.463 Å c= 7.776 Å V= 233.95 Å^3 β= 89.97 ° ($P2_1/n$)	Mn/Ni—O: 1.955 ($R\bar{3}c$) Mn_1/Ni_1—O_1: 1.936 Mn_1/Ni_1—O_2: 1.884 Mn_1/Ni_1—O_3: 1.901 Mn_2/Ni_2—O_1: 2.022 Mn_2/Ni_2—O_2: 2.039 Mn_2/Ni_2—O_3: 2.030 ($P2_1/n$)	Mn/Ni—O—Mn/Ni: 163.01 ($R\bar{3}c$) Mn_1/Ni_1—O_1—Mn_2/Ni_2: 159.10 Mn_1/Ni_1—O_2—Mn_2/Ni_2: 162.51 Mn_1/Ni_1—O_3—Mn_2/Ni_2: 161.20 ($P2_1/n$)
	R_{Braggs}= 3.61% R_f= 4.11% χ^2 = 1.50			

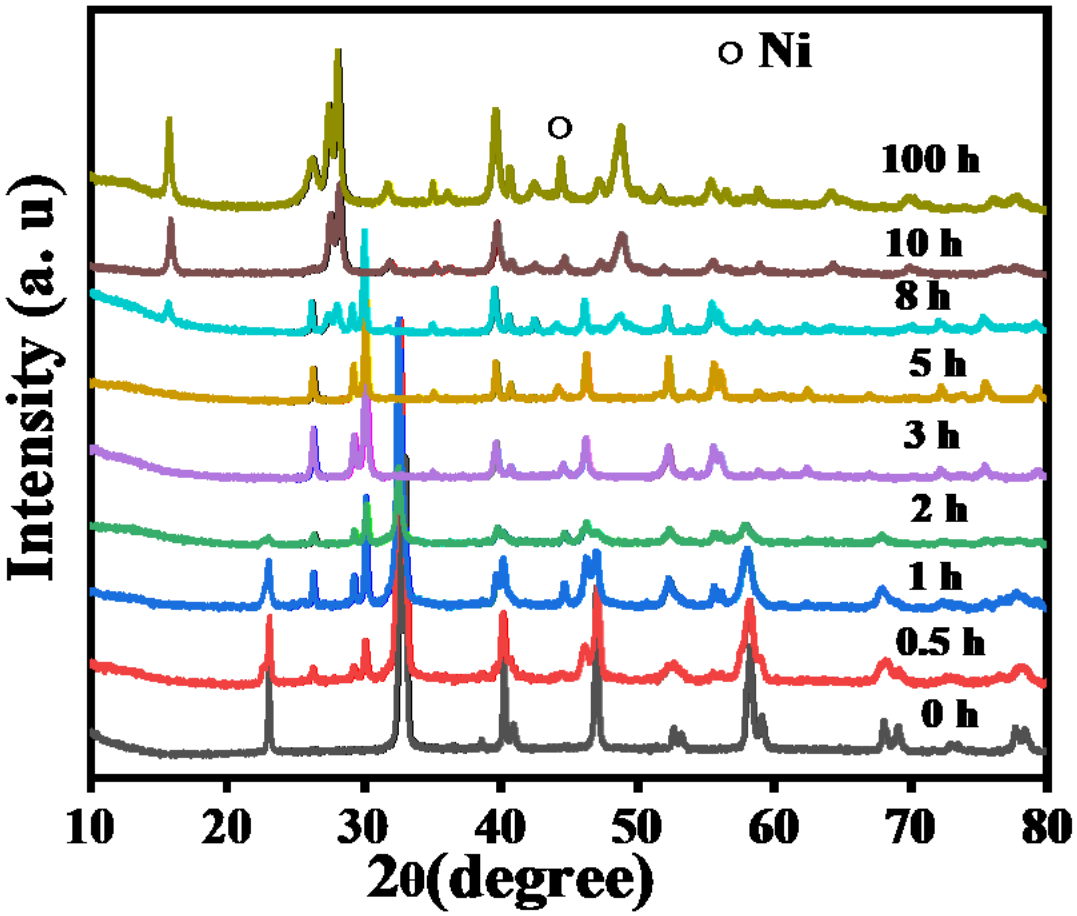

Fig. 4.5: PXRD patterns of LNMnO at various time intervals of DRM reaction. At any specified time, the reaction was stopped and then cooled in helium flow to ~100 °C. The catalyst mesh was ground to powder and subsequently analysed for bulk phase analyses.

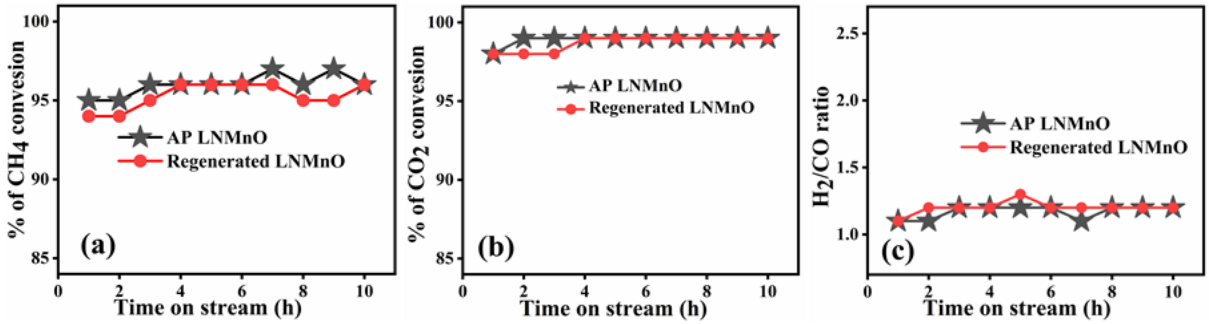

Fig. 4.6: DRM activity of the as-prepared and regenerated LNMnO catalyst materials for 10 h: (a) CH_4 conversion, (b) CO_2 conversion, and (c) H_2/CO ratio at GHSV of 34000 mL g_{cat}^{-1} h^{-1} and temperature of 800 °C.

The phase decomposition-regeneration patterns of the other double perovskite catalyst systems are also investigated. In addition to the most active LNMnO system, the three other LNMO systems (M= Cr, Fe, and Co) also exhibit similar behaviour in DRM. **Fig. 4.7** displays the powder XRD patterns of these three oxide samples following 10 h DRM reaction and regeneration. It is very apparent that in the reaction environment, each of the as-prepared catalysts breaks down into its corresponding individual metal oxide. However, calcination at 800 °C for 3 h regenerated the parent double perovskite phase.

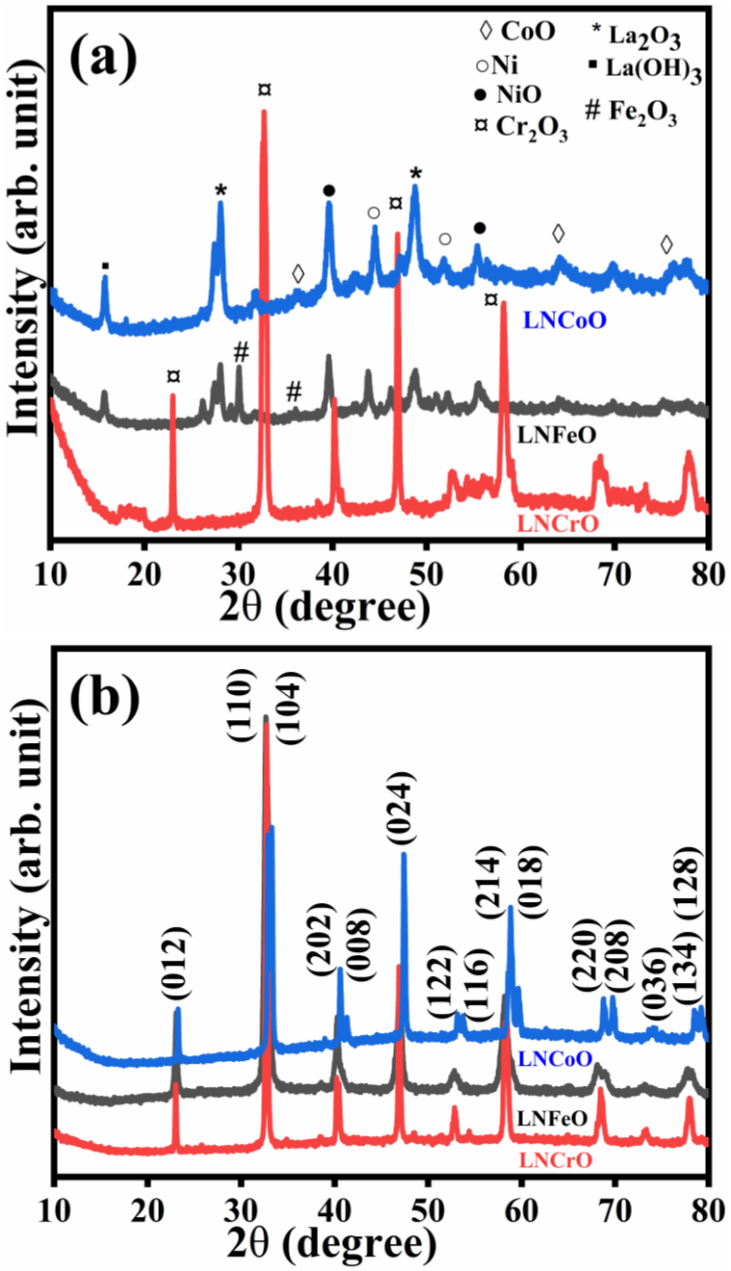

Fig. 4.7: PXRD patterns of LNMO (M= Cr, Fe, and Co) double perovskite materials: (a) aged for 10 h and (b) regenerated ex-situ in static air at 800 °C for 3 h.

4.3.4. BET surface area analyses

The BET nitrogen adsorption-desorption isotherms (in the P/P_0 range 0 to 1) of all the as-prepared catalysts LNCrO, LNMnO, LNFeO, LNCoO, aged LNMnO and regenerated LNMnO are displayed in **Fig. 4.8** and their pore size distribution graphs are given in their corresponding inset. The specific BET surface area (S_{BET}) data of the catalysts are given in **table 4.2.** The N_2 gas adsorption is lower at low relative pressure and rises gradually at high relative pressures, indicating the formation of Type IV isotherm with H3 type hysteresis loop. In a report, Zhang et al. have shown how the calcination temperature effects on the surface area of the La_2NiMnO_6 catalyst is synthesized via SGCA method [51]. It comes to light that the surface areas are low, ranging from 2.70–2.86 $m^2\ g^{-1}$ based on the temperature (800−1000 °C) used for annealing. Qu et al. have also reported the low surface areas (8−14 $m^2\ g^{-1}$) for La_2NiMnO_6 and $La_{2-x}Sr_xNiMnO_6$ synthesized via SGCA process [52]. The LNCrO, LNMnO, LNFeO, LNCoO, aged LNMnO, and regenerated LNMnO double perovskite materials in this investigation have surface areas of approximately 21, 34, 25, 24, 71, and 57 $m^2\ g^{-1}$, respectively. Compared to previous findings, the surface area of the as-prepared LNMnO is relatively higher (34 vs. 2.7 $m^2\ g^{-1}$) [51, 52]. Among the other catalysts, the as-prepared LNMnO has the highest surface area, which contributes to its maximum DRM activity. In the aged system, the surface area increased by a factor greater than twice. This may be caused by the breaking down of the catalyst into its component oxides as well as the reduction in particle size to 13 nm, which has been confirmed by XRD analysis. The larger value of the surface area in the reaction medium plays a significant role in improving the DRM activity. The decomposition of the double perovskite catalyst into component oxides under reaction conditions may be associated with the higher thermal expansion of the lattice system and lower thermal conductivity of the system. The regenerated catalyst's surface area is intermediate between the fresh and aged forms of LNMnO catalyst. Its larger surface area might be the reason for the similar DRM activity of the regenerated catalyst with the as-prepared catalyst.

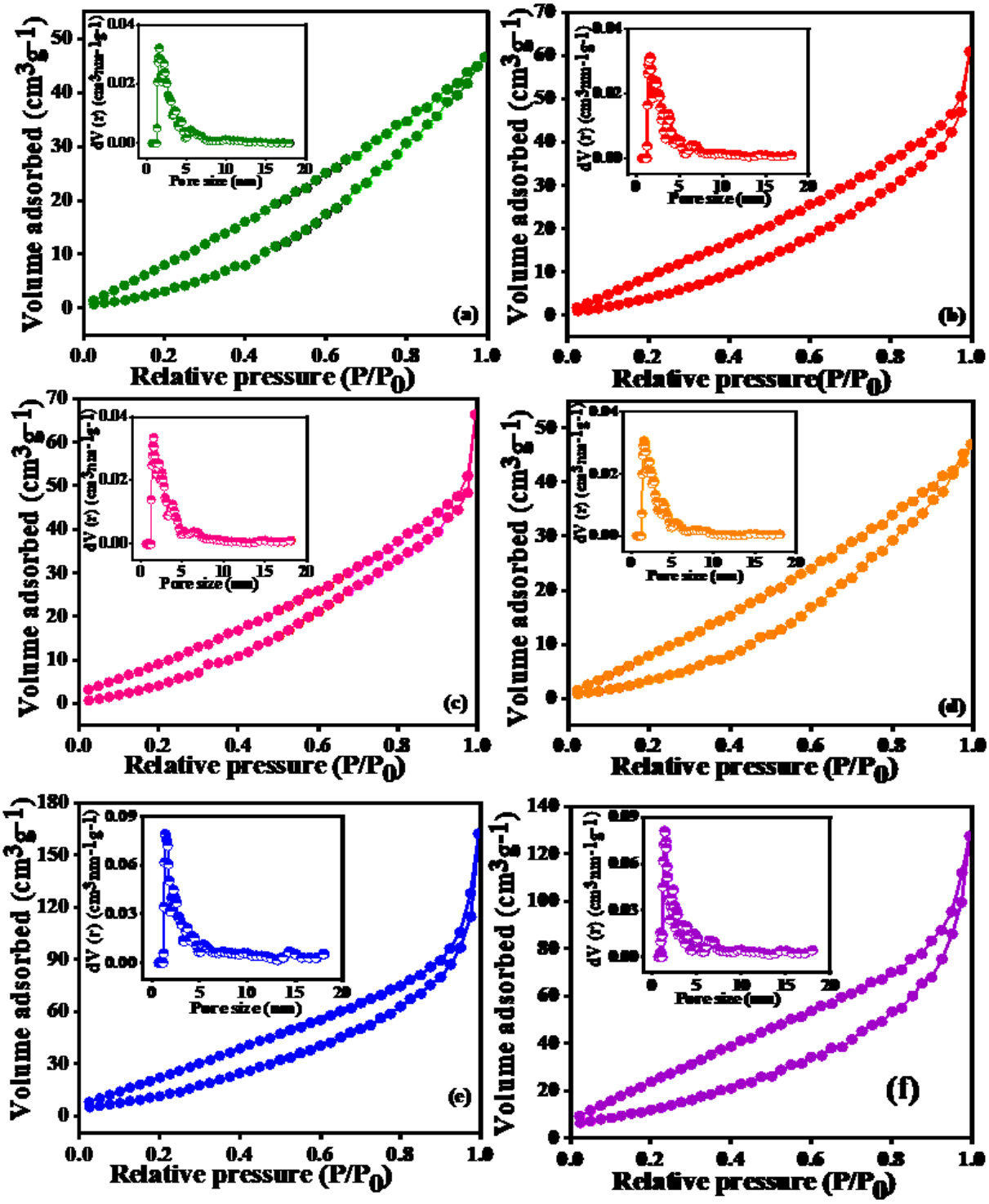

Fig. 4.8: Nitrogen adsorption-desorption isotherms and pore size distribution curves (in the inset) of (a) LNCrO, (b) LNMnO, (c) LNFeO, (d) LNCoO, (e) aged LNMnO and (f) regenerated LNMnO.

Table 4.2: Textural features of various LN(M)O (M= Cr, Mn, Fe, and Co) catalysts.

Catalyst	Specific surface area (m^2 g^{-1})	Pore volume (cm^3 g^{-1})	Pore size (nm)
LNCrO	21	0.074	1.59
LNMnO	34	0.072	1.59
LNFeO	25	0.066	1.59
LNCoO	24	0.065	1.59
Aged LNMnO	71	0.175	1.39
Regenerated LNMnO	57	0.153	1.38

4.3.5. FESEM analyses of different forms of the catalyst

The surface morphology and elemental composition of the as-prepared, aged, and regenerated catalysts were investigated using a FESEM microscopic analysis. LNMnO is a highly aggregated combination of smooth cubic nanoparticles and spherical or semi-spherical in shape (see **Fig. 4.9(a))**. This observation is consistent with the findings of Nasir et al. [53]. The surface morphology of the aged LNMnO catalyst (see **Fig. 4.9(c)**) has been transformed from its original morphology to a nano rod-shaped morphology. It is noted that the regenerated LNMnO catalyst resembles the as-prepared (see **Fig. 4.9(e)).** The EDXS spectra of fresh, aged and regenerated catalysts of LNMnO (see **Fig. 4.9(b-e))** show the existence of La, Mn, Ni, and O as elements. It has been found that the fresh and regenerated LNMnO catalyst materials have a smooth and clear surface, whereas the aged sample has a less smooth surface, most likely as the catalyst being degraded in DRM environment.

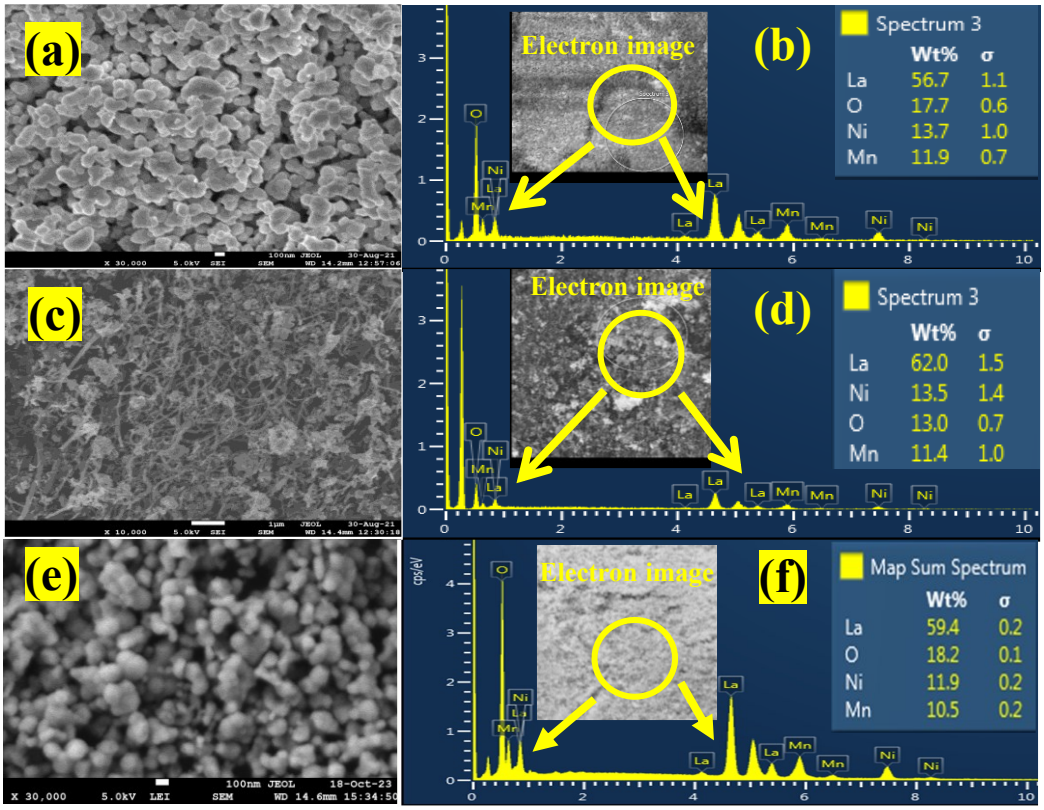

Fig. 4.9: FESEM images of (a, c, e) and EDXS spectra (b, d, f) of as-prepared, aged, and regenerated forms of LNMnO material, respectively.

4.3.6. HRTEM analyses of different forms of the catalyst

TEM and HRTEM analyses were carried out to investigate the microstructure of as-prepared, aged, and regenerated forms of LNMnO catalyst. The as-prepared LNMnO has an irregular cube-like morphology with some sphere-like particles, as shown in **Fig. 4.10(a)**. However, following ageing, this morphology changes to an aggregated irregular granular-like morphology, (see **Fig. 4.10(e)).** The shape of the regenerated catalyst appears to be identical to the pristine catalysts (see **Fig. 4.10(i))**. It is found that the as-prepared LNMnO sample consists a lattice fringe (*d* spacing) of 0.275 nm that corresponds to (110) lattice plane of LNMnO [52] (**Fig. 4.10(b, c))** which is well-supported by the XRD patterns of pure LNMnO. The 0.165 nm lattice fringe in the aged LNMnO catalyst corresponds to (202) lattice plane of NiO (see **Fig. 4.10(g))**. The result supports the transformation of pure LNMnO into distinct oxide phases after the DRM reaction and is consistent with the XRD analysis of aged catalyst. The lattice fringe (d spacing) of 0.191 nm corresponds to (024) lattice plane in the regenerated LNMnO sample (see **Fig. 4.10(j, k)),** and matches well with the as-prepared LNMnO catalyst. The corresponding lattice planes of as-prepared (**Fig. 4.10(d))**, aged (**Fig. 4.10(h)**), and regenerated

LNMnO (**Fig. 4.10(l)**) are shown by their selected area electron diffraction (SAED) patterns. The polycrystalline nature of the catalyst is indicated by the ring-type diffraction patterns.

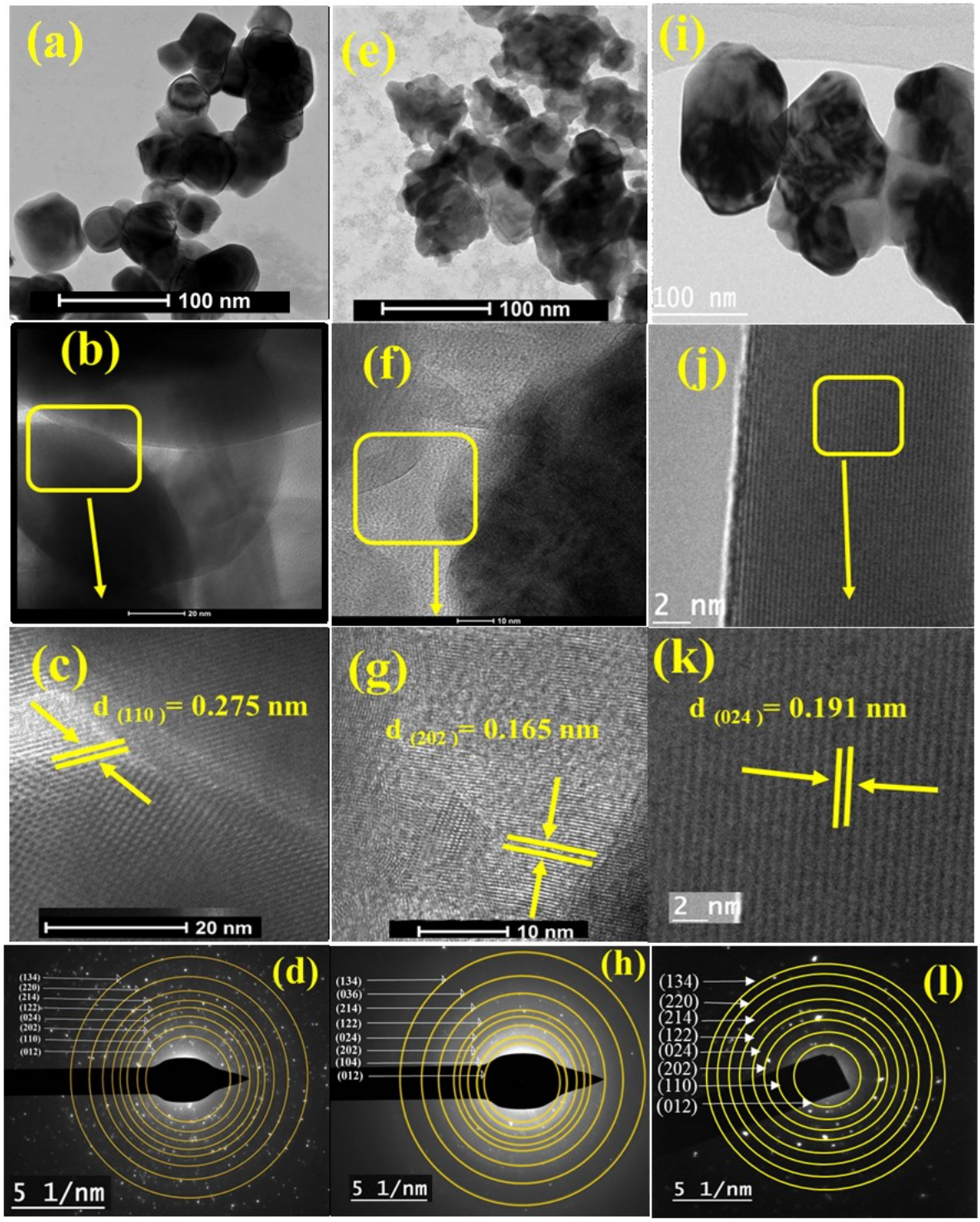

Fig. 4.10: (a, e, i) TEM images, (b, f, j) HRTEM images, (c, g, k) zoomed portions of HRTEM, and (d, h, l) SAED patterns of as-prepared, aged, and regenerated forms of LNMnO catalyst, respectively.

4.3.7. XPS analyses

The XPS analyses have been done in order to understand the surface composition of different forms of LNMnO catalyst. XPS of La 3d + Ni 2p, Mn 2p, C 1s and O 1s core levels of LNMnO are shown in **Fig. 4.11**. According to the XPS survey spectra, La, Ni, Mn C, and O elements are present in the various forms of the catalyst (see **Fig. 4.11(a))**. For the overlap of La 3d and Ni $2p_{3/2}$ core regions, La 3d and Ni 2p core level spectra were recorded simultaneously. Relatively intense peak at around 855 eV binding energy value of the spectrum of as-prepared catalyst indicates the presence of Ni species in La 3d core level region. The spectrum is resolved by curve fitting for the assessment of the oxidation state of Ni. The curve-fitted La 3d + Ni 2p core level spectrum of as-prepared LNMnO is displayed in **Fig. 4.11(a)**. La 3d core level region shows doublets corresponding to spin-orbit peaks at 834.6 and 851.4 eV as well as splitting of respectively component by about 4 eV that is consistent with the La^{3+} species in these kinds of materials [56–58]. These doublet peaks are consequence of contributions from some initial and final states corresponding to $3d^94f^1$ (lower value of binding energy) and $3d^94f^0$ (higher value of binding energy). The peak at 855.8 eV is ascribed for La^{3+} species related to La $3d_{3/2}$ $3d^94f^0$ final state. The peak at 854.3 eV is attributed to Ni $2p_{3/2}$ of Ni^{2+} species [59, 60]. The intense peak at 863.2 eV comprises satellite peaks of Ni^{2+} and La^{3+}. A small satellite peak at 847.5 eV is associated with the La^{3+}. Peaks position at 872.9 and 879.4 eV correspond to Ni $2p_{1/2}$ of Ni^{2+} species and associated with satellite. Spectral nature of La 3d + Ni 2p core level of the aged catalyst is different from that of the as-prepared catalyst (see **Fig. 4.11(b)**). Overall intensity of the Ni 2p core level spectral region for the aged catalyst is found to decrease. The peak at 834.7 eV confirms the presence of La^{3+} species in the aged catalyst. In the aged catalyst, two different contributions from nickel are found. Observed component peaks of $2p_{3/2,1/2}$ at 852.7 and 869.3 eV corresponds to Ni metal species and another $2p_{3/2,1/2}$ peaks at 854.4 and 872.1 eV stands for Ni^{2+} species on the surface of aged catalyst [59, 60]. Therefore, it is inferred that metallic Ni as well as nickel oxide species are formed in course of DRM reaction which is consistent with PXRD results (see **Fig. 4.3**). It is to be noted that the intensity of Ni^{2+} component is less compared to as-synthesized catalyst. However, the La 3d + Ni 2p core level region spectrum nature of regenerated form of the catalyst looks similar to as-prepared catalyst which is evident from **Fig. 4.11(c)**. The spin-orbit peaks observed at 834.7 and 854.1 eV correspond to La^{3+} species and $2p_{3/2,1/2}$ peaks at 854.2 and 873.3 eV are for Ni^{2+} species. Hence, it is confirmed that aged catalyst can be regenerated. Mn 2p core level spectra of as-prepared, aged, and regenerated forms of LNMnO catalyst are shown in **Fig. 4.11(d)**. The

spectral nature of as-prepared catalyst resembles regenerated form of the catalyst, whereas aged catalyst spectrum looks different from as-prepared and regenerated forms of the catalyst. Observed intense Mn $2p_{3/2,1/2}$ core level peaks at 642.2 and 653.7 eV in as-prepared and regenerated forms of catalyst are for the Mn^{4+} species [61]. A broad spectral envelope of Mn 2p in the aged sample, suggests the presence of multiple Mn species which is resolved by curve-fitting as shown in **Fig. 4.11 (e)**. Accordingly, $2p_{3/2,1/2}$ spin-orbit peaks at 640.6 and 652.4 eV along with a typical satellite peak at 645.5 eV are assigned to Mn^{2+} species. The component peaks observed at 641.7 and 653.5 eV correspond to Mn^{3+}. In all the catalysts, a low intense peak around 637.6 eV is attributed to Ni LMM Auger peak. C 1s core level spectra of as-prepared, aged, and regenerated forms of LNMnO catalyst indicate that different carbon components are present on the catalyst surface which are shown in **Figs. 4.11(f, g, h)**. Peaks at 284.9, 286.3, and 289.1 eV are associated with C–C/C–H, C–O, and carbonate species (CO_3^{2-}) on the catalyst surface, respectively [62, 63]. The intensity of C–O species increases and that of carbonate species decreases in the aged catalyst. However, C 1s core level spectral feature is observed to be similar to as-prepared catalyst. It is important to note that carbon concentration is found to increase in the aged form. But in regenerated form of the catalyst, the concentration of carbon looks similar to as-prepared catalyst. O 1s core level spectra of different forms of catalyst are found to be broad and are decomposed by curve-fitting as presented in **Fig. 4.11(i, j, k)**. Spectra of as-prepared and regenerated forms of the catalyst are observed to be similar. In the as-prepared form of the sample, decomposed peaks at 529.6, 531.8, and 533.6 eV are associated with lattice oxygen, adsorbed hydroxyl (OH^-), and adsorbed water species, respectively. Relative surface concentrations of different oxygen species calculated from O 1s core level data are presented in **Table 4.3**. It is to be mentioned that relative surface concentrations of the component species are similar in both as-prepared and regenerated forms of the catalyst, however concentration of lattice oxygen component species increases in aged sample compared to as-prepared and regenerated samples. This indicates the disintegration of LNMnO catalyst into component oxide species.

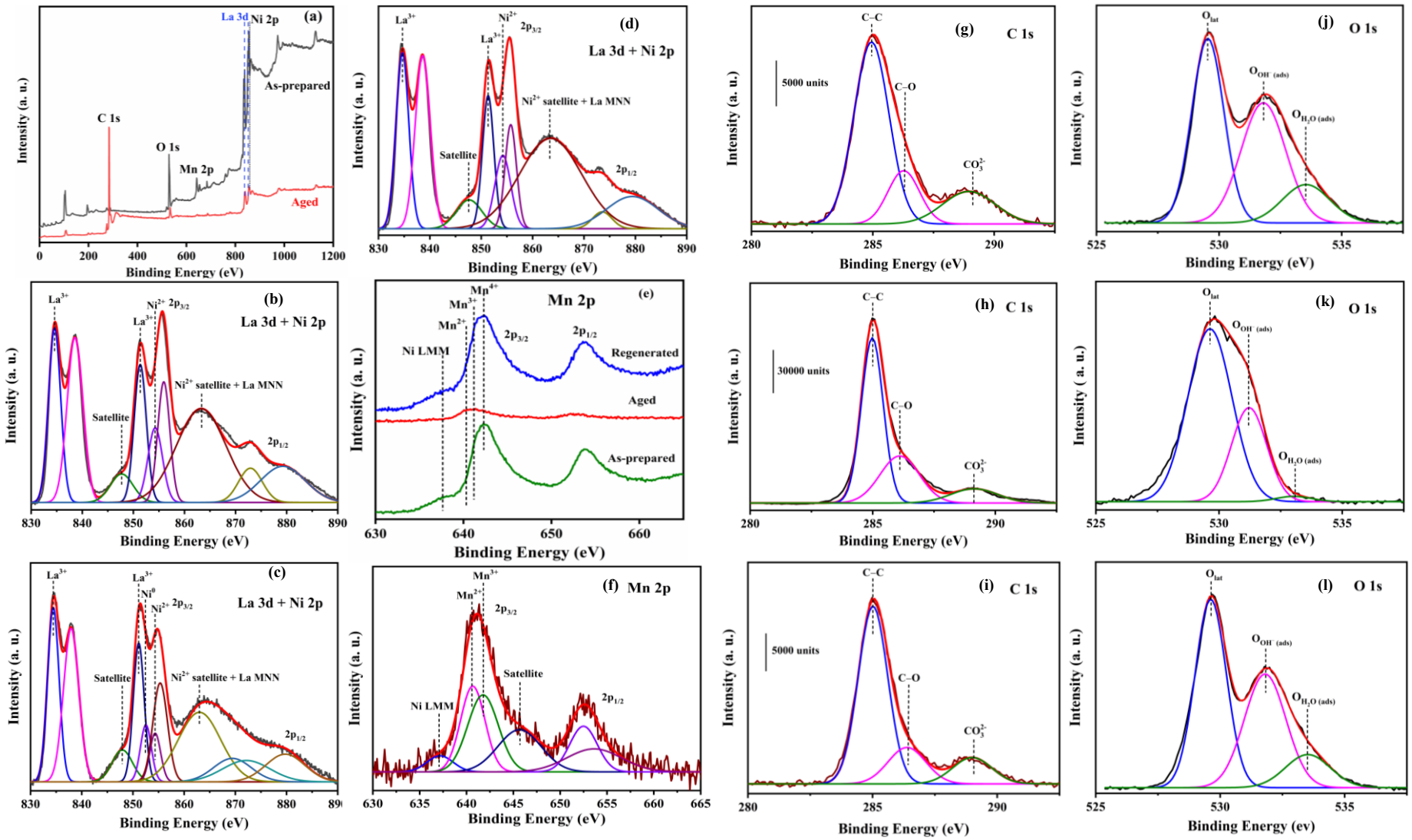

Fig. 4.11: XPS (a) survey spectra, and core level spectra of as-prepared, aged, and regenerated LNMnO catalysts: (b-d) La 3d + Ni 2p, (e, f) Mn 2p, (g-i) C 1s and (j-l) O 1s.

Table 4.3. Binding energies and relative peak area (%) of various oxygen species in the as-prepared, aged, and regenerated forms of the LNMnO catalyst evaluated using the O 1s core level data.

Form of catalyst	Species	Binding energy (eV)	Relative peak area (%)
As-prepared	O_{lat}	529.5	45
	O_{OH^-}	531.8	41
	O_{H_2O}	533.5	14
Aged	O_{lat}	529.6	69
	O_{OH^-}	531.3	29
	O_{H_2O}	533.1	2
Regenerated	O_{lat}	529.6	48
	O_{OH^-}	531.8	39
	O_{H_2O}	533.5	13

The standard relation has been used to estimate the surface concentrations of La, Ni, and Mn in different forms of the catalyst from the corresponding area under the peak, photoionization cross-section, and mean escape depth [62]. The relationship for estimating La concentration can be expressed as follows:

$$C_{La}= \frac{\frac{A_{La}}{\sigma_{La}\lambda_{La}}}{\frac{A_{La}}{\sigma_{La}\lambda_{La}}+\frac{A_{Ni}}{\sigma_{Ni}\lambda_{Ni}}+\frac{A_{Mn}}{\sigma_{Mn}\lambda_{Mn}}} \quad \text{..... (4.1)}$$

Integrated areas under La 3d, Ni 2p, and Mn 2p core level spectra have been considered into account for estimation of their concentrations, photoionization cross-sections and mean escape depths have been obtained from the literature [63, 64]. **Table 4.4** shows the relative surface concentrations (at. %) of La, Ni, and Mn in the aged, regenerated, and as-prepared catalysts.

Table 4.4. Binding energies and surface concentrations (at. %) of various species in the as-prepared, aged, and regenerated forms of the LNMnO catalyst, estimated from their corresponding core level data.

Catalyst	Species	Core level	Binding energy (eV)	Surface concentration (at. %)
As-prepared	La^{3+}	$3d_{5/2}$	834.6	2.16
	Ni^{2+}	$2p_{3/2}$	854.3	1.24
	Mn^{4+}	$2p_{3/2}$	642.2	0.60
Aged	La^{3+}	$3d_{5/2}$	834.7	2.24
	Ni^{2+}	$2p_{3/2}$	854.4	1.50
	Ni^{0}	$2p_{3/2}$	852.7	
	Mn^{3+}	$2p_{3/2}$	641.7	0.09
	Mn^{2+}	$2p_{3/2}$	640.6	
Regenerated	La^{3+}	$3d_{5/2}$	834.7	2.00
	Ni^{2+}	$2p_{3/2}$	854.2	1.52
	Mn^{4+}	$2p_{3/2}$	642.2	0.48

The **Table 4.4** shows that, in comparison to those of La and Ni, the relative surface concentration of Mn in the as-prepared sample is lower than expected by stoichiometry. On ageing, La concentration somewhat increases. Mn concentrations are on the lowest side in each and every instance. These results suggest that Ni is preferentially enriched or segregated on the surface of the double perovskite base catalyst system over Mn. Remarkably, Ni-enrichment/segregation improves with ageing in the DRM atmosphere and with regeneration, which accounts for the long-term persistence of DRM activity. Findings from the table may be attributed to disintegration of the initial perovskite into individual metal oxides, lanthanum hydroxide and metallic nickel species during DRM as identified by PXRD and XPS studies. Due to the decomposition of original LNMnO in the DRM medium, the XRD pattern of the aged catalyst shows the presence of $La(OH)_3$, La_2O_3, NiO, Ni, and MnO. Similarly, XPS results shows La 3d of La_2O_3 and $La(OH)_3$, Metallic Ni, Ni^{2+}, Mn^{2+} and Mn^{3+} species are present on the catalyst surface.

4.3.8. Advantage of SGCA process over conventional CM process

All the as-prepared catalysts decomposed into individual oxide phases in the reaction medium beyond 1 h (initial signature of phase decomposition beyond 30 min of reaction) of DRM reaction. XRD and XPS analyses of the aged LNMnO sample have revealed that the sample is decomposed into individual oxides together with a certain amount of metallic Ni. However, these phases formed in-situ can retain the DRM activity up to 100 h. Also, the aged catalyst can be regenerated back to the pristine double perovskite phase, making the decomposition-regeneration process reversible, where the first process is facilitated through the reforming atmosphere and the second one through calcination. The XRD analysis of the individual phases are presented in **Fig. 4.12.**

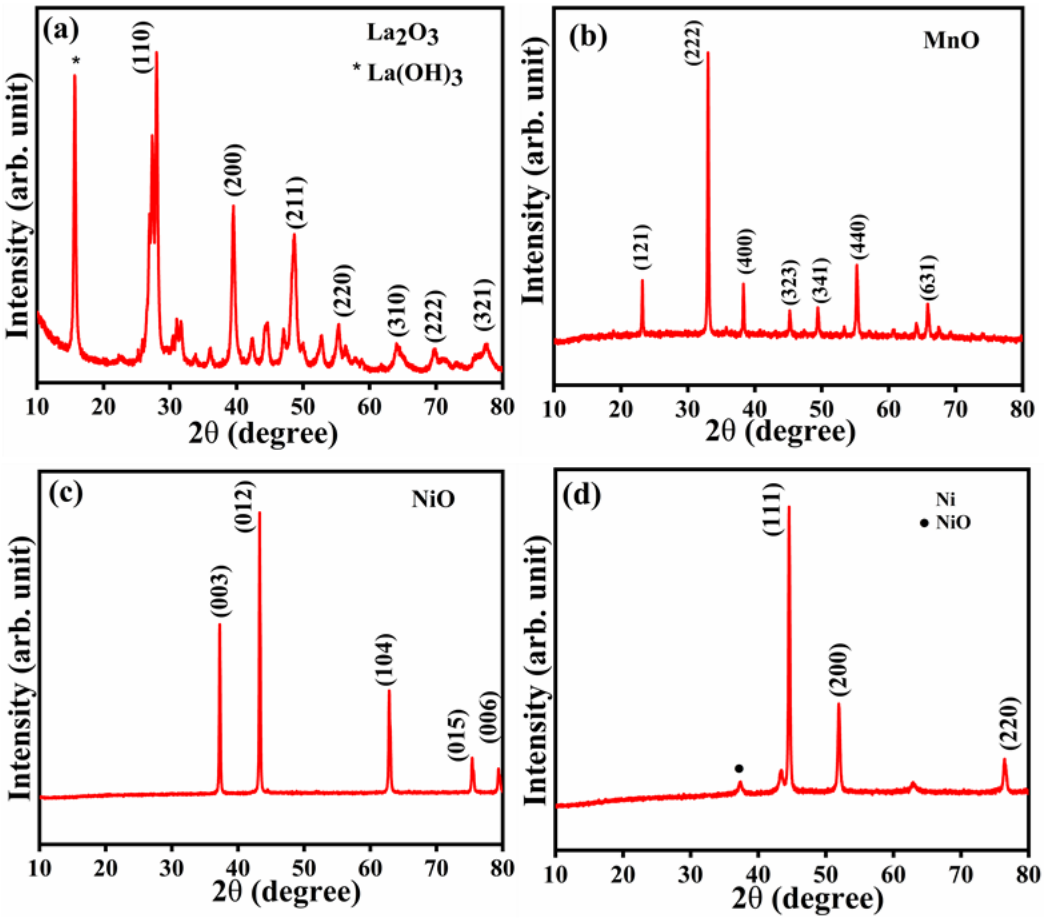

Fig. 4.12: PXRD patterns of (a) La_2O_3, (b) MnO, (c) NiO, and (d) metallic nickel.

The PM was then divided into two portions; the first part was directly used for the DRM reaction under similar reaction condition to compare its catalytic activity behaviour with the aged catalyst. But the PM did not show any methane conversion. The DRM activity of another part (LNMnO CM) catalyst was also investigated (see **Fig. 4.13.**). It is interesting to note that the catalyst synthesized via CM process showed less DRM activity behaviour than

the catalyst made using the SGCA method, suggesting the superiority of the SGCA method. Specifically, the catalyst made by CM route shows 79% CH_4 conversion, 84% CO_2 conversion, and H_2/CO ratio ~ 1 throughout 10 h of DRM reaction as shown in **Fig. 4.13,** which are 20–15% less than the catalyst made by SGCA route. However, DRM activity of the double perovskite catalyst prepared via CM process is quite significant. Thus, Ni^0 is generated only when the double perovskite catalyst, either via SGCA or via conventional CM route, gets broken down, and its presence is very significant for the sample to show DRM activity. This finding leads us to conclude that the distribution of the components in space is more important than only the presence of component phases in the catalyst matrix.

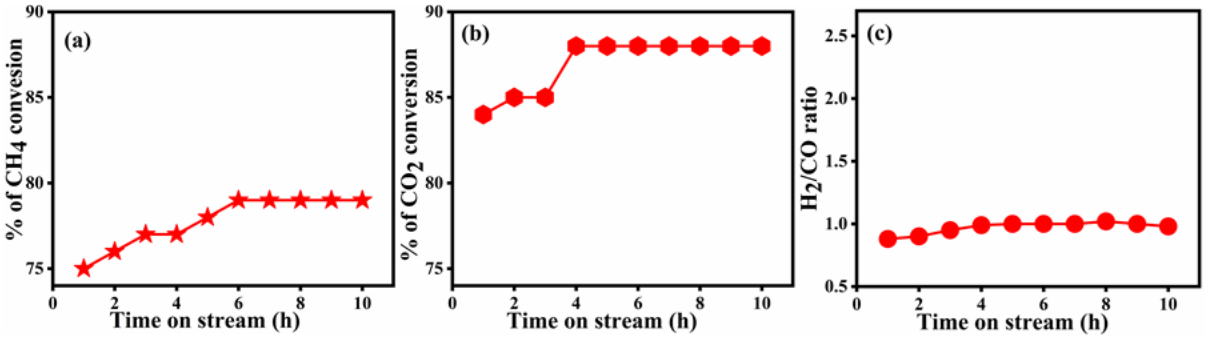

Fig. 4.13: DRM behaviour of the La_2NiMnO_6 catalyst material (prepared by CM process) for 10 h of DRM reaction: (a) CH_4 conversion, (b) CO_2 conversion, and (c) H_2/CO ratio at GHSV of 34000 mL g_{cat}^{-1} h^{-1} and temperature of 800 °C.

4.3.9. Insights of catalyst regeneration at different calcination temperature

The DRM test as well as ex-situ regeneration of the catalyst were all done at the same temperature of 800 °C. Whether the aged catalyst can be regenerated at lower temperatures, the aged catalyst was also calcined at 700 °C and at 600 °C for 3 h. Interestingly, the LNMnO double perovskite phase could be recovered effectively at 700 °C, while calcination at 600 °C results in the appearance of small peak of NiO as an impurity (see **Fig. 4.14(a)**). Consequently, the lowest calcination temperature required for the regeneration of the double perovskite phase is at least 100 °C lower than the synthesis temperature. The average particle sizes of the regenerated catalyst decrease slightly from 18 nm (calcined at 800 °C) to 15 nm (calcined at 600 °C). Similar trends are also observed for the catalyst prepared via CM method. In this case, the synthesis temperature is higher than that of the SGCA catalyst by 100 °C (see **Fig. 4.14(b)**). The Scherrer size of the regenerated LNMnO double perovskite catalyst prepared by CM is ~15 nm that is quite similar to the SGCA made catalyst.

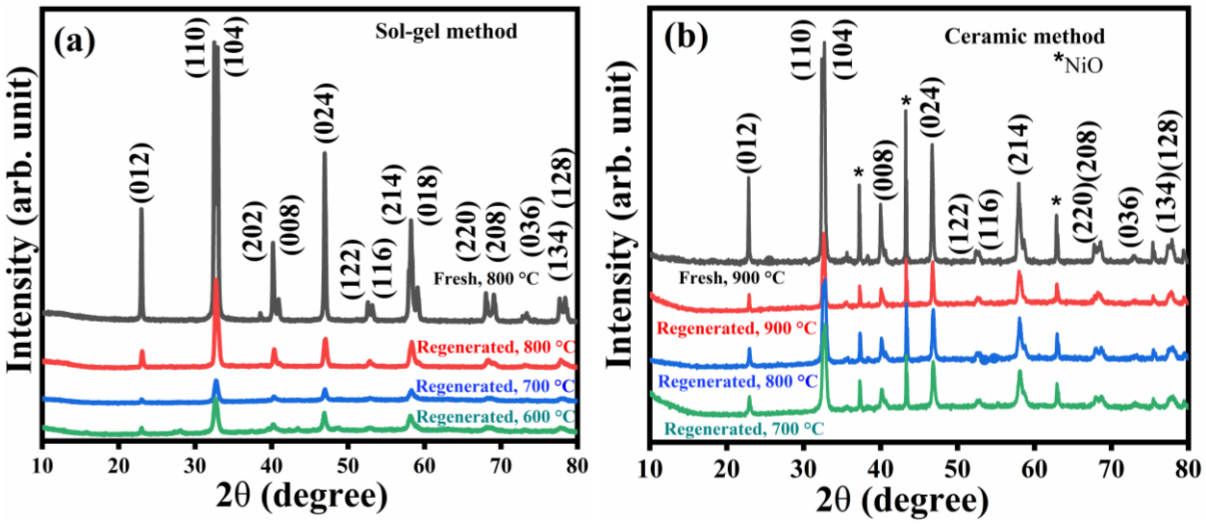

Fig. 4.14: PXRD patterns of as-prepared and regenerated LNMnO catalysts synthesized via (a) SGCA and (b) CM synthesis.

The catalytic activity of these regenerated catalysts was investigated under the same reaction conditions. The samples that were regenerated at 700 and 600 °C showed similar CH_4 and CO_2 conversion and H_2/CO ratio to the sample that was regenerated at 800 °C (see **Fig. 4.15**). Therefore, it may be proposed that the DRM activity is practically the same regardless of the regeneration temperature.

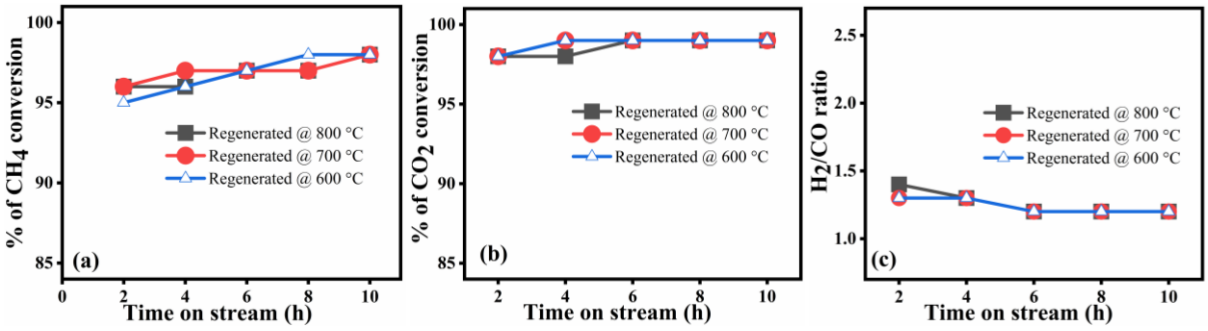

Fig. 4.15: Catalytic activity of regenerated LNMnO catalysts (at 800 °C, 700 °C, and 600 °C): (a) CH_4 conversion (b) CO_2 conversion, and (c) H_2/CO ratio.

4.3.10. TGA studies

Thermogravimetric analysis of the fresh as well as aged LNMnO samples has been carried out to comprehend the characteristics of coke deposition on the sample surface. The thermogravimetric analysis graph is displayed in **Fig. 4.16.** For the as-prepared sample, there is almost no mass loss with the gradual rise in temperature up to 900 °C. However, for the aged form of the sample, there are two mass loss peaks, the small one at 383 °C and the major one

at 505 °C. The loss of mass accompanied by the removing carbon is basically due to CO_2 formation. Donphai et al. have investigated the effects of carbon structure on the DRM catalytic activity and stability in Ni-carbon composite samples over mesocellular silica made through catalytic chemical vapor deposition method (CCVD) [65]. The synthesis temperature of the CCVD process was reported to rapidly affect the conversion from amorphous carbon to (graphitic carbon (002) peak at 26°) CNTs. So, the catalytic activity and durability of the catalysts were also affected. They ascribed mass losses occurring at 300–400 °C due to amorphous carbon, 400–540 °C due to less stable CNTs and 540–750 °C for more stable CNTs. While amorphous carbon and less stable CNTs cover the surface of the nickel clusters partially in Ni/CNTs composites that could be hydrogenated via methanation. They checked the DRM activity of their catalyst for 5 h attaining 79% of methane conversion with H_2/CO ratio 0.52 at 750 °C for Ni/CNTs (700)/MS catalyst. Xu et al. have reported two occasions of mass losses; the peak at ~500 °C is for the oxidation of amorphous carbon, whereas that at ~640 °C is for the carbon nanotubes [66]. Thus, lower temperatures promote the formation of amorphous carbon, which is ultimately transformed into graphite carbon at higher temperatures. The $In_{0.5}Ni@SiO_2$ catalyst reported by Liu et al. is also related to the formation of amorphous along with graphitic carbon after 430 h of DRM reaction, but the degree of carbon formation is clearly smaller than that of $Ni@SiO_2$ or $In_{0.5}Ni/SiO_2$ catalysts [26]. In a report, Montero et al. have investigated the filament-like nature of coke forming from both CO disproportion and methane disintegration that gets converted to non-filamentous carbon with the gradual progress of reaction time making deactivated the $Ni/La_2O_3–\alpha Al_2O_3$ catalysts [67].

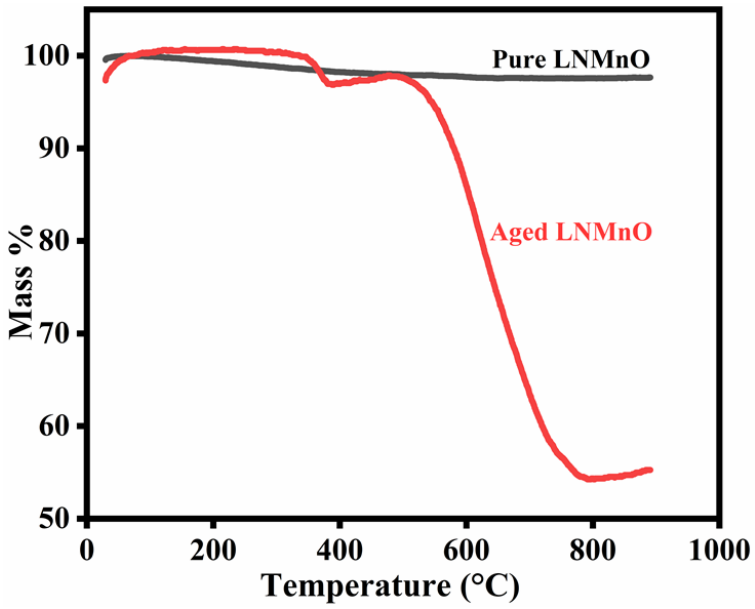

Fig. 4.16: TGA curves of the as-prepared and aged LNMnO catalysts.

It is observed that the structure of the deposited carbon has a greater influence than its content [35]. Methane conversion is said to be slowed down when active kinds of catalyst particles have been enclosed in both graphitic and amorphous carbon layers [39]. The XRD and HRTEM analyses of the aged catalyst did not reveal any evidence of crystalline forms of carbon, indicating the amorphous nature of the coke. The TGA study indicates that mass losses were completed at around 500 °C, further supporting the amorphous nature of the deposited coke [65]. It's also possible to be proposed that the carbon that formed remains separate from the catalyst matrix along with the nanocomposite. **Fig. 4.17** shows a schematic representation of one possible reversible in-situ structural transition out of many potential structures that could be formed. The initial double perovskite $La_2NiMnO6$ (left) breaks down into its constituent metal oxides and metal in-situ (right) in DRM without substantially changing its original arrangement. When heated in air at ≥600 °C, the proximity of the components (~order of atomic dimension) facilitates an easy transition back to the original double perovskite structure. Additionally, it seems reasonable that a structure like this is good agreement that the deposited amorphous carbon species may be easily removed during calcination, leaving a clean catalyst surface. As a result, DRM activity is same in both the phases. In conclusion, the real performer is a molecular level nanocomposite made up of individual oxides with a metallic Ni. This nanocomposite exhibits reversible thermal switching between aged and the parent double perovskite, making it a novel catalyst for the DRM.

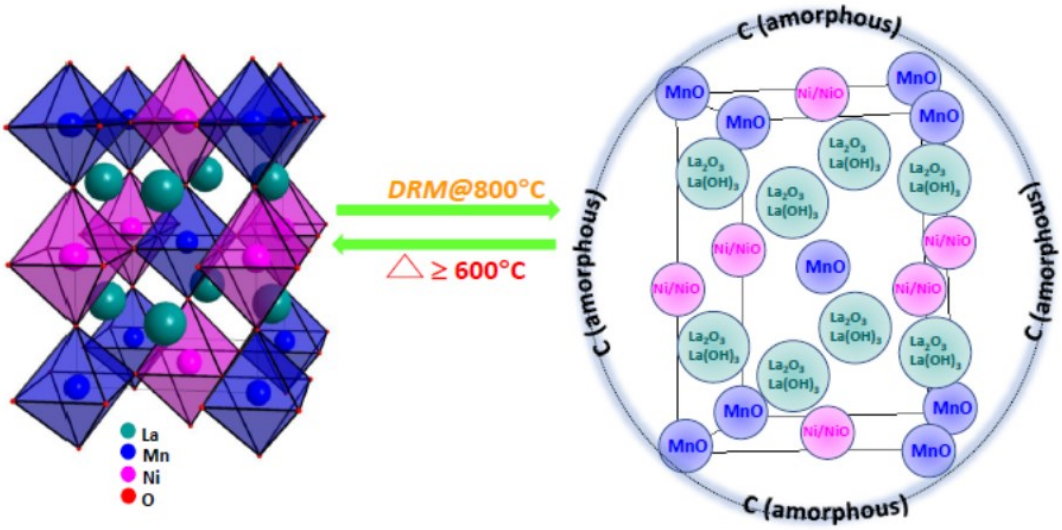

Fig. 4.17: Schematic diagram representing reversible thermal switching (≥ 600 °C) of double perovskite oxide and its molecular level nanocomposite formed in-situ in DRM. Deposition of amorphous carbon on the nanocomposite is also shown schematically.

4.4. Conclusions

It has been demonstrated that La_2NiMnO_6 is the most durable and active catalyst for the DRM (100 h) process among the synthesized materials. The PXRD, XPS and HRTEM investigations show that the double perovskite phase broke down into its component phases in the reaction atmosphere. These types of catalysts are unique because, despite the fact that it breaks down in the DRM environment, heat treatment allows the phase to be restored from the disintegrated phases. The typical characteristic of this investigation is the regeneration of the catalyst from the aged sample with full retention of activity. The similar DRM activity of the pristine, degraded and regenerated phases as well as thermal switching between them have been rationalised, within the framework of molecular level nanocomposite formation in the aged sample. To validate this proposition, we have checked catalytic activity of PM catalyst. However, the DRM activity behaviour of the PM lags far from the in-situ generated aged composite phases. This helps us to suggest that the real spatial arrangement of the component phases is far more significant than only the physical occurrence of component phases in the catalyst matrix. This again supports the retention of DRM activity even when the double perovskite oxide is decomposed and regenerated from the aged phase. We believe this finding will encourage further investigation in this field to find new materials capable of generating molecular level nanocomposite in DRM reaction and thorough understanding of the structure-property relationship.

References

[1] W.H. Chen, S.C. Lin, Characterization of catalytic partial oxidation of methane with carbon dioxide utilization and excess enthalpy recovery. Appl. Energy., 2016, 162, 1141-1152.

[2] Y. Zhan, J. Hana, Z. Bao, B. Cao, Y. Li, J. Street, F. Yu, Biogas reforming of carbon dioxide to syngas production over Ni–Mg–Al catalysts. Mol. Catal., 2017, 436, 248-258.

[3] T.Y Liang, C.Y. Lin, F.C. Chou, M. Wang, D.H. Tsa, Gas-Phase synthesis of Ni–CeO_x hybrid nanoparticles and their synergistic catalysis for simultaneous reforming of methane and carbon dioxide to syngas. J. Phys. Chem. C, 2018, 122, 11789-11798.

[4] W.H. Chen, S.C. Lin, characterization of catalytic partial oxidation of methane with carbon dioxide utilization and excess enthalpy recovery. Appl. Energy., 2016, 162, 1141-1152.

[5] D. Wang, P. Littlewood, T.J. Marks, P.C. Stair, E. Weitz, coking can enhance product yields in the dry reforming of methane. ACS Catal., 2022, 12, 8352−8362.

[6] S. Chen, J. Zaffran, B. Yang, descriptor design in the computational screening of Ni–based catalysts with balanced activity and stability for dry reforming of methane reaction. ACS Catal., 2020, 10, 3074−3083.
[7] B. Abdullah, N.A.A. Ghani, D.V.N. Vo, recent advances in dry reforming of methane over Ni-based catalysts. J. Clean. Prod. 2017, 162, 170-185.
[8] W.J. Jang, J.O. Shim, H.M. Kim, S.Y. Yoo, H.S. Roh, a review on dry reforming of methane in aspect of catalytic properties. Catal. Today., 2019, 324, 15-26.
[9] M. Kushida, A. Yamaguchi, M. Miyauchi, Photocatalytic dry reforming of methane by rhodium supported monoclinic TiO_2-B nanobelts, J. Energy Chem., 2022, 71, 562–571.
[10] S. You, Y.S. OK, S.S. Chen, D.C.W Tsang, E.E. Kwon, J. Lee, C.H. Wang, A critical review on sustainable biochar system through gasification: Energy and environmental applications, Bioresour. Technol., 2017, 246, 242-253.
[11] M. Fiore, V. Magi, A. Viggiano, Internal combustion engines powered by syngas: A review, Appl. Energy., 2020, 276, 115415.
[12] M. Costa, G.D. Blasio, M.V. Prati, M.A. Costagliola, D. Cirillo, M.L. Villetta, C. Caputo, G. Martoriello, Multi-objective optimization of a syngas powered reciprocating engine equipping a combined heat and power unit, Appl. Energy., 2020, 275, 115418.
[13] X. Qi, T. Lin, K. Gong, X. Wang, D. Lv, F. Yu, Y. An, Z. Tang, L. Zhong, Direct synthesis of higher oxygenates via syngas over zinc oxide modified CoMn-based catalysts, Appl. Catal., 2022, 648, 118925.
[14] M.A. Zareer, I. Dincer, M.A. Rosen, Effects of various gasification parameters and operating conditions on syngas and hydrogen production, Chem Eng Res Des., 2016, 115, 1−18.
[15] P. Nikolaidis, A. Poullikkas, A comparative overview of hydrogen production processes, Renew. Sust. Energ. Rev., 2017, 67, 597−611.
[16] B. Cifuentes, F. Bustamante, D.G. Araiza, G. Diaz, M. Cobo, Hydrogen purification of actual syngas streams for energy applications: Au−Cu supported over nano-shaped CeO_2 as stable catalysts for the carbon monoxide removal, Appl. Catal. A, 2020, 598, 117568.
[17] R. Fan, M. Kyodo, L. Tan, X. Peng, G. Yang, Y. Yoneyama, R. Yang, Q. Zhang, N. Tsubaki, Preparation and application of Cu/ZnO catalyst by urea hydrolysis method for low-temperature methanol synthesis from syngas, Fuel Process. Technol., 2017, 167, 69-77.

[18] Z. Chu, H. Chen, Y. Yu, Q. Wang, D. Fang, Surfactant-assisted preparation of $Cu/ZnO/Al_2O_3$ catalyst for methanol synthesis from syngas, J. Mol. Catal. A Chem., 2013, 366, 48-53.

[19] J. Guilera, Jos A.D. Lopez, A. Berenguer, M.B. Peiro, T. Andreu, Fischer-Tropsch synthesis: Towards a highly-selective catalyst by lanthanide promotion under relevant CO_2 syngas mixtures, Appl. Catal. A, 2022, 629, 118423.

[20] Q. Hu, D. Yao, Y. Xie, Y. Zhu, H. Yang, Y. Chen, H. Chen, Study on intrinsic reaction behavior and kinetics during reduction of iron ore pellets by utilization of biochar, Energy Convers. Manag., 2018, 158, 1–8.

[21] L.A. Schulz, L.C.S. Kahle, K.H. Delgado, S.A. Schunk, A. Jentys, O. Deutschmann, J.A. Lercher, On the coke deposition in dry reforming of methane at elevated pressures, Appl. Catal. A, 2015, 504, 599–607.

[22] I.V. Yentekakis, P. Panagiotopoulou, G. Artemakis, A review of recent efforts to promote dry reforming of methane (DRM) to syngas production via bimetallic catalyst formulations, Appl. Catal., 2021, 296, 120210.

[23] K. Yuan, X.C. Sun, H.J. Yin, L. Zhou, H.C Liu, C.H. Yan, Y.W. Zhang, Boosting the water gas shift reaction on Pt/CeO_2-based nano catalysts by compositional modification: Support doping versus bimetallic alloying, J. Energy Chem., 2022, 67, 241–249.

[24] L. Dehimi, M. Gaillard, M. Virginie, A. Erto, Y. Benguerba, Investigation of dry reforming of methane over Mo-based catalysts, Int. J. Hydrog. Energy., 2020, 45, 24657–24669.

[25] M. Keller, A. Matsumura, A. Sharma, Spray-dried Fe/Al_2O_3 as a carbon carrier for CO_x-free hydrogen production via methane cracking in a fluidized bed process, J. Chem. Eng., 2020, 398, 125612.

[26] W. Liu, L. Li, S. Lin, Y. Luo, Z. Bao, Y. Mao, K. Li, D. Wu, H. Peng, Confined Ni–In intermetallic alloy nano catalyst with excellent coking resistance for methane dry reforming, J. Energy Chem., 2022, 65, 34–47.

[27] J. Horlyck, C. Lawrey, E.C. Lovell, R. Amal, J. Scott, Elucidating the impact of Ni and Co loading on the selectivity of bimetallic NiCo catalysts for dry reforming of methane, J. Chem. Eng., 2018, 352, 572–580.

[28] F. Wang, J.C. Zhang, W.Z. Li, B.H. Chen, Coke-resistant Au–$Ni/MgAl_2O_4$ catalyst for direct methanation of syngas, J. Energy Chem., 2019, 39, 198–207.

[29] T.G.A. Moreira, J.F.S.C. Filho, Y. Carvalho, J.M.A.R. Almeida, P.N. Romano, E.F.S. Aguiar, Highly stable low noble metal content rhodium-based catalyst for the dry reforming of methane, Fuel., 2021, 287, 119536.
[30] J. Ren, H. Lou, N. Xu, F. Zeng, G. Pei, Z. Wang, Methanation of CO/CO_2 for power to methane process: Fundamentals, status, and perspectives, J. Energy Chem., 2023, 80, 182–206.
[31] W.Y. Kim, J.S. Jang, E.C. Ra, K.Y. Kim, E.H. Kim, J.S. Lee, Reduced perovskite $LaNiO_3$ catalysts modified with Co and Mn for low coke formation in dry reforming of methane, Appl. Catal. A, 2019, 575, 198–203.
[32] Y. Li, D. Sun, X. Zhao, Y. Yamada, S. Sato, Control of coke deposition in solid acid catalysis through the doping of transition metal combined with the assistance of H_2: A review, Appl. Catal. A, 2021, 626, 118340.
[33] L.A. Schulz, L.C.S. Kahle, K.H. Delgado, S.A. Schunk, A. Jentys, O. Deutschmann, J.A. Lercher, On the coke deposition in dry reforming of methane at elevated pressures, Appl. Catal. A, 2015, 504, 599–607.
[34] L. Azancot, L.F. Bobadilla, M.A. Centeno, J.A. Odriozola, IR spectroscopic insights into the coking-resistance effect of potassium on nickel-based catalyst during dry reforming of methane, Appl. Catal. A, 2021, 285, 119822.
[35] R. Khalighi, F. Bahadoran, M.H. Panjeshahi, A. Zamaniyan. N. Tahouni, High catalytic activity and stability of $X/CoAl_2O_4$ (X = Ni, Co, Rh, Ru) catalysts with no observable coke formation applied in the autothermal dry reforming of methane lined on cordierite monolith reactors, Microporous Mesoporous Mater., 2020, 305, 110371.
[36] M. Kennema, P.A. Rowntree, The reactivity and initial carbonization of an unsupported nickel catalyst in dry reforming of methane, J. Power Sources., 2020, 453, 226753.
[37] A.J. Carrillo, J.M. Serra, exploring the stability of Fe–Ni alloy nanoparticles exsolved from double-layered perovskites for dry reforming of methane, Catalyst., 2021, 11, 741.
[38] S. Bhattar, M.A. Abedin, S. Kanitkar, J.J. Spivey, A review on dry reforming of methane over perovskite derived catalysts, Catal. Today., 2021, 365, 2–23.
[39] O.U. Osazuwa, H.D. Setiabudi, R.A. Rasid, C.K. Cheng, J. Nat. Gas Eng., 2017, **37**, 435–448.
[40] S. Dama, S.R. Ghodke, R. Bobade, H.R. Gurav, S. Chilukuri, Active and durable alkaline earth metal substituted perovskite catalysts for dry reforming of methane, Appl. Catal. B, 2018, 224, 146–158.

[41] P. Qiu, X. Yang, S. Sun, L. Jia, J. Li, F. Chen, Enhanced electrochemical performance and durability for direct CH_4–CO_2 solid oxide fuel cells with an on-cell reforming layer, Int. J. Hydrog. Energy., 2021, 46, 22974–22982.

[42] S. Zhang, M. Ying, J. Yu, W Zhan, L Wang, Y. Guo, Y. Guo, $Ni_xAl_1O_{2-\delta}$ mesoporous catalysts for dry reforming of methane: The special role of $NiAl_2O_4$ spinel phase and its reaction mechanism, Appl. Catal. B., 2021, 291, 120074.

[43] R. Jalali, M. Rezaei, B. Nematollahi, M. Baghalha, Preparation of Ni/$MeAl_2O_4$–$MgAl_2O_4$ (Me= Co, Cu, Fe, Mg, Ni, Zn) nanocatalysts for the syngas production via combined dry reforming and partial oxidation of methane, Renew. Energ., 2020, 149, 1053–1067.

[44] U. Dutta, O.I. Lebedev A.K. Kundu, M.M. Seikh, Bi-doped suppression of antisite disordering and associated magnetic properties of $La_{2-x}Bi_xMnNiO_6$ (x= 0 and 1), J. Condens. Matter Phys., 2020, 32, 085803.

[45] N.S. Rogado, J. Li, A.W. Sleight, M.A. Subramanian Adv. Mater., 2005, 17, 2225–2227.

[46] R.I. Dass, J.Q. Yan, J.B. Goodenough, Phys. Rev. B, 2003, 68, 064415.

[47] D. Choudhury, P. Mandal, R. Mathieu, A. Hazarika, S. Rajan, A. Sundaresan, U.V. Waghmare, Near-room-temperature colossal magneto dielectricity and multi glass properties in partially disordered La_2NiMnO_6, Phys. Rev. Lett., 2012, 108, 127201.

[48] R.A. Ricciardo, A.J. Hauser, F.Y. Yang, H. Kim, W. Lu, P.M. Woodward Mater. Structural, magnetic, and electronic characterization of double perovskites $Bi_xLa_{2-x}MnMO_6$ (M = Ni, Co; x = 0.25, 0.50), Res. Bull., 2009, 44, 239–247.

[49] A.K. Biswal, J. Ray, P.D. Babu, V. Siruguri, P.N. Vishwakarma, Effect of Cu substitution on the magnetic and dielectric properties of La_2NiMnO_6, J. Appl. Phys., 2015, 117, 17B728.

[50] U. Dutta, A. Haque, M.M. Seikh, Synthesis, structure and magnetic properties of Ti doped La_2MnNiO_6 double perovskite, Chim. tech. acta, 2019, 6, 80-92.

[51] L. Zhang, W. Gao, X. Song, L. Chi, B. Liu, X. Yu, Synergistic effects of redox couples and oxygen vacancies improve the tetracycline degradation property of La_2NiMnO_6 Langmuir, 2022, 38, 2314−2326.

[52] M. Qu, X. Ding, Z. Shen, M. Cui, F.E. Oropeza, G. Gorni, V.A.P. O'Shea, W. Li, D.C Qi, K.H.L. Zhang, Tailoring the electronic structures of the La_2NiMnO_6 double perovskite as efficient bifunctional oxygen electrocatalysis**,** Chem. Mater., 2021, 33, 2062−2071.

[53] M. Nasir, M. Khan, S. Kumar, S. Bhatt, N. Patra, D. Bhattacharya, S.N. Jha, S. Biring, S. Sen, The effect of high temperature annealing on the antisite defects in ferromagnetic La_2NiMnO_6 double perovskite, J. Magn. Magn. Mater., 2019, 483, 114–123.

[54] K. Ghorai, A. Panda, A. Hossain, M. Bhattacharjee, M. Chakraborty, S.K. Bhattacharya, B. Show, A. Sarkar, P. Bera, H Kim, M.M. Seikh, A. Gayen, $LaNiO_3$/g-C_3N_4 nanocomposite: An efficient Z-scheme photocatalyst for wastewater treatment using direct sunlight, J. Rare Earths, 2022, 40, 725−736.

[55] M.C.A. Galvan, V.A.P. OShea, G. Arzamendi, B. Pawelec, L.M. Gandıa and J.L.G. Fierro, Methyl ethyl ketone combustion over La-transition metal (Cr, Co, Ni, Mn) perovskites Appl. Catal. B, 2009, 92, 445−453.

[56] S. Mickevicius, S. Grebinskij, V. Bondarenka, B. Vengalis, K. Sliuziene, B.A. Orlowski, V. Osinniy. W. Drube, Investigation of epitaxial $LaNiO_{3-x}$ thin films by high-energy XPS, J. Alloys Compd., 2006, 423, 107–111.

[57] S. Viswanathan, L. Mohan, S. John, P. Bera, C. Anandan, Carbon plasma immersion ion implantation and DLC deposition on Ni−Ti alloy, RSC Adv., 2016, 6, 74493−74499.

[58] S. Viswanathan, L. Mohan, S. John, P. Bera, C. Anandan, Effect of surface finishing on the formation of nanostructure and corrosion behavior of Ni–Ti alloy, Surf. Interface Anal., 2017, 49, 450–456.

[59] R. Grissa, H. Martinez, S. Cotte, J. Galipaud, B. Pecquenard, F.L. Cras, Thorough XPS analyses on overlithiated manganese spinel cycled around the 3V plateau, Appl. Surf. Sci., 2017, 411, 449–456.

[60] M. Richard, R.D. Short, Plasma treatment of polymers: The effects of energy transfer from an argon plasma on the surface chemistry of polystyrene, and polypropylene. A high-energy resolution X-ray photoelectron spectroscopy study, Langmuir, 1998, 14, 4827–4835.

[61] R. Prakasha, M. Sathish, P. Bera, A.S. Prakash, Mitigating the surface degradation and voltage decay of $Li_{1.2}Ni_{0.13}Mn_{0.54}Co_{0.13}O_2$ cathode material through surface modification using Li_2ZrO_3, ACS Omega, 2017, 2, 2308–2316.

[62] C.J. Powell, P.E. Larson, Quantitative surface analysis by X-ray photoelectron spectroscopy, Appl. Surf. Sci, 1978, 1, 186.

[63] J.H. Scofield, Hartree-Slater subshell photoionization cross-sections at 1254 and 1487 eV, J. Electron Spectrosc. Relat. Phenom., 1976, 8, 129.

[64] D.R. Penn, Quantitative chemical analysis by ESCA, J. Electron Spectrosc. Relat. Phenom., 1976, 9, 29.

[65] W. Donphai, T. Witoon, K. Faungnawakij, M. Chareonpanich, Carbon-structure affecting catalytic carbon dioxide reforming of methane reaction over Ni-carbon composites, J. CO_2 Util., 2016, 16, 245–256.

[66] D. Xu, Y. Xiong, S. Zhang, Y. Su, The synergistic mechanism between coke depositions and gas for H_2 production from co-pyrolysis of biomass and plastic wastes via char supported catalyst, J. Waste Manag., 2021, 121, 23–32.
[67] C. Montero, A. Ochoa, P. Castano, J. Bilbao, A.G. Gayubo, Monitoring Ni^0 and coke evolution during the deactivation of a $Ni/La_2O_3–\alpha Al_2O_3$ catalyst in ethanol steam reforming in a fluidized bed, J. Catal., 2015, 331, 181–192.

Chapter 5

Studies on $Ln(Mn_{0.2}Fe_{0.2}Co_{0.2}Ni_{0.2}Cu_{0.2})O_3$ (Ln= lanthanide elements) high entropy perovskite oxides

Chapter Abstract: *We report here the synthesis of $Ln(Mn_{0.2}Fe_{0.2}Co_{0.2}Ni_{0.2}Cu_{0.2})O_3$ (Ln= La, Ce, Pr, Nd, Sm, and Gd) high entropy perovskite oxide (HEPO) materials that have subsequently been tested for their activities in the dry reforming of methane. The pure phase $La(Mn_{0.2}Fe_{0.2}Co_{0.2}Ni_{0.2}Cu_{0.2})O_3$ has shown the highest catalytic activity with 86% methane conversion and 90% CO_2 conversion for 100 h DRM with H_2/CO~1. It is interesting to see how the original HEPO gets decomposed in the reaction medium and is regenerated from the individual oxide phases by the calcination at temperatures close to phase formation temperature, without compromising the DRM activity. The samples were thoroughly characterized via PXRD, BET surface area, XPS, FESEM, TEM, HRTEM, and TGA.*

5.1. Introduction

Ever since the introduction of high entropy alloys (HEAs) by Yeh et al. [1] and by Cantor et al. [2] in 2004, HEAs have gradually attracted extensive attention for its several potential applications in various fields. This is followed by a pivotal work on the development of a new type of materials, subsequently recognized as high entropy oxides (HEOs) or entropy stabilised oxides, specifically a five metal containing rock salt component (Mg, Co, Ni, Cu, Zn)O in 2015 by Rost et al. [3]. The HEOs, one of the high entropy materials, are a quickly developing arena of oxides with high potential in numerous fields. There are four primary stabilising features for HEOs formation, such as high entropy, lattice distortion, delayed diffusion and cocktail effects [4, 5]. In the crystal structure of HEOs, there are five or more major cations that are dispersed inconsistently in the crystal matrix. The entropy of mixing associated with the formation of HEOs may be determined from the Gibbs-Helmholtz equation, $\Delta G_{mix} = \Delta H_{mix} - T\Delta S_{mix} \dots\dots\dots\dots (5.1)$.

Firstly, high temperatures facilitate an increase in mixing entropy (ΔS_{mix}), which lowers ΔG_{mix}. The more negative value of ΔG_{mix} results in forming more stable HEOs [6, 7]. Secondly, due to the lattice distortion effect, defects in HEOs are easily generated. Different major cations have different radii, which causes lattice distortion thereby promoting the formation of oxygen vacancies in the lattice through lowering of energy [8, 9]. Furthermore, HEOs have better chemical stability because of the delayed diffusion effect [10, 11], which also makes it difficult for negative effects like grain coarsening and recrystallization to occur during the catalytic process, as opposed to the agglomeration of the HEO system. Lastly, HEOs are capable of

carrying out several catalytic activities owing to the cocktail effect. As HEO is constituted by a variety of cations, the roles of the cations may differ or be similar based on their radii [12]. Various types of HEO systems have been reported, such as rock salt [13, 8], perovskite [14, 15], fluorite [16], spinel [17, 18], and pyrochlore [19, 20]. HEOs find widespread applications in various fields, such as thermal conductivity [21], water splitting applications [22], hydrogen production [23], oxygen production [24], catalytic CO oxidation [25], electrochemical capacitors [26], lithium-ion battery [27], sodium-ion battery [28], magnetic properties [29], electrical properties [30], piezoelectric properties [31], dielectric properties [32], optical properties [33], etc.

The main energy source that now meets our daily energy needs is fossil fuel. However, one of the main hazards to the fashionable lifestyle and the environment is pollution, which occurs when fossil fuels are used in a variety of activities brought about by humankind to fulfil energy demands. Combustion of fossil fuels produces greenhouse gases (GHGs), mostly CO_2 and CH_4, which has the effect of gradually raising the temperature of the environment. Several studies have shown that hydrogen energy is one of the most possible replacements for fossil fuels. H_2 fuel is considered an environment friendly fuel source due to its high energy content and low impact on the environment. Conventional H_2 is obtained via a variety of photocatalytic or catalytic reactions, including the partial oxidation of methane (POM), photochemical and electrochemical reactions, as well as the dry and steam reforming of methane (DRM and SRM) reactions. Among all these methods, the DRM process is known as one of the most promising one for producing H_2, because it produces a large amount of H_2 at low-price, has stability throughout the long run, and needs simple preparation procedures to prepare the catalysts. Furthermore, one of the main benefits of the DRM reaction is the efficient formation of syngas (mixture of hydrogen and carbon monoxide) by using two main greenhouse gases (CO_2 and CH_4). However, the production of H_2 energy through other methods, such as electrochemical splitting of water or photocatalytic production of H_2 is actually not reasonable due to the low volume of H_2 output that hardly meets the current demand for H_2 energy, the need for expensive metals (Ru, Pd, Ir, Pt etc.), and the involvement of multiple steps in catalyst synthesis. As a result, DRM has attracted a lot of attention from researchers in recent times due to its numerous potentials uses in the chemical industry [34, 35] and environmental concerns [36]. Syngas has multiple industrial applications, including the production of hydrogen [37], methanol preparation [34], diesel preparation [38], iron ore reduction to sponge iron [39], etc. A few disadvantages of the DRM process are catalyst instability and carbon deposition for which the

active sites of catalysts are blocked and quickly deactivates them during the reaction. The reactions related to DRM are discussed in **Chapter 1** (**Sec.1.1**).

Thus, the primary causes of coke formation are for reactions (**eq. 1.3**) and (**eq. 1.4**). In this regard, it is important to be pointed out that the catalyst material has a crucial role in DRM. Therefore, synthesis of appropriate catalysts that have substantial DRM activity, excellent durability, and great resistance to coking are the subject of extensive research.

The literature review shows that in the DRM, nickel and noble metal containing catalysts, including Ru, Rh, and Pt have exhibited high activity and low coke deposition. However, noble metal catalysts are not effective in terms of high cost and lower extent of availability. In this aspect, it is to be noted that the HEO catalysts feature several unique structures that could promote DRM reaction. Shao et al. have synthesized $(MgCoNiMnFe)O_x/ZrO_2$ HEO catalyst [40] and deployed it for DRM reaction for 100 h with methane conversion of 43%. Liao et al. have studied DRM activity of $Fe_xNi_2CrCoMn_{0.55}O_y$ HEO [41] that demonstrated 98% CH_4 conversion, and 72% CO_2 conversion. The role of $LaFe_{0.7}Ni_{0.1}Co_{0.1}Cu_{0.05}Pd_{0.05}O_3$ perovskite catalyst in DRM have been investigated by Shah et al. [42], where the methane and carbon dioxide conversions were ~64% and ~68%, respectively and the H_2/CO ratio was observed to be ~0.8 for 24 h of reaction. In a study, Zhang et al. have tested the $(Ni_3MoCoZn)Al_{15}O_x$ [43] spinel type HEOs for DRM reaction. The catalyst has shown high activity in the DRM process throughout 100 h, converting 98% of CO_2 and 92 to 97% of CH_4, resulting in the H_2/CO ratio varying from 0.94 to 0.98. Gangwar et al. have explored the role of HEO $CoFeGaNiZn/CeO_2$ [44] catalyst in DRM reaction. They found the methane and carbon dioxide conversions of 98% and 86%, respectively with H_2/CO ratio ~1.3 for 30 h of reaction. According to Su et al. [45], there is significant lattice distortion in perovskite-type $La(Cr_{0.2}Mn_{0.2}Fe_{0.2}Co_{0.2}Ni_{0.2})O_3$ HEOs. The lattice distortion increases with the abundance of the constituent elements, thereby increasing the possibility of oxygen vacancies, which is much needed for DRM. Furthermore, exceptional catalysis frequently occurs at the boundary between two compounds with distinct roles. A catalyst $(NiMgCuZnCo)O/CeO_x$ that combines common oxide and HEO has been synthesized by Chen et al. [46], and they have subsequently investigated the CO oxidation activity. The heterostructure interface produced by the two oxides enhances the activity and stability of the catalyst at high temperature.

In light of the aforementioned findings on the catalytic activities of HEO-based materials, it would be worthwhile to look into lanthanide-based high entropy perovskite oxides (HEPOs), $Ln(Mn_{0.2}Fe_{0.2}Co_{0.2}Ni_{0.2}Cu_{0.2})O_3$ (where Ln= La, Ce, Pr, Nd, Sm, and Gd) as potential DRM catalysts. This study shows $La(Mn_{0.2}Fe_{0.2}Co_{0.2}Ni_{0.2}Cu_{0.2})O_3$ to exhibit the maximum

DRM activity, 86% methane conversion, and 90% CO_2 conversion, with full activity maintenance up to 100 h. The XRD analysis of the aged catalyst sample has been performed after the 100 h run, which has revealed the full breakdown of the initial HEPO phase into the individual oxides together with nickel metal. The fragmented components can be thought of as a nanocomposite at molecular level where there is very little dispersal of component ions from their actual positions in the original perovskite structure. It is well-supported by the phenomenon that the original perovskite phase can be restored by heating the nanocomposite at a lower than synthesis temperature. The regenerated forms (at different temperatures) of the catalyst have been shown to exhibit similar DRM activity. The ability to go back and forth while maintaining the excellent catalytic activity of HEPO catalysts and *in situ* produced molecular level nanocomposite opens a window of opportunity for additional investigation and thorough comprehension of the structure-property correlation in such HEPO materials.

5.2. Experimental

Chapter 2 **(Sec. 2.3.1.1.)** discusses the details of synthesis, characterization and DRM activity tests of the HEPOs included in this chapter.

5.3. Results and discussion

5.3.1. PXRD studies of as-prepared HEPOs

Fig. 5.1. displays the PXRD patterns of the Ln(TM)O HEPO samples. The diffraction patterns indicate that the samples are well-crystalline. The peaks of the HEPOs are appeared at 2θ values 23.0°, 32.5°, 32.8°, 40.0°, 40.9°, 47.0°, 52.6°, 53.2°, 58.1°, 59.1°, 68.1°, 69.1°, 77.6°, and 78.5° that correspond to the lattice planes are (012), (110), (104), (202), (006), (024), (122), (116), (214), (018), (220), (208), (134), and (128), respectively. The Ln(TM)O HEPO system forms a rhombohedral phase which matches well with the JCPDS PDF # 880633. Furthermore, Rietveld refinement shows that the rhombohedral phase properly fits with this pattern (see **Section 5.3.3**). The Scherrer sizes derived from the full-width-at-half-maximum (FWHM) of the maximum intense diffraction peak of HEPOs of La(TM)O, Ce(TM)O, Pr(TM)O, Nd(TM)O, Sm(TM)O, and Gd(TM)O materials, are about 23, 63, 61, 50, 61, and 57 nm, respectively. For Ce(TM)O, an impurity of CeO_2 appears at 2θ value of 28.8°. Small impurity peaks related to La_2O_3 are appeared at 2θ values of 26.2° and 30.06° for Pr(TM)O, Nd(TM)O, Sm(TM)O, and Gd(TM)O. The as-synthesized La(TM)O catalyst shows no detectable peaks associated with any of these impurities, attesting to the phase purity of the catalyst. Except La(TM)O, all other HEPOs have the impurity peak of the corresponding metal oxides.

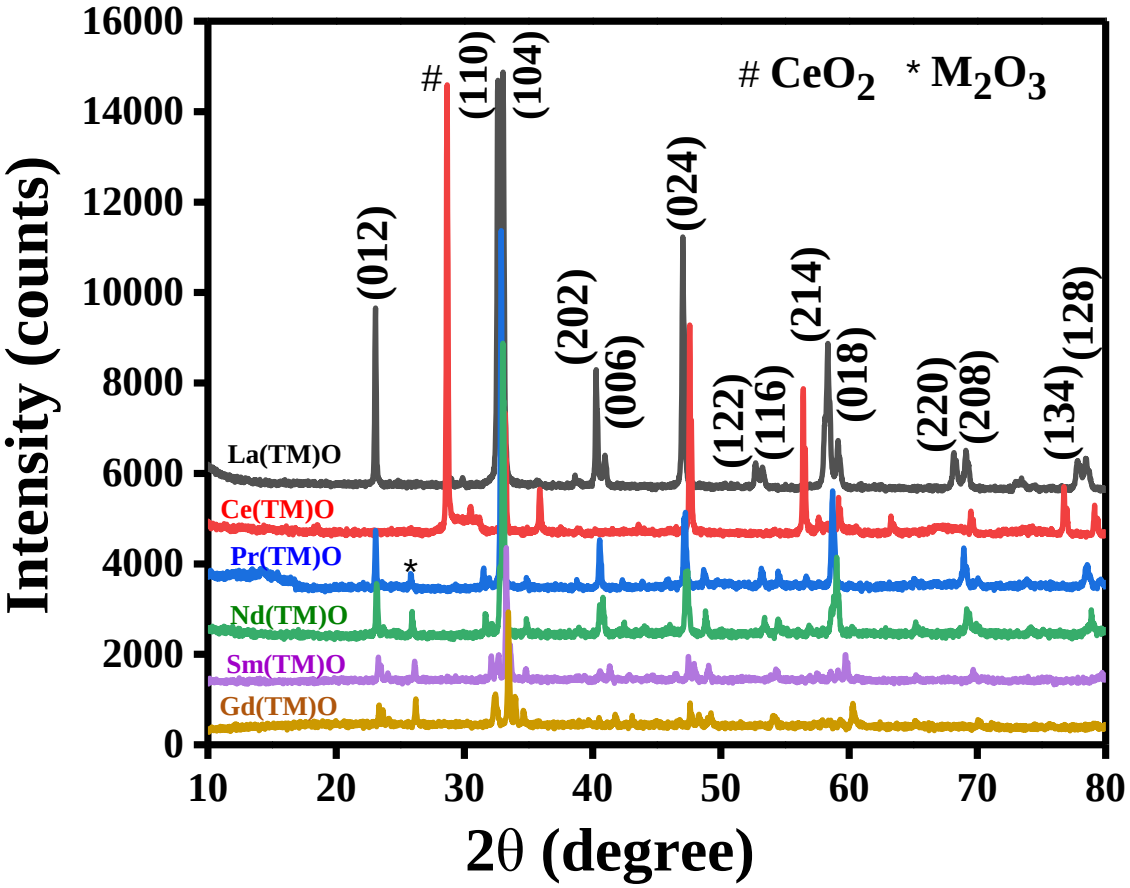

Fig. 5.1: PXRD patterns of as-prepared Ln(TM)O (Ln= La, Ce, Pr, Nd, Sm, and Gd & TM= Mn, Fe, Co, Ni, and Cu in equimolar proportion) HEPO catalysts.

5.3.2. DRM activity screening of materials

In order to find out the most active catalyst for DRM reaction, a primary DRM behaviour tests of the as-synthesized HEPOs were carried out for 10 h. **Fig. 5.2(a–c)** demonstrate the methane conversion, carbon dioxide conversion, and the ratio of H_2/CO of all the as-synthesized HEPOs samples. The methane conversions of the HEPOs, La(TM)O, Ce(TM)O, Pr(TM)O, Nd(TM)O, Sm(TM)O, and Gd(TM)O are 86%, 35%, 45%, 27%, 42%, and 30%, respectively. On the other hand, the respective CO_2 conversions of these HEPOs are 90%, 40%, 49%, 32%, 46%, and 35%. The H_2/CO ratio of all the HEPOs varies from 0.6 to 1 owing to some parallel side reactions which are thermodynamically possible. The H_2/CO ratio value lower than unity, suggests the existence of the reverse water gas shift reaction that involves –reaction of CO_2 with the hydrogen that is produced via DRM in the reaction medium. **Fig. 5.2** clearly indicates that except La(TM)O, all other samples show methane conversions below 50%. Similarly, CO_2 conversions also lie below 50%. The

$La(Mn_{0.2}Fe_{0.2}Co_{0.2}Ni_{0.2}Cu_{0.2})O_3$, La(TM)O displays the maximum methane and carbon dioxide conversions of 86% and 90%, respectively, having H_2/CO ratio of ~1. Based on the preliminary screening results, a continuous 100 h DRM reaction was then conducted using $La(Mn_{0.2}Fe_{0.2}Co_{0.2}Ni_{0.2}Cu_{0.2})O_3$ as catalyst, in order to put additional focus on the robustness as well as DRM activity of this HEPO catalyst. **Fig. 5.2(d–f)** display, the methane conversion, carbon dioxide conversion, and the ratio of H_2/CO of $La(Mn_{0.2}Fe_{0.2}Co_{0.2}Ni_{0.2}Cu_{0.2})O_3$ catalyst, respectively, for 100 h of DRM reaction. The graph also contains the DRM activity behaviour data for an additional catalytic run in order to further guarantee the reproducibility. From the graph, it is found that $La(Mn_{0.2}Fe_{0.2}Co_{0.2}Ni_{0.2}Cu_{0.2})O_3$ shows 86% methane conversion, 90% carbon dioxide conversion, and the H_2/CO ratio varies from 1.1 to 1. The ratio of H_2/CO is slightly higher than unity, indicating the existence of the Boudouard reaction in the reaction medium when CO is disproportionated to C and CO_2. Gradually, the H_2/CO ratio reaches 1, which is theoretically expected, and remains stable for the rest of the DRM reaction. After 100 h of nonstop reaction, it was stopped, and the helium atmosphere was used to cool the aged catalyst to room temperature. Characterization of the aged catalyst has been done thoroughly to compare the findings with those of the as-prepared along with the *ex situ* regenerated (at 900 °C for 3 h) catalysts in order to comprehend the relationship between structure and activity.

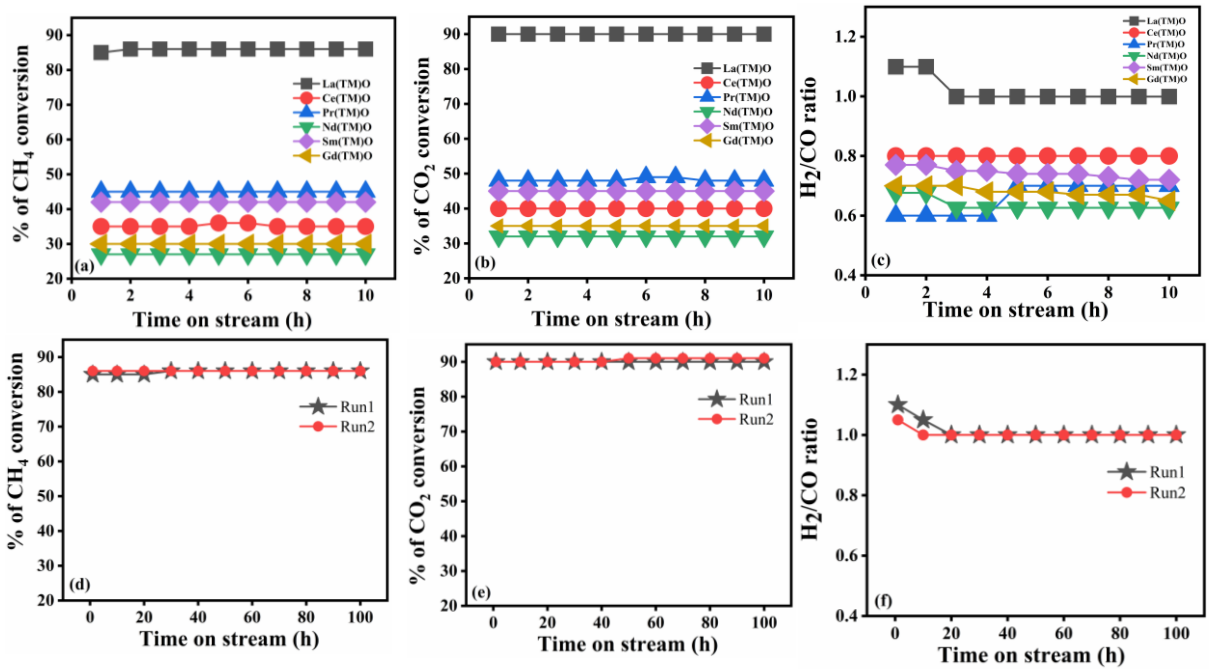

Fig. 5.2: DRM activity behaviour of Ln(TM)O (Ln= La, Ce, Pr, Nd, Sm, and Gd) HEPO catalyst materials for 10 h (upper row) and of the most active La(TM)O HEPO catalyst for 100 h (lower row) at GHSV of 33500 mL g_{cat}^{-1} h^{-1} and reaction temperature of 800 °C: (a, d) methane conversion, (b, e) carbon dioxide conversion and (c, f) ratio of H_2/CO.

Table 5.1: DRM activity of all the as-synthesized HEPO catalysts (for 10 h).

Catalyst	**CH_4 conversion (%)**	**CO_2 conversion (%)**	**H_2/CO ratio**
La(TM)O	86	90	1
Ce(TM)O	35	40	0.8
Pr(TM)O	45	49	0.65
Nd(TM)O	27	32	0.65
Sm(TM)O	42	46	0.75
Gd(TM)O	30	35	0.7

The apparent activation energies of the DRM reaction related to the various forms of La(TM)O have been determined to compare them with the activity performance. For the kinetic studies, the fixed-bed flow reactor was loaded with 30 mg of La(TM)O catalyst that had been mixed with 70 mg of pure silica of the similar mesh size (85–100) and all other experimental conditions were unchanged. The temperature range was 400–460 °C to keep all the conversions below 20%. Arrhenius plots of various forms of La(TM)O catalyst are shown in **Fig. 5.3**. The apparent activation energies, determined from the slopes of the Arrhenius plots for the formation rates of H_2 over the specified temperature range, were found to be 109 kJ mol^{-1} for the as-prepared La(TM)O, 88 kJ mol^{-1} for the aged La(TM)O, and 100 kJ mol^{-1} for the regenerated La(TM)O form of the catalyst (see **Fig. 5.3(a)**). In comparison, the apparent activation energies for CO production were relatively lower than those for H_2 production, with values of 90 kJ mol^{-1} for the as-prepared La(TM)O, 54 kJ mol^{-1} for the aged La(TM)O, and 74 kJ mol^{-1} for the regenerated form of La(TM)O (see **Fig. 5.3(b)**). It is clear that the as-prepared La(TM)O catalyst exhibits the highest activation energies for both H_2 (109 kJ mol^{-1}) and CO (90 kJ mol^{-1}) production, whereas the aged La(TM)O catalyst shows the lowest activation energy barriers, with values of 88 kJ mol^{-1} and 54 kJ mol^{-1} for H_2 and CO production, respectively. This suggests that the La(TM)O catalyst reaches its most activated state on being aged. While the regenerated catalyst has a higher activation energy value than the aged catalyst, it still demonstrates lower apparent activation energies than the as-prepared

form of the La(TM)O catalyst. So, the regenerated form of the catalyst is less active than the aged form but more active than the as-prepared form.

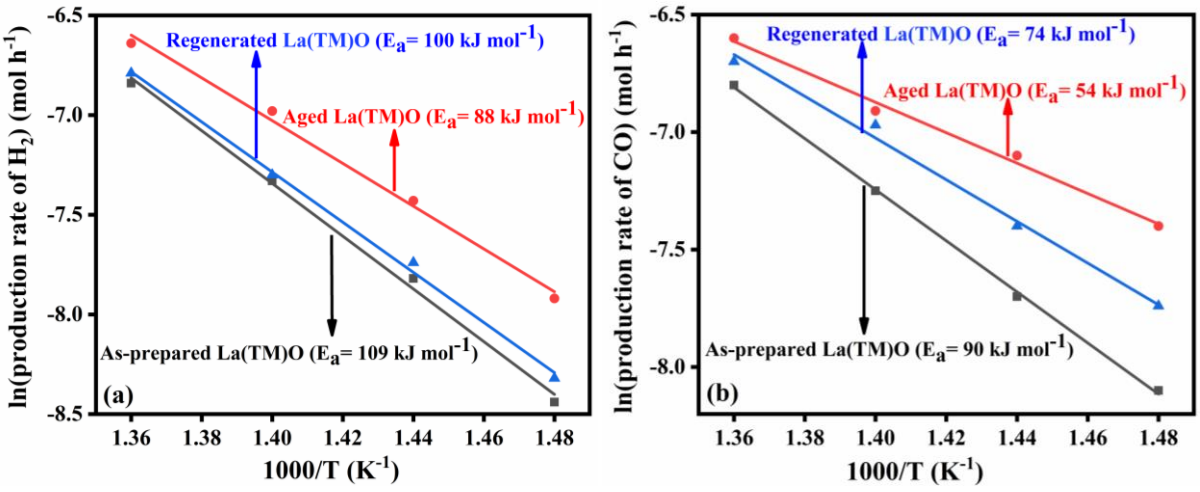

Fig. 5.3: Arrhenius plots for the production of (a) H_2 and (b) CO for various forms La(TM)O HEPO catalysts at GHSV of 113400 mL g_{cat}^{-1} h^{-1}.

5.3.3. PXRD analyses of different forms of La(TM)O catalyst: Correlation with DRM activity behaviour

Fig. 5.4 displays the PXRD patterns of different forms of the La(TM)O catalyst. It evident from the characteristic diffraction patterns of the aged (100 h) sample that the original perovskite phase is fully disappeared and some new diffraction peaks appeared. These newly appeared peaks resembled to the individual oxide components together with metallic nickel, as assigned in **Fig. 5.4**. It is also important to be noted that the similar structural change (PXRD patterns not added here) is found to be observed for 10 h of reaction. Several studies have reported that the initial phase of the catalyst typically disintegrated into its constituent oxides in the reaction atmosphere [23, 41, 43, 47, 48], trailing its original oxide phases in the DRM environment. The decomposed components have been recognized La_2O_3 (*) peaks observed at 2θ values of 26.3°, 30° and 39.3, $La(OH)_3$ (▪) at 2θ values 15.7° and 28°, CuO (◊) at 2θ values of 35°, 40.8° and 55.5°, MnO (◊) at 2θ values 34° and 55.4°, CoO (ɤ) at 2θ values 60° and 75.3°, Fe_2O_3 (α) at 2θ values 49.2°, NiO (•) at 2θ values of 31.8°, 43.3°, and 55.3° and nickel metal at 2θ value of 44.2°. These degraded components closely correspond to JCPDS PDF # 831349 for La_2O_3 (*), 832034 for $La(OH)_3$ (▪), 751090 for MnO (◊), 082233 for Fe_2O_3 (α), 780431 for CoO (ɤ) 140481 for NiO (•), 897128 for metallic Ni (○), and 782076 for CuO (Φ).

The interesting fact of this La(TM)O catalyst is that the catalyst's pristine phase is degraded in the DRM environment (aged form), but the pristine phase of the HEPO catalyst can be regenerated fully from the degraded components by heating at synthesis temperature in air for 3 h (see **Fig. 4**). The as-synthesized, aged, and regenerated forms of the La(TM)O catalyst have the corresponding Scherer sizes of 22.7, 6.0, and 15.0 nm, respectively. Enhanced specific surface area values (from 30 to 52 m^2 g^{-1} after ageing) from BET surface area analysis is in good agreement with the reduction of size of aged catalyst in DRM reaction atmosphere.

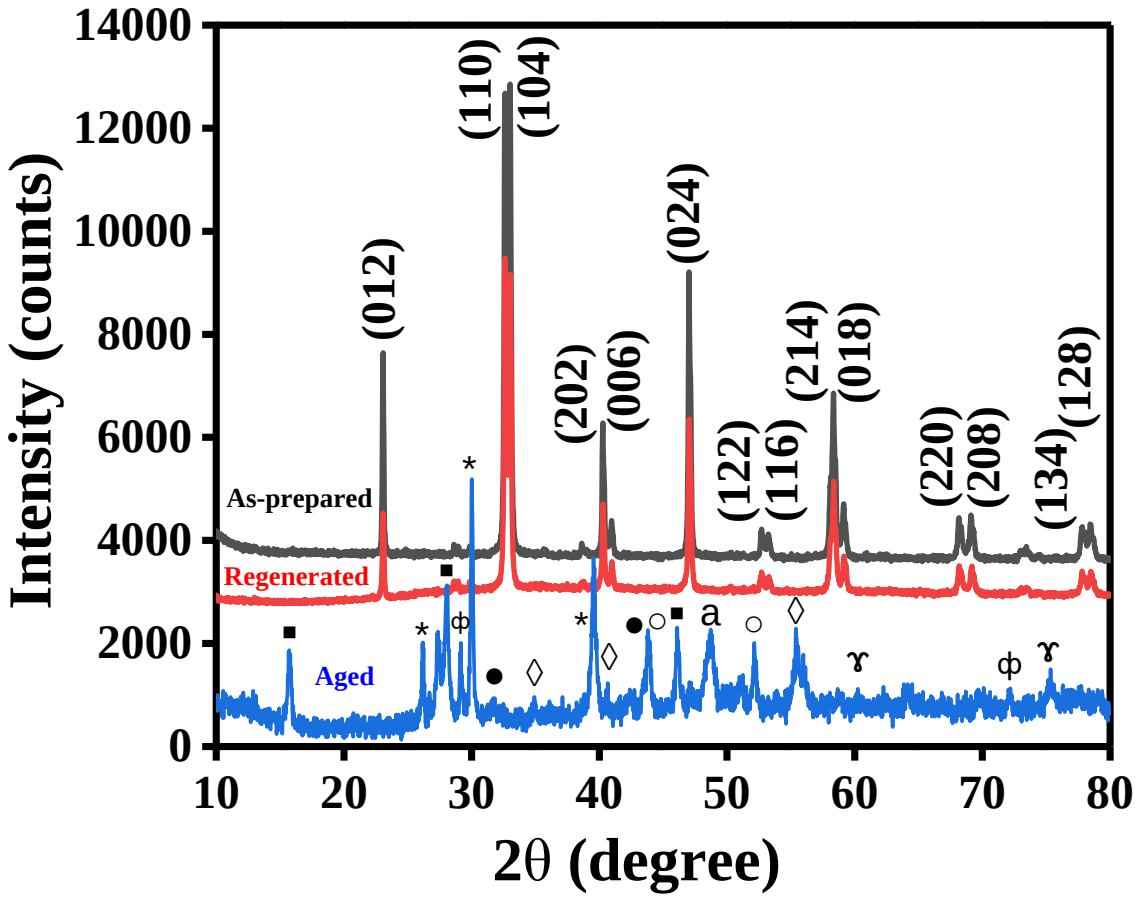

Fig. 5.4: PXRD patterns of different forms of La(TM)O HEPO catalyst.

The refinement of the PXRD patterns of both the phases, fresh and regenerated La(TM)O, has been performed in order to find out the structural characteristics of the catalyst (see **Fig. 5.5**). The refinement of the XRD patterns has been done using the FullProf Suite software. The refinement of both the phases have shown that the rhombohedral $R\bar{3}c$ space group is appropriate for this system. The absence of any impurity peak in the refined XRD

forms confirms the pure phase of the catalysts. The structural change and the refinement parameters of both the phases are listed in **Table 5.2**. It is apparent that the peaks intensity in the regenerated phase of the catalyst is not similar as they are in the original phase.

This is because there was less sample used for diffraction for the regenerated form. This result confirms the structural similarity between the original and the regenerated phases of the HEPO catalyst as previously reported in our work [47, 48].

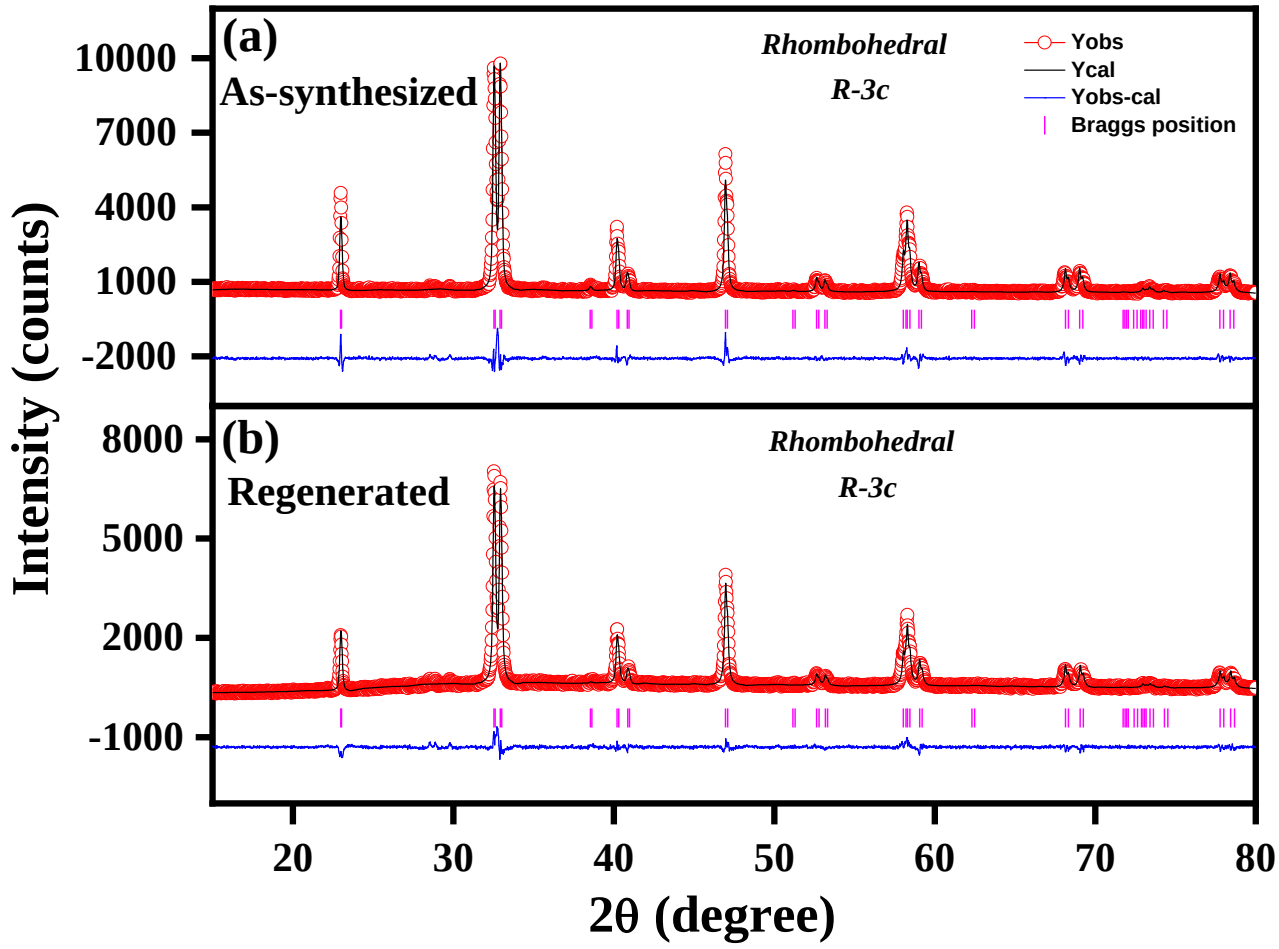

Fig. 5.5: Rietveld refined PXRD patterns of the (a) as-synthesized and (b) regenerated La(TM)O HEPO catalyst materials. The experimental pattern, calculated data, difference curve, and Bragg positions are symbolized, respectively, by the empty red circles, black lines, lowermost blue lines, and vertical magenta bars.

Table 5.2: Rietveld refinement and Structural data of the La(TM)O $La(Mn_{0.2}Fe_{0.2}Co_{0.2}Ni_{0.2}Cu_{0.2})O_3$ catalyst material of as-synthesized and regenerated forms.

Catalyst composition	**Cell parameters**	**Bond length (Å)**	**Bond angle (°)**
$La(Mn_{0.2}Fe_{0.2}Co_{0.2}Ni_{0.2}Cu_{0.2})O_3$ As-prepared Rhombohedral $R\bar{3}c$	a = 5.500 Å b = 5.500 Å c = 13.246 Å V = 347.06 Å^3 R_{Bragg} = 2.75 % R_f= 2.17 % χ^2= 3.10	Mn/Fe/Co/Ni/Cu: 1.955	Mn/Fe/Co/Ni/Cu—O—Mn/Fe/Co/Ni/Cu: 162.85
$La(Mn_{0.2}Fe_{0.2}Co_{0.2}Ni_{0.2}Cu_{0.2})O_3$ Regenerated Rhombohedral $R\bar{3}c$	a = 5.501 Å b = 5.501 Å c = 13.245 Å V= 347.07 Å^3 R_{Bragg} = 4.16 % R_f= 2.66 % χ^2= 3.13	Mn/Fe/Co/Ni/Cu: 1.941	Mn/Fe/Co/Ni/Cu—O—Mn/Fe/Co/Ni/Cu: 169.10

Regeneration of the aged catalyst has been performed *in situ* for additional assurance that the DRM activity does not change on regeneration of the aged catalyst. First, the DRM activity of the La(TM)O sample has been tested for 10 h under identical reaction conditions. Following the reaction's termination, helium gas was used for 30 min to clean the gas lines. The aged catalyst was subsequently regenerated at 900 °C (similar to the phase formation temperature for initial perovskite) for 3 h using zero grade air flow. The regenerated La(TM)O was then subjected to DRM test under similar reaction conditions. **Fig. 5.6** shows DRM activity of the as-synthesized and regenerated La(TM)O forms of HEPO catalyst that shows almost full retention of catalytic activity upon regeneration of the catalyst. Amazingly, regeneration at lower than the phase formation temperatures of 700 and 800 °C is also possible, and these regenerated forms of HEPO catalyst also show comparable catalytic activity (**Fig. 5.14**). The

H_2/CO value of ~1 suggests that both side reactions are taking place to a lower extent **(see Fig. 5.6)**. In the Boudouard reaction, where CO transforms into carbon dioxide and carbon, giving a higher H_2/CO ratio than unity. Whereas in RWGS, CO_2 reacts with the produced hydrogen, making the H_2/CO ratio slightly lower than unity.

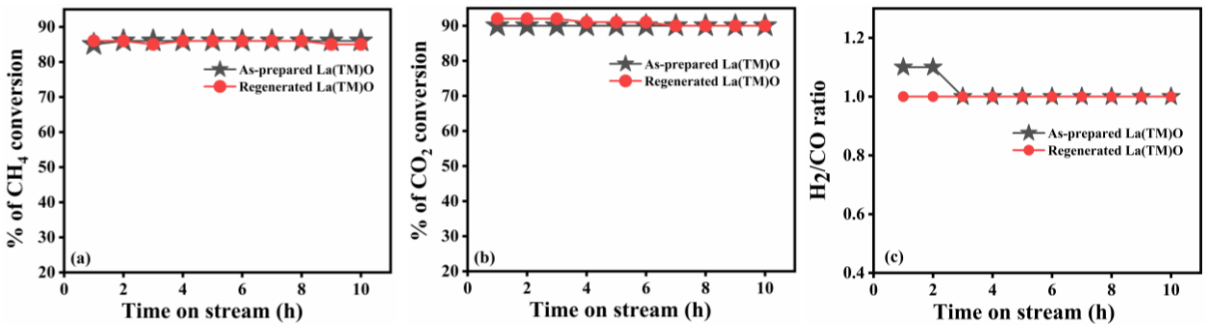

Fig. 5.6: (a) Methane conversion, (b) carbon dioxide conversion, and (c) ratio of H_2/CO of the as-synthesized and *in situ* regenerated La(TM)O HEPO catalysts for 10 h of DRM reaction (under similar reaction conditions).

Therefore, for the HEPO catalyst material, the mixture of separate oxides and nickel metal at the molecular level is the real performer for the high DRM activity. The pristine HEPO catalyst degraded into component metal oxides along with nickel metal on ageing. These degraded phases form the "molecular level nanocomposites" in the reaction medium. We propose that the observed high DRM activity behaviour is caused by the molecular level nanocomposite that is generated by metallic nickel and nickel oxide. This *in situ* formed nanocomposite is the real performer in the HEPO catalyst for DRM activity, whereas other oxides in the reaction media, such as La_2O_3 [47–51] acts as supports, MnO [52, 53] acts as promoter, Fe_2O_3 [54, 55] and CoO [56, 57] act as oxygen carrier, and CuO [47, 58] acts as promoter. Meanwhile, the disintegrated catalyst components can be switched back to its pristine perovskite phase, allowing the process to be reversible in nature. The first step was facilitated by a reforming environment, and the next one by the calcination process.

5.3.4. Specific BET surface area measurement

Fig. 5.7 shows the BET nitrogen adsorption and desorption isotherms of the as-synthesized Ln(TM)O (where Ln= La, Ce, Pr, and Nd), aged and regenerated La(TM)O samples and the inset figure includes their corresponding pore size distribution curves. **Table 5.3** provides the specific surface area, pore volume, and distribution of pore sizes of the

respective catalysts. The P/P_0 values range from 0 to 1, indicating that the volume of N_2 gas adsorption is lower at relatively low pressure and gradually rises at high P/P_0 values which suggests the formation of type IV isotherm and the nature of the hysteresis loop is like H3 type.

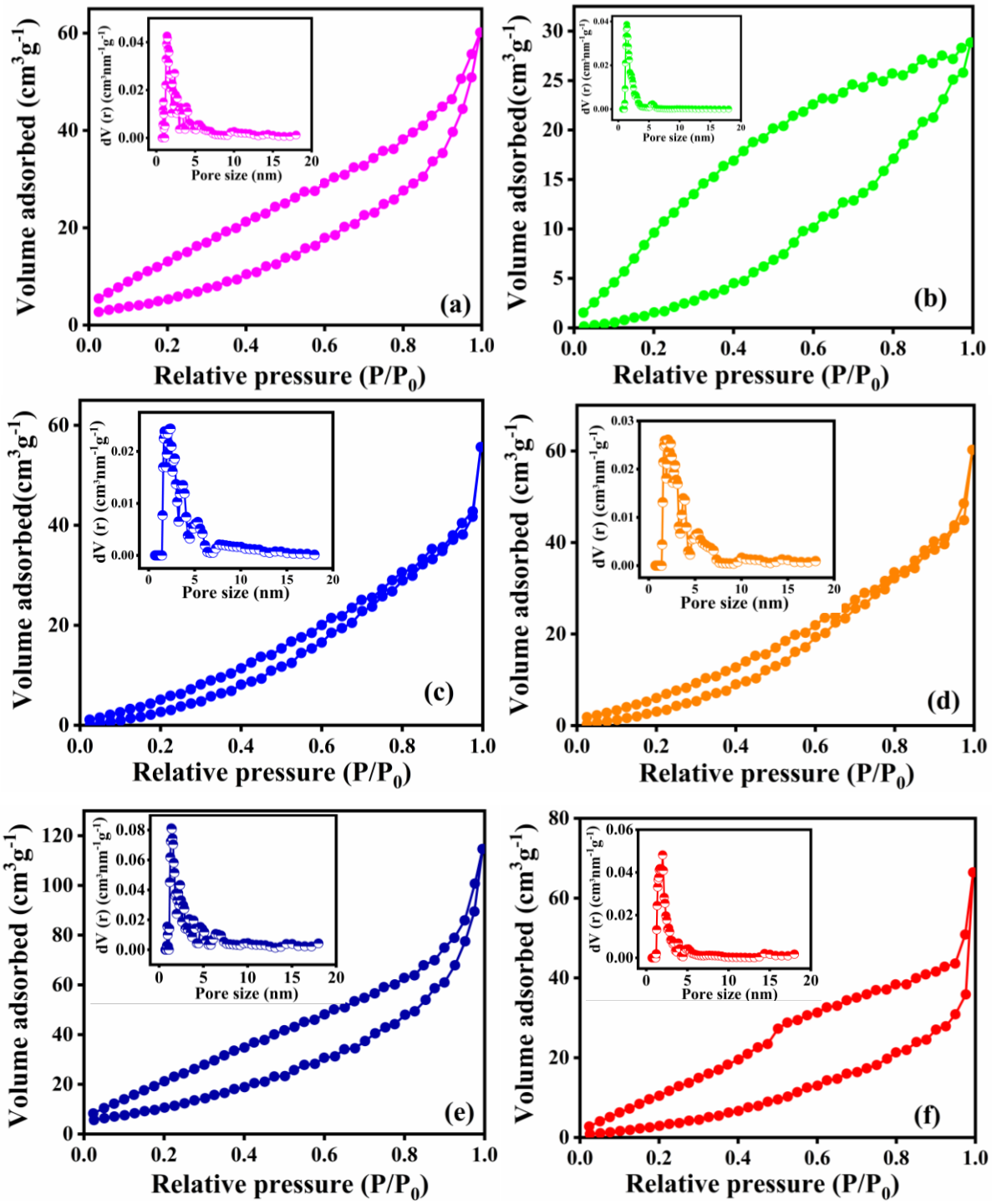

Fig. 5.7: N_2 adsorption-desorption isotherms curves and porosity (in the inset) of (a) La(TM)O, (b) Ce(TM)O, (c) Pr(TM)O, (d) Nd(TM)O, (e) aged La(TM)O and (f) regenerated La(TM)O HEPO catalysts.

The specific surface areas (S_{BET}) of the various forms of catalyst materials, La(TM)O, Ce(TM)O, Pr(TM)O, Nd(TM)O, aged La(TM)O and regenerated La(TM)O, are approximately 30, 23, 20, 22, 52, and 35 m^2 g^{-1}, respectively. La(TM)O has the highest BET surface area amongst as-prepared catalysts, which results in its high DRM activity. The specific surface area of the La(TM)O catalyst increased from 30 m^2 g^{-1} to 52 m^2 g^{-1} on being aged in DRM medium [47, 48]. The reason for this is due to the catalyst having broken down into its individual oxide components, as confirmed by XRD, XPS and HRTEM analyses. XRD analysis has also verified that the particle size of the aged catalyst was reduced to ~6 nm from 22.7 nm. Smaller sizes and higher surface area of the aged HEPO La(TM)O catalyst is in good agreement for high DRM activity and long-term durability. The particle size and surface area of the regenerated catalyst are 15 nm and 35 m^2 g^{-1}, respectively. The regenerated La(TM)O catalyst also has higher surface area than the pristine catalyst, which nicely supports the similar DRM activity of the regenerated La(TM)O catalyst (**Fig. 5.6**). Both the aged and regenerated forms of the catalyst have higher surface area and smaller particle size compared to the pristine catalyst. These results nicely support the sustained 100 h DRM activity of the aged catalyst as well as the similar DRM activity of the regenerated La(TM)O catalyst.

Table 5.3: Textural features of different Ln(TM)O (where Ln=La, Ce, Pr, and Nd), aged and regenerated forms of La(TM)O HEPO catalysts.

Catalyst	**Specific surface area (m^2 g^{-1})**	**Pore volume (cm^3 g^{-1})**	**Pore size (nm)**
La(TM)O	30	0.070	1.98
Ce(TM)O	23	0.079	1.38
Pr(TM)O	20	0.062	2.01
Nd(TM)O	22	0.069	2.07
Aged La(TM)O	52	0.152	1.38
Regenerated La(TM)O	35	0.079	1.39

5.3.5. FESEM analyses

FESEM microscopic analysis was used to examine the morphology and basic composition of the as-synthesized and aged forms of the catalyst. From FESEM studies, it is observed that the as-prepared La(TM)O catalyst is found to exist as a uniformly distributed spherical shape along with some irregular shaped nanoparticles, as presented in **Fig. 5.8(a)**.

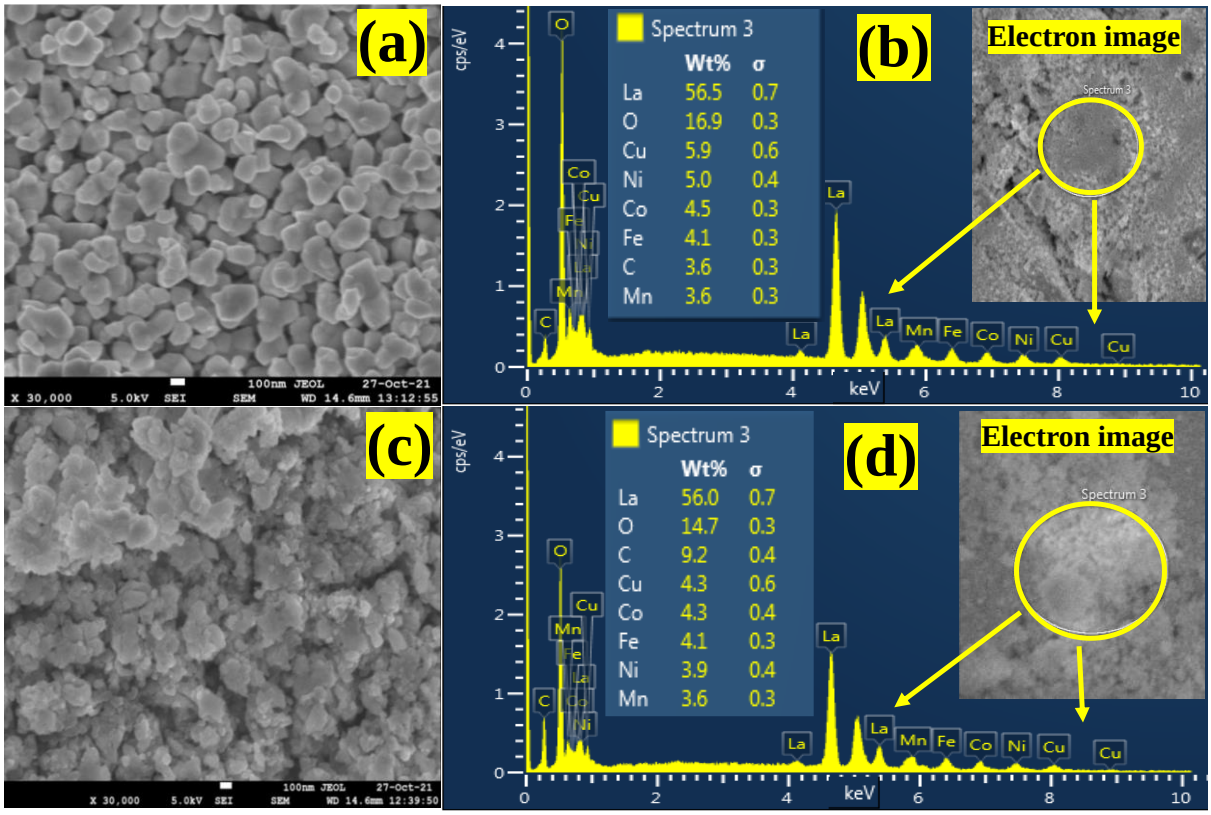

Fig. 5.8: FESEM images (a, c) and EDX spectra (b, d) of pure and aged forms of La(TM)O HEPO catalyst.

Morphology of aged forms of the catalyst has transformed into highly aggregated, irregular shaped particles, and this is for the degradation of the catalyst in the reaction environment (see **Fig. 5.8(c)).** The aged form of the catalyst contains the individual oxide phases in aggregated form. The EDX data of the as-synthesized and aged form of catalyst La(TM)O shows La, Mn, Fe, Co, Ni, Cu, and O are the elements present in the samples, as shown in **Fig. 5.8(c, d)**. For the as-prepared sample, the surface of the La(TM)O catalyst appears transparent and smooth, but for the aged sample, its surface smoothness decreases and becomes rough, most likely due to the catalyst's reduction to its individual oxides.

5.3.6. HRTEM studies

The microstructural study of the as-synthesized and aged forms of La(TM)O was done by the TEM and HRTEM analyses as shown in **Fig. 5.9**. It is found that the as-synthesized La(TM)O catalyst surface has a spherical morphology, as observed in **Fig. 5.9(a)**, whereas it is transformed into granular-like assembled asymmetrical morphology in aged form, as shown in **Fig. 5.9(e)**. The as-synthesized La(TM)O catalyst has a lattice fringe of 0.27 nm that correlates to the (110) lattice plane of the catalyst (see **Fig. 5.9(c)**).

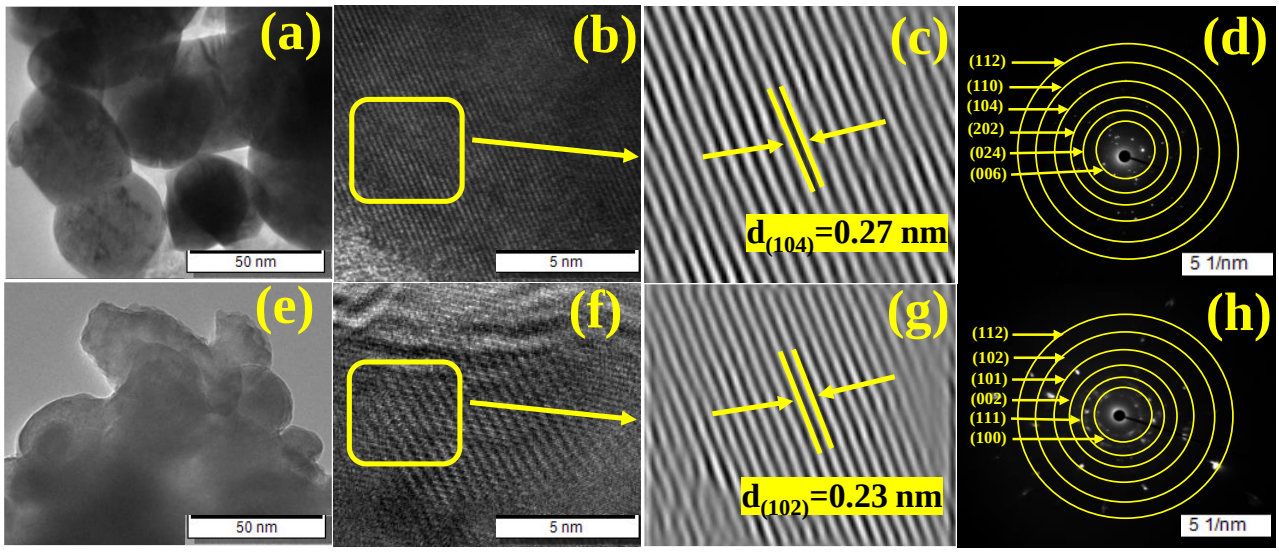

Fig. 5.9: (a, e) TEM images (b, f) HRTEM images, (c, g) enlarged area of HRTEM and (d, h) SAED patterns of pure and used La(TM)O HEPO catalysts, respectively.

The obtained data is in good agreement with the XRD result of the as-prepared La(TM)O sample. On the other hand, the aged La(TM)O catalyst has a lattice fringe of 0.23 nm and correlates with the (102) plane of Ni–O as shown in **Fig. 5.9(g)**. The fringe spacing corresponding to metal-oxygen for the other transition metals are very similar and hence this spacing may in general be attributed to be arising out of (102) planes of TM–O. This result indicates that as-prepared La(TM)O catalyst changes into different binary oxide phases in DRM, which is further supported by the XRD analysis of the aged La(TM)O sample. **Fig.** 5.**9(d)** displays the selected area electron diffraction (SAED) of the pure La(TM)O catalyst and the SAED pattern of the aged La(TM)O catalyst is displayed in **Fig. 5.9(h)**, where the relevant lattice planes are indicated.

5.3.7. XPS analyses

XPS studies of different forms of La(TM)O HEPO catalyst have been carried out to understand their detailed elemental information and compositions (see **Fig. 5.10**). The survey spectra of different forms of the HEPO catalyst show that La, Mn, Fe, Co, Ni, Cu, O and C elements are present in the catalyst (see **Fig. 5.10 (a**)). La 3d with Ni 2p core region spectra of as-synthesized, aged, and regenerated forms of the HEPO catalyst have been recorded instantaneously because of the overlapping of the La $3d_{3/2}$ along with Ni $2p_{3/2}$ core level spectral regions as presented in **Fig. 5.10(b)** [47, 48]. A comparatively intense peak near 855 eV related to the nearby peak is found to be detected in the spectra of the different forms of the catalysts indicating the existence of Ni components in the La 3d core region. The La 3d core region of as-synthesized catalyst shows La $3d_{5/2,\ 3/2}$ the doublet peaks at 833.7, 850.9 eV, corresponding to presence of La_2O_3 component in the catalyst. The values agree well with the literature values. So, these observed doublet peaks are related to some initial and final forms of the catalyst, related to $3d^9 4f^1$ (for lower binding energy) and $3d^9 4f^0$ (for higher value of binding energy). The board strong peak about 855.0 eV is formed of both La $3d_{3/2}$ $3d^9 4f^0$ final state of La^{3+} species, and Ni $2p_{3/2}$ of Ni^{3+} component. The peak at 854.4 eV is attributed to La^{3+} species corresponding to La $3d_{3/2}$ $3d^9 4f^0$ final form. The observed peak at 855.8 eV is ascribed to Ni $2p_{3/2}$ of Ni^{3+} species. The broad strong peak at 862.4 eV has satellite peaks of Ni^{3+} and La^{3+}. A slight satellite peak at 846.2 eV is related with La^{3+}. The Peaks at 871.8 and 879.1 eV are associated to Ni $2p_{1/2}$ of Ni^{3+} components and associated with the satellite peaks. For the spent catalyst, the feature of La 3d + Ni 2p spectra is to some extent different from that of the original form of the catalyst (see **Fig. 5.10(b)**) [47, 48, 59]. The strong $3d_{5/2}$ peak observed at 835.4 eV implies the presence of $La(OH)_3$ on catalyst surface. In XRD pattern, a peak for $La(OH)_3$ is observed, which corroborates with the XPS analyses. In the spent catalyst, the obtained component peak of $2p_{3/2}$ at 854.5 corresponds to Ni^{2+} species on the surface of spent catalyst. Therefore, NiO is produced in DRM reaction that is reliable with the PXRD results (see **Fig. 5.10(b)**). The regenerated catalyst has La 3d core level spectrum similar to that of as-synthesized catalyst indicating the proper regeneration of the spent catalyst. The Mn 2p core level spectra of different forms of catalysts are shown in **Fig. 5.10(c)**. In as-prepared catalyst, peaks observed at 641.8 and 653.3 eV are recognized to Mn^{3+} components present in the catalyst [47, 48, 60]. However, peaks at 640.7 and 652.3 eV together with the satellite observed peak at 647.3 eV correspond to Mn^{2+} species, indicating the reduction of Mn species during DRM reaction. Mn 2p binding energy peak positions in core level spectrum of the fully regenerated catalyst are comparable to as-synthesized catalyst. A hump at 636.3 eV is attributed

to Cu LMM peak [48]. **Fig. 5.10(d)** represents Fe 2p core level spectra of various forms of the catalyst. Fe $2p_{3/2,1/2}$ peaks observed at 711.1 and 724.6 eV with a small satellite peak at 719.2 eV are assigned to Fe^{3+} species [61]. A hump around 713.4 eV is associated with Co LMM contribution from Co species present in the catalyst. However, spectral feature of Fe 2p core level spectrum of the regenerated catalyst looks like as-synthesized catalyst. As-prepared catalyst shows Co $2p_{3/2,1/2}$ peaks at 779.5 and 794.9 eV together with a typical weak satellite peak at 790.7 eV, which is assigned to Co^{3+} species [61, 62].

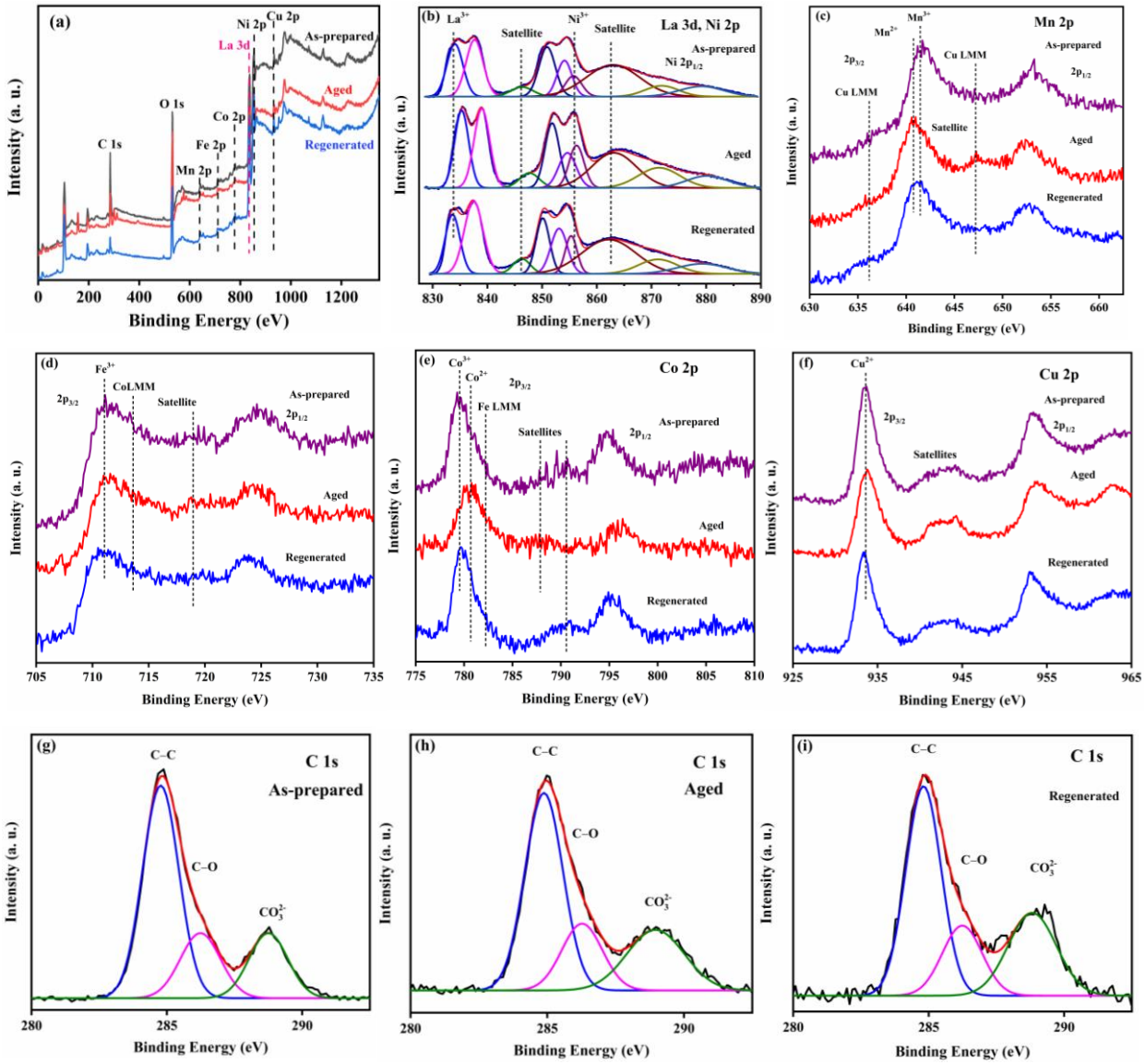

Fig. 5.10: XPS core level spectra of the various forms of La(TM)O catalysts (a) survey spectra, (b) La 3d + Ni2p, (c) Mn 2p, (d) Fe 2p, (e) Co 2p, (f) Cu 2p, and (g–i) C

Spectral features have been changed in the aged catalyst. Peaks at 780.8 and 796.2 eV with the typical satellite peak observed at 787.8 eV are ascribed to Co^{2+} species (see **Fig. 5.10(e)**). The peak at 782.3 eV corresponds to Fe LMM peak of Fe species present in the catalyst. Binding energy peak positions of regenerated form of the catalyst are similar to as-synthesized catalyst with sharper features compared to as-prepared catalyst. Cu 2p core level spectra of various forms of the catalyst are displayed in **Fig. 5.10(f)**. Observed Cu $2p_{3/2,1/2}$ peaks at 933.6 and 953.4 eV together with the satellite peaks at 941.2, 943.9, and 962.9 eV signifying the presence of Cu^{2+} species in the sample [47, 63–65]. The satellite peaks are the characteristics feature of the oxides of transition metal element. There is no substantial change in the spectral feature of Cu 2p in the aged and regenerated catalysts. However, the aged HEPO catalyst is regenerated as apparent from the conforming Cu 2p core level spectrum of the regenerated form of the catalyst [48]. C 1s core level spectra of various forms of the regenerated HEPO catalysts are broad and asymmetric, indicating the existance of different forms of carbon species on the surface of the catalyst, which are resolved by curve fitting as presented in **Fig. 5.10(g–i)**. Accordingly, the peaks observed at 284.9, 286.3, and 288.9 eV are related with C–C/C–H, C–O, and (CO_3^{2-}) carbonate type compounds, respectively [47, 48, 66, 67]. The intensities of oxidized carbon species are observed to increase in the aged form of the catalyst component. There is no substantial variation in C 1s core level spectrum of the regenerated form of the catalyst in comparison with as-synthesized catalyst, which confirm the successful regeneration of the aged catalyst. The O 1s core level spectra of different forms of the catalyst are broad and contributions are separated by curve fitting. The observed peaks at 528.6, 530.6, 531.7, 532.6, and 533.5 eV are related to the La–O, Cu–O, adsorbed hydroxyl (OH^-) species, adsorbed carbonate species (CO_3^{2-}), and adsorbed water molecule, respectively [47].

5.3.8. Advantage of SGCA process compared to the SCS process

The catalytic performance of DRM reactions was evaluated using catalysts prepared through different methods, namely La(TM)O (SG), La(TM)O (PM), and La(TM)O (SCS), under identical reaction conditions. Notably, the sol-gel method appeared to be superior to both the PM and SCS methods in terms of catalytic activity as shown in **Fig. 5.11**. The catalyst made by the SCS method demonstrated 66% CH_4 conversion, 78% CO_2 conversion, and ratio of H_2/CO of around 1.1. The H_2/CO ratio higher than unity for the SCS catalyst suggests that the Boudouard reaction is more dominant than the RWGS reaction in this case. In contrast, the sol-gel prepared La(TM)O catalyst showed superior DRM activity compared to the SCS catalyst.

Interestingly, the PM method showed practically no DRM performance (data not shown in the graph). After 10 h of DRM, XRD analysis revealed no significant changes of the PM catalyst. This suggests that the simple physical combination of the catalyst components does not affect the DRM performance. Thus, it is evident that molecular nanocomposite formation occurs only when the perovskite phase of the HEPO catalyst decomposes, regardless of whether it is produced via sol-gel or solution combustion methods. This observation indicates that the spatial arrangement of the catalyst components plays a more crucial role in catalytic activity than their mere presence in the matrix.

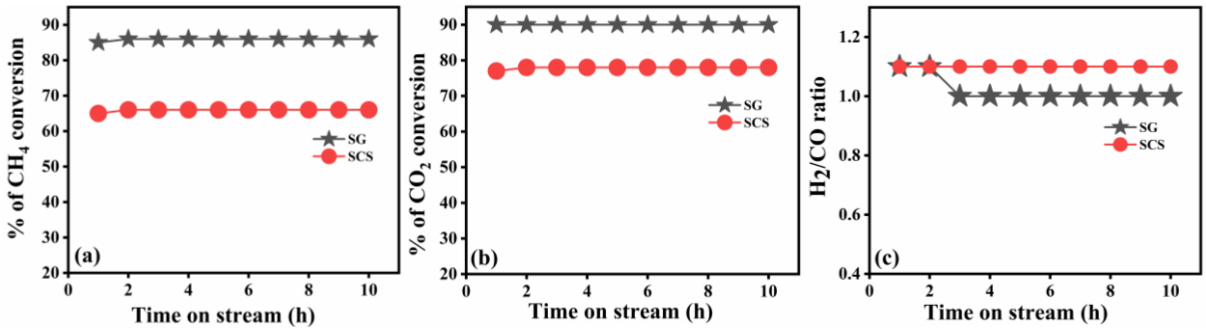

Fig. 5.11: Activity performance of the La(TM)O HEPO (made via sol-gel (SG) and solution combustion synthesis (SCS) routes) catalysts for 10 h of DRM reaction: (a) methane conversion, (b) carbon dioxide conversion and (c) ratio of H_2/CO (under similar reaction conditions).

Table 5.4 shows a comparison of the La(TM)O catalyst with other HEPO catalysts from the literature, focusing on the parameters such as CH_4 and CO_2 conversions, H_2/CO ratio, GHSV, reaction temperature, and the duration of the DRM test. It is noteworthy that the majority of DRM tests are conducted at a reaction temperature of 800 °C. The $Fe_4Ni_2CrCoMn_{0.55}O_y$ catalyst have shown CH_4 and CO_2 conversion 98 and 73%, respectively, for 100 h [41]. The catalytic activity of the $LaFe_{0.7}Ni_{0.1}Co_{0.1}Cu_{0.05}Pd_{0.05}O_3$ catalyst have 64% CH_4 and 68% CO_2 conversion for 24 h with H_2/CO ratio 0.8 [42]. The HEO $(Ni_3MoCoZn)Al_{15}O_x$ catalyst have demonstrated 92% methane and 98% carbon dioxide conversion at GHSV 100000 mL g_{cat}^{-1} h^{-1} for 100 h DRM reaction [43]. The HEO $CoFeGaNiZn/CeO_2$ catalyst was found to convert methane and carbon dioxide 98% and 86%, respectively with H_2/CO ratio ~1.3 for 30 h of reaction [44]. Thus, the DRM performance data in **Table 5.4,** indicates that the present $La(Mn_{0.2}Fe_{0.2}Co_{0.2}Ni_{0.2}Cu_{0.2})O_3$ catalyst has commendable DRM activity.

Table 5.4: A comparison of DRM behaviour of the La(TM)O catalyst with other pertinent catalysts that are reported in the open literature.

Catalyst	**CH_4 conversion (%)**	**CO_2 conversion (%)**	**H_2/CO ratio**	**GHSV (mL g_{cat}^{-1} h^{-1})**	**Stability checked (h)**	**Temperature (°C)**	**Reference**
$Fe_4Ni_2CrCoMn_{0.55}O_y$	98	73	–	9000	100	550	41
$LaFe_{0.7}Ni_{0.1}Co_{0.1}Cu_{0.05}Pd_{0.05}O_3$	64	68	0.80	–	24	800	42
$(Ni_3MoCoZn)Al_{15}O_x$	92	98	0.94	100000	100	800	43
$CoFeGaNiZn/CeO_2$	98	86	1.3	20000	30	750	44
$La(Mn_{0.2}Fe_{0.2}Co_{0.2}Ni_{0.2}Cu_{0.2})O_3$ [La(TM)O]	86	90	~1	33500	100	800	our work

5.3.9. Insights into catalyst regeneration: Influence of changes in calcination temperature

Thus, earlier it has been shown that heat treatment at the reaction temperature of 900 °C can fully regenerate the aged form of the catalyst. It is evident that the aged forms of the catalyst have undergone complete phase regeneration since all the characteristic diffraction peaks appear at the same 2θ positions as those observed for the pure catalyst (see **Fig. 5.12**). XPS analysis reveals that the core level spectra of La 3d, Ni 2p, Mn 2p, Fe 2p, Co 2p, Cu 2p, C 1s, and O 1s for both the as-prepared and regenerated catalysts show similar features. These results therefore suggests that the HEPO catalyst material has a good prospective application in DRM reaction simply because this catalyst can be used in a repeated way.

Even the more intriguing fact is that the 100 h aged catalyst could be effectively regenerated by calcination for 3 h, even at the lower temperatures 800 °C and 700 °C than the initial phase formation temperature (900 °C) (see **Fig. 5.12**). In resemblance to this, the SCS catalyst was regenerated at the lowest temperature of 450 °C, which is the synthesis temperature for the SCS catalyst (see **Fig. 5.13**) [47, 48].

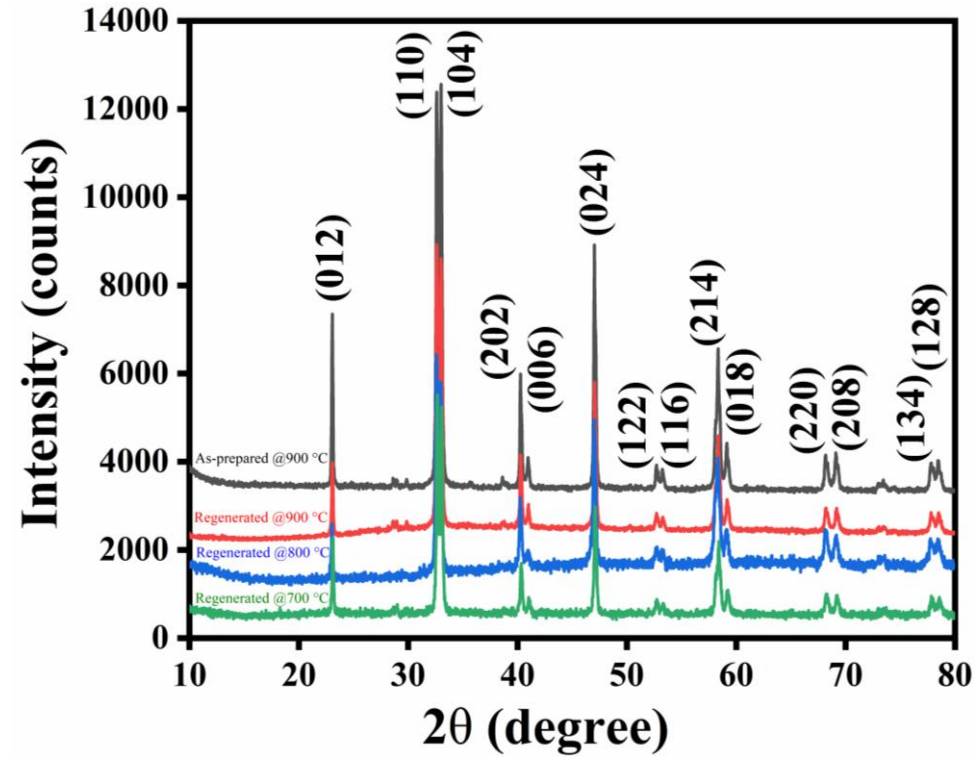

Fig. 5.12: PXRD patterns of as-synthesized along with regenerated (at different temperatures) La(TM)O HEPO catalyst synthesized adopting sol-gel citrate combustion route.

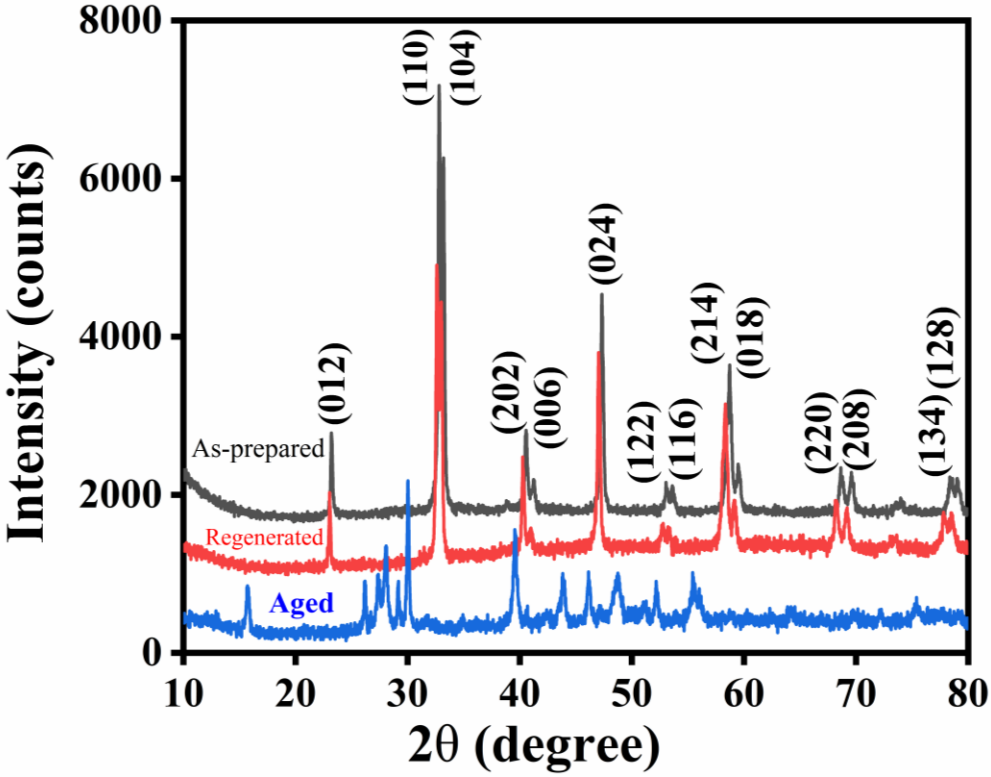

Fig. 5.13: PXRD patterns of various forms of the La(TM)O HEPO catalyst prepared via solution combustion method.

Fig. 5.14 shows the DRM performance of the sol-gel produced La(TM)O catalyst regenerated at different calcination temperatures under identical reaction conditions. The catalysts regenerated at different temperatures demonstrate similar CH_4 and CO_2 conversion and the ratio of H_2/CO. So, the DRM performance remains essentially similar irrespective of the regeneration temperatures. The temperatures required for regeneration do not affect the catalytic performance of the regenerated forms of HEPO catalyst (see **Fig. 5.14(a–c)**). The H_2/CO ratio varies because of some side reactions that take place inside the reaction medium. For the catalyst regenerated at 900 °C, it showed H_2/CO ratio ~1. This indicates that the occurrence of side reactions is minimal. The H_2/CO ratio of the regenerated catalyst at 800 °C and at 700 °C is ~ 0.97 and 0.96, respectively (see **Fig. 5.14(c)**). This value is nearly equal to unity, signifying that RWGS reactions may have occurred to a small extent in the reaction medium.

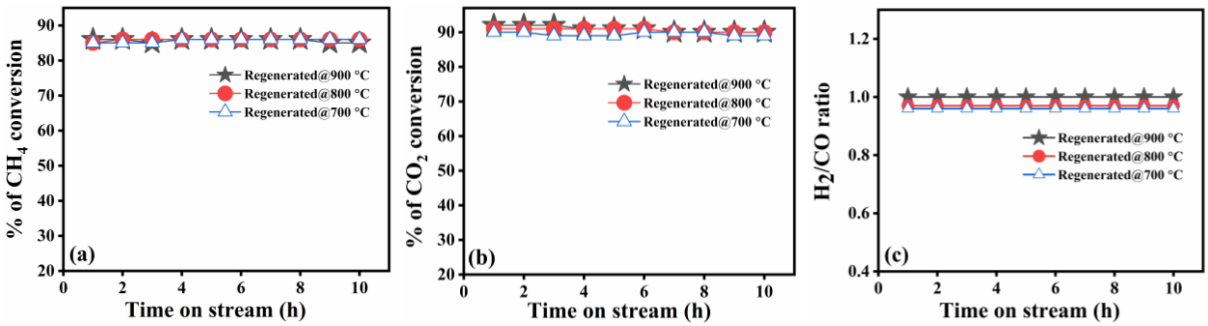

Fig. 5.14: Catalytic performance of La(TM)O HEPO regenerated at different temperatures: (a) methane conversion (b) carbon dioxide conversion, and (c) ratio of H_2/CO (under similar reaction conditions).

5.3.10. TGA analyses

Carbon accumulation on the surface of the aged $La(Mn_{0.2}Fe_{0.2}Co_{0.2}Ni_{0.2}Cu_{0.2})_3$ catalyst was evaluated using thermogravimetric analysis (TGA). The result was compared with the as-prepared catalyst (see **Fig. 5.15**). The as-prepared sample does not lose mass when the temperature steadily rises to 900 °C. For the aged sample, mass loss starts from 250°C, gradually decreases up to 500 °C and then a higher mass loss happens. About 10% of the mass loss is caused by the elimination of deposited coke from the aged catalyst surface, most likely in the form of CO_2. The effect of the deposited carbon structure on the stability of catalysts on mesocellular silica made via catalytic chemical vapour deposition (CCVD) method has been

investigated by Donphai et al. [68]. Their studies have shown that the amorphous carbon changes to carbon nanotubes (CNTs) at higher temperature. The mass losses were attributed to the following: lower stable carbon nanotubes (CNTs) at 400–540 °C, very high stable CNTs at 540–750 °C, and the amorphous carbon at the temperature of 300–400 °C. However, the amorphous and lower stable CNTs partly covering the active nickel clusters of catalyst could be hydrogenated or gasified by the methanation process. Two incidences of mass loss are reported by Xu et al. [69]. The peak at approximately ~500 °C is responsible for amorphous carbon oxidation, while the peak at around ~640 °C is responsible for the carbon nanotubes. Consequently, the amorphous form of carbon is generally observed more readily at a lower temperature and lastly converts to the graphite carbon when temperature increases. It is observed that the form of deposited carbon has shown a greater impact in DRM than its existence [70]. DRM activity is supposed to be reduced when the active sites of catalysts are covered by the graphitic layers of carbon [71]. The PXRD and HRTEM studies of the La(TM)O aged form of the catalyst show no signature of crystalline carbon, possibly signifying the amorphous form of the deposited carbon. The TGA analysis shows that the mass losses of the aged catalyst were completed at around 640 °C. This indicates that few carbon nanotubes might also be produced [47, 48]. It is also reasonable to believe that the carbon that forms inside the reaction medium remains discrete from the catalyst particles. **Fig. 5.16** displays a schematic illustration of one possible *in situ* structural transformation that might appear reversible. The initial HEPO La(TM)O (left) decomposed into the corresponding metal oxides inside the DRM atmosphere (right) medium without considerably shifting their primary positions in the lattice of perovskite structure. For the regenerated catalyst, the component oxides can be simply relocated to their original position in HEPO phase owing to their proximity (~atomic dimension). Furthermore, it appears that this structure would help to remove the amorphous carbon readily during the calcination step, giving an unchanged surface of the catalyst. Consequently, catalytic activity remains identical in both the phases. The stable activity behaviour over a long run of 100 h duration also indicates the simultaneous occurrence of Boudouard and reverse Boudouard processes [40]. The first process gives the formation of coke, the second process also occurs instantaneously to remove the coke for smooth running of DRM. In a nutshell, the HEPO La(TM)O catalyst material is likely to form a nanocomposite at the molecular level, consisting of distinct oxide phases corresponding to La(TM)O and a certain proportion of nickel metal.

Based on the aforementioned results, it has been ascribed that the experimentally observed long-term DRM activity is due to the distinct oxide components together with nickel

metal generating a molecular nanocomposite, which are the real operators in the HEPO catalyst. The other oxide components like La_2O_3 [47–50] acts as supports, MnO [51, 52] acts as promoter, Fe_2O_3 [53, 54] and CoO [55, 56] act as oxygen carrier, and CuO [57] acts as promoter. The active species in the DRM process, the resultant Ni^0/NiO nanocomposite, remain vastly dispersed across the surface of the supporting materials. These simple supports are well-defined structures where small active nanocomposite species, formed *in situ* in DRM environment, are homogeneously distributed. The small metal particles assist to inhibit the carbon formation and enhanced activity and stability of the active catalyst. Carbon deposition may be restrained via the reaction with supports to form $La_2O_2CO_3$ *in situ* [57]. This is then decomposed to release CO_2, regenerating pure La_2O_3 support and restoring Ni activity for methane reforming. These *in situ* formed nanocomposites demonstrate reversible thermal switching between the original HEPO and the nanocomposite, which contributes to the high DRM performance of the La(TM)O catalyst material [47. 48].

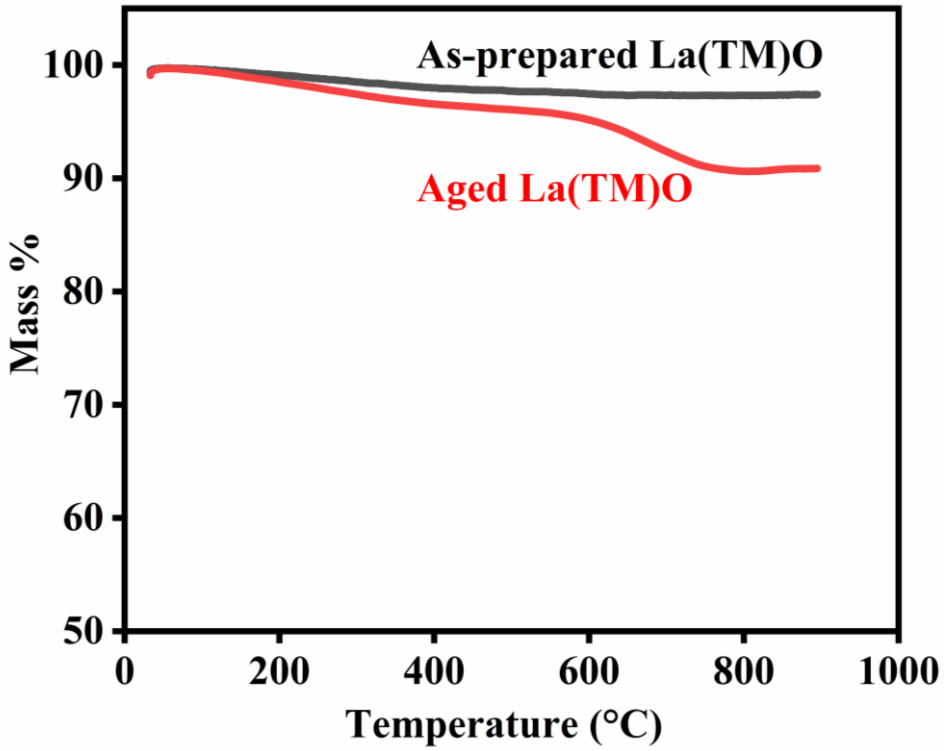

Fig. 5.15: TGA analyses curves of the as-synthesized and used La(TM)O HEPO catalyst.

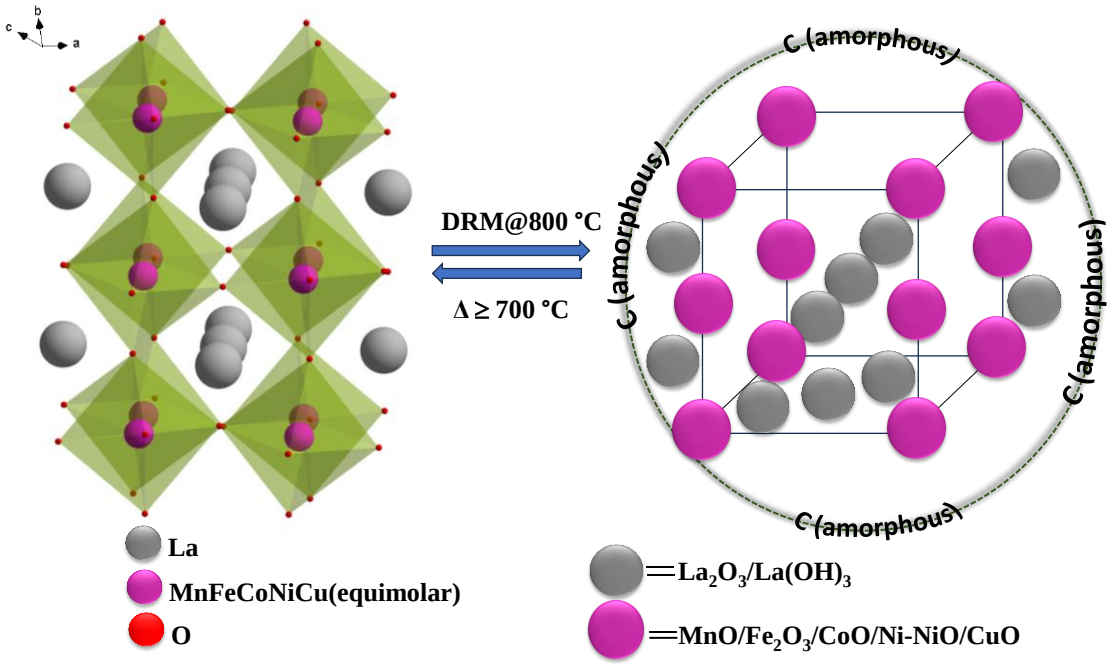

Fig. 5.16: Diagram demonstrating the reversible thermal interchanging (~700 °C) between the original HEPO and nanocomposite at molecular level that is produced *in situ* in DRM atmosphere. Additionally, a schematic illustration of the amorphous coke deposition on the surface of nanocomposite is also given.

5.4. Conclusions

In the present study, the nano-sized $Ln(Mn_{0.2}Fe_{0.2}Co_{0.2}Ni_{0.2}Cu_{0.2})O_3$ (Ln(TM)O) HEPO catalysts have been synthesized using the conventional sol-gel citrate method. The initial DRM tests have suggested $La(Mn_{0.2}Fe_{0.2}Co_{0.2}Ni_{0.2}Cu_{0.2})O_3$ to be the most active catalyst. The disintegration of the active catalyst component in the DRM environment, produced the individual oxides/metals are La_2O_3, $La(OH)_3$, MnO, Fe_2O_3, CoO, Ni, NiO, and CuO. The presence of smaller distinct metal oxides and nickel metal on the surface of the sample is essential for high DRM activity in the reaction medium. These oxides and nickel metal together form a molecular level nanocomposite, which is the real performer in the HEPO system. Even though the original catalyst breaks down into different distinct oxides inside the reaction atmosphere. The lost perovskite phase of the aged catalyst has been regenerated by calcining at 900 °C for 3 h. More intriguingly, the aged catalyst can be regenerated at the lowest calcination temperature of 700 °C. The results of the XPS surface characterisation match with the other information as well. Thus, the HEPO catalyst, $La(Mn_{0.2}Fe_{0.2}Co_{0.2}Ni_{0.2}Cu_{0.2})_3$, has a robust DRM catalytic activity behaviour and has the required potential for commercialization.

Reference

[1] J.W. Yeh, S.K. Chen, J.Y. Gan, S.J. Lin, T.S. Chin, T.T. Shun, C.H. Tsau, S.Y. Chang, Formation of simple crystal structures in Cu-Co-Ni-Cr-Al-Fe-Ti-V alloys with multiprincipal metallic elements, Metall. Mater. Trans. A: Phys. 35A (2004) 2533–2536.

[2] B. Cantor, I.T.H. Chang, P. Knight, A.J.B. Vincent, Microstructural development in equiatomic multicomponent alloys, Mater. Sci. Eng. A. 375-377 (2004) 213–218.

[3] C.M. Rost, E. Sachet, T. Borman, A. Moballegh, E.C. Dickey, D. Hou, J.L. Jones, S. Curtarolo, J.-P. Maria, Entropy-stabilized oxides, Nat. Commun. 6 (2015) 8485.

[4] H. Nan, S. Lv, Z. Xu, Y. Feng, Y. Zhou, M. Liu, T. Wang, X. Liu, X. Hu, H. Tian, Inducing the cocktail effect in yolk-shell high-entropy perovskite oxides using an electronic structural design for improved electrochemical applications, J. Chem. Eng. 452 (2023) 139501.

[5] L. Wang, L. Zhang, X. Lu, F. Wu, X. Sun, H. Zhao, Q. Li, Surprising cocktail effect in high entropy alloys on catalyzing magnesium hydride for solid-state hydrogen storage, J. Chem. Eng. 465 (2023) 142766.

[6] S.S. Aamlid, M. Oudah, J. Rottler, and A.M. Hallas, Understanding the Role of Entropy in High Entropy Oxides, J. Am. Chem. Soc. 145 (2023) 5991−6006.

[7] S. Jiang, T. Hu, J. Gild, N. Zhou, J. Nie, M. Qin, T. Harrington, K. Vecchio, Jian Luo, A new class of high-entropy perovskite oxides, Scr. Mater. 142 (2018) 116–120.

[8] G. Anand, A.P. Wynn, C.M. Handley, C.L. Freeman, Phase stability and distortion in high-entropy oxides, Acta Mater. 146 (2018) 119–125.

[9] B. Cheng, H. Lou, A. Sarkar, Z. Zeng, F. Zhang, X. Chen, L. Tan, K. Glazyrin, H.P. liermann, J. Yan, L. Wang, R. Djenadic, H. Hahn, Q. Zeng, Lattice distortion and stability of $(Co_{0.2}Cu_{0.2}Mg_{0.2}Ni_{0.2}Zn_{0.2})O$ high entropy oxide under high pressure, Mater. Today Adv. 8 (2020) 100102.

[10] C. Zhao, F. Ding, Y. Lu, L. Chen, and Y.S. Hu, High-entropy layered oxide cathodes for sodium-ion batteries, Angew. Chem. Int. Ed. 59 (2020) 264–269.

[11] H. Wang, Y. Cao, W. Liu, Y. Wang, Oxidation behavior of $(Hf_{0.2}Ta_{0.2}Zr_{0.2}Ti_{0.2}Nb_{0.2})C$-xSiC ceramics at high temperature, Ceram. Int. 46 (2020) 11160–1116.

[12] A. Mao, F. Quan, H.Z. Xiang, Z.G. Zhang, K. Kuramoto, A.L. Xia, Facile synthesis and ferrimagnetic property of spinel $(CoCrFeMnNi)_3O_4$ high-entropy oxide nanocrystalline powder, J. Mol. Struct. 1194 (2019) 11–18.

[13] A. Mao, H.Z. Xiang, Z.G. Zhang, K. Kuramoto, H. Yu, S. Ran, Solution combustion synthesis and magnetic property of rock-salt ($Co_{0.2}Cu_{0.2}Mg_{0.2}Ni_{0.2}Zn_{0.2}$)O high-entropy oxide nanocrystalline powder, J. Magn. Magn. Mater. 484 (2019) 245–252.
[14] Z. Liu, S. Xu, T. Li, B. Xie, K. Guo, J. Lu, Microstructure and ferroelectric properties of high-entropy perovskite oxides with A-site disorder, Ceram. Int. 47 (2021) 33039–33046.
[15] J. Ma, K. Chen, C. Li, X. Zhang, L. An, High-entropy stoichiometric perovskite oxides based on valence combinations, Ceram. Int. 47 (2021) 24348–24352.
[16] L. Spiridigliozzi, C. Ferone, R. Cioffi, G.D. Agli, A simple and effective predictor to design novel fluorite-structured High Entropy Oxides (HEOs), Acta Mater. 202 (2021) 181–189.
[17] A. Mao, H.X Xie, H.Z. Xiang, Z.G. Zhang, H. Zhang, S. Ran, A novel six-component spinel-structure high-entropy oxide with ferrimagnetic property, J. Magn. Magn. Mater. 503 (2020) 166594.
[18] H. Zhu, H. Xie, Y. Zhao, S. Dai, M. Li, X. Wang, Structure and magnetic properties of a class of spinel high-entropy oxides, J. Magn. Magn. Mater. 535 (2021) 168063.
[19] Z. Teng, Y. Tan, S. Zeng, Y. Meng, C. Chen, X. Han, H. Zhang, Preparation and phase evolution of high-entropy oxides $A_2B_2O_7$ with multiple elements at A and B sites, J. Eur. Ceram. Soc. 41 (2021) 3614–3620.
[20] A.J. Wright, Q. Wang, C. Hu, Y.T. Yeh, R. Chen, J. Luo, Single-phase duodenary high-entropy fluorite/pyrochlore oxides with an order-disorder transition, Acta Mater. 211 (2021) 116858.
[21] F. Otto, Y. Yang, H. Bei, E.P. George, Relative effects of enthalpy and entropy on the phase stability of equiatomic high-entropy alloys, Acta Mater. 61 (2013) 2628–2638.
[22] Z. Lei, X. Liu, R. Li, H. Wang, Y. Wu, Z. Lu, Ultrastable metal oxide nanotube arrays achieved by entropy-stabilization engineering, Scr. Mater. 146 (2018) 340–343.
[23] C. Wang, W. Liu, M. Liao, J. Weng, J. Shen, Y. Chena and Y. Du, Novel nano spinel-type high-entropy oxide (HEO) catalyst for hydrogen production using ethanol steam reforming, Nanoscale. 15 (2023) 8619–8632.
[24] P. Edalati, Y. Itagoe, H. Ishihara, T. Ishihara, H. Emami, M. Arita, M. Fuji, K. Edalati, Visible-light photocatalytic oxygen production on a high-entropy oxide by multiple-heterojunction introduction, J. Photochem. Photobiol. A: Chem. 433 (2022) 114167.
[25] M. Fracchia, P. Ghigna, T. Pozzi, U.A. Tamburini, V. Colombo, L. Braglia, and P. Torelli, stabilization by configurational entropy of the Cu(II) active site during CO oxidation on $Mg_{0.2}Co_{0.2}Ni_{0.2}Cu_{0.2}Zn_{0.2}O$, J. Phys. Chem. Lett. 11 (2020) 3589−3593.

[26] B. Talluri, M.L. Aparna, N. Sreenivasulu, S.S. Bhattacharya, T. Thomas, High entropy spinel metal oxide $(CoCrFeMnNi)_3O_4$ nanoparticles as a high-performance supercapacitor electrode material, J. Energy Storage. 42 (2021) 103004.

[27] B. Xiao, G. Wu, T. Wang, Z. Wei, Y. Sui, B. Shen, J. Qi, F. Wei, J. Zheng, High-entropy oxides as advanced anode materials for long-life lithium-ion Batteries, Nano Energy. 95 (2022) 106962.

[28] J. Feng, Y. Liu, D. Fang, J. Li, Reusing the steel slag to design a gradient-doped high-entropy oxide for high-performance sodium ion batteries, Nano Energy. 118 (2023) 109030.

[29] A. Mao, H.Z. Xiang, Z.G. Zhang, K. Koji, H. Zhang, Y. Jia, A new class of spinel high-entropy oxides with controllable magnetic properties, Journal of J. Magn. Magn. Mater. 497 (2020) 165884.

[30] X. Li, J. Ma, K. Chen, C. Li, X. Zhang, L. An, Design and investigate the electrical properties of $Pb(Mg_{0.2}Zn_{0.2}Nb_{0.2}Ta_{0.2}W_{0.2})O_3–PbTiO_3$ high-entropy ferroelectric ceramics, Ceram. Int. 48 (2022) 12848–12855.

[31] S.C. Chang, H.Y. Chen, P.H. Chen, J.T. Lee, J.M. Wu, Piezo-photocatalysts based on a ferroelectric high-entropy oxide, Appl. Catal. B: Environ. 324 (2023) 122204.

[32] S. Zhou, Y. Pu, Q. Zhang, R. Shi, X. Guo, W. Wang, J. Ji, T. Wei, T. Ouyang, Microstructure and dielectric properties of high entropy Ba $(Zr_{0.2}Ti_{0.2}Sn_{0.2}Hf_{0.2}Me_{0.2})O_3$ perovskite oxides, Ceram. Int. 46 (2020) 7430–7437.

[33] X. Zhang, J. Zhang, C. Zhou, L. Li, X. Qi, Optical properties and irradiation resistance of novel high-entropy oxide glasses $La_2O_3–TiO_2–Nb_2O_5–WO_3–M_2O_3$ (M=B/Ga/In), J. Rare Earths. 41 (2023) 507–515.

[34] J.J.T.Herrera, S. A. Korili, A. Gil, Recent progress in the application of Ni-based catalysts for the dry reforming of methane, Catal. Rev. Sci. Eng. 65 (2023) 1300–1357.

[35] M.M. Naira, S. Kaliaguinen, Structured catalysts for dry reforming of methane, New J. Chem. 40 (2016) 4049–4060.

[36] L.E.S.Diaz, R. Schlogl, T. Lunkenbein, Quo vadis dry reforming of methane—a review on its chemical, environmental, and industrial prospects. Catalysts. 12 (2022) 465.

[37] J.N. Heo, N. Son, J. Shin, J.Y. Do, M. Kang, Efficient hydrogen production by low-temperature steam reforming of propane using catalysts with very small amounts of Pt loaded on $NiMn_2O_4$ particles, Int. J. Hydrogen Energy. 45 (2020) 20904–20921.

[38] C. Zhang, Y. Li, Z. Chu, Y. Fang, K. Han, Z. He, Analysis of integrated CO_2 capture and utilization via calcium-looping in-situ dry reforming of methane and Fischer-Tropsch for synthetic fuels production, Sep. Purif. Technol. 329 (2024) 125109.

[39] J. Plou, P. Duran, J. Herguido, J.A. Pena, Purified hydrogen from synthetic biogas by joint methane dry reforming and steam-iron process: Behaviour of metallic oxides and coke formation, Fuel. 118 (2014) 100–106.

[40] Y. Shao, C. Wu, S. Xi, P. Tan, X. Wu, S. Saqline, W. Liu, Halite-structured $(MgCoNiMnFe)O_x$ high entropy oxide (HEO) for chemical looping dry reforming of methane, Appl. Catal. B: Environ. 355 (2024) 124191.

[41] Y. Liao, Y. He, X. Cui, L. Liu, Elemental Fe conditioning for the synthesis of highly selective and stable high entropy catalysts for CO_2 methanation, Fuel. 355 (2024) 129494.

[42] S. Shah, M. Xu, X. Pan, K.L.A. Aziz, Complex alloy and heterostructure nanoparticles derived from perovskite oxide precursors for catalytic dry methane reforming, ACS Appl. Nano Mater. 5 (2022) 17476−17481.

[43] S. Zhang, Q. Niu, P. Zhang, An entropy engineering strategy to design sulfur-resistant catalysts for dry reforming of methane, Chem. Eng. J. 482 (2024) 149026.

[44] B.P. Gangwar, P. Tripathi, R. Das, S. Sarkar, A.K. Singh, C.S. Tiwary, S. Sharma, Low-temperature dry reforming using high entropy alloy (Co-Fe-Ga-Ni-Zn)-cerium oxide (CeO_2) hybrid nanostructure, Chem. Eng. J. 495 (2024) 153291.

[45] L. Su, H. Huyan, A. Sarkar, W. Gao, X. Yan, C. Addiego, R. Kruk, H. Hahn, X. Pan, Direct observation of elemental fluctuation and oxygen octahedral distortion-dependent charge distribution in high entropy oxides, Nat. Commun. 13 (2022) 2358-2367.

[46] H. Chen, K. Jie, C.J. Jafta, Z. Yang, S. Yao, M. Liu, Z. Zhang, J. Liu, M. Chi, J. Fua, S. Dai, An ultrastable heterostructured oxide catalyst based on high-entropy materials: A new strategy toward catalyst stabilization via synergistic interfacial interaction, Appl. Catal. B: Environ. 276 (2020) 119155.

[47] A. Hossain, M. Bhattacharjee, K. Ghorai1, J. Llorca, M. Vasundhara, S. Roy, P. Bera, M.M. Seikh, A. Gayen, High activity in dry reforming of methane by thermally switchable double perovskite and in-situ generated molecular level nanocomposite, Phys. Chem. Chem. Phys. 26 (2024) 5447–5465.

[48] A. Hossain, K. Ghorai, T. Bhunia, J. Llorca, M. Vasundhara, P. Bera, A.Bhaskaran, S. Roy, M.M. Seikh, A. Gayen, Cu-doped $LaNiO_3$ perovskite catalyst for DRM: Revisiting it in the light of molecular level nanocomposite, Phys. Chem. Chem. Phys. 26 (2024) 26603–26621.

[49] W.Y. Kim, J.S. Jang, E.C. Ra, K.Y. Kim, E.H. Kim, J.S. Lee, Reduced perovskite $LaNiO_3$ catalysts modified with Co and Mn for low coke formation in dry reforming of methane, Appl. Catal. A, 575 (2019) 198–203,

[50] S. Sun, Y. Zhang, C. Li, Y. Wang, C. Zhang, X. Zhao, H. Sun, C. Wu, Upgrading CO_2 from simulated power plant flue gas via integrated CO_2 capture and dry reforming of methane using Ni-CaO, Sep. Purif. Technol. 308 (2023) 122956.

[51] H. Wang, X Dong, T. Zhao, H. Yu, M. Li, Dry reforming of methane over bimetallic Ni-Co catalyst prepared from $La(Co_xNi_{1-x})_{0.5}Fe_{0.5}O_3$ perovskite precursor: Catalytic activity and coking resistance, Appl. Catal. B. 245 (2019) 302–313.

[52] P. Littlewood, X. Xie, M. Bernicke, A. Thomas, R. Schomacker, $Ni_{0.05}Mn_{0.95}O$ catalysts for the dry reforming of methane, Catal. Today. 242 (2015) 111–118.

[53] S.H. Seok, S.H Han, J.S. Lee, The role of MnO in Ni/MnO-Al_2O_3 catalysts for carbon dioxide reforming of methane, Appl. Catal. A, 215 (2001) 31–38.

[54] Q. Rao, J. Zhang, T. Yang, Y. Li, Z. Gai, P. Li, X. Wang, Y. Pan, H. Jin, A nickel-modified perovskite-supported iron oxide oxygen carrier for chemical looping dry reforming of methane for syngas production, Chem. Eng. J. 485 (2024) 150033.

[55] X. Mao, A.C. Foucher, E.A. Stach, R.J. Gorte, Changes in Ni-NiO equilibrium due to $LaFeO_3$ and the effect on dry reforming of CH_4, J. Catal. 381 (2020) 561–569.

[56] H. Ay, D. Uner, Dry reforming of methane over CeO_2 supported Ni, Co and Ni–Co Catalysts, Appl. Catal. B. 179 (2015) 128–138.

[57] Z. Xie, B. Yan, S. Kattel, J.H. Lee, S. Yao, Q. Wu, N. Rui, E. Gomez, Z. Liu, W. Xu, L. Zhang, J.G. Chen, Dry reforming of methane over CeO_2-supported Pt-Co catalysts with enhanced activity, Appl. Catal. B. 236 (2018) 280–293.

[58] G.R. Moradi, F. Khosravian, M. Rahmanzadeh, effects of partial substitution of Ni by Cu in $LaNiO_3$ perovskite catalyst for dry methane reforming, Chin. J. Catal. 33 (2012) 797–801.

[59] S. Mickevicius, S. Grebinskij, V. Bondarenka, B. Vengalis, K. Sliuzien, B.A. Orlowski, V. Osinniy, W. Drube, Investigation of epitaxial $LaNiO_{3-x}$ thin films by high-energy XPS, J. Alloys Compd. 423 (2006) 107–111.

[60] R. Grissa, H. Martinez, S. Cotte, J. Galipaud, B. Pecquenard, F.L. Cras, Appl. Surf. Sci. 411 (2017) 449–456.

[61] R.V. Lakshmi, P. Bera, M. Hiremath, V. Dubey, A.K Kundu, H.C Barshilia, Structural, magnetic, and dielectric properties of solution combustion synthesized $LaFeO_3$, $LaFe_{0.9}M_{0.1}O_3$, and $LaMnO_3$ perovskites, Phys. Chem. Chem. Phys. 24 (2022) 5462–5478.

[62] T. Baidya, T. Murayama, P. Bera, O.V. Safonova, P. Steiger, N.K. Katiyar, K. Biswas, M. Haruta, Low-Temperature CO Oxidation over combustion made Fe– and Cr–doped Co_3O_4 catalysts: Role of dopant's nature toward achieving superior catalytic activity and stability, J. Phys. Chem. C. 121, 28 (2017) 15256–15265.

[63] T. Baidya, T. Mazumder, K.Y. Koltunov, P.R. Likhar, A.H. Clark, K. Tiwari, V.I. Sobolev, S. Payra, T. Murayama, M. Lin, P. Bera, S. Roy, K. Biswas, O. Safonova, B.S. Rao, M. Haruta, Low-temperature propylene epoxidation activity of $CuO{-}CeO_2$ catalyst with CO + O_2: Role of metal−support interaction on the reducibility and catalytic property of CuO_x Species, J. Phys. Chem. C. 124 (2020) 14131−14146.

[64] S. Maiti, A.K. Kundu, O.I. Lebedev, P. Bera, C Anandan, A. Gayen, M.M. Seikh, Synthesis and magnetic properties of nano-dimensional $Fe_{1-x}Cu_xAl_2O_4$ ($0.3 \leq x \leq 0.8$), RSC Adv. 5 (2015) 83809–83817.

[65] S. Malwadkar, P. Bera, C.V.V. Satyanarayana, Influence of cobalt on performance of $Cu–CeO_2$ catalysts for preferential oxidation of CO, J. Rare Earths. 38 (2020) 941–950.

[66] K. Ghorai, A. Panda, A. Hossain, M. Bhattacharjee, M. Chakraborty, S.K. Bhattacharya, B. Show, A. Sarkar, P. Bera, H. Kim, M.M. Seikh, A. Gayen, $LaNiO_3$/g-C_3N_4 nanocomposite: An efficient Z-scheme photocatalyst for wastewater treatment using direct sunlight, J. Rare Earths. 40 (2022) 725–736.

[67] S.D. Senanayake, D. Stacchiola, P. Liu, C.B. Mullins, J. Hrbek, J.A. Rodriguez, Interaction of CO with OH on Au(111): HCOO, CO_3, and HOCO as key intermediates in the water-gas shift reaction, J. Phys. Chem. 113 (2009) 19536–19544.

[68] W. Donphai, T. Witoon, K. Faungnawakij, M. Chareonpanich, Carbon-structure affecting catalytic carbon dioxide reforming of methane reaction over Ni-carbon composites, J. CO2 Util. 16 (2016) 245–256.

[69] D. Xu, Y. Xiong, S. Zhang, Y. Su, The synergistic mechanism between coke depositions and gas for H_2 production from co-pyrolysis of biomass and plastic wastes via char supported catalyst, J. Waste Manag. 121 (2021) 23–32.

[70] A.J. Carrillo, J.M. Serra, Exploring the stability of Fe–Ni alloy nanoparticles exsolved from double-layered perovskites for dry reforming of methane, Catalysts, 11 (2021) 741.

[71] O.U. Osazuwa, H.D. Setiabudi, R.A. Rasid, C.K. Cheng, Syngas production via methane dry reforming: A novel application of $SmCoO_3$ perovskite catalyst, J. Nat. Gas Sci. Eng. 37 (2017) 435–448.

Chapter 6

Studies on $(Mn_{0.2}Fe_{0.2}Co_{0.2}Ni_{0.2}Cu_{0.2})(TM)_2O_4$ (TM= transition metal) high entropy spinel oxides

Chapter Abstract: *The study focuses on synthesizing a series of high entropy spinel oxides (HESOs) is to investigate their potential role for catalysis in the dry reforming of methane (DRM) reaction. $(Mn_{0.2}Fe_{0.2}Co_{0.2}Ni_{0.2}Cu_{0.2})Al_2O_4$ has demonstrated high catalytic activity, converting 97% of CH_4 and 99% of CO_2 during 100 h DRM process with H_2/CO~1. The initial spinel phase has broken down in the reaction medium and then regenerated itself from the degraded phases by annealing nearly at synthesis temperatures. That is an intriguing observation, since it does not alter the DRM activity. PXRD, BET surface area, XPS, FESEM, TEM, HRTEM, and TGA techniques are used to characterize the samples.*

6.1. Introduction

High entropy alloys (HEAs) were first introduced by Yeh et al. [1] and Cantor et al. [2] in 2004. Since then, a lot of attention has gathered on HEAs due to their numerous potentials uses in various fields. Rost et al. developed a new class of materials (Mg, Co, Ni, Cu, Zn)O in 2015, called high-entropy oxides (HEOs), also referred as entropy stabilised oxides [3]. After this pivotal publication describing the finding of five components containing rock salt structure (Mg, Co, Ni, Cu, Zn)O in a single phase was reported to be stabilised by entropy. Thus, the new area of HEOs is developing quickly and has great potential across many fields. The four main stabilizing factors of HEOs are high entropy, lattice distortion, delayed diffusion, and cocktail effect [4, 5]. First, the high entropy effect maintains HEO's phase stability at high temperatures. Five or more main cations are unevenly distributed across the crystal matrix in the HEO crystal structure. The entropy of mixing related to the development of HEOs may be estimated from the Gibbs-Helmholtz equation (**eq. 5.1**). Initially, high temperatures facilitate the mixing of entropy (ΔS_{mix}), which makes (ΔG_{mix}) lower. This higher negative value of the (ΔG_{mix}) helps in forming highly stable HEO [6, 7] materials. Second, for the lattice distortion effect, the defects are easily appeared in HEOs. Dissimilar main metal cations have different radii, which facilitates lattice distortion that helps the creation of oxygen vacancies in the lattice [8, 9]. Additionally, due to the delayed diffusion effect, HEOs have improved chemical stability [10, 11]. It also prevents undesirable outcomes from happening during this process, such as grain coarsening and recrystallisation. Finally, the cocktail effect enables HEOs to perform a variety of catalytic activities. As HEOs are formed by a variety of metal cations, the roles of

the cations may vary or be parallel based on their radius [12]. There have been reports of several types of HEO systems based on the features, such as rock salt oxides [8, 13], perovskite oxides [14, 15], fluorite oxides [16], spinel oxides [17, 18], pyrochlore oxides [19, 20]. HEOs are extensively used in various fields, such as water splitting reactions [21], thermal conductivity [22], oxygen production [23], hydrogen production [24], catalytic CO oxidation [25], electrochemical capacitors [26], sodium-ion battery [27], lithium-ion battery [28], electrical properties [29], magnetic properties [30], dielectric properties [31], piezoelectric properties [32], optical properties [33], etc. The HEOs catalysts have a few distinct configurations that could facilitate DRM.

Fossil fuel is currently the primary energy source that satisfies our everyday energy needs. However, pollution resulting from the use of fossil fuels in a variety of activities brought about by civilisation is one of the major threats to modern life. Fossil fuel combustion releases greenhouse gases (GHGs), primarily CH_4 and CO_2, which progressively increase global temperatures. According to several reports, hydrogen energy is one of the most promising alternatives to fossil fuels. H_2 fuel is considered as an environmentally beneficial fuel source because of its high energy content and minimal environmental impact. Many photocatalytic or catalytic processes, such as the partial oxidation of methane (POM), electrochemical, and photochemical reactions, as well as the steam and dry reforming of methane (SRM and DRM), are used in conventional H_2 production. The DRM reaction is regarded as one of the most promising processes for the production of H_2, as it can produce a significant amount of H_2 at a low cost, has long-term stability, and requires just basic synthetic procedures to prepare the catalysts. Additionally, one of the major advantages of the DRM reaction is the fruitful formation of syngas (H_2 + CO) by consuming two greenhouse gases (CH_4 and CO_2). However, the other methods like electrochemical water splitting or photocatalytic H_2 production are not viable because of their low yield, which barely satisfies the present demand for H_2 energy. The requirement for costly materials (Pt, Pd, Ir, Ru, etc.), and the multistep for catalyst synthesis. Thus, DRM has gathered significant interest from researchers in recent times because of its many potential applications in the chemical industry [34–36] and environmental aspects [37, 38]. Syngas has many industrial applications, such as production of diesel via the Fischer-Tropsch synthesis [39], hydrogen production [40–42], preparation of methanol [34], reduction of iron ore to sponge iron [43], etc. A few drawbacks of the DRM method are catalyst instability and coke deposition, which quickly deactivates the active sites in the reaction atmosphere. The reactions related to DRM are discussed in **Chapter 1** (**Sec.1.1**). Thus, the main sources of

coking are reactions (**eq. 1.3**) and (**eq. 1.4**). Thus, extensive research is needed to synthesize suitable catalysts with high coking resistance, good durability, and significant DRM activity. The literature survey shows that in the DRM reaction, transition metal nickel and noble metal catalysts such as Ru, Rh, and Pt have revealed high catalytic activity and low carbon deposition. Noble metal catalysts are ineffective in DRM due to their expensive cost and limited availability. It is important to note that the HEO catalysts possess characteristic structures that could enhance the DRM activity. Shao et al. have synthesized $(MgCoNiMnFe)O_x/ZrO_2$ HEO catalyst [44] and deployed it for DRM reaction for 100 h. Methane conversion of the catalyst has been found to 43%. In their report, Liao et al. have demonstrated the DRM activity of $Fe_xNi_2CrCoMn_{0.55}O_y$ HEO catalyst [45]. 98% CH_4 conversion and 72% CO_2 conversion have been demonstrated by the catalyst. The DRM activity of $LaFe_{0.7}Ni_{0.1}Co_{0.1}Cu_{0.05}Pd_{0.05}O_3$ HEO have been explored by Shah et al. [46]. The DRM activity of the catalyst was found to be observed ~64%, and ~68% CH_4 and CO_2 conversion, respectively, and H_2/CO ratio ~0.8 for 24 h reaction. Zhang et al. investigated the DRM catalytic activity of the spinel type HEO $(Ni_3MoCoZn)Al_{15}O_x$ [47]. Throughout the course of the 100 h DRM, the catalyst has shown high activity, converting 92% to 97% of CH_4 and 98% of CO_2, with the H_2/CO ratio ranging from 0.94 to 0.98. The role of the HEO $CoFeGaNiZn/CeO_2$ catalyst in the DRM process has been investigated by Gangwar et al. [48]. For 30 h of DRM reaction, they have observed that the methane and carbon dioxide conversions were 98% and 86% respectively, with H_2/CO ratio1.3. In a report, Su et al. have shown there is substantial lattice distortion in La-based $La(Cr_{0.2}Mn_{0.2}Fe_{0.2}Co_{0.2}Ni_{0.2})O_3$ [49] HEOs. The possibility of oxygen vacancies increased as the lattice distortion increased with the number of the component elements. Moreover, intriguing catalysis often takes place at the interface between two distinct compounds. The $(NiMgCuZnCo)O/CeO_x$ catalyst have synthesized by the combination of a common oxide with HEO by Chen et al. [50], and investigated the role of the catalyst for CO oxidation. The heterostructure boundary formed by the two different oxides increases the catalytic activity and stability of the catalyst.

In the backdrop of aforementioned reports, it would be beneficial to investigate the HESO systems MM'_2O_4, where M= equimolar proportions of Mn, Fe, Co, Ni and Cu while M′= Al, Cr, Mn, Fe and Co, i.e., $(Mn_{0.2}Fe_{0.2}Co_{0.2}Ni_{0.2}Cu_{0.2})M'_2O_4$ as potential catalyst materials for DRM reaction. The phase pure $(Mn_{0.2}Fe_{0.2}Co_{0.2}Ni_{0.2}Cu_{0.2})Al_2O_4$ is shown to be the most active catalyst that exhibits maximum DRM activity of 97% CH_4 conversion, and 99% CO_2 conversion, maintaining full activity for 100 h. After the 100 h DRM, the XRD analysis of the

aged sample has been carried out and it was observed that the primary HESO phase has completely broken down. This result helps to consider that the *in situ* fragmented phases formed a molecular level nanocomposite where the constituent ions displace very little from the lattice sites of individual spinel structures. The regeneration of the original spinel phase can be done following a thermal treatment of the nanocomposite at a temperature lower than that of the synthesis temperature while maintaining complete catalytic activity. It is possible to go back and forth between them the two forms of the catalyst, while retaining the catalytic performance of pristine HESO and *in situ* generated nanocomposites. This finding opens a scope of possibility for more research and better comprehension of the structure-property relationship for this promising $(Mn_{0.2}Fe_{0.2}Co_{0.2}Ni_{0.2}Cu_{0.2})Al_2O_4$ HESO catalyst.

6.2. Experimental details

Chapter 2 **(Sec. 2.3.1.1.)** discusses details of catalyst synthesis as well as the experimental techniques used for characterization and tests of reforming activity.

6.3. Results and discussion

6.3.1. PXRD analyses of the as-synthesized HESOs

Fig. 6.1. shows the PXRD patterns of the HESO MM'_2O_4 $(Mn_{0.2}Fe_{0.2}Co_{0.2}Ni_{0.2}Cu_{0.2})M'_2O_4$ ((where M = equimolar Mn, Fe, Co, Ni and Cu) and M′ = Al, Cr, Mn, Fe and Co)) materials. Diffraction patterns show that the samples are well-crystalline. Diffraction peaks are observed to appear at 2θ values of 18.8°, 30.9°, 36.8°, 44.5°, 55.4°, 59.1°, 65.0°, and 77.6°, which correspond to the lattice planes are (111), (220), (311), (400), (422), (511), (440), and (533), respectively. The PXRD patterns indicate that the HEO spinel MM'_2O_4 system forms cubic phase. The XRD data of MM'_2O_4 matches well with the JCPDS PDF # 34-0192. The Scherrer sizes obtained from the full-width-at-half-maximum (FWHM) of the most intense diffraction peak of the HESO of MAlO, MCrO, MMnO, MFeO, and MCoO materials are about 20, 21, 24, 50, and 41 nm, respectively. For MAlO, MCrO, MMnO, and MFeO pure phases are obtained. But for MCoO, small peaks associated with α-Al_2O_3 (*) appears at 2θ values of 25.2° and 41.6°. The as-prepared MAlO catalyst material exhibits no characteristic peaks related to any other impurities, confirming the phase purity of the samples.

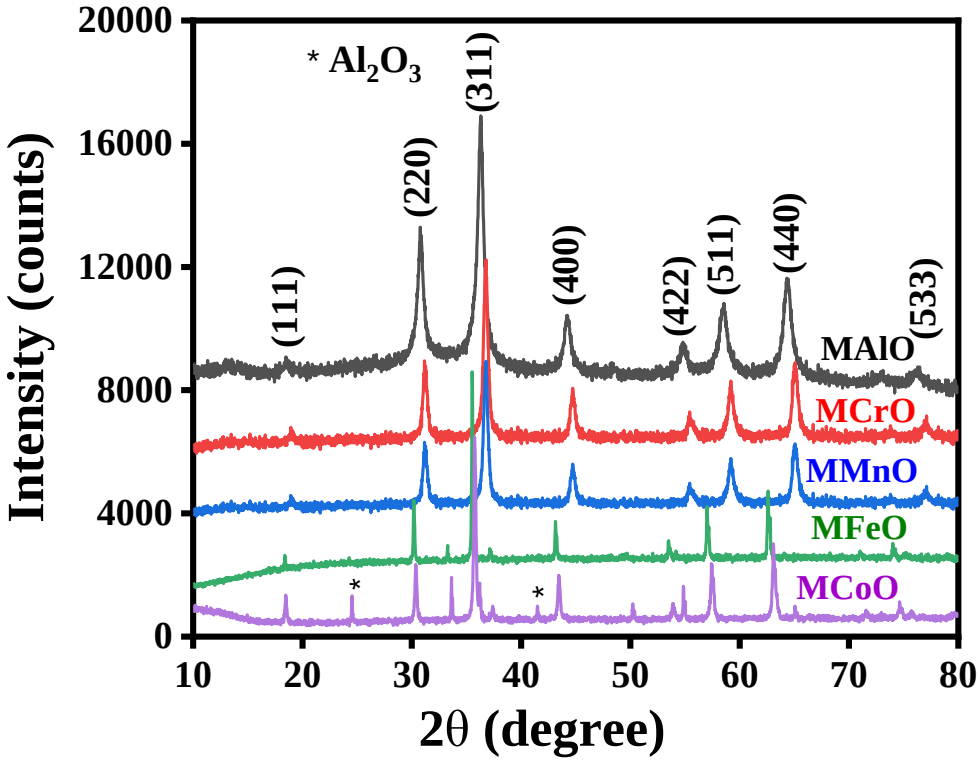

Fig. 6.1: PXRD patterns of as-prepared MAlO, MCrO, MMnO, MFeO, and MCoO HESO materials.

6.3.2. Screening of materials for DRM activity

In order to find out the most active catalyst from the as-prepared samples DRM, an initial activity test of the as-prepared HESOs was carried out for 10 h. The catalytic activities. The CH_4 conversions, CO_2 conversions, and ratio of H_2/CO of HESOs are shown in **Fig. 6.2** in a comparable summary. **Fig. 6.2(a–c)** display the CH_4 conversions, CO_2 conversions, and ratio of H_2/CO of all the as-prepared HESOs materials. The methane conversions of the HESOs are MAlO, MCrO, MMnO, MFeO, and MCoO are 97%, 84%, 52%, 36%, and 85%, respectively. In contrast, the CO_2 conversions of the HESOs samples are 99%, 90%, 60%, 44%, and 90%, respectively. The H_2/CO ratio of all the HESOs varies from 0.97 to 1.5. The variation of H_2/CO ratio of as-prepared samples is because of some side reactions which are thermodynamically possible at that temperature. **Fig. 6.2(a–c)**. show that the $(Mn_{0.2}Fe_{0.2}Co_{0.2}Ni_{0.2}Cu_{0.2})Al_2O_4$ (MAlO) catalyst has shown the highest catalytic activity amongst the as-prepared samples.

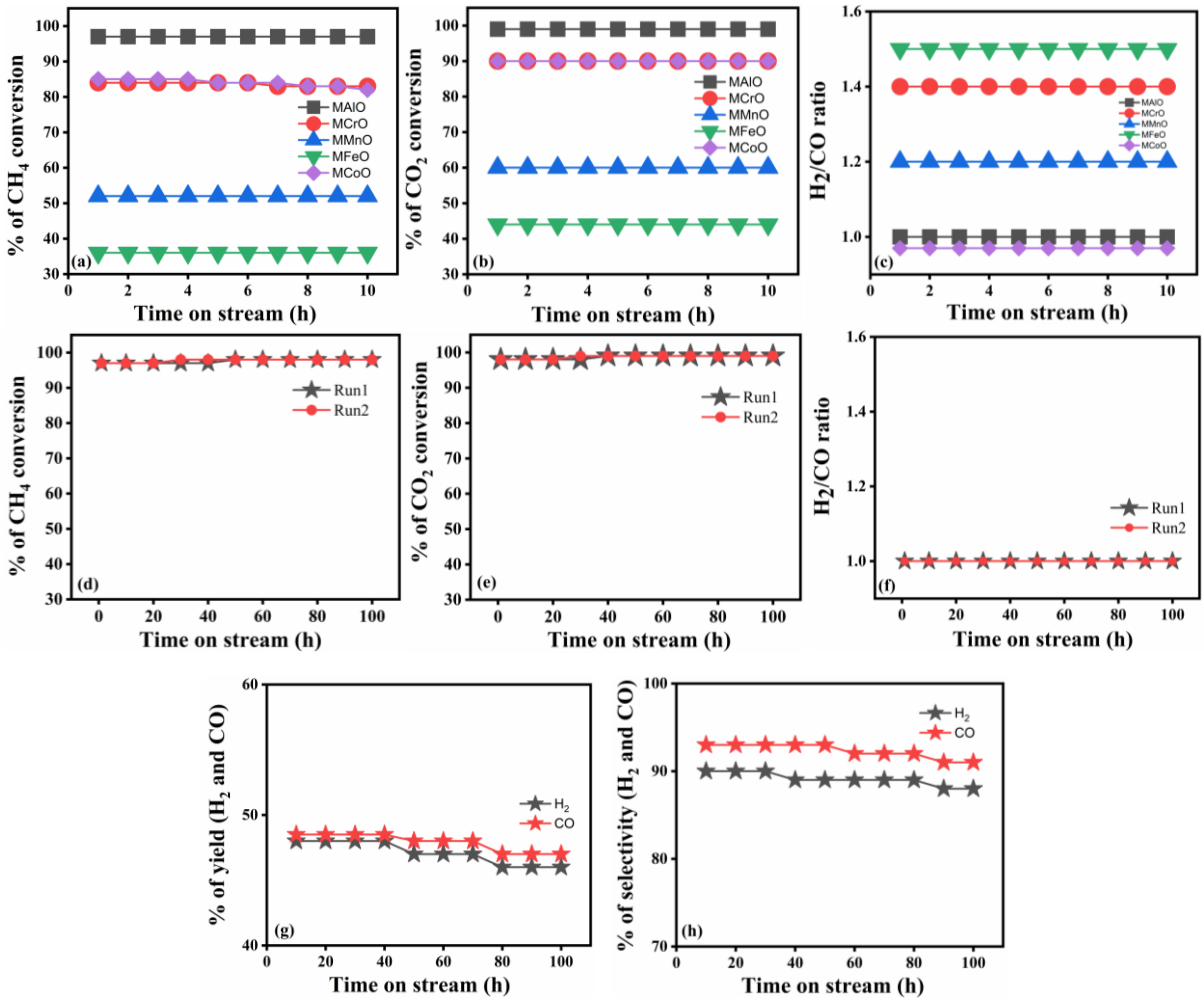

Fig. 6.2: DRM activity of HESO catalysts MAlO, MCrO, MMnO, MFeO, and MCoO for 10 h (upper row) and for the most active MAlO catalyst for 100 h (middle row): at GHSV of 34000 mL g_{cat}^{-1} h^{-1} and reaction temperature of 800 °C (a, d) methane conversion, (b, e) carbon dioxide conversion and (c, f) ratio of H_2/CO, (g, h) H_2 and CO yield and selectivity (lower row).

Based on these primary screening data, a continuous 100 h DRM reaction was carried out using MAlO as catalyst in order to put additional light on this HESO catalyst. This activity outcome helped us to find out the catalytic activity as well as the durability of this HESO catalyst. The activity data of the MAlO catalyst during a 100 h DRM reaction are displayed in **Fig. 6.2(d–f).** To ensure that the results are repeatable, the data from a second catalytic run is also included in the figure. From the graph, it is found that MAlO shows 97% CH_4 conversion, 99% CO_2 conversion, and the H_2/CO ratio ~1 for 100 h of DRM. For the other materials, the H_2/CO ratio varies from 0.9 to 1.5. The H_2/CO ratio lower than unity for MCoO (0.97) suggests the occurrence of the reverse water gas shift reaction (RWGS) which involves the reaction of

CO_2 with the hydrogen produced in the DRM reaction. The H_2/CO ratio is more than unity indicates the existence of the Boudouard reaction, where CO is disintegrated into carbon and carbon dioxide. The H_2/CO ratio becomes relatively higher than unity for MCrO (1.4), MMnO (1.2), and MFeO (1.5). Following a continuous 100 h reaction, the catalyst bed was cooled to ambient temperature in a helium atmosphere. The aged catalyst has been regenerated *ex situ* simply by calcination at synthesis temperature and air-quenched to obtain the expected HESO materials. To comprehend the structure-activity correlation, the aged and regenerated forms of the catalyst has subsequently been thoroughly characterised and compared with the as-prepared catalyst.

Table 6.1: DRM activity of as-prepared catalysts for 10 h.

Catalyst	**CH_4 conversion (%)**	**CO_2 conversion (%)**	**H_2/CO ratio**
MAlO	97	99	1
MCrO	84	90	1.4
MMnO	52	60	1.2
MFeO	36	44	1.5
MCoO	85	90	0.97

The apparent activation energies of the reforming reaction for different forms of MAlO catalyst were calculated and compared with their catalytic performance. For the kinetic analysis, the same fixed-bed flow reactor was loaded with 30 mg of MAlO catalyst that was mixed with 70 mg of purified silica of the same mesh size (85−100) keeping rest of the experimental conditions constant. The temperature range was 400–460 °C to ensure that all the conversion values remained below 20%. The Arrhenius plots for different MAlO catalysts are shown in **Fig. 6.3.** The apparent activation energies derived from the slopes of these Arrhenius plots for H_2 formation rates within the specified temperature range, were 108.88 kJ mol^{-1} for the as-prepared MAlO, 85.71 kJ mol^{-1} for the aged MAlO, and 103.09 kJ mol^{-1} for the regenerated MAlO catalyst (see **Fig. 6.3(a)**). In contrast, the activation energies for CO production were generally lower than those for H_2 production, with the energies of 84.88 kJ mol^{-1} for the as-prepared MAlO, 59.08 kJ mol^{-1} for the aged MAlO, and 73.16 kJ mol^{-1} for the regenerated MAlO (see **Fig. 6.3(b)**). It is thus evident that the as-prepared MAlO catalyst

requires the highest activation energies for both H_2 (108.88 kJ mol^{-1}) and CO (84.88 kJ mol^{-1}) formation, while the aged MAlO catalyst has the lowest activation energy values, 85.71 kJ mol^{-1} for H_2 and 59.08 kJ mol^{-1} for CO production. This indicates that the MAlO catalyst is in the most activated form on being aged. Although the regenerated catalyst has comparatively higher activation energy than the aged one, its values are still lower than those of the as-prepared MAlO catalyst. So, the activity of the regenerated catalyst remains in between the as-prepared and aged forms of the catalyst. These outcomes of apparent activation energies are in good agreement with the DRM activity.

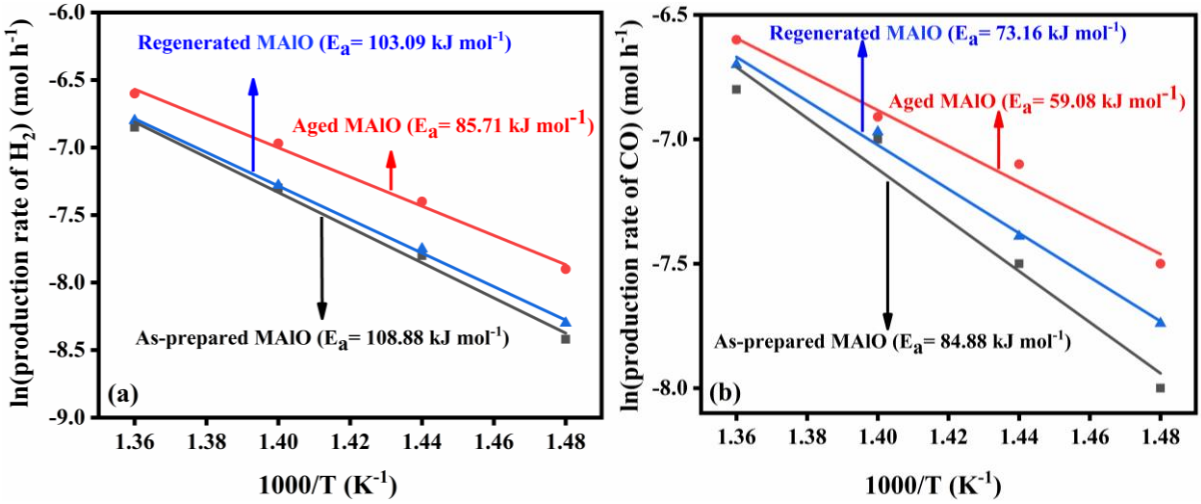

Fig. 6.3: Arrhenius plots for the production of (a) H_2 and (b) CO for different forms of MAlO catalyst at GHSV of 113400 mL g_{cat}^{-1} h^{-1}).

6.3.3. PXRD analyses of different forms of MAlO catalyst: Relationship with DRM activity

The powder XRD patterns of all forms of the MAlO catalyst are displayed in **Fig. 6.4**. It is evident that the pristine spinel phase is entirely suppressed in the aged sample along with the appearance of some new diffraction peaks. These newly formed peaks, which are attributed to the simple individual oxide phases and metallic nickel in **Fig. 6.4**. It should be mentioned that the same structural changes are observed after 10 h of reaction (powder XRD patterns not shown here). Several reports have confirmed that the active catalyst is typically degraded into its component oxide phases in the reaction atmosphere [23, 42, 44, 51, 52], losing its original phase in the reaction environment. The decomposed components have been recognized as α-Al_2O_3 (*) of the peaks at 2θ values of 26.2°, 43.6°, 56.1° and 65.8°, CuO (Φ) at 2θ values of 36.5°, and 73.9°, MnO (◊) at 2θ values 41.8° and 55.9°, MnO_2 (▪) at 2θ values 37.3°, CoO (ɤ)

at 2θ values 42.4°, 60.1° and 73.3°, Fe_2O_3 (α) at 2θ values 54.2° and 64.1°, NiO (•) at 2θ values of 31.9°, 43.2°, and 51.5° and metallic nickel at 2θ value of 44.3° and 51.5°. These fragmented components closely match with JCPDS PDF # 897717 for α-Al_2O_3, 751090 for MnO, 440141 for MnO_2, 898104 for Fe_2O_3, 780431 for CoO, 897128 for Ni, 140481 for NiO, and 782076 for CuO. The interesting fact of this MAlO catalyst is that the catalyst's original spinel phase is degraded during DRM reaction (as in the aged form of the catalyst), but the original spinel phase can be regenerated fully from the degraded component phases by annealing at synthesis temperature in static air for 3 h (see **Fig. 6.4**). The as-synthesized, aged, and regenerated forms of MAlO spinel catalyst have Scherer sizes of 20, 13, and 28 nm, respectively. Enlarged specific surface area values of the aged form (from 51 to 77 $m^2\ g^{-1}$ on ageing) from BET specific surface area analysis is thus consistent with the size of aged catalyst in the DRM environment due to reduction of the parent oxide phase of the catalyst.

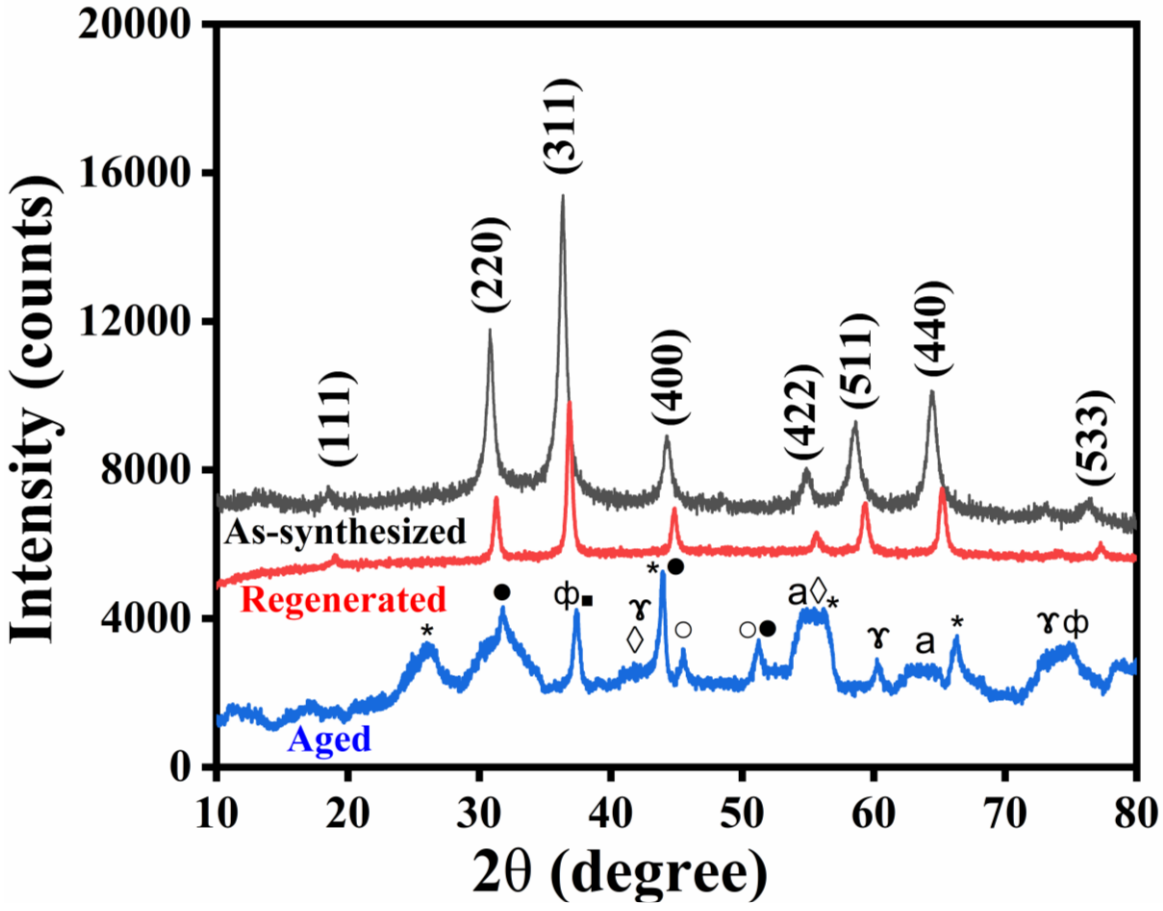

Fig. 6.4: PXRD patterns of different forms MAlO spinel catalyst.

To determine the structural features of the as-prepared and regenerated MAlO catalysts, structural refinement was done to the powder XRD patterns of both the phases (see **Fig. 6.5**).

FullProf Suite software has been used to refine the XRD patterns. The cubic group is needed in order to appropriately index the phase patterns during the analyses, both as-prepared and regenerated. The catalysts' phase purity is confirmed by the absence of any impurity signature in the refined powder XRD patterns. The refinement results reveal the complete regeneration of the aged form of the catalyst. **Table 6.2** provides the structural and refinement parameters for both the phases. It is found to be observed that the peak intensity in the diffraction pattern of the regenerated phase is not as strong as those in the pristine phase because less amount of sample could be used for PXRD diffraction analysis of the regenerated form. This result supports the structural similarity of as-prepared and regenerated forms of MAlO catalyst as observed in our earlier report [51, 52].

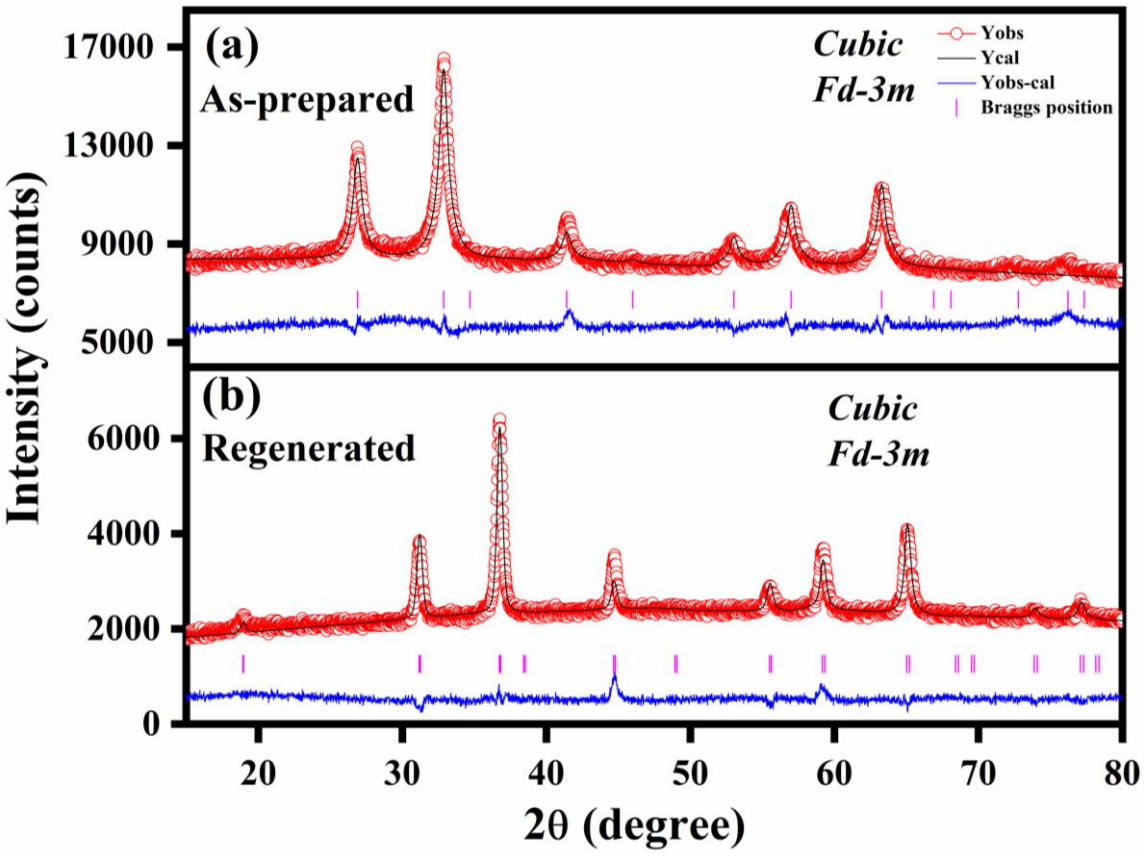

Fig. 6.5: Rietveld refinement of PXRD patterns of the (a) as-synthesized and (b) regenerated MAlO catalysts. The experimental patterns, calculated patterns, difference curves, and Bragg position are represented by the red circles, black lines, bottom blue lines, and vertical magenta bars, respectively.

Table 6.2: Rietveld refinement parameters of the MAlO ($Mn_{0.2}Fe_{0.2}Co_{0.2}Ni_{0.2}Cu_{0.2})Al_2O_4$ spinel catalyst material of as-prepared and regenerated phases.

Composition	**Cell parameter**	**Bond length (Å)**	**Bond angle (°)**	**Atom**	**Wyckoff position**	**Atomic coordinates**		
MAlO As-prepared Cubic (F*d–3m*)	a= 8.157(2) Å V= 542.90 (2) Å^3 R_{Bragg}= 4.27 % R_f= 3.72 % χ^2 = 2.70	M_t—O bond length: 1.885(4) M_o—O bond length: 1.975(5)	<M_t—O—M_o: 122.5°(3)			x	y	z
				Mn	8a	0.12500	0.12500	0.12500
				Fe	8a	0.12500	0.12500	0.12500
				Co	8a	0.12500	0.12500	0.12500
				Ni	8a	0.12500	0.12500	0.12500
				Cu	8a	0.12500	0.12500	0.12500
				Al	8a	0.12500	0.12500	0.12500
				Fe	16d	0.50000	0.50000	0.50000
				Al	16d	0.50000	0.50000	0.50000
				O	32e	0.25830	0.25830	0.25830
MAlO Regenerated Cubic (F*d–3m*)	a= 8.106(4) Å V= 532.68 (3) Å^3 R_{Bragg}= 12.3 % R_f= 10.5 % χ^2 = 2.16	M_t—O bond length: 1.918(7) M_o—O bond length: 1.936(6)	<M_t—O—M_o: 121.28°(4)			x	y	z
				Mn	8a	0.12500	0.12500	0.12500
				Fe	8a	0.12500	0.12500	0.12500
				Co	8a	0.12500	0.12500	0.12500
				Ni	8a	0.12500	0.12500	0.12500
				Cu	8a	0.12500	0.12500	0.12500
				Al	8a	0.12500	0.12500	0.12500
				Fe	16d	0.50000	0.50000	0.50000
				Al	16d	0.50000	0.50000	0.50000
				O	32e	0.26171	0.26171	0.26171

Regeneration of the aged catalyst has also been done *in situ* for further confirmation that the DRM activity does not alter upon regeneration of the catalyst. First, the catalytic activity of the as-prepared MAlO catalyst has been checked for 10 h at 800 °C with similar reaction conditions. After the reaction was stopped, the gas lines were cleaned for 30 minute

using helium gas. The catalyst was then regenerated at 900 °C for 3 h (the synthesis temperature being more important here) for 3 h with zero air flow followed by degassing in helium flow and subsequently a DRM activity test was conducted on the regenerated MAlO catalyst. The activity data of the as-synthesized and regenerated forms of MAlO catalyst are displayed in **Fig. 6.6**, which indicates that about all the catalytic activity is retained when the catalyst is regenerated. The as-prepared catalyst's H_2/CO ratio is nearly unity, which suggests that side reactions are occurring at a lower extent. The ratio of H_2/CO is greater than unity as a result of the Boudouard reaction. In contrast, RWGS causes the H_2/CO ratio to be less than unity when CO_2 combines with the hydrogen that is formed in DRM. The H_2/CO value ~1 indicates that both the side reactions are taking place to a lower extent **(see Fig. 6.6)**.

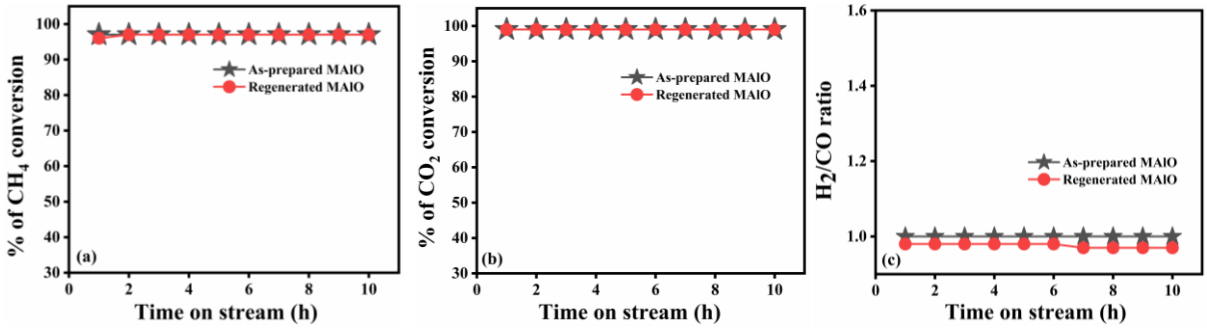

Fig. 6.6: (a) Methane conversion, (b) carbon dioxide conversion, and (c) ratio of H_2/CO of as-synthesized and *in situ* regenerated MAlO spinel catalyst material for 10 h of DRM reaction (under similar reaction condition).

Thus, the real performer in the reported DRM activity in the chosen reaction conditions is therefore the HESO catalyst system constituted by a nanocomposite of discrete oxides and nickel metal corresponding to the pristine spinel phase at the molecular level. As the original HESO catalyst is aged, it has been broken down into distinct metal oxides and metallic nickel. The "molecular level nanocomposite" in the reaction medium is made up of these fragmented phases. We suggest that a "molecular level nanocomposite" formed by metallic nickel and nickel oxides is primarily responsible for the observed high DRM activity. This nanocomposite is the actual performer in the HESO catalyst for enhanced DRM catalytic activity under the chosen reaction conditions. On the other hand, other metal oxides in the reaction atmosphere, such as α-Al_2O_3 acts as support [41, 53–56], MnO as promoter [51, 57, 58], MnO_2 as support [38, 57, 58], Fe_2O_3 and CoO act as oxygen carrier [59–62], and CuO also acts as promoter [52, 63]. The decomposition-regeneration procedure is reversible as the aged

phase of the catalyst can be restored to its pure spinel phase. The reforming environment facilitated the first step, whereas the calcination procedure facilitated the second.

6.3.4. BET specific surface area measurement

Fig. 6.7 displays the specific surface area (S_{BET}) nitrogen adsorption-desorption isotherms of as-prepared $(Mn_{0.2}Fe_{0.2}Co_{0.2}Ni_{0.2}Cu_{0.2})M'_2O_4$ (where M′ = Al, Cr, Mn, Fe and Co) (MAlO, MCrO, MMnO, MCoO, aged MAlO, and MAlO) materials and their corresponding pore size distribution curves are in the inset. The surface area, pore volume, and pore size distribution of the particular catalysts are shown in **Table 6.3**. A Type IV isotherm with an H3 type hysteresis loop is formed and the volume of N_2 gas adsorption is lower at low relative pressure and gradually rises at high P/P_0 (ranges from 0 to 1) values. The specific surface areas (S_{BET}) of different types of catalysts MAlO, MCrO, MMnO, MCoO, aged MAlO and regenerated MAlO, are approximately 52, 26, 44, 23, 77, and 61 $m^2\ g^{-1}$, respectively. Among all the as-prepared catalysts, the MAlO sample has the highest BET surface area, which impacts its long-term activity behaviour. In the case of aged MAlO catalyst, the specific surface area is increased from 52 $m^2\ g^{-1}$ to 77 $m^2\ g^{-1}$ [51, 52]. Further, XRD analyses have revealed that the breakdown of catalyst into its constituent oxide components is responsible for this. The catalyst's particle size was confirmed to have decreased from 20 nm to ~13 nm by XRD, XPS and HRTEM studies. The aged HESO MAlO catalyst's smaller size and larger surface area are in good agreement with its high DRM activity and long-term durability. The regenerated catalyst has surface area of 61 $m^2\ g^{-1}$ and the particle size of 28 nm. In addition, the surface area of the regenerated MAlO catalyst is greater than that of the pristine catalyst, which helps to explain its comparable DRM activity (**Fig. 6.6**). In comparison to the pristine catalyst, the surface area of the aged and regenerated forms is higher. These findings nicely support the high DRM activity of the aged and the regenerated forms of MAlO catalyst.

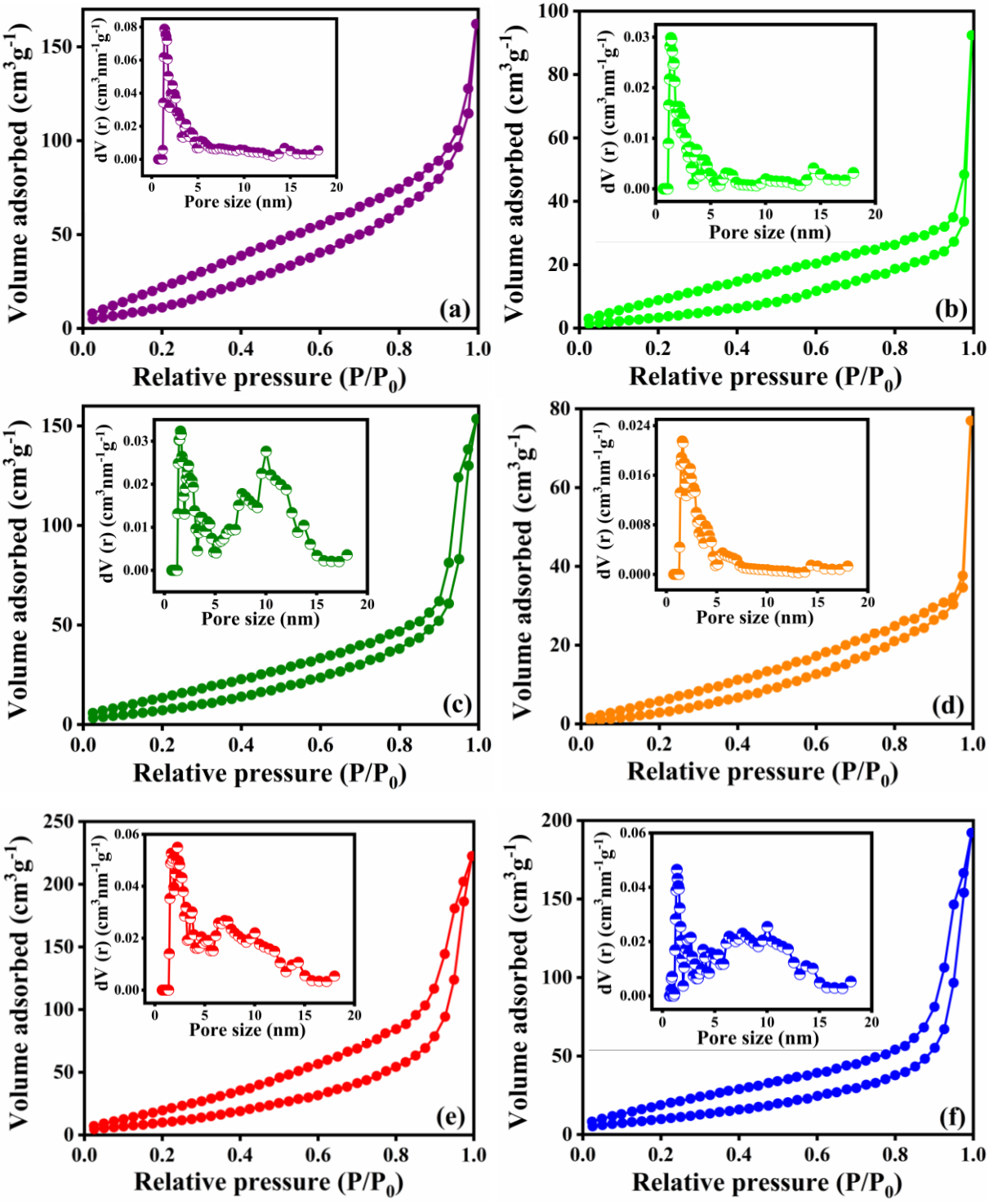

Fig. 6.7: N_2 adsorption-desorption curves and porosity (inset) of (a) MAlO, (b) MCrO, (c) MMnO, (d) MCoO, (e) aged MAlO and (f) regenerated MAlO spinel catalyst.

Table 6.3: Textural features of different MAlO, MCrO, MMnO, MCoO, aged MAlO and regenerated MAlO materials.

Catalyst	Specific surface area (m^2 g^{-1})	Pore volume (cm^3 g^{-1})	Pore size (nm)
MAlO	52	0.237	1.38
MCrO	26	0.216	1.38
MMnO	44	0.202	1.58
MCoO	23	0.161	1.58
Aged MAlO	77	0.290	1.18
Regenerated MAlO	61	0.258	1.29

6.3.5. Morphology studies

The surface morphology and elemental content of the as-synthesized and aged form of the catalysts have been assessed using FESEM microscopic study. The as-prepared MAlO spinel catalyst is shown to exist as a consistently dispersed spherical shape along with some irregularly shaped nanoparticles as shown in **Fig. 6.8(a)**. The aged catalyst's morphology has been changed to a highly aggregated semi-spherical or irregular shape as shown in **Fig. 6.8(c)**. This is because the catalyst has been fragmented in DRM environment and due to presence of small amount of carbon. The EDX of the as-prepared and aged form of the MAlO spinel catalysts is presented in **Fig. 6.8(b, d)**, which indicates that the elements Al, Mn, Fe, Co, Ni, Cu, and O are present in the samples. The MAlO spinel catalyst's surface is smooth and transparent in the as-prepared sample, but its surface smoothness diminishes and becomes rough in aged form, most likely as a result of the catalyst breaking down into its component oxides.

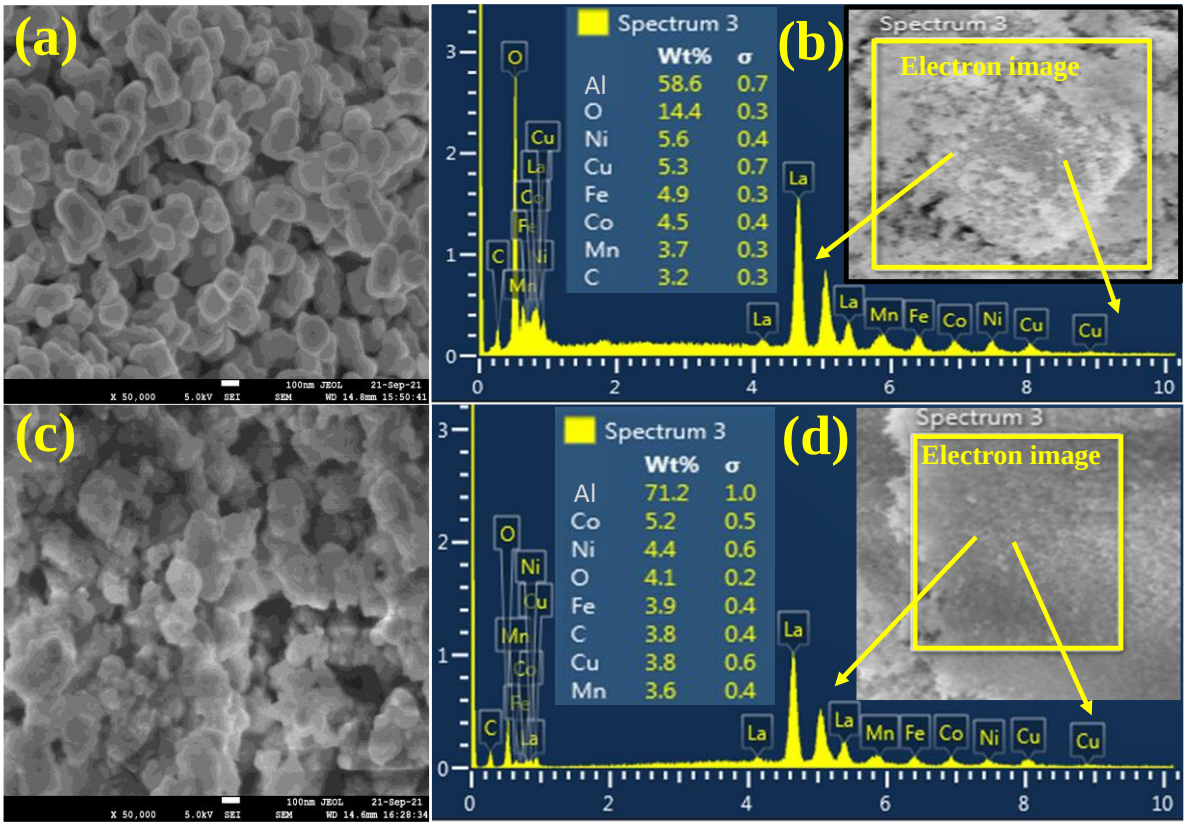

Fig. 6.8: FESEM images (a, c), and (b, d) EDX spectra of as-prepared and aged MAlO spinel catalyst, respectively.

6.3.6. HRTEM studies

The TEM and HRTEM investigations were performed to analyse the microstructures of the as-prepared and aged MAlO catalyst. **Fig. 6.9** displays the TEM and HRTEM results for both forms of MAlO catalyst. The HRTEM image reveals that the as-prepared MAlO catalyst surface has a hexagonal morphology as observed in **Fig. 6.9(a)**. However, it changes to a granular-like asymmetrical assembly in aged form as shown in **Fig. 6.9(e)**. The as-prepared MAlO sample's lattice fringe (d spacing), 0.24 nm corresponds to the (311) lattice plane (see **Fig. 9(b, c)**). Conversely, the aged MAlO catalyst's 0.23 and 0.26 nm lattice fringe correlates to the (102) lattice plane of (NiO) and the (104) lattice plane of Al_2O_3, respectively, as demonstrated in **Fig. 6.9(f, g)**. XRD analyses of the pristine and aged MAlO catalyst are in good agreement with the HRTEM analysis. The selected area electron diffraction (SAED) patterns indicate the crystalline nature of the sample.

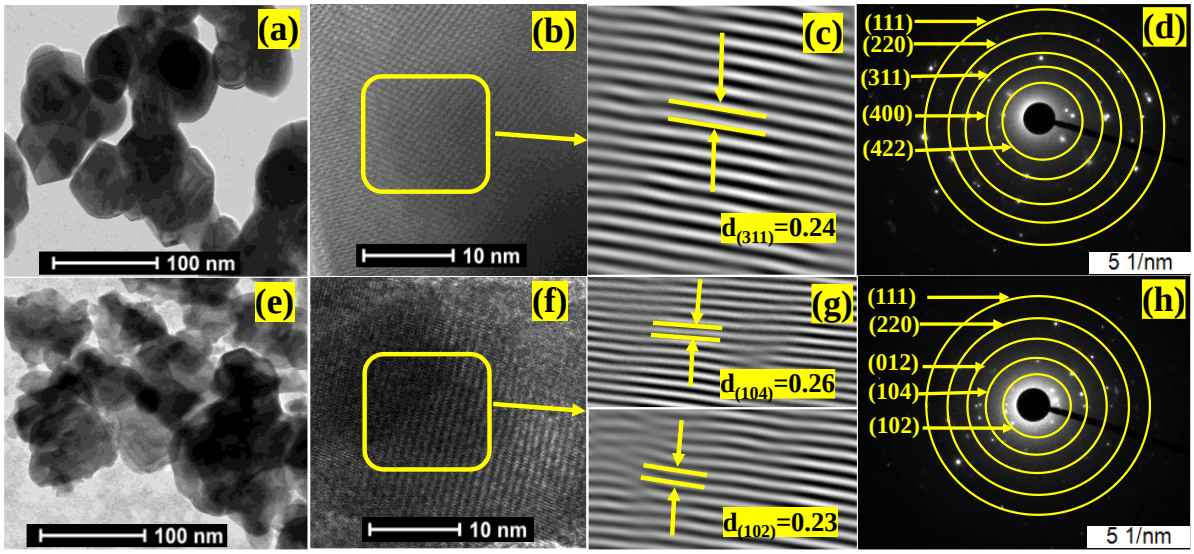

Fig. 6.9: (a, e) TEM figures, (b, f) HRTEM figures, (c, g) enlarged area of HRTEM and (d, h) SAED forms of pure and used MAlO spinel catalyst, respectively.

6.3.7. XPS analyses

It is to be noted that as per definition HESO materials contain several metal ions occupied in tetrahedral and octahedral sites, thereby making them mixed spinel oxides in nature. In the view of this, some metal ions may be present in both the sites, some may be in single site. XPS can enlighten the chemical nature of the metal ions in this type of mixed spinel oxides. In this aspect, XPS studies of as-prepared, aged, and regenerated MAlO catalysts have been carried out for detailed understanding of their elemental information and chemical states as presented in **Fig. 6.10**. The survey spectra of different forms of the HESO catalyst show that Mn, Fe, Co, Ni, Cu, Al, O and C elements are present in the catalyst as shown in **Fig. 5.10 (a)**). In as-prepared MAlO catalyst, Al is in octahedral site and other metals are in tetrahedral site. Al 2p core level spectra in different catalysts are displayed in **Fig. 6.10(b)**. Observed peak at 74.4 eV in as-prepared catalyst corresponds to Al^{3+} species present in the catalyst indicating that Al is in octahedral site. A long tail in the lower binding energy region indicates the presence of tetrahedral component of Al^{3+} species present in the catalyst [64]. In aged catalyst, core level peak is shifted to high binding energy position at 75.7 eV which can be assigned for highly oxidized aluminium species, may be $Al(OH)_3$ formed during DRM condition. **Fig. 6.10(c)** shows Mn 2p core level spectra of the as-synthesized, aged, and regenerated catalysts. In as-prepared catalyst, peaks observed at 640.9 and 652.8 eV with a weak satellite peak at 646.2 eV correspond to Mn^{2+} species present in the catalyst. Mn^{2+} ions may occupy octahedral sites in the HESO. However, peaks at 642.4 and 654.2 eV are related to Mn^{4+} species indicating the

formation of higher oxidation state Mn species during DRM reaction [51, 65]. Mn 2p binding energy peak positions in core level spectrum of the regenerated catalyst are similar to as-prepared catalyst. A hump at 648.1 eV is attributed to Cu LMM peak. **Fig. 6.10(d)** represents Fe 2p core level spectra of as-prepared, aged, and regenerated catalysts. Fe $2p_{3/2,1/2}$ peaks at 711.8 and 725.2 eV with a weak satellite peak at 719.7 eV are assigned to Fe^{3+} species [66], which can occupy preferably occupy tetrahedral site. Considering the broad spectral envelope and mixed kind nature of these spinel oxides there is a possibility of the presence of octahedral Fe^{3+} species in the present HESO catalyst. A hump around 713.6 eV is related to Co LMM contribution from Co species present in the catalyst. Corresponding Fe 2p core level spectrum of aged catalyst is observed to be very weak and spectral characteristics indicate the highly oxidised Fe species such as FeOOH formed in the DRM condition. However, the feature of Fe 2p core level spectrum of regenerated catalyst looks similar to as-prepared catalyst. Intense Co $2p_{3/2,1/2}$ peaks around 781.1 and 796.9 eV along with characteristic strong satellite peaks at 786.5 and 802.9 eV in as-prepared HESO catalyst as shown in **Fig. 6.10(e)** are assigned to Co^{2+} species in tetrahedral site. Co 2p core level spectrum of aged catalyst is very faint with the signature of oxide species [67]. Binding energy peak positions of regenerated catalyst are similar to as-prepared catalyst with sharper features compared to as-prepared catalyst. Ni 2p core level spectra of all the catalysts are displayed in **Fig. 6.10(f)**. Ni $2p_{3/2,1/2}$ core level peaks at 855.7 and 873.6 eV with intense satellites at 862.3 and 880.4 eV are associated with Ni^{2+} species in tetrahedral site of this type of spinel materials [51, 52]. In aged catalyst, like Fe 2p and Co 2p core level spectra, Ni 2p core level spectrum is also found to be very weak. However, an observable Ni $2p_{3/2}$ peak around 853.1 eV can be attributed to reduced Ni oxide as well as metallic species. Upon regeneration of the aged catalyst Ni 2p core level spectral feature is observed to return to that of as-prepared catalyst. Cu 2p core level spectra of as-prepared, aged, and regenerated catalyst are presented in **Fig. 6.10(g)**. Observed Cu $2p_{3/2,1/2}$ peaks at 933.6 and 953.4 eV along with typical $2p_{3/2}$ satellite peaks at 940.8 and 942.9 eV indicating the presence of Cu^{2+} species [52, 68, 69]. Satellite peaks are the characteristic features of the transition metal oxides. There is a noticeable variation in the Cu 2p spectral nature in the aged form of the catalyst. Two Cu $2p_{3/2,1/2}$ tail peaks at 934.8 and 955.1 eV along with intense peaks at 933.6 and 953.4 eV can be attributed to $Cu(OH)_2$ species formed during DRM. However, aged catalyst is properly regenerated as apparent from the corresponding Cu 2p core level spectrum of regenerated form of the catalyst.

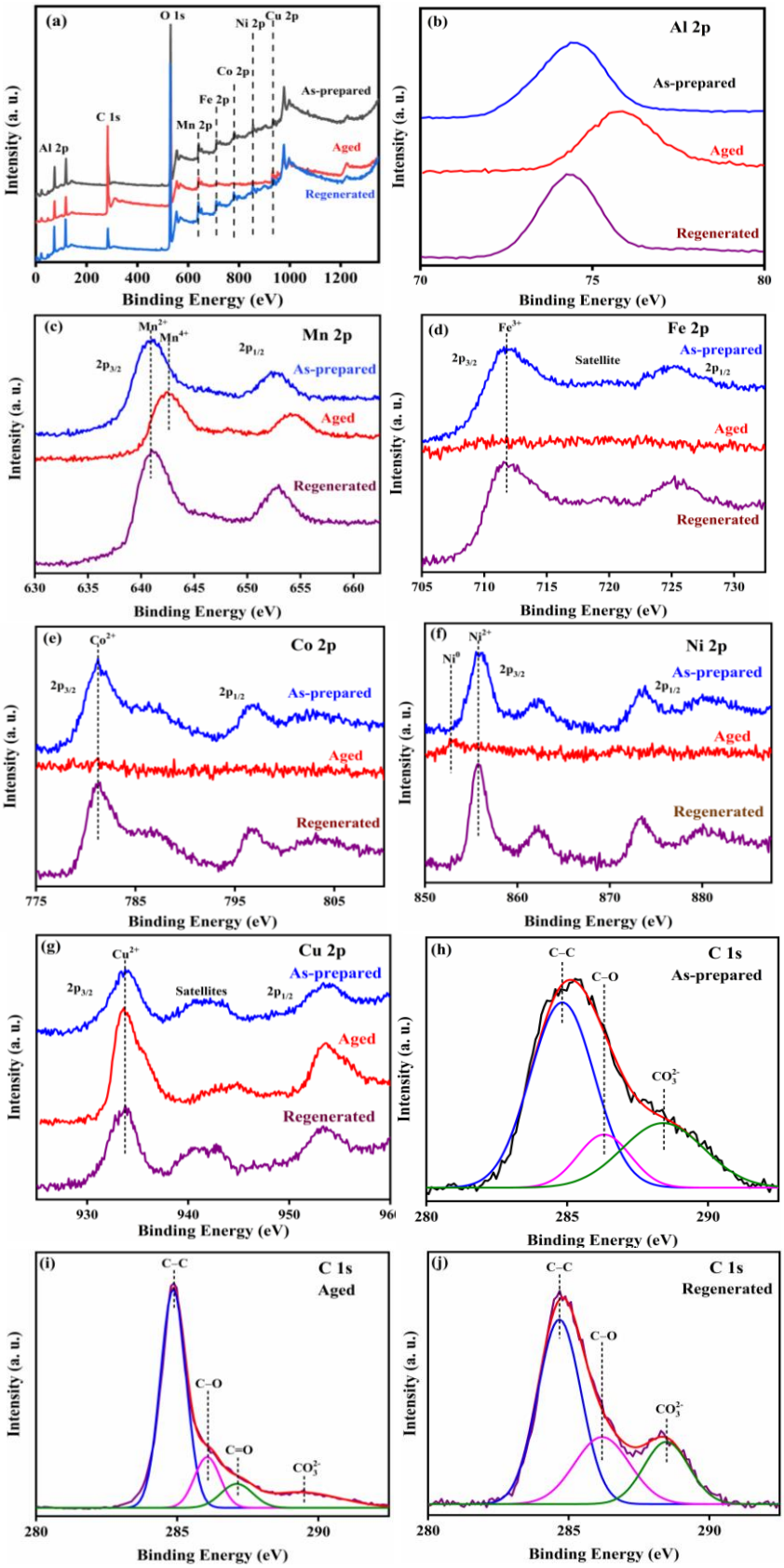

Fig. 6.10: XPS core level spectra of the different forms of MAlO catalysts (a) survey spectra (b) Al 2p (c) Mn 2p, (d) Fe 2p, (e) Co 2p, (f) Ni 2p, (g) Cu 2p and (h–j) C 1s.

C 1s core level spectra of as-prepared, aged, and regenerated HESO catalysts are broad and asymmetric indicating the presence of different carbon species on the catalyst surface which are resolved by curve fitting. Accordingly, the core level peaks at 284.9, 286.2, and 288.9 eV are attributed to C–C/C–H, C–O, and carbonate species (CO_3^{2-}), respectively as shown in **Fig. 6.10(h–i)**. The intensity of oxidized carbon species is observed to increase in the aged catalyst. An additional peak at 287.3 eV is observed in the aged catalyst indication the different chemical environment during DRM [51, 52]. There is no substantial variation in C 1s core level spectrum of regenerated form of the catalyst in comparison with as-synthesized catalyst, which confirms the effective regeneration of aged form of the catalyst. O 1s core level spectra of as-synthesized, aged, and regenerated catalysts are broad and contributions are separated by curve fitting. Peaks observed at 530.5, 531.7, 532.5, and 533.4 eV are associated with M–O, adsorbed hydroxyl (OH^-), adsorbed carbonate, and adsorbed water species, respectively.

6.3.8. Advantage of sol-gel method compared to solution combustion method

Based on the aforesaid results, we have synthesized the same catalyst composition adopting solution combustion synthesis and checked its DRM activity. The activity behaviours of the SG and SCS catalysts were also compared with that of a physical mixture of the constituting phases, Al_2O_3, $Al(OH)_3$, MnO, MnO_2, Fe_2O_3, CoO, NiO, Ni^0, and CuO, as per the required stoichiometry of the HESO catalyst. The oxides were prepared through the conventional sol-gel method [51, 52], and were mixed carefully in a mortar and pestle for 3 h with the gradual addition of acetone. It is important to note that the sol-gel synthesized catalysts are superior in terms of catalytic activity to both the PM and SCS catalysts. The SCS synthesized MAlO, MCrO, MMnO, MFeO, and MCoO catalyst have shown 81%, 75%, 46%, 32%, and 75% CH_4 conversion, respectively. On the other hand, the CO_2 conversions are 87%, 83%, 52%, 36%, and 80%, respectively for 10 h of DRM. For these SCS synthesized catalysts the H_2/CO ratios vary from 0.77 to 1.3 as shown in **Fig. 6.11**. The H_2/CO ratios higher than unity for MAlO, MCrO, and MMnO catalysts suggest that the Boudouard reaction is predominant over the RWGS reaction. On the other hand, the H_2/CO ratio lying below the unity indicates that the extent of the RWGS reaction is higher than the Boudouard reaction. Thus, the sol-gel synthesized catalysts have superior DRM activity compared to the SCS synthesized catalysts. Amazingly, almost no DRM activity was observed for the MAlO PM (data not shown in the figure). Powder XRD analysis of the physical mixture after 10 h of DRM reaction shows

no variations to the constituent phase. Therefore, whether the MAlO catalyst is synthesized by SG or SCS methods, it is reasonable to conclude that the molecular nanocomposite is only generated when the spinel phase of HESO catalyst is decomposed. This result leads us to the conclusion that spatial distribution of the component phases (in the form of molecular nanocomposite, which is formed out of the SG and SCS catalysts in the DRM environment) affects the DRM activity much more than their simple presence (as in the physical mixture, MAlO PM).

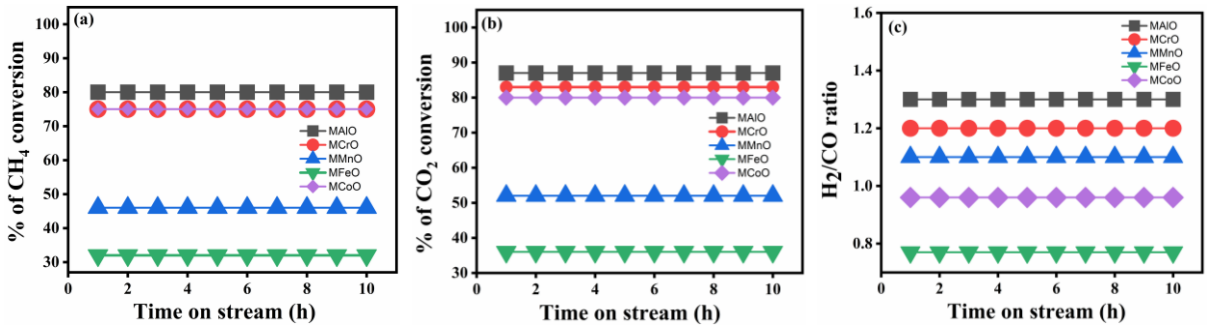

Fig. 6.11: Activity performance of the HESO MAlO, MCrO, MMnO, MFeO, and MCoO HESO catalyst materials prepared by SCS process for 10 h of DRM reaction: (a) methane conversion, (b) carbon dioxide conversion and (c) ratio of H_2/CO (under similar reaction conditions).

In **Table 6.4,** we have done a comparison of the MAlO catalyst with similar types of HEO catalysts existing in the literature in terms of CH_4 and CO_2 conversions, ratio of H_2/CO, reaction temperature, GHSV as well as time on stream of DRM. In majority of the reports, DRM reactions have been done at 800 °C. The DRM of $Fe_4Ni_2CrCoMn_{0.55}O_y$ catalyst has demonstrated methane and carbon dioxide conversion of 98 and 73%, respectively, for 100 h of DRM [45]. The DRM catalytic activity of the catalyst $LaFe_{0.7}Ni_{0.1}Co_{0.1}Cu_{0.05}Pd_{0.05}O_3$ catalyst has shown 64% of CH_4 and 68% of CO_2 conversion for 24 h reaction with H_2/CO ratio 0.8 [46]. The HEO $(Ni_3MoCoZn)Al_{15}O_x$ catalyst [47] has shown 92% CH_4 and 98% CO_2 conversion at fixed GHSV 100000 mL g_{cat}^{-1} h^{-1} for 100 h reaction. 30 h of DRM activity of $CoFeGaNiZn/CeO_2$ [48] catalyst have been investigated which have shown 98% and 86% CO_2 and CH_4 conversions, respectively. Thus, the DRM activity data in **Table 6.4**, suggests that the current HESO $(Mn_{0.2}Fe_{0.2}Co_{0.2}Ni_{0.2}Cu_{0.2})Al_2O_3$ catalyst has high potential in DRM.

Table 6.4: Comparison of the MAlO catalyst with other pertinent catalysts that are reported in the open literature for DRM.

Catalyst	CH_4 conv. (%)	CO_2 conv. (%)	H_2/CO ratio	GHSV (mL g_{cat}^{-1} h^{-1})	Stability tested (h)	Temp. (°C)	Ref.
$Fe_4Ni_2CrCoMn_{0.55}O_y$	98	73	–	9000	100	550	45
$LaFe_{0.7}Ni_{0.1}Co_{0.1}Cu_{0.05}Pd_{0.05}O_3$	64	68	0.80	–	24	800	46
$(Ni_3MoCoZn)Al_{15}O_x$	92	98	0.94	100000	100	800	47
$CoFeGaNiZn/CeO_2$	98	86	1.3	20000	30	750	48
$(Mn_{0.2}Fe_{0.2}Co_{0.2}Ni_{0.2}Cu_{0.2})Al_2O_4$	97	99	~1	34000	100	800	This work

6.3.9. Understandings of catalyst regeneration: Impact of variation of the calcination temperature

Thermal treatment at the synthesis temperature has already been demonstrated to give complete regeneration of the aged HESO catalyst. It is evident that the aged catalyst has undergone complete phase regeneration since all the characteristic diffraction peaks appear at the same 2θ positions as the pure catalyst (see **Fig. 6.12**). XPS investigations further reveal similarities between the core level spectra of the as-prepared and regenerated catalysts for Al 2p, Mn 2p, Fe 2p, Co 2p, Ni 2p, Cu 2p, C 1s, and O 1s. Since the catalyst can be used in a cyclic manner, these results suggest that it has a promising potential application in DRM. The more interesting fact is that, even at lower temperatures of 800 °C and 700 °C, the catalyst could be effectively regenerated by simple calcination in air followed by quenching (see **Fig. 12**). However, the synthesis temperature of 450 °C was used for the regeneration (calcination at this temperature in air for 3 h followed by quenching to room temperature) of the SCS catalyst (see **Fig. 13**).

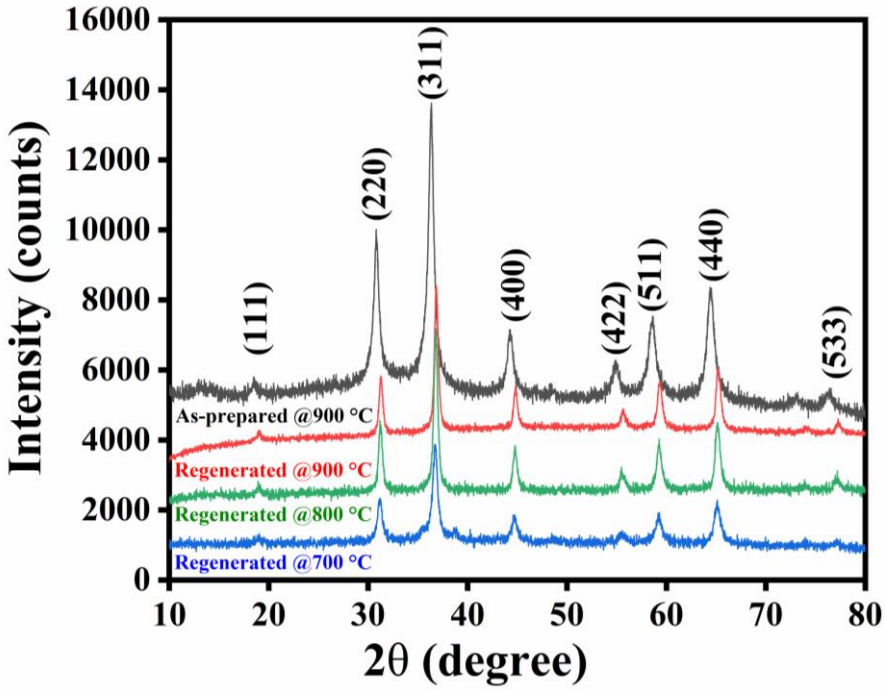

Fig. 6.12: PXRD forms of as-prepared along with regenerated (at various temperatures) MAlO catalyst synthesized adopting sol-gel citrate route.

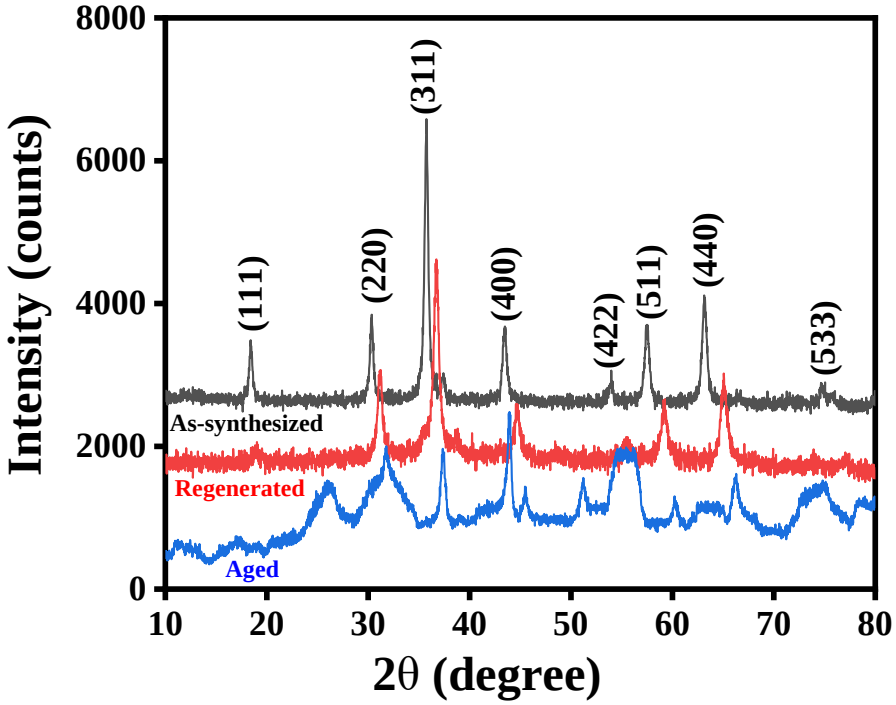

Fig. 6.13: PXRD patterns of various forms of the MAlO catalysts prepared using SCS method.

Fig. 6.14 displays the DRM activity of the MAlO, SG catalysts that were regenerated at various calcination temperatures. The catalyst regenerated at various temperature show comparable DRM activity irrespective of the regeneration temperature. So, the regeneration

temperatures do not affect the catalytic activity of the MAlO catalyst (see **Fig. 6.14(a)–(c)**). Some side reactions occur in the reaction medium, which causes the variations of the H_2/CO ratio. The catalyst regenerated at 900°C exhibited H_2/CO ratio of ~1. This suggests that very slight extent of side reactions have occurred. For the catalysts that were regenerated at 800 °C and 700 °C, the H_2/CO ratio are 0.98 and 0.95, respectively (see **Fig. 6.14(c)**). This is lower than unity suggesting that the extent of RWGS reactions is slightly higher than the Boudouard reaction in the reaction media. In RWGS reaction, the produced H_2 reacts with CO_2, as a result of that, the H_2/CO ratio decreases.

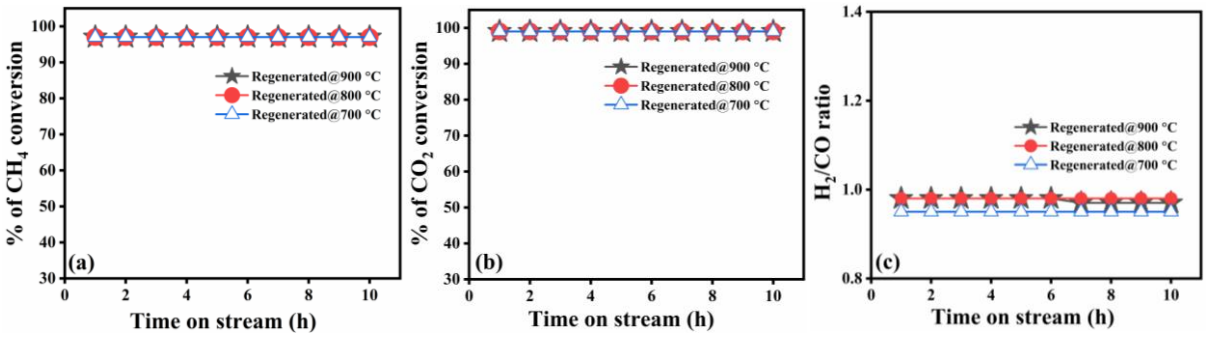

Fig. 6.14: Catalytic performance of MAlO catalyst regenerated at different temperatures: (a) methane conversion (b) carbon dioxide conversion and (c) ratio of H_2/CO (under similar reaction conditions).

6.3.10. TGA studies

Thermogravimetric studies of the as-prepared and aged forms of $(Mn_{0.2}Fe_{0.2}Co_{0.2}Ni_{0.2}Cu_{0.2})Al_2O_4$ catalyst have been done to analyse the carbon deposition on the catalyst after100 h DRM reaction (see **Fig. 6.15**). As the temperature steadily increases to 900 °C, the as-prepared sample does not lose mass. Whereas, mass loss for the aged catalyst sample increases progressively with temperature and becomes steady after 560 °C. The removal of carbon from the catalyst surface, most likely in the form of CO_2 accounts for around 4% of the mass loss. The impact of carbon structure deposited on the catalyst surface on the dry reforming activity of Nickel-carbon composite on the surface of mesocellular silica (MS) made by catalytic chemical vapour deposition (CCVD) method has been studied by Donphai et al. [70]. Their study has shown that the amorphous carbon transforms into carbon nanotubes (CNTs) at higher temperatures. The mass losses have been identified by the following: amorphous carbon at 300–400 °C, low stable carbon nanotubes (CNTs) at 400–550 °C, and very high stable carbon nanotubes (CNTs) at 550–750 °C. However, methanation has the potential to hydrogenate or gasify the less stable carbon nanotubes (CNTs) and amorphous

carbon which partly coated the active site of the nickel clusters in DRM. In a report, Xu et al. have revealed two instances of mass losses [71]. The amorphous carbon oxidation is caused by the peak at about ~400 °C, while the formation of carbon nanotubes is caused by the peak at about ~650 °C. As a result of that amorphous carbon eventually turns into graphite carbon at higher temperatures. It is found that the structure of deposited carbon affects more than simply its content on the catalyst surface [72]. When graphitic carbon layers are present on the active sites of catalyst particles, DRM activity is expected to be decreased [73]. The absence of crystalline forms of deposited carbon in the XRD and HRTEM analyses of the MAlO aged catalyst indicate that the deposited coke was amorphous in nature. According to the TGA analysis, the aged catalyst's mass losses has ended at a temperature of about 560 °C. This suggests that the nature of the deposited coke is amorphous [51, 52]. It is also plausible to assume that the carbon formed in the DRM reaction remains separately from the catalyst. A schematic representation of a potential reversible *in situ* structural transition is shown in **Fig. 6.16**. When the aged HESO catalyst is heated in air at approximately 700 °C, the component oxides can be easily moved to their pristine HESO structure due to their close proximity (~atomic dimension). This process occurs without significantly altering their initial sites in the spinel structure. The starting HESO MAlO (left) gets decomposed into the individual metal oxides in the reforming environment (right), and is then placed at the same sites of the metal ions in the original HESO under heat treatment. Furthermore, it appears that this particular structure would allow for the easy elimination of the generated amorphous carbon at the time of the calcination step, maintaining the catalyst surface unaltered. Consequently, DRM activity in both the phases remains almost unaffected. The simultaneous occurrence of Boudouard and reverse Boudouard processes is also shown by the consistent activity behaviour over a 100 h reaction [43, 51, 52]. While the former process produces coke, the latter occurs quickly to enable the DRM process to facilitate DRM reaction effectively. Based on the aforementioned findings, it has been suggested that the observed high DRM catalytic behaviour is due to the formation of molecular level nanocomposites by the nickel oxide and nickel metal. So, the molecular level nanocomposites are the real performers in the HESO catalyst system for the high DRM activity under the selected reaction condition where other oxide components like α-Al_2O_3 acts as support [41, 53–56], MnO acts as promoter [51, 57, 58], MnO_2 acts as support [38, 57, 58], Fe_2O_3 and CoO act as oxygen carrier [59–62], and CuO acts as promoter [52, 63]. The resulting active species Ni^0/NiO are widely distributed on the surface of the support components. These support systems are simply well-defined structures with uniformly

dispersed tiny active metal particles that are generated *in situ* in the DRM atmosphere. Small metal particles improve the stability and activity of the catalyst while preventing carbon deposition. The high DRM activity of the MAlO catalyst is explained by the formation of this nanocomposite, which exhibits reversible thermal switching between the parent HESO catalyst and the *in situ* produced nanocomposites [51, 52].

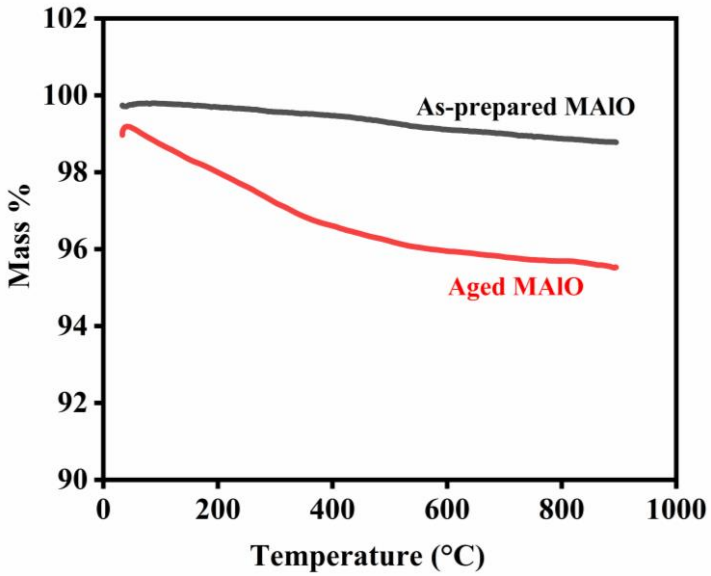

Fig. 6.15: TGA analyses curves of as-prepared and aged MAlO catalyst.

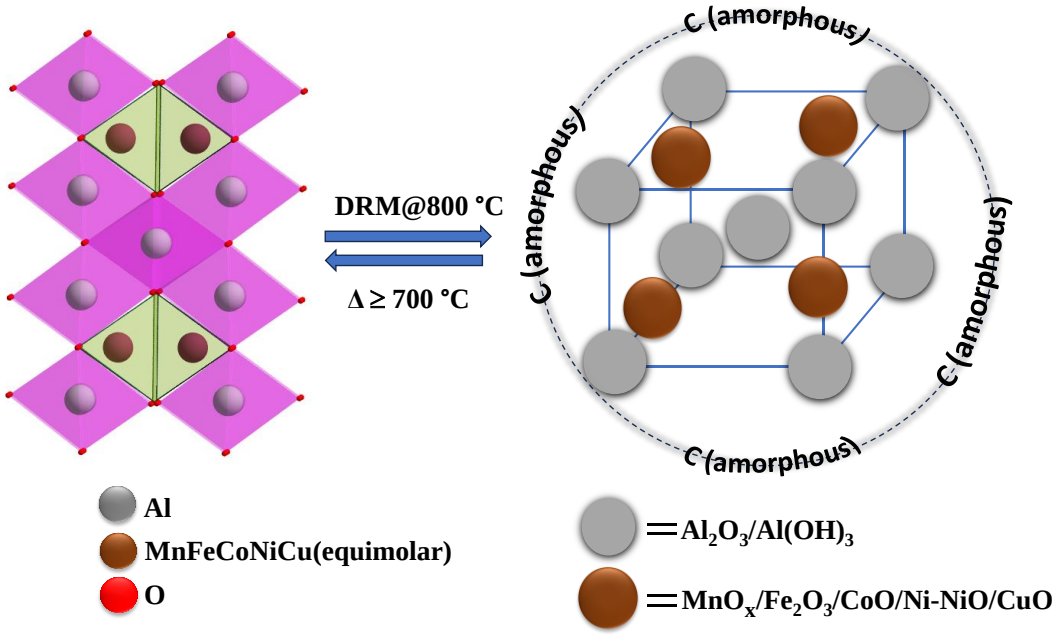

Fig. 6.16: Diagram showing the molecular level nanocomposite that forms *in situ* during DRM and the pristine HESO that can be thermally switched back and forth at a temperature of about ~700 °C. A schematic illustration of the deposition of amorphous carbon on the nanocomposite is also given.

6.4. Conclusions

The nano-sized $(Mn_{0.2}Fe_{0.2}Co_{0.2}Ni_{0.2}Cu_{0.2})M'_2O_4$ (M′ = Al, Cr, Mn, Fe, and Co) high entropy spinel oxide (HESOs) catalysts have been prepared following the traditional sol-gel citrate approach. The PXRD result confirms that cubic phase was adopted by the as-synthesized catalyst. The first DRM test was conducted for 10 h to sort out the superior catalyst. The most active $(Mn_{0.2}Fe_{0.2}Co_{0.2}Ni_{0.2}Cu_{0.2})Al_2O_4$ catalyst is then used in the DRM for 100 h that breakdown in the DRM atmosphere. The decomposed phases have been identified as Al_2O_3, MnO, MnO_2, Fe_2O_3, CoO, Ni, NiO, and CuO. The actual performer of this high DRM activity is a molecular level nanocomposite made up of the nickel oxides and metallic nickel along with other component oxides. The as-prepared MAlO catalyst has a specific surface area of 52 m^2 g^{-1}, while the aged catalyst has a higher area of 77 m^2 g^{-1}. This increase in surface area value for aged catalyst, suggests that smaller components were formed during the DRM reaction that causes disintegration of the original HESO catalyst. Despite the fact that the original catalyst disintegrated into individual oxides in the reaction environment, the degraded phases of the aged catalyst have been restored by calcining it at 900 °C for 3 h. The XRD analyses demonstrate that the spinel phase's characteristic peaks in the regenerated form reappeared at the same 2θ positions as the as-prepared HESO form. The most interesting fact of this catalyst is that phase regeneration can occur at the lowermost calcination temperature of 700 °C. The PXRD, FESEM, HRTEM and XPS results are consistent with the other data that support the complete regeneration of the aged phases. As a result, different forms of $(Mn_{0.2}Fe_{0.2}Co_{0.2}Ni_{0.2}Cu_{0.2})Al_2O_4$ catalyst exhibit a high DRM catalytic activity behaviour suitable for commercialization.

Reference

[1] J.W. Yeh, S.K. Chen, J.Y. Gan, S.J. Lin, T.S. Chin, T.T. Shun, C.H. Tsau, S.Y. Chang, Formation of simple crystal structures in Cu-Co-Ni-Cr-Al-Fe-Ti-V alloys with multiprincipal metallic elements, Metall. Mater. Trans. A: Phys. 35A (2004) 2533-2536.

[2] B. Cantor, I.T.H. Chang, P. Knight, A.J.B. Vincent, Microstructural development in equiatomic multicomponent alloys, Mater. Sci. Eng. A. 375-377 (2004) 213-218.

[3] C.M. Rost, E. Sachet, T. Borman, A. Moballegh, E.C. Dickey, D. Hou, J.L. Jones, S. Curtarolo, J.P. Maria, Entropy-stabilized oxides, Nat. Commun. 6 (2015) 8485.

[4] H. Nan, S. Lv, Z. Xu, Y. Feng, Y. Zhou, M. Liu, T. Wang, X. Liu, X. Hu, H. Tian, Inducing the cocktail effect in yolk-shell high-entropy perovskite oxides using an electronic structural design for improved electrochemical applications, J. Chem. Eng. 452 (2023) 139501.
[5] L. Wang, L. Zhang, X. Lu, F. Wu, X. Sun, H. Zhao, Q. Li, Surprising cocktail effect in high entropy alloys on catalyzing magnesium hydride for solid-state hydrogen storage, J. Chem. Eng. 465 (2023) 142766.
[6] S.S. Aamlid, M. Oudah, J. Rottler, A.M. Hallas, Understanding the role of entropy in high entropy oxides, J. Am. Chem. Soc. 145 (2023) 5991−6006.
[7] S. Jiang, T. Hu, J. Gild, N. Zhou, J. Nie, M. Qin, T. Harrington, K. Vecchio, Jian Luo, A new class of high-entropy perovskite oxides, Scr. Mater. 142 (2018) 116–120.
[8] G. Anand, A.P. Wynn, C.M. Handley, C.L. Freeman, Phase stability and distortion in high-entropy oxides, Acta Mater. 146 (2018) 119–125.
[9] B. Cheng, H. Lou, A. Sarkar, Z. Zeng, F. Zhang, X. Chen, L. Tan, K. Glazyrin, H.P. liermann, J. Yan, L. Wang, R. Djenadic, H. Hahn, Q. Zeng, Lattice distortion and stability of $(Co_{0.2}Cu_{0.2}Mg_{0.2}Ni_{0.2}Zn_{0.2})O$ high entropy oxide under high pressure, Mater. Today Adv. 8 (2020) 100102.
[10] C. Zhao, F. Ding, Y. Lu, L. Chen, Y.S. Hu, High-entropy layered oxide cathodes for sodium-ion batteries, Angew. Chem. Int. Ed. 59 (2020) 264 –269.
[11] H. Wang, Y. Cao, W. Liu, Y. Wang, Oxidation behavior of $(Hf_{0.2}Ta_{0.2}Zr_{0.2}Ti_{0.2}Nb_{0.2})C$-xSiC ceramics at high temperature, Ceram. Int. 46 (2020) 11160–1116.
[12] A. Mao, F. Quan, H.Z. Xiang, Z.G. Zhang, K. Kuramoto, and A.L. Xia, Facile synthesis and ferrimagnetic property of spinel $(CoCrFeMnNi)_3O_4$ high-entropy oxide nanocrystalline powder, J. Mol. Struct. 1194 (2019) 11–18.
[13] A. Mao, H.Z. Xiang, Z.G. Zhang, K. Kuramoto, H. Yu, S. Ran, Solution combustion synthesis and magnetic property of rock-salt $(Co_{0.2}Cu_{0.2}Mg_{0.2}Ni_{0.2}Zn_{0.2})O$ high-entropy oxide nanocrystalline powder, J. Magn. Magn. Mater. 484 (2019) 245–252.
[14] Z. Liu, S. Xu, T. Li, B. Xie, K. Guo, and J. Lu, Microstructure and ferroelectric properties of high-entropy perovskite oxides with A-site disorder, Ceram. Int. 47 (2021) 33039–33046.
[15] J. Ma, K. Chen, C. Li, X. Zhang, L. An, High-entropy stoichiometric perovskite oxides based on valence combinations, Ceram. Int. 47 (2021) 24348–24352.
[16] L. Spiridigliozzi, C. Ferone, R. Cioffi, G.D. Agli, A simple and effective predictor to design novel fluorite-structured High Entropy Oxides (HEOs), Acta Mater. 202 (2021) 181–189.

[17] A. Mao, H.X Xie, H.Z. Xiang, Z.G. Zhang, H. Zhang, S. Ran, A novel six-component spinel-structure high-entropy oxide with ferrimagnetic property, J. Magn. Magn. Mater. 503 (2020) 166594.
[18] H. Zhu, H. Xie, Y. Zhao, S. Dai, M. Li, X. Wang, Structure and magnetic properties of a class of spinel high-entropy oxides, J. Magn. Magn. Mater. 535 (2021) 168063.
[19] Z. Teng, Y. Tan, S. Zeng, Y. Meng, C. Chen, X. Han, H. Zhang, Preparation and phase evolution of high-entropy oxides $A_2B_2O_7$ with multiple elements at A and B sites, J. Eur. Ceram. Soc. 41 (2021) 3614–3620.
[20] A.J. Wright, Q. Wang, C. Hu, Y.T. Yeh, R. Chen, J. Luo, Single-phase duodenary high-entropy fluorite/pyrochlore oxides with an order-disorder transition, Acta Mater. 211 (2021) 116858.
[21] Z. Lei, X. Liu, R. Li, H. Wang, Y. Wu, Z. Lu, Ultrastable metal oxide nanotube arrays achieved by entropy-stabilization engineering, Scr. Mater. 146 (2018) 340–343.
[22] F. Otto, Y. Yang, H. Bei, E.P. George, Relative effects of enthalpy and entropy on the phase stability of equiatomic high-entropy alloys, Acta Mater. 61 (2013) 2628–2638.
[23] P. Edalati, Y. Itagoe, H. Ishihara, T. Ishihara, H. Emami, M. Arita, M. Fuji, K. Edalati, Visible-light photocatalytic oxygen production on a high-entropy oxide by multiple-heterojunction introduction, J. Photochem. Photobiol. A: Chem. 433 (2022) 114167.
[24] C. Wang, W. Liu, M. Liao, J. Weng, J. Shen, Y. Chena, Y. Du, Novel nano spinel-type high-entropy oxide (HEO) catalyst for hydrogen production using ethanol steam reforming, Nanoscale. 15 (2023) 8619–8632.
[25] M. Fracchia, P. Ghigna, T. Pozzi, U.A. Tamburini, V. Colombo, L. Braglia, P. Torelli, Stabilization by configurational entropy of the Cu(II) active site during CO oxidation on $Mg_{0.2}Co_{0.2}Ni_{0.2}Cu_{0.2}Zn_{0.2}O$, J. Phys. Chem. Lett. 11 (2020) 3589−3593.
[26] B. Talluri, M.L. Aparna, N. Sreenivasulu, S.S. Bhattacharya, T. Thomas, High entropy spinel metal oxide $(CoCrFeMnNi)_3O_4$ nanoparticles as a high-performance supercapacitor electrode material, J. Energy Storage. 42 (2021) 103004.
[27] J. Feng, Y. Liu, D. Fang, J. Li, Reusing the steel slag to design a gradient-doped high-entropy oxide for high-performance sodium ion batteries, Nano Energy. 118 (2023) 109030.
[28] B. Xiao, G. Wu, T. Wang, Z. Wei, Y. Sui, B. Shen, J. Qi, F. Wei, J. Zheng, High-entropy oxides as advanced anode materials for long-life lithium-ion batteries, Nano Energy. 95 (2022) 106962.

[29] X. Li, J. Ma, K. Chen, C. Li, X. Zhang, L. An, Design and investigate the electrical properties of $Pb(Mg_{0.2}Zn_{0.2}Nb_{0.2}Ta_{0.2}W_{0.2})O_3$–$PbTiO_3$ high-entropy ferroelectric ceramics, Ceram. Int. 48 (2022) 12848–12855.

[30] A. Mao, H.Z. Xiang, Z.G. Zhang, K. Koji, H. Zhang, Y. Jia, A new class of spinel high-entropy oxides with controllable magnetic properties, Journal of J. Magn. Magn. Mater. 497 (2020) 165884.

[31] S. Zhou, Y Pu, Q. Zhang, R. Shi, X. Guo, W. Wang, J. Ji, T. Wei, T. Ouyang, Microstructure and dielectric properties of high entropy Ba $(Zr_{0.2}Ti_{0.2}Sn_{0.2}Hf_{0.2}Me_{0.2})O_3$ perovskite oxides, Ceram. Int. 46 (2020) 7430–7437.

[32] S.C. Chang, H.Y. Chen, P.H. Chen, J.T. Lee, J.M. Wu, Piezo-photocatalysts based on a ferroelectric high-entropy oxide, Appl. Catal. B: Environ. 324 (2023) 122204.

[33] X. Zhang, J. Zhang, C. Zhou, L. Li, X. Qi, Optical properties and irradiation resistance of novel high-entropy oxide glasses La_2O_3–TiO_2–Nb_2O_5–WO_3–M_2O_3 (M=B/Ga/In), J. Rare Earths. 41 (2023) 507–515.

[34] J.J.T.Herrera, S.A. Korili, A. Gil, Recent progress in the application of Ni-based catalysts for the dry reforming of methane, Catal. Rev. Sci. Eng. 65 (2023) 1300–1357.

[35] M.M. Naira, S. Kaliaguinen, Structured catalysts for dry reforming of methane, New J. Chem. 40 (2016) 4049–4060.

[36] L.E.S. Diaz, R. Schlogl, T. Lunkenbein, Quo vadis dry reforming of methane—a review on its chemical, environmental, and industrial prospects. Catalysts. 12 (2022) 465.

[37] C. Zhang, Y. Li, Z. Chu, Y. Fang, K. Han, Z. He, Analysis of integrated CO_2 capture and utilization via calcium-looping in-situ dry reforming of methane and Fischer-Tropsch for synthetic fuels production, Sep. Purif. Technol. 329 (2024) 125109.

[38] J.N. Heo, N. Son, J. Shin, J.Y. Do, M. Kang, Efficient hydrogen production by low-temperature steam reforming of propane using catalysts with very small amounts of Pt loaded on $NiMn_2O_4$ particles, Int. J. Hydrogen Energy. 45 (2020) 20904–20921.

[39] J. Plou, P. Duran, J. Herguido, J.A. Pena, Purified hydrogen from synthetic biogas by joint methane dry reforming and steam-iron process: Behaviour of metallic oxides and coke formation, Fuel. 118 (2014) 100–106.

[40] Z. Bian, Z. Wang, B. Jiang, P. Hongmanorom, W. Zhong, S. Kawi, A review on perovskite catalysts for reforming of methane to hydrogen production, Renew. Sustain. Energy Rev. 134 (2020) 110291.

[41] Z. Boukha, C.J. Gonzalez, B. Rivas, J.R. Velasco, J.I.G. Ortiz, R.L. Fonseca, Synthesis, characterisation and performance evaluation of spinel-derived Ni/Al_2O_3 catalysts for various methane reforming reactions, Appl. Catal. B: Environ. 158–159 (2014) 190–201

[42] J. Wu, Y. Zheng, J. Fu, Y. Guo, J. Yu, J. Chu, P. Huang, C. Zhao, Synthetic Ni–CaO–CeO_2 dual function materials for integrated CO_2 capture and conversion via reverse water–gas shift reaction, Sep. Purif. Technol. 317 (2023) 123916.

[43] G. Li, H. Hao, P. Jin, M. Wang, Y. Yu, C. Zhang, Dry reforming of methane over Ni/Al_2O_3 catalysts: Support morphological effect on the coke resistance, Fuel. 362 (2024) 130855.

[44] Y. Shao, C. Wu, S. Xi, P. Tan, X. Wu, S. Saqline, W. Liu, Halite-structured $(MgCoNiMnFe)O_x$ high entropy oxide (HEO) for chemical looping dry reforming of methane, Appl. Catal. B: Environ. 355 (2024) 124191.

[45] Y. Liao, Y. He, X. Cui, L. Liu, Elemental Fe conditioning for the synthesis of highly selective and stable high entropy catalysts for CO_2 methanation, Fuel. 355 (2024) 129494.

[46] S. Shah, M. Xu, X. Pan, K.L.A. Aziz, Complex alloy and heterostructure nanoparticles derived from perovskite oxide precursors for catalytic dry methane reforming, ACS Appl. Nano Mater. 5 (2022) 17476−17481.

[47] S. Zhang, Q. Niu, P. Zhang, An entropy engineering strategy to design sulfur-resistant catalysts for dry reforming of methane, Chem. Eng. J. 482 (2024) 149026.

[48] B.P. Gangwar, P. Tripathi, R. Das, S. Sarkar, A.K. Singh, C.S. Tiwary, S. Sharma, Low-temperature dry reforming using high entropy alloy (Co-Fe-Ga-Ni-Zn)-cerium oxide (CeO_2) hybrid nanostructure, Chem. Eng. J. 495 (2024) 153291.

[49] L. Su, H. Huyan, A. Sarkar, W. Gao, X. Yan, C. Addiego, R. Kruk, H. Hahn, X. Pan, Direct observation of elemental fluctuation and oxygen octahedral distortion-dependent charge distribution in high entropy oxides, Nat. Commun. 13 (2022) 2358−2367.

[50] H. Chen, K. Jie, C.J. Jafta, Z. Yang, S. Yao, M. Liu, Z. Zhang, J. Liu, M. Chi, J. Fua, S. Dai, An ultrastable heterostructured oxide catalyst based on high-entropy materials: A new strategy toward catalyst stabilization via synergistic interfacial interaction, Appl. Catal. B: Environ. 276 (2020) 119155.

[51] A. Hossain, M. Bhattacharjee, K. Ghorai, J. Llorca, M. Vasundhara, S. Roy, P. Bera, Md. M. Seikh, A. Gayen, High activity in dry reforming of methane by thermally switchable double perovskite and *in situ* generated molecular level nanocomposite, Phys. Chem. Chem. Phys. 26 (2024) 5447−5465.

[52] A. Hossain, K. Ghorai, T. Bhunia, J. Llorca, M. Vasundhara, P. Bera, A. Bhaskaran, S. Roy, Md. M. Seikh, A. Gayen, Cu-doped $LaNiO_3$ perovskite catalyst for DRM: revisiting it as a molecular-level nanocomposite, Phys. Chem. Chem. Phys. 26 (2024) 26603–26621.
[53] K. Li, C. Pei, X.Li, S. Chen, X. Zhang, R. Liu, J. Gong, Dry reforming of methane over $La_2O_2CO_3$ modified Ni/Al_2O_3 catalysts with moderate metal support interaction, Appl. Catal. B: Environ. 264 (2020) 118.
[54] I. Luisetto, C. Sarno, D.D. Felicis, F. Basoli, C. Battocchio, S. Tuti, S. Licoccia, E.D. Bartolomeo, Ni supported on γ-Al_2O_3 promoted by Ru for the dry reforming of methane in packed and monolithic reactors, Fuel Process. Technol. 158 (2017) 130–140.
[55] J.L. Ewbank, L. Kovarik, F.Z. Diallo, C. Sievers, Effect of metal–support interactions in Ni/Al_2O_3 catalysts with low metal loading for methane dry reforming, Appl. Catal. A. 494 (2015) 57–67.
[56] N. Salhi, A. Boulahouache, C. Petit, A. Kiennemann, C. Rabia, Steam reforming of methane to syngas over $NiAl_2O_4$ spinel catalysts, Int. J. Hydrogen Energy. 36 (2011) 11433–11439.
[57] P. Littlewood, X. Xie, M. Bernicke, A. Thomas, R. Schomacker, $Ni_{0.05}Mn_{0.95}O$ catalysts for the dry reforming of methane, Catal. Today, 242 (2015) 111–118.
[58] S.H. Seok, S.H. Han, J.S. Lee, The role of MnO in $Ni/MnO\text{-}Al_2O_3$ catalysts for carbon dioxide reforming of methane, Appl. Catal. A, 215 (2001) 31–38.
[59] Q. Rao, J. Zhang, T. Yang, Y. Li, Z. Gai, P. Li, X. Wang, Y. Pan, H. Jin, A nickel-modified perovskite-supported iron oxide oxygen carrier for chemical looping dry reforming of methane for syngas production, Chem. Eng. J. 485 (2024) 150033.
[60] X. Mao, A.C. Foucher, E.A. Stach, R.J. Gorte, Changes in Ni-NiO equilibrium due to $LaFeO_3$ and the effect on dry reforming of CH_4, J. Catal. 381 (2020) 561–569.
[61] H. Ay, D. Uner, Dry reforming of methane over CeO_2 supported Ni, Co and Ni–Co Catalysts, Appl. Catal. B. 179 (2015) 128–138.
[62] Z. Xie, B. Yan, S. Kattel, J.H. Lee, S. Yao, Q. Wu, N. Rui, E. Gomez, Z. Liu, W. Xu, L. Zhang, J.G. Chen, Dry reforming of methane over CeO_2-supported Pt-Co catalysts with enhanced activity, Appl. Catal. B. 236 (2018) 280–293.
[63] G.R. Moradi, F. Khosravian, M. Rahmanzadeh, effects of partial substitution of Ni by Cu in $LaNiO_3$ perovskite catalyst for dry methane reforming, Chin. J. Catal. 33 (2012) 797–801.
[64] K. Pal, A. Dey, R. Jana, P.P. Ray, P. Bera, L. Kumar, T.K. Mandal, P. Mohanty, M.M. Seikh, A. Gayen, Citrate combustion synthesized Al-doped CaCu3Ti4O12 quadruple

perovskite: Synthesis, characterization and multifunctional properties, Phys. Chem. Chem. Phys. 22 (2020) 3499–3511.

[65] R. Grissa, H. Martinez, S. Cotte, J. Galipaud, B. Pecquenard, F.L. Cras, Thorough XPS analyses on overlithiated manganese spinel cycled around the 3V plateau, Appl. Surf. Sci. 411 (2017) 449–456.

[66] C.L Aravinda, P. Bera, V. Jayaram, S.M. Mayanna, An X-ray photoelectron spectroscopic study of electrochemically deposited Fe–P thin films on copper substrate, Appl. Surf. Sci. 191, (2002) 128−137.

[67] P. Bera, H. Seenivasan, K.S. Rajam, C. Shivakumar, S.K. Parida, Characterization and microhardness of Co−W coatings electrodeposited at different pH using gluconate bath: A comparative study, Surf. Interface Anal. 45 (2013) 1026−1036.

[68] S. Maiti, A.K. Kundu, O.I. Lebedev, P. Bera, C. Anandan, A. Gayen, M.M. Seikh, Synthesis and magnetic properties of nano-dimensional $Fe_{1-x}Cu_xAl_2O_4$ ($0.3 \leq x \leq 0.8$), RSC Adv. 5 (2015) 83809–83817.

[69] S. Malwadkar, P. Bera, C.V.V. Satyanarayana, Influence of cobalt on performance of Cu−CeO_2 catalysts for preferential oxidation of CO, J. Rare Earths. 38 (2020) 941−950.

[70] W. Donphai, T. Witoon, K. Faungnawakij, M. Chareonpanich, Carbon-structure affecting catalytic carbon dioxide reforming of methane reaction over Ni-carbon composites, J. CO2 Util. 16 (2016) 245–256.

[71] D. Xu, Y. Xiong, S. Zhang, Y. Su, The synergistic mechanism between coke depositions and gas for H_2 production from co-pyrolysis of biomass and plastic wastes via char supported catalyst, J. Waste Manag. 121 (2021) 23–32.

[72] A.J. Carrillo, J.M. Serra, Exploring the stability of Fe–Ni alloy nanoparticles exsolved from double-layered perovskites for dry reforming of methane, Catalysts, 11 (2021) 741.

[73] O.U. Osazuwa, H.D. Setiabudi, R.A. Rasid, C.K. Cheng, Syngas production via methane dry reforming: A novel application of $SmCoO_3$ perovskite catalyst, J. Nat. Gas Sci. Eng. 37 (2017) 435–448.

Chapter 7
Concluding remarks and future directions

Chapter Abstract: *On the basis of the doctoral research work included in the present thesis, general concluding remarks on DRM using oxide-based nano materials are presented here that is followed by future directions of this work.*

Metal oxide-based materials are very important in dealing with the many environmental and industrial problems. In this regard, transition metals and rare earth metal oxides and their nanocomposites play a pivotal role. Over the last decades, research works in these important areas have shown that transition metal oxide-based catalysts as well as their nanocomposite counterparts are considered as one of the most important materials for different types of homogeneous as well as heterogeneous catalytic applications. These catalyst materials are easy to synthesize, thermodynamically stable, structurally flexible and highly active for various types of catalytic purposes. The research work included in different chapters of this thesis are devoted towards the preparation and development of some highly active catalysts and nanocomposite materials for the dry reforming of methane. We have prepared pure oxide-based single perovskite ($LaNi_{0.8}Cu_{0.2}O_3$, named as Cu20LNO), double perovskite (La_2NiMnO_6, named as LNMnO), high entropy perovskite oxide ($La(Mn_{0.2}Fe_{0.2}Co_{0.2}Ni_{0.2}Cu_{0.2})O_3$), named as HEPO) and high entropy spinel oxide ($(Mn_{0.2}Fe_{0.2}Co_{0.2}Ni_{0.2}Cu_{0.2})Al_2O_4$), named as HESO) materials for DRM. The nanocomposites are constituted by the individual metal/metal oxides of the corresponding catalysts that are formed *in situ* from the pristine catalysts in the DRM process. There are several reports available in the open literature on LNO [1–6], LNMnO [7–12], HEPO [13–17], HESO [18–22] and their doped systems for application in numerous fields like organic transformations, photocatalytic dye degradation, catalysis etc. When we started the research work, the study of $LaNi_{0.8}Cu_{0.2}O_3$ in DRM was already reported by Moradi et al. We have done further DRM investigation using $LaNi_{0.8}Cu_{0.2}O_3$ as catalyst. The sustained DRM activity of this catalyst have been explained with the formation of *in situ* nanocomposite due to the degradation of pristine perovskite catalyst in DRM. The pristine catalyst degraded into individual oxide components in DRM atmosphere, but it does not interrupt the methane conversion. The reaction was stopped after 100 h continuous reaction. The aged catalyst was thoroughly characterized to understand the structure-activity relationship.

The aged catalyst can be regenerated by simply calcining in static air at the synthesis temperature. The regeneration can also be done even at 600 °C, which is ~200 °C lower than the synthesis temperature. Thorough characterizations of the aged and regenerated forms of the finalized catalysts have been done to compare them with the as-prepared forms of the catalyst. The DRM activity of La_2NiMnO_6, $La(Mn_{0.2}Fe_{0.2}Co_{0.2}Ni_{0.2}Cu_{0.2})O_3$ and $(Mn_{0.2}Fe_{0.2}Co_{0.2}Ni_{0.2}Cu_{0.2})Al_2O_4$ materials was not available in the literature. Some researchers had reported nanocomposite components of other materials with significant DRM activity [23–26], but the *in situ* formed nanocomposite materials were not explored. Thus, we were motivated to synthesize some *in situ* nanocomposites, where Cu20LNO, LNMnO, HEPO and HESO pure oxide-based materials are used as precursors. Even though the reports on oxide-based *in situ* nanocomposite materials in DRM are very limited, the choice of preparing the nanocomposite materials depend on some key factors: (1) nanocomposite materials should show comparable activity with the pristine catalyst, (2) the long-term durability should not be compromised, (3) active components must be highly dispersed, (4) aged catalyst is expected to be regenerated to pristine phase by simple calcination at the synthesis temperature and others. There are hardly any reports on the formation of nanocomposite in the process of dry reforming. Thus, the *in situ* generated nanocomposite materials, which forms the basis of this research work, can be projected as a new class of catalyst materials for DRM. To synthesize the nanocomposite materials, we have employed various synthetic methods like sol-gel citrate method, solution combustion synthesis, and ceramic method. The catalyst materials have been successfully synthesized by all the aforesaid synthetic methods. The sol-gel citrate method appears to be superior to the solution combustion synthesis, and ceramic method in terms of DRM activity. The different forms of the catalyst have been thoroughly characterized by modern instrumentation techniques. The potential role of these nanocomposite materials has been investigated in a systematic way for DRM and found to be interesting.

The phase purity of all the as-synthesized catalysts, their corresponding nanocomposite materials as well as the regenerated form have been confirmed by PXRD analyses using a Bruker D8 Advance Diffractometer fitted with Lynxeye fast detector with a reasonably slow scan rate of 1 s per step. It was found that the diffraction patterns of the as-prepared and regenerated forms of the catalyst material formed pure phases without any noticeable impurity peak. The regenerated form has shown no remarkable change in PXRD patterns, confirming the successful regeneration of the aged catalyst. For the aged catalyst, the degradation of the pristine catalyst was very evident that is characterized by the formation of a nanocomposite of

the metal/ metal oxide components of the parent oxide catalyst. PXRD has also been used to comprehend the structural-activity relationship of the catalyst materials.

The morphological and microstructure analyses by FESEM, TEM and HRTEM are observed to be useful in understanding the morphology and microstructure of different forms (as-prepared, aged and regenerated) of the catalyst. All materials have shown different types of morphologies that possibly correlate to different classes of the oxides. As expected, different types of lattice fringe patterns have been identified for different forms of the catalyst. The elemental mapping of the corresponding sample showed a homogeneous distribution of the elements in the catalyst. EDX analysis was also very useful to find out the elemental content and the nominal composition of the different forms of the catalyst systems.

BET surface area and porosity of the catalyst materials are important parameters in regard to the long term DRM activity. All the catalyst materials in this work are mesoporous in nature and showed reasonably good to high surface area compared to other reports, which is one of the parameters in heterogeneous catalytic materials in order to explain the high activity of the different catalysts.

The XPS analysis of different forms of the catalyst helped us to correlate the structure-activity relationship. From the XPS analyses, we could find out the oxidation state as well as the atomic percentage of each metal as well as oxygen vacancy, which is very helpful and convincing to explain the comparable catalytic activities of different forms of the catalyst. All the as-prepared samples have shown the expected oxidation state and atomic percentage, confirming the phase purity of the corresponding catalysts. In all the aged forms, any change in binding energies has been attributed to change in oxidation states and or change in the coordination environment of the metal/ metal ions subsequent to degradation of the pristine phase of the catalyst materials. This confirms the *in situ* (in the DRM reaction atmosphere) formation of the nanocomposite materials. The XPS spectra of all the regenerated catalysts look similar to the corresponding as-prepared catalyst, which meant that the oxidation states and the atomic percentages remain almost similar to the as-prepared catalyst. Similar types of XPS spectra of the as-prepared and regenerated forms of the catalyst material confirm the successful regeneration of the aged catalyst.

In order to determine the extent of coke that was deposited on the sample's surface during the DRM, thermogravimetric analysis was done to compare with the as-prepared catalyst. There is no sharp change in mass loss in TGA for all the as-prepared catalyst materials, but for the aged catalysts, different mass losses are observed due to coke deposition.

We have investigated the potential role of all the catalyst materials in DRM at a reasonably good GHSV of 34000 mL g_{cat}^{-1} h^{-1}. The as-prepared catalysts were found to be most active at 800 °C. All the optimized samples have shown high activity for 100 h DRM reaction. The different forms of all the catalyst materials have shown comparable DRM activities. We have employed all the available instruments to understand the structure-activity relationship of the catalyst materials. The roles of the individual oxides and metallic nickel have been discussed. A summary of the most important catalysts developed through the research work are included is summarized in **Table 7.1**. In each of the catalyst systems, the catalytic role is played by the *in situ* generated nanocomposite at the molecular level and could potentially compete with the traditional ones.

Table 7.1: Brief overview of the finalized catalyst materials of this research work in DRM (Reaction condition: GHSV of 34000 mL g_{cat}^{-1} h^{-1} and temperature of 800 °C)

Catalyst	**CH_4 conversion (%)**	**CO_2 conversion (%)**	**H_2/CO ratio**
$LaNi_{0.8}Cu_{0.2}O_3$ (Cu20LNO)	97	98	1.2
La_2NiMnO_6 (LNMnO)	97	99	0.9
$La(Mn_{0.2}Fe_{0.2}Co_{0.2}Cu_{0.2}Ni_{0.2})O_3$ (HEPO)	86	90	~1
$(Mn_{0.2}Fe_{0.2}Co_{0.2}Cu_{0.2}Ni_{0.2})Al_2O_4$ (HESO)	97	99	~1

At first, we desired to understand more about the role of the catalyst in DRM and to find out the answer of few questions about the structure-activity of the catalyst. Why does the single-phase catalyst degrade in the reaction medium? What are the active components responsible for sustained activity? Why do the same catalysts synthesized via different methods show different activity?

Initially, our goal was to synthesize oxide-based single phase nano catalysts for DRM with improved activity and coke resistivity. In this regard, some metal oxide-based catalysts

have been synthesized. But, during the DRM tests, the pristine phase of the catalyst gets degraded into binary oxides forming a nanocomposite of these with metallic nickel as revealed thorough characterization of the various forms of the catalyst. These nanocomposite are responsible for the high DRM activity of the corresponding catalysts. The structure-activity relationship is explained with the help of PXRD, FESEM, HRTEM and XPS analyses. But it would have been more relevant if any *in situ* characterization/ tests could be done. For heterogeneous catalysis, the mechanism of the reaction is very important to correlate the structure of the catalyst with the observed activity behavior. For this purpose, *in situ* DRIFTS is an important technique which could not be done due to the lack of availability of the instrument. We could not continue the DRM reaction beyond 100 h (as desired for industrial applications) due to some reasons beyond our control. But we believe that the catalysts will show a durability behavior that is desirable. We, have checked the DRM activity at different temperatures and the optimized temperature was 800 °C. But we could not check the DRM activity at different gas hourly space velocities. We were unable to perform any theoretical studies due to unavailability of the computing facility. For better information about the electronic structure and the environment of atoms/ ions within a material at the surface, X-ray absorption near edge structure (XANES) spectroscopy is a very useful technique, but we could not manage it for analysis. It was also not possible for us to do extended X-ray absorption fine structure (EXAFS) spectroscopy, which is a very helpful technique to study the local structure of materials by evaluating the fine structure in the X-ray absorption spectrum. Inductively coupled plasma-optical emission spectrometry (ICP-OES) gives the elemental composition of a catalyst material which could not be done for the lack of proper instrumental facility. We could not manage to do the CHN analysis, which is a good supportive analysis for the carbon quantification.

At this backdrop, the following aspects may be of interest for future work:

- Synthesis of more numbers of high entropy oxide-based catalysts with tuneable redox and acid-base properties to achieve improved activity and high coke resistivity.
- The detailed mechanism of the DRM reaction needs to be investigated to understand how the active species interacts with the support systems.
- Mechanism of coke deposition needs to be understood through *in situ* characterization and the nature of coke needs to be understood better, since all the deposited carbon does not deactivate the catalyst.

- The role of different synthetic methods in DRM has to be examined further.
- DFT studies are to be done to predict better the active sites and reaction pathways.
- The roles of different metal oxides vis-à-vis metallic nickel needs extensive studies to ascertain and explain the DRM activity behaviour of the molecular level nanocomposite formed *in situ* in the reaction environment.

Reference

[1] D.K. Hwang, S. Kim, J.H. Lee, I.S. Hwang, D. Kim, Phase evolution of perovskite $LaNiO_3$ nanofibers for supercapacitor application and p-type gas sensing properties of LaOCl–NiO composite nanofibers, J. Mater. Chem., 2011, 21, 1959–1965.

[2] C. Chen, R. Bao, L. Yang, S. Tai, Y. Zhao, W. Wang, J. Xia, H. Li, Application of inorganic perovskite $LaNiO_3$ partial substituted by Ce and Cu in absorbance and photocatalytic degradation of antibiotics, Appl. Surf. Sci., 2022, 579, 152026.

[3] C. Lykos, K. Tsalpatouros, G. Fragkos, I. Konstantinou, Synthesis, characterization, and application of Cu-substituted $LaNiO_3$ perovskites as photocatalysts and/or catalysts for persulfate activation towards pollutant removal, Chemosphere, 2024, 352, 141477.

[4] G. Perin, J. Fabro, M. Guiotto, Q. Xin, M.M. Natile, P. Cool, P. Canu, A. Glisenti, Cu@$LaNiO_3$ based nanocomposites in TWC applications, Appl. Catal. B: Environ., 2017, 209, 214–227.

[5] H.S. Kim, S.H. Park, M.J. Han, Epitaxially strained ultrathin $LaNiO_3$/$LaAlO_3$ and $LaNiO_3$/$SrTiO_3$ superlattices: A density functional theory + U study, Curr. Appl. Phys., 2023, 50, 53–60.

[6] S. Iqbal, I. Bibi, F. Majid, S. Kamal, N. Alwadai, M. Iqbal, Band gap tuning by Gd and Fe doping of $LaNiO_3$ to boost solar light harvesting for photocatalytic application: A mechanistic approach, Opt. Mater., 2022, 124. 111962.

[7] A. Hossain, A.K.M.A Ullah, P.S. Guin, S. Roy, An overview of La_2NiMnO_6 double perovskites: synthesis, structure, properties, and applications, J. Solgel Sci. Technol., 2020, 93, 479–494.

[8] C. Lan, S. Zhao, T. Xu, J. Ma, S. Hayas, T. Ma, Investigation on structures, band gaps, and electronic structures of lead free La_2NiMnO_6 double perovskite materials for potential application of solar cell, J. Alloys Compd., 2016, 655, 208–214.

[9] T. Sharmili, A.J. Preethi, J. Vigneshwaran, K. Ganesan, M. Ragam, Dielectric, electrochemical and magnetic properties of the hydrothermally synthesized double perovskite La_2NiMnO_6 for energy storage applications, Ceram. Int., 2024, 50, 3005–3017.

[10] T. Sangavi, S. Vasanth, C. Viswanathan, N. Ponpandian, Synergizing experimental and theoretical insights: Unveiling the solar potential of La_2NiMnO_6 double perovskite for enhanced efficiency and sustainability in photovoltaics, Chem. Eng. J., 2024, 486, 150216.

[11] K.I. Nassar, N. Rammeh, S.S. Teixeira, M.P.F. Graca, Effect of Pr substitution in the A site on the structural, dielectric and magnetic properties of double perovskite La_2NiMnO_6, Appl. Phys. A., 2022, 128, 373.

[12] U. Dutta, A. Haque, M.M. Seikh, Synthesis, structure and magnetic properties of Ti doped La_2MnNiO_6 double perovskite, Chim. tech. acta., 2019, 6, 80–92.

[13] S Jiang., T. Hu, J. Gild, N. Zhou, J. Nie, M. Qin, T. Harrington, K, Vecchio, J. Luo, A new class of high-entropy perovskite oxides, Scr. Mater., 2018, 142, 116–120.

[14] J. Ma, T. Liu, W. Ye, Q. He, K. Chen, High-entropy perovskite oxides for energy materials: A review, J. Energy Storage, 2024, 90, 111890.

[15] S. Ye, J. Zhu, S. Zhu, Y. Zhao, M. Li, Z. Huang, H. Wang, J. He, design strategies for perovskite-type high-entropy oxides with applications in optics, ACS Appl. Mater. Interfaces 2023, 15, 47475–47486.

[16] J. Ma, K. Chen, C. Li, X. Zhang, L. An, High-entropy stoichiometric perovskite oxides based on valence combinations, Ceram. Int., 2021, 47, 24348–24352.

[17] Y. Shi, Q. Xu, Z Tian, G. Liu, C. Ma. W. Zheng, Ionic liquid-hydroxide-mediated low-temperature synthesis of high-entropy perovskite oxide nanoparticles, Nanoscale, 2022, 14, 7817.

[18] Z. Sun, Y. Zhao, C. Sun, Q. Ni, C. Wang, H. Jin, High entropy spinel-structure oxide for electrochemical application, Chem. Eng. J., 2022, 431 133448.

[19] H.X. Guo, W.M. Wang, C.Y. He, B.H. Liu, D.M. Yu, G. Liu, X.H. Gao, Entropy-assisted high-entropy oxide with a spinel structure toward high-temperature infrared radiation materials, ACS Appl. Mater. Interfaces., 2022, 14, 1950−1960.

[20] Y. Xu, X. Xu, L. Bi, A high-entropy spinel ceramic oxide as the cathode for proton-conducting solid oxide fuel cells, J Adv Ceram 2022, 11(5): 794–804.

[21] K. Iwase, I. Honma, High-entropy spinel oxide nanoparticles synthesized via supercritical hydrothermal processing as oxygen evolution electrocatalysts, ACS Appl. Energy Mater., 2022, 5, 8, 9292–9296.

[22] T. Hashishin, H. Taniguchi, F. Li, H. Abe, Useful high-entropy source on spinel oxides for gas detection, Sensors 2022, 22 (11), 4233.

[23] M.S. Aw, M. Zorko, I.G.O. Crnivec, A. Pintar, Progress in the synthesis of catalyst supports: synergistic effects of nanocomposites for attaining long-term stable activity in CH_4–CO_2 dry reforming, Ind. Eng. Chem. Res. 2015, 54, 15, 3775–3787.

[24] R.R. Ikreedeegh, M.Tahir, Facile fabrication of well-designed 2D/2D porous g-C_3N_4–GO nanocomposite for photocatalytic methane reforming (DRM) with CO_2 towards enhanced syngas production under visible light, Fuel, 2021, 305, 121558.

[25] A.H. Khoja, M. Tahir, N.A.S. Amin, Cold plasma dielectric barrier discharge reactor for dry reforming of methane over Ni/ɣ-Al_2O_3-MgO nanocomposite, Fuel Processing Technology, 2018, 178, 166–179.
[26] T. Wu, Q. Zhang, W. Cai, P. Zhang, X. Song, Z. Sun, L. Gao, Phyllosilicate evolved hierarchical Ni- and Cu–Ni/SiO_2 nanocomposites for methane dry reforming catalysis, Applied Appl. Catal. A: Gen., 2015, 503, 94–102.